

UNIVERSIDAD COMPLUTENSE DE MADRID

FACULTAD DE CIENCIAS FÍSICAS



TESIS DOCTORAL

Los efectos de la rotación y la metalicidad sobre la merma de litio en
estrellas de tipo solar

The effects of rotation and metallicity on the lithium depletion of solar-type stars

MEMORIA PARA OPTAR AL GRADO DE DOCTOR

PRESENTADA POR

Diego Cuenda Muñoz

DIRIGIDA POR

David Barrado Navascués

UNIVERSIDAD COMPLUTENSE DE MADRID

Facultad de Ciencias Físicas

Programa de Doctorado en Astrofísica



TESIS DOCTORAL

**Los efectos de la rotación y la metalicidad sobre la merma de litio en
estrellas de tipo solar**

The effects of rotation and metallicity on the lithium depletion of solar-type stars

MEMORIA PARA OPTAR AL GRADO DE DOCTOR PRESENTADA POR:

Diego Cuenda Muñoz

Supervisado por:

Dr. David Barrado Navascués



U N I V E R S I D A D
COMPLUTENSE
M A D R I D

**DECLARACIÓN DE AUTORÍA Y ORIGINALIDAD DE LA TESIS
PRESENTADA PARA OBTENER EL TÍTULO DE DOCTOR**

D./Dña. Diego Cuenda Muñoz,
estudiante en el Programa de Doctorado en Astrofísica,
de la Facultad de Ciencias Físicas de la Universidad Complutense de
Madrid, como autor/a de la tesis presentada para la obtención del título de Doctor y
titulada:

The effects of rotation and metallicity on the lithium depletion of solar-type stars

Los efectos de la rotación y la metalicidad sobre la merma de litio en estrellas de tipo solar

y dirigida por: Dr. David Barrado Navascués

DECLARO QUE:

La tesis es una obra original que no infringe los derechos de propiedad intelectual ni los derechos de propiedad industrial u otros, de acuerdo con el ordenamiento jurídico vigente, en particular, la Ley de Propiedad Intelectual (R.D. legislativo 1/1996, de 12 de abril, por el que se aprueba el texto refundido de la Ley de Propiedad Intelectual, modificado por la Ley 2/2019, de 1 de marzo, regularizando, aclarando y armonizando las disposiciones legales vigentes sobre la materia), en particular, las disposiciones referidas al derecho de cita.

Del mismo modo, asumo frente a la Universidad cualquier responsabilidad que pudiera derivarse de la autoría o falta de originalidad del contenido de la tesis presentada de conformidad con el ordenamiento jurídico vigente.

En Madrid, a 11 de diciembre de 2024

Firmado por CUENDA MUÑOZ
DIEGO - ***4916**
Fecha: 11/12/2024
11:15:15 CET

Fdo.: _____

Esta DECLARACIÓN DE AUTORÍA Y ORIGINALIDAD debe ser insertada en
la primera página de la tesis presentada para la obtención del título de Doctor.

Resumen

Dado que en la base de la zona convectiva de estrellas G y K se destruye litio (Li) gradualmente, la abundancia superficial de este elemento constituye indicador de la edad para estos tipos espectrales. Sin embargo, la abundancia de Li no sólo depende de la edad, sino que otros factores como la metalicidad, la actividad y la rotación de la estrella también juegan un papel importante. Caracterizar la influencia de cada uno de ellos en cada etapa de la evolución estelar resulta enormemente complejo. No obstante, los cúmulos abiertos constituyen objetos de estudio perfectos para este tipo de análisis, dado que todos sus miembros comparten la misma edad y metalicidad.

A lo largo de este trabajo hemos estudiado la influencia de la rotación y la metalicidad sobre la merma de Li en miembros GK del cúmulo abierto M35, cuya edad es similar a la de las Pleiades. Para ello, partimos de una muestra de 165 estrellas observadas con el espectrógrafo WIYN/Hydra que ha sido complementada gracias a estudios previos de Li en este cúmulo. La muestra resultante incluye 396 estrellas, las cuales fueron separadas en miembros y no miembros de M35. A partir de los espectros de los 110 miembros añadidos por nosotros a la muestra existente hemos medido abundancias de Li y hierro para esas estrellas. Además, obtuvimos periodos de rotación a partir de curvas de luz de Zwicky Transient Facility y de estudios previos. Gracias a estos datos hemos confirmado que los rotadores rápidos de tipo GK son ricos en Li en comparación con rotadores más lentos de temperatura efectiva similar. A pesar de que nosotros hemos calculado una metalicidad promedio para M35 de $[Fe/H] = -0.26 \pm 0.09$, su distribución de Li es similar a la observada en M34 y las Pleiades, cúmulos de metalicidades solares y edades ligeramente distintas a la de M35. Así pues, concluimos que una diferencia de 0.2–0.3 dex en metalicidad no tiene efectos observables en las distribuciones de Li de cúmulos entre 100 y 250 Myr.

Además, también hemos estudiado la influencia de estos factores sobre la merma de Li en miembros de dos cúmulos abiertos de 600 Myr: Coma Berenices y Praesepe. Para ello, partimos de muestras de miembros GK de cada cúmulo provenientes de publicaciones anteriores. Para estos objetos hemos medido anchuras equivalentes de Li a partir de espectros de alta resolución tomados por nosotros o recuperados de archivos. Además, hemos aprovechado estudios anteriores de Li en estos cúmulos para configurar nuestras muestras finales, las cuales incluyen 55 miembros de Praesepe y 37 de Coma. Dado que Coma ha sido observado por el satélite TESS en varios ciclos, hemos utilizado las curvas de luz tomadas por esta misión para obtener periodos de rotación para sus miembros. Además, también hemos recuperado periodos de rotación de estudios fotométricos previos tanto en el caso de Coma como en el de Praesepe. Sólo hemos observado valores atípicos de Li en una binaria espectroscópica en cada cúmulo. En otras palabras, la dispersión en Li observada en el rango de las K es debida a binarias de corto periodo que rotan rápido, mientras que la dispersión en el rango de las G es despreciable. Al comparar la distribución de Li en Coma con la que presentan Praesepe y las Hyades, que tienen metalicidades más altas y edades similares, se observa una sutil tendencia hacia anchuras equivalentes de Li mayores para miembros G de Coma.

Palabras clave: estrellas: abundancias – estrellas: tipo tardío – estrellas: rotación – cúmulos abiertos: Coma Berenices – cúmulos abiertos: Praesepe – cúmulos abiertos: M35

Abstract

Since lithium (Li) is gradually destroyed at the base of the convective envelope of G and K stars, the Li surface abundance constitutes an useful age tracer for these stellar types. However, the abundance of this element depends not only on age but also on additional factors, such as rotation, activity, and metallicity. Determining the effects of these factors on Li depletion along stellar evolution is a challenging task. Nevertheless, open clusters constitute perfect targets for this kind of studies as all the members of these associations share the same age and metallicity.

We have investigated how Li depletion is affected by rotation and metallicity in GK members of the roughly Pleiades-aged open cluster M35. To do so, we have collected an initial sample of 165 candidate members observed with the WIYN/Hydra spectrograph and we have taken advantage of three previous spectroscopic studies of Li in M35. As a result, we have collected a final sample of 396 stars observed with the same instrument, which we have classified as members and non-members of the cluster. We have measured iron and Li abundances for the 110 M35 members added to the existing sample by this study. Besides this, rotation periods for cluster members have been obtained from the literature or derived from Zwicky Transient Facility light curves. From these data, we have confirmed that fast GK rotators are Li-rich in comparison with slow rotators of similar effective temperature. Furthermore, while we derived an average metallicity of $[\text{Fe}/\text{H}] = -0.26 \pm 0.09$ from our spectra, the distribution of Li in M35 is similar to those observed for the Pleiades and M34 open clusters, which have solar metallicity and slightly different ages. Consequently, we conclude that a 0.2–0.3 dex difference in metallicity makes little difference in the Li distributions of open clusters with ages between 100 and 250 Myr.

We have also studied the influence of rotation and metallicity on the Li abundance in members of two 600 Myr open clusters: Coma Berenices and Praesepe. To achieve this goal, we have selected a sample of GK members for each cluster from previous studies. We have measured Li equivalent widths for them from high resolution spectra taken by us or from archival spectra. In addition, we have taken advantage of the Li equivalent widths available in the literature to increase the sizes of our samples. As a result, our final samples of Praesepe and Coma are composed of 55 and 37 dwarfs, respectively. Since Coma has been observed by the Transiting Exoplanet Survey Satellite in several cycles, we have used the light curves provided by this mission to derive rotation periods for the members of this cluster. Besides this, we have taken advantage of previous studies to obtain rotation periods for members of both clusters. Lithium overabundance linked to fast rotation has only been observed for one spectroscopic binary in each cluster. In other words, the Li spread observed in these clusters in the range of the K stars is due to fast-rotating close binaries, and the spread is negligible for hotter objects. Finally, we have compared the distribution of Li in Coma with those of Praesepe and Hyades, which have higher metallicity and similar ages, finding a subtle trend towards higher Li equivalent widths in G Coma members.

Keywords: stars: abundances – stars: late-type – stars: rotation – open clusters and associations: Coma Berenices – open clusters and associations: Praesepe – open clusters and associations: M35

A mis padres

Agradecimientos

Este documento resume el trabajo que he llevado a cabo durante los últimos cinco años. A lo largo de este tiempo, muchas personas han enriquecido mi experiencia como estudiante de doctorado de muy distintas maneras. No obstante, quiero dejar claro que a las dos personas a las que más tengo que agradecer es a quienes va dedicado este trabajo, mis padres, sin cuyo apoyo, educación y aliento no me hubiera convertido en quien soy a día de hoy. Mamá, papá, gracias por contagiarme desde niño el amor por la ciencia y por animarme siempre a perseguir mis sueños.

Durante estos años he tenido la oportunidad de crecer como investigador de la mano de David Barrado, un gran profesional a quien le agradezco enormemente sus enseñanzas y que nunca tirara la toalla conmigo. También agradezco con mucho cariño las enseñanzas de Marcel Agüeros, cuya implicación en este trabajo ha ido mucho más allá de su papel de supervisor de estancia. Asimismo, también quiero agradecer a Hervé Bouy, mi otro supervisor de estancia, todas las facilidades que me brindó durante mi paso por Burdeos. Aprender de ellos ha sido un gran honor.

Como estudiante de doctorado del Centro de Astrobiología me he cruzado a diario con muchas personas que han enriquecido esta experiencia. Con ellas he compartido innumerables comidas, cafés, discusiones científicas, animadas charlas y risas. De entre estas personas quiero mencionar con especial cariño a Miguel Cerviño, Albert Domingo, Félix Llorente y Benjamín Montesinos, cuyo apoyo y consejo valoro enormemente. Asimismo, no puedo dejar de hablar de la larga lista de estudiantes a quienes he tenido el placer de conocer: Jorge, Amadeo, Jaime, Raquel, Diego, Jose Luis, Patricia, Carlos, Emilio, Federico, Carmen, Diego, Luis, Miki, Samuel y un largo etcétera. De esta lista me gustaría destacar a tres personas. Dos de ellas son Alberto y Pedro, con quienes he compartido la mayor parte de este trayecto, y cuyo humor y amistad iluminaron los oscuros y tristes meses tras la pandemia. La otra es Olga, mi "compi", cuyo apoyo permanente desde el día en que la conocí ha sido de un incalculable valor para mí.

Ha sido un camino que he disfrutado mucho, pero que también ha tenido momentos duros. Sin embargo, si estuviéramos a día 11 de diciembre de 2019, volvería a comenzar sin dudar.

Table of Contents

1	Introduction	1
2	Lithium, rotation and metallicity in the open cluster M35	11
2.1	Assembling our spectroscopic sample	12
2.1.1	New Hydra spectra	12
2.1.2	Previously published spectra from these campaigns	14
2.1.3	Other Hydra surveys of M35	14
2.1.4	The complete sample	15
2.2	Revisiting the membership and multiplicity of stars in our sample	15
2.2.1	An initial membership selection based on Bouy et al. (2015) and our own proper-motion analysis	15
2.2.2	Measuring radial velocities and distinguishing between single and binary stars in our sample	17
2.2.3	Summary	20
2.3	Assembling our sample of rotation periods	21
2.3.1	Rotation periods from the literature	21
2.3.2	New rotational periods from ZTF light curves	23
2.3.3	Final sample of M35 members with Li measurements and rotation periods	23
2.4	Analysis	24
2.4.1	Deriving effective temperatures and luminosities	24
2.4.2	Measuring equivalent widths and abundances	26
2.5	Results	33
2.5.1	The metallicity of M35	33
2.5.2	The Li-rotation connection in M35	35

2.5.3	Comparison with other clusters	38
3	The effects of rotation and metallicity on the lithium depletion in 600 Myr open clusters	45
3.1	Assembling the sample	46
3.1.1	Target selection for Coma Berenices	46
3.1.2	Target selection for Praesepe	47
3.1.3	Spectroscopic observations	47
3.1.4	Archival spectra and data from the literature	48
3.1.5	Multiple systems in our samples	49
3.1.6	The final samples	50
3.2	Obtaining rotation periods	53
3.2.1	Coma Berenices	53
3.2.2	Praesepe	54
3.3	Analysis	55
3.3.1	Deriving effective temperatures and luminosities	55
3.3.2	Measuring Li equivalent widths	56
3.4	Results	59
3.4.1	Lithium distributions in Coma Berenices and Praesepe	59
3.4.2	Comparison between them and with other clusters	63
4	Summary and conclusions	68
	Bibliography	79
	Acknowledgements	81
A	M35 tables	82
B	Coma Berenices tables	123

C Praesepe tables	127
D Rotation periods derived from TESS light curves for Coma Berenices members	133
E On the origin of high-metal lithium-poor stars	167

Chapter 1

Introduction

Lithium (Li) is gradually destroyed in the interiors of solar-like F, G, and K main-sequence (MS) stars due to convection currents that transport atoms of this element to deeper (and hotter) zones of the convective envelope of these stars. When the temperature reaches 2.5 MK, lithium is transformed into helium following Equation 1.1. As a result, Li surface abundance decreases as the star evolves in the MS.



Evidence of this process was first provided by [Herbig \(1965\)](#) and [Zappala \(1972\)](#). The former study was focused on a sample of 100 nearby F5-G8 dwarfs including a few members of the Pleiades, Hyades, and Coma Berenices (Coma) open clusters (OCs), whereas the latter was focused on F-K dwarfs in the Hyades, Pleiades, Praesepe, and NGC 2264. Both analysis pointed to a gradual depletion of Li as a result of which Hyades members are Li poor in comparison with Pleiades members.

Not all stars burn Li at the same rate. As the process takes place in the convective envelope of the star, stars of different spectral types (and therefore with different internal structures) burn Li at different rates. For the range of effective temperatures (T_{eff}) that includes late F, G, K, and early M spectral types, the hotter the star, the thinner the convective envelope and the slower the rate of Li depletion. In fact, standard models predicted no Li depletion in F stars due to their thin convective envelopes ([Deliyannis & Pinsonneault, 1997](#)). However, Li-poor stars with effective

temperatures around 6600 K, that is, mid F stars, have been observed in several open clusters (see, for instance, [Boesgaard & Tripicco, 1986](#); [Steinhauer & Deliyannis, 2004](#)). This feature is called the "Li gap" in the literature, and its discovery contradicted predictions at that time. Consequently, several explanations were proposed to account for this unexpected result, but discussing them is out of the scope of this work, which is focused on G and K stars.

On the other hand, fully convective M dwarfs deplete Li very fast. Since the mass of the star conditions the timescale in which it reaches the Li-burning temperature limit, a sharp gap arises in which stars are strongly depleted in Li in comparison with cooler and hotter stars that have not started to burn Li yet. Given that the shape of this gap depends on age, an effective stellar dating technique based on this Lithium Depletion Boundary (LDB) was developed ([Rebolo et al., 1992, 1996](#); [Stauffer et al., 1998, 1999](#); [Soderblom et al., 2014](#); [Barrado, 2016](#)). However, this technique requires estimating Li abundances in cool-faint members of stellar associations, which is problematic in the case of distant objects.

If the Li surface abundance would depend only on the age and the effective temperature of the star, a powerful stellar dating technique based on spectra of G and K stars would arise. Determining if one star is older or younger than other star of similar effective temperature would be as simple as comparing the equivalent widths (EWs) of the Li doublet at 670.78 nm measured from their spectra. However, observations carried out during the last decades have demonstrated that the actual picture is much more complex than initially believed because of the existence of several factors that also have important effects on the Li depletion. Consequently, characterizing the influence of these factors, which will be introduced next in this chapter, is vital for the right use of the Li abundance as an age indicator for solar-like stars.

[Skumanich \(1972\)](#) linked rotation braking and Li depletion from a sample of G members of the Pleiades and the Hyades (see Fig. 1.1). In that study, it was proposed that the angular velocity and the Li abundance of these stars decay following a square-root relation between the age of the Pleiades and that of the Hyades. In fact, the gradual spin down of solar-type (and late-type) stars is the base of stellar gyrochronology ([Barnes, 2003](#)), another powerful tool for stellar dating.

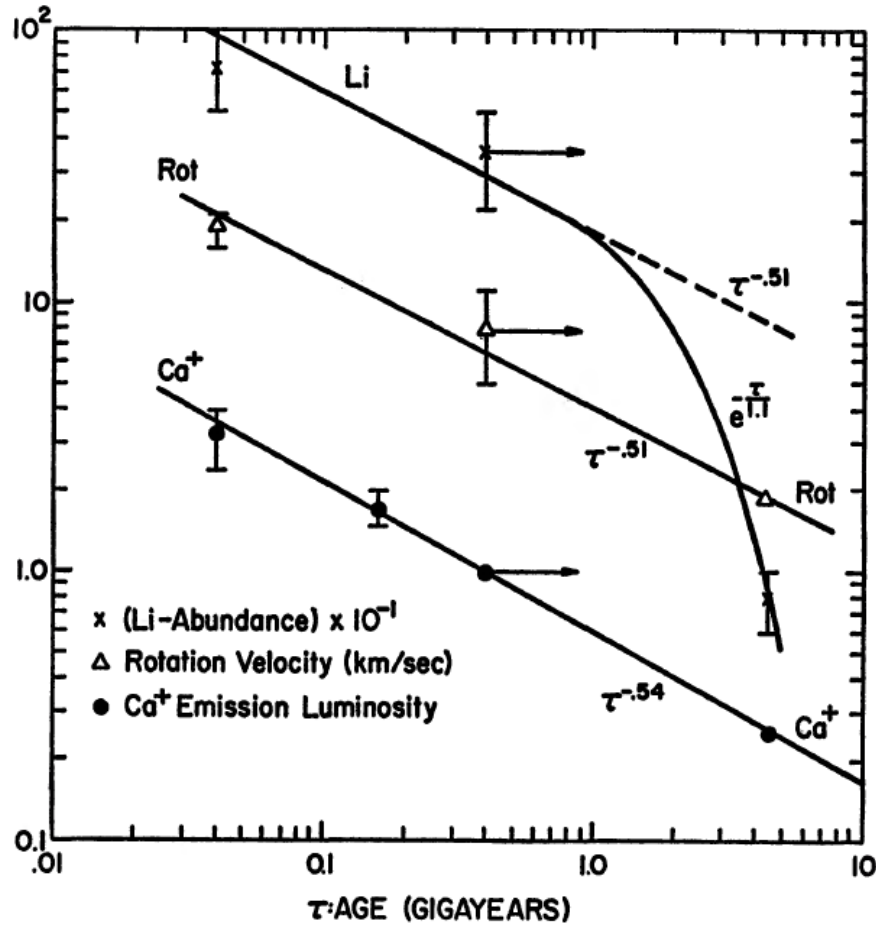


Figure 1.1: Ca^+ emission, rotation velocity, and Li abundance versus stellar age for the Pleiades, the Hyades, and the Sun. Ca^+ emission for the Ursa Major group is also plotted. This figure has been taken from [Skumanich \(1972\)](#).

However, the connection between Li and rotation runs much further. [Soderblom et al. \(1993b\)](#) revealed that G and K slow rotators in the Pleiades (125 Myr old) were Li-poor compared to fast rotators of the same spectral types. Before that work, tentative evidence of this connection had already been observed in G and K members of the Pleiades by [Duncan & Jones \(1983\)](#) and [Butler et al. \(1987\)](#), respectively. [Soderblom et al. \(1993b\)](#) confirmed that the Li spread is highly correlated with rotation, and discarded the idea that this link is due to age differences between fast and slow rotators. The connection between Li depletion and rotation was also observed in tidally locked binaries, both in the field ([Barrado y Navascues et al., 1997](#)) and in open clusters like

Hyades (Barrado y Navascués & Stauffer, 1996). As the link between Li and rotation contradicted predictions at that time, many stellar associations have been observed in the decades since, and several different explanations have been proposed to account for this unexpected result.

Siess & Livio (1997) linked rotation and Li depletion through the mixing length parameter α . In this scenario, when α decreases during the pre-main sequence (PMS), the convective envelope shrinks and, consequently, less Li is destroyed. If α scales with the inverse of the angular velocity (see Equation 9 in Siess & Livio, 1997), rapid rotators would be richer in Li than slow rotators. On the other hand, Bouvier (2008) proposed that the star-disk interaction, known as disk locking, that takes place during the early PMS enhances differential rotation, preventing the star from spinning up. Consequently, a longer disk lifetime should result in a slower rotator that will reach the zero-age-main-sequence (ZAMS) with less Li due to this externally enforced rotational mixing.

Multiple authors have studied the observed evolution of the Li–rotation connection from the PMS to the ZAMS. Bouvier et al. (2016) investigated this relationship in the 5-Myr-old, star-forming region NGC 2264, and demonstrated that the Li overabundance is detected in fast rotators even at this early stage of stellar evolution. Barrado et al. (2016) and Bouvier et al. (2018) confirmed the tight Li–rotation connection in the Pleiades, and Arancibia-Silva et al. (2020) also demonstrated its existence in the 125-Myr-old Psc-Eri stellar stream. These studies indicate that the Li overabundance increases during the PMS: Li abundance in fast rotators is 120% the Li abundance in slow rotators at 5 Myr, and it reaches 600% on the ZAMS, which is the evolutionary status of K dwarfs at the age of the Pleiades. Besides this, Llorente de Andrés et al. (2021) analysed the Li-rotation connection in FGK members of different OCs and associations, concluding that each stellar group exhibits a characteristic minimum Li depletion connected to a specific large rotation velocity. This velocity changes with age, ranging from $v \sin i \sim 50 \text{ km s}^{-1}$ at 45 Myr to $v \sin i < 20 \text{ km s}^{-1}$ at 250 Myr.

An additional consideration is the magnetic activity in these stars, which is connected with both, stellar rotation and Li abundance (Barrado y Navascués, 1996; Barrado y Navascués et al., 2001b; Takeda et al., 2010; Mishenina et al., 2012; Llorente de Andrés et al., 2024). Somers &

[Pinsonneault \(2014, 2015\)](#) suggested that strong magnetic activity inflates the radius of young stars, reducing the temperature at the base of the convective envelope and, consequently, limiting PMS Li depletion. If fast rotators have stronger magnetic fields than slow ones, their Li abundance will consequently be higher. Some years later, [Jeffries et al. \(2021\)](#) found that the fastest rotating dwarfs in M35 have inflated radii and higher Li equivalent widths with respect to the slow rotators of similar effective temperatures. However, the authors of that work acknowledged that the data were also consistent with a scenario in which magnetic inflation reduces the PMS Li depletion of all stars by a similar amount and that subsequent, rotation-dependent mixing causes the slow rotators to be Li poor.

In this context, it is worth noting that while it is generally accepted that the observed Li spread for a given mass corresponds to real abundance differences, [Barrado et al. \(2016\)](#) showed that part of the Li overabundance observed in fast rotators could be an observational effect due to increased activity in these stars, reinforcing the conclusions drawn by [Barrado y Navascués et al. \(2001b\)](#). Despite this, [Barrado et al. \(2016\)](#) pointed that magnetic activity cannot account for the link between rotation and Li abundance observed in NGC 2264 ([Bouvier et al., 2016](#)) because that 5 Myr sample is saturated.

The Li–rotation connection has also been studied in 600-700-Myr-old clusters, mainly Praesepe and the Hyades. [Soderblom et al. \(1990\)](#) studied Li in solar-type members of the Hyades and Coma Berenices, concluding that there is little or even no scatter in Li abundance at 600-700 Myr for stars of similar effective temperatures. Despite this, [Soderblom et al. \(1990\)](#) also reported two close binaries with higher Li abundance, two Hyades members deficient in Li, and two Coma members deficient in Li. A few years later, [Thorburn et al. \(1993\)](#) studied Li abundance in a broader range of effective temperatures that included F, G, and K members of the Hyades. The authors of this work observed a small scatter for G-K stars as well as tidally locked binaries whose primary components have very high Li abundances in comparison with other stars of similar effective temperatures. Finally, [Barrado y Navascués & Stauffer \(1996\)](#) confirmed the Li overabundance of tidally locked binaries in the Hyades. As the authors of that work pointed out,

one explanation for this is that the angular momentum transfer from the binary orbit to stellar rotation in these systems brings faster rotation and lower Li depletion.

On the other hand, [Soderblom et al. \(1993a\)](#) studied Li in F and G members of Praesepe, finding many cases of stars of the same color with different Li abundances. The authors of that work also compared their results with previous analyses of the Hyades, with the most striking differences between both clusters being that Praesepe has several stars with very little Li and that Praesepe members with effective temperatures lower than 5700 K are richer in Li than similar members of the Hyades. To account for the latter result, [Soderblom et al. \(1993a\)](#) proposed that Praesepe could have lower metallicity than the Hyades or, alternatively, be younger than that cluster. In addition, these authors also derived Li abundance for a close binary, finding similar values than those obtained for other stars of similar color, unlike what had been observed in the Hyades. [King & Hiltgen \(1996\)](#) estimated Li abundance for a different close binary in Praesepe and did not obtain a remarkable higher value neither. In both cases, the possible presence of a tertiary companion is proposed to account for this result.

The problem of Li in solar-type members of Praesepe and the Hyades was revisited more recently by [Cummings et al. \(2017\)](#). The authors of that work took advantage of previous analyses of Li in these clusters to obtain Li abundances for 90 members of the Hyades and 110 members of Praesepe in a wide range of effective temperatures that included A, F, G, and K spectral types. [Cummings et al. \(2017\)](#) built prime samples cleaned from spectroscopic binaries and concluded that the distributions of Li in both clusters are indistinguishable in the whole range of effective temperatures considered. Since the authors of that work obtained very similar values for the turnoff ages of these clusters (635 ± 25 Myr for the Hyades and 670 ± 25 Myr for Praesepe) as well as for their metallicities ($[\text{Fe}/\text{H}] = 0.146 \pm 0.004$ for the Hyades and $[\text{Fe}/\text{H}] = 0.156 \pm 0.004$ for Praesepe), they concluded that members of clusters of consistent age and metallicity undergo consistent Li depletion.

[Gallet & Bouvier \(2013\)](#) demonstrated that the members of a particular cluster display a large spread in rotation period for a given mass during the first hundred Myr, but at around 1 Gyr the

rotation rates have well defined values that principally depend on age. Therefore, an intriguing issue is whether the Li overabundance disappears with the spread in rotation period or it can still be detected at around 1 Gyr. In any case, the aforementioned studies and the limited data available for OCs of intermediate ages (see, for instance, [Jones et al., 1997](#); [Sun et al., 2023](#)) clearly point to a strong connection between Li and rotation, at least until 600-700 Myr.

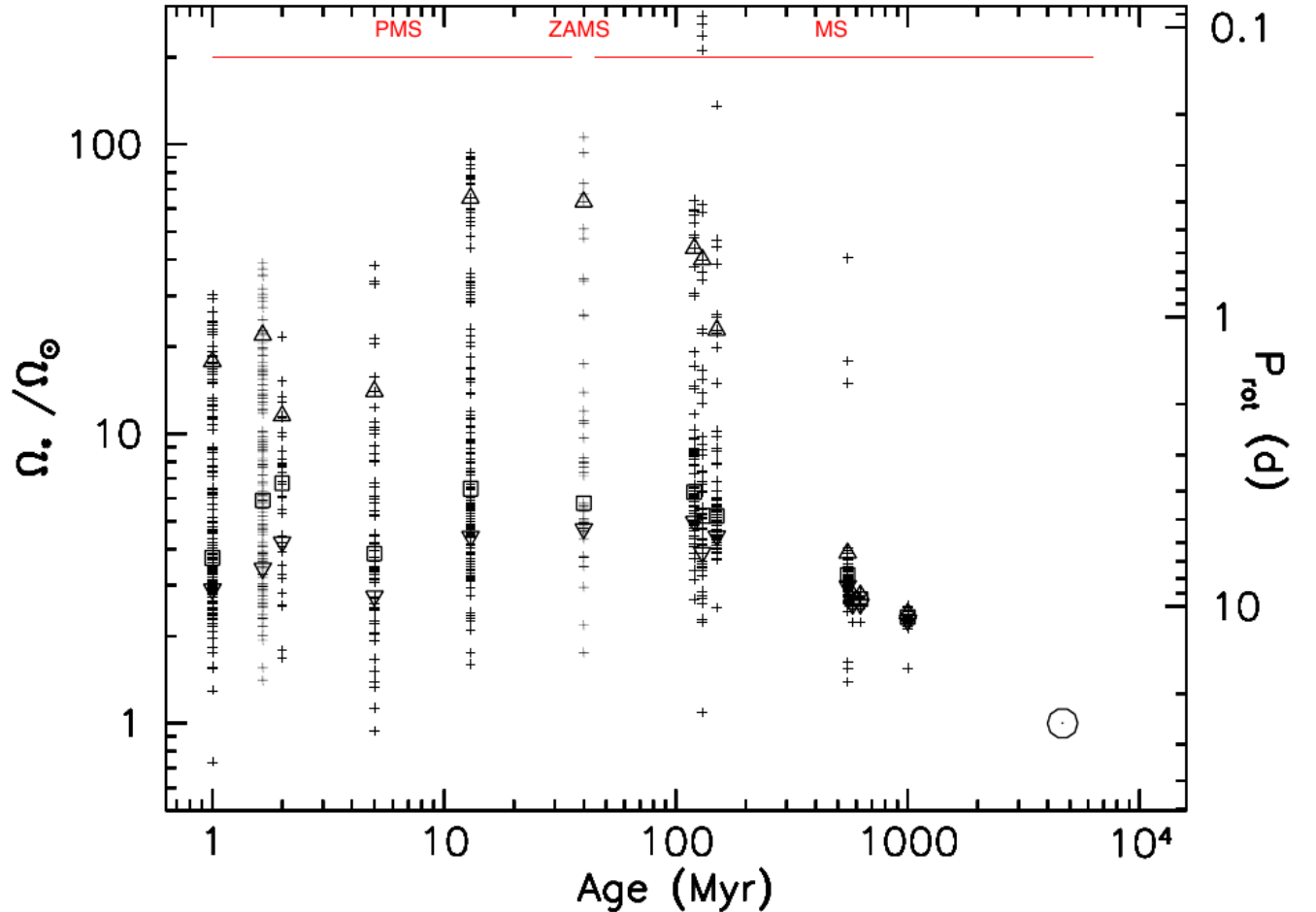


Figure 1.2: Angular velocity distributions of solar-type stars in young open clusters and the Sun. The left axis indicates angular velocities normalized to the Sun's, while the right axis provides rotation periods. The open circle shows the angular velocity of the Sun. This figure has been taken from [Gallet & Bouvier \(2013\)](#).

Metallicity also conditions Li depletion: stars with lower metallicity have thinner convective envelopes and, consequently, their Li depletion is less efficient. This correlation between metallic-

ity and Li depletion was observed by [Ramírez et al. \(2012\)](#) for stars with masses $<1.1M_{\odot}$ and has recently been confirmed for solar analogs by [Martos et al. \(2023\)](#). As a result, these observations strengthen the stellar models proposed by [Castro et al. \(2009\)](#) and [Dumont et al. \(2021\)](#).

In fact, [Ford et al. \(2001\)](#) observed that G and K members of the open cluster Coma Berenices are richer in Li than similar members of the Hyades, which is an OC with higher metallicity but very similar in age. However, [Jeffries et al. \(2002\)](#) estimated Li abundances for G and K members of the ~ 600 Myr-old open cluster NGC 6633, obtaining a pattern very similar to the ones observed in OCs of similar ages and different metallicities, namely the Hyades, Praesepe and Coma Berenices. On the other hand, the authors of that work also reported some evidence pointing to less Li depletion in late G and K stars in comparison with members of the Hyades.

The possible influence of planets on the Li abundance of their host stars has been a matter of intense debate during the last decades. [Gonzalez & Laws \(2000\)](#) opened this debate when the authors of that work concluded that G stars with planets tend to have smaller Li abundances. More recently, [Israeli et al. \(2004, 2009\)](#); [Chen & Zhao \(2006\)](#); and [Delgado Mena et al. \(2014\)](#) obtained similar results from larger samples of solar type stars and the models presented in [Castro et al. \(2009\)](#) supported that conclusion. On the other hand, [Ryan \(2000\)](#) concluded that Li abundances of stars with detected planets mimic Li abundances of similar stars without planets. Furthermore, [Luck & Heiter \(2006\)](#); [Baumann et al. \(2010\)](#); [Ghezzi et al. \(2010\)](#); [Ramírez et al. \(2012\)](#); and [Bensby & Lind \(2018\)](#) did not observe differences between the Li abundances measured for planet-host stars and the Li abundances measured for stars of the same age, metallicity, and effective temperature without detected planets.

The presence of planets may influence the Li abundance of the host star in different ways. On the one hand, planet engulfment events can trigger an increase in the Li abundance of stars that have already burned most of their Li reserve ([Spina et al., 2021](#); [Meléndez et al., 2017](#)). On the other hand, [Deal et al. \(2015\)](#) proposed that the accretion of planetary matter could account for the low Li abundance of a solar analog in comparison with the Li abundance derived for its companion. [Sevilla et al. \(2022\)](#) took advantage of the MESA stellar models ([Paxton et al., 2011](#),

2019) to shed more light on the effect of planet engulfment on the Li abundance. The authors of that work concluded that the Li increase produced by an engulfment event can last for Gyrs in G-type stars ($\sim 0.9M_{\odot}$) whereas for more massive stars ($1.3-1.4 M_{\odot}$) it can enhance internal mixing and diffusion processes, decreasing the Li surface abundance as a result. In addition to engulfment events, planets can trigger tidal forces that could increase Li depletion in the convective envelopes of their host stars (see [Llorente de Andrés et al., 2024](#)).

The different scenarios in which planets can affect the Li abundances of their host stars were recently addressed by a study co-authored by me ([Llorente de Andrés et al., 2024](#)). In that work, we looked for differences between the Li abundances of planet-host stars and stars without planets in a large sample of 1332 MS stars of FGK spectral types, 257 of them have detected planets. From our results, we concluded that there is not evidence of Li enrichment due to engulfment events or of enhanced Li depletion due to tidal forces, that is, planets do not play an important role on Li depletion.

As the aforementioned sample of 1332 MS stars includes dwarfs with super-solar metallicities and low lithium abundances, we explored different explanations for the origin and existence of these stars in [Llorente de Andrés et al. \(2024\)](#). My contribution to that work was determining whether those objects reached the solar neighborhood from inner regions of the Galaxy. To do so, I took advantage of *Gaia* DR3 astrometry and *galpy*, a Python package for Galactic dynamics calculations. More details are provided in [Appendix E](#).

Disentangling the effects of each of these factors on Li depletion to obtain a reliable Li-age relation is a challenging task. Despite this, important steps have been recently taken in that direction thanks to the wealth of spectra provided by the Gaia-ESO survey ([Gutiérrez Albarrán et al., 2020, 2024](#); [Jeffries et al., 2023](#)).

To fully understand the role age, activity, rotation, and metallicity play in Li depletion, it is crucial to have a reliable and extensive set of observations of MS FGK stars with well-determined ages, metallicities, and rotation rates. As stars in OCs share the same age and metallicity, they constitute the perfect targets for this kind of studies.

In this work, we have studied the effects of rotation and metallicity on the Li depletion in members of several clusters of different ages and metallicities. To do so, we have carefully selected the ideal OCs to achieve our purpose and we have collected high-resolution spectra for G and K members of these associations. In all cases, we have taken advantage of *Gaia* astrometry and photometry to ensure cluster belonging. In addition, we have derived the rotation periods of these stars from light curves taken by the Zwicky Transient Facility (ZTF) or by the Transiting Exoplanet Survey Satellite (TESS). Finally, we have derived Li abundances and/or Li EWs from the aforementioned spectra, obtaining surface lithium for GK dwarfs with a large variety of rotation periods. These data have been used to study the effect of rotation on the Li depletion at different ages. Besides this, the effect of metallicity on the Li depletion has been studied by comparing the Li distributions obtained for clusters of similar ages but different metallicities.

Chapter 2 of this work is devoted to the roughly Pleiades-aged OC M35. We provide new Li abundances as well as new rotation periods for G and K members of this cluster. In addition, we address the controversy over the metallicity of this cluster and we compare its Li distribution with other OCs of similar ages. Chapter 3 is focused on ~600 Myr-old OCs, which have lower Li abundances. We provide new Li EWs and rotation periods for G and K members of Coma Berenices and Praesepe, and we compare the Li distributions obtained for them. Chapter 4 summarizes the main conclusions of this work.

Chapter 2

Lithium, rotation and metallicity in the open cluster M35

The focus of this chapter is on the open cluster M35 (NGC 2168), a compact ([Barrado y Navascués et al., 2001c](#); [Bouy et al., 2015](#)), relatively distant (885 pc; [Jeffries et al., 2021](#)) cluster that is often thought of as a much richer analog of the Pleiades.

[Jeffries et al. \(2021\)](#) have investigated the Li–rotation connection for G and K members of M35, finding a strong correlation between the equivalent width of the Li line, $EW(\text{Li})$, rotation, and radius inflation. However, the position of the cluster in the age–metallicity plane is still ambiguous: while [Jeffries et al. \(2021\)](#) quote an age of 140 ± 15 Myr, [Abdelaziz et al. \(2022\)](#) derived an age of 126 Myr for M35, closer to that of the Pleiades. More significantly, only a few authors have provided values for M35’s metallicity: [Barrado y Navascués et al. \(2001a\)](#) and [Steinhauer & Deliyannis \(2004\)](#) found sub-solar values ($[\text{Fe}/\text{H}] = -0.21 \pm 0.10$ and -0.143 ± 0.014 , respectively), while, based on their measurements of the EW of the Ca I line for stars in their sample, [Anthony-Twarog et al. \(2018\)](#) assumed a solar metallicity for the cluster.

In [Cuenda-Muñoz et al. \(2024\)](#), we presented our analysis of unpublished spectra and new light curves, which expanded the sample of M35 members with $EW(\text{Li})$ and rotation period measurements presented in [Jeffries et al. \(2021\)](#). In addition, we derived the metallicity of M35 by analyzing the spectra collected for a sample of single GK dwarfs with very high probability of being cluster members. Finally, we compared our results for M35 to those for the Pleiades and for

M34, another open cluster with an age quite similar to that of M35. Most of what is presented in the following sections comes from that work. Except for deriving rotation periods (Section 2.3.2), task that was performed by J.L. Curtis, the author of this thesis carried out the analysis presented in Cuenda-Muñoz et al. (2024) and wrote the corresponding discussion (under the guidance of the coauthors).

2.1 Assembling our spectroscopic sample

Our sample is made up of M35 candidate members observed with the Hydra multifiber spectrograph. This multi-object instrument is installed in the 3.5-m telescope of the WIYN Observatory, Kitt Peak, USA. Hydra has more than 80 fibers with which one can cover a field 60 arcminutes in diameter. Since half of M35's members are contained within a diameter of less than 40 arcminutes (Cantat-Gaudin & Anders, 2020), Hydra is able to observe most of the cluster within a single observation. The light collected by each fiber is transmitted to the bench spectrograph and scattered by the selected grating. Two different science cables are available for each configuration of fibers, the red one covering 400–1100 nm and the blue one covering 300–800 nm. The spectral resolution of the former ranges from 0.19 to 5.72 Å depending on the selected grating, whereas the spectral resolution of the latter ranges from 0.30 to 8.87 Å.

2.1.1 New Hydra spectra

Over the course of four observational campaigns between 1998 January and 2001 March, more than 300 M35 candidate members were observed with Hydra. Here we focus on the two campaigns with unpublished data. During 1999 December 12–15, eight science images were taken using the blue Hydra fiber cable, each with the same configuration of 17 sky fibers and 76 science fibers. During 2001 February 22–23, five science images were taken using the same fiber cable, but the configuration was slightly different: there were five sky fibers and 89 science fibers. None of the sources observed in 1999 was observed again in 2001 February. Table 2.1 list the dates of the observations, the central coordinates, and the exposure times for each image.

Table 2.1: Science exposures taken during the December 1999 and February 2001 WIYN/Hydra campaigns. Date, central coordinates, and exposure time are shown for each exposure.

Image	$\alpha(2000)$ hh:mm:ss	$\delta(2000)$ dd:mm:ss	Date	Exposure Time (s)
N2017	06:09:06.0	24:20:42	1999 Dec 12	4355
N2018	06:09:06.1	24:20:42	1999 Dec 12	7200
N2019	06:09:06.1	24:20:42	1999 Dec 12	7200
N2020	06:09:06.1	24:20:42	1999 Dec 12	4920
N3033	06:09:06.0	24:20:42	1999 Dec 13	7200
N3034	06:09:06.0	24:20:42	1999 Dec 13	4500
N4049*	06:09:06.0	24:20:42	1999 Dec 14	2725
N5036	06:09:06.0	24:20:42	1999 Dec 15	6300
N1033	06:09:04.4	24:18:48	2001 Feb 22	7200
N1034	06:09:04.4	24:18:48	2001 Feb 22	7200
N1036	06:09:04.4	24:18:48	2001 Feb 22	7800
N2099	06:09:04.4	24:18:48	2001 Feb 23	7200
N2100	06:09:04.4	24:18:48	2001 Feb 23	9000

*We used N4049 to derive RVs, but not to measure Li EWs.

We reduced the 165 stellar spectra obtained as follows. For homogeneity with previous studies with Hydra (section 2.1.2), we used standard IRAF¹ tools to obtain the smoothed and continuum-normalized spectrum corresponding to each source in each of the images. First, we smoothed the spectra taken during each exposure using the `boxcar` task included in the `images.imfilter` package. Second, we removed the continuum by fitting a cubic spline function to each spectrum taking advantage of the `continuum` task included in `noao.onedspec`. Finally, we employed the `scopy` task in `imred.hydra` to extract the individual (smoothed and continuum normalized) spectrum for each observed source. Each of the resulting spectra covers the wavelength interval between 640 and 690 nm and has a resolution of $R \approx 20\,000$, as measured in ThAr comparison lamps. The Li doublet at 670.78 nm is included in this range as well as a number of iron lines.

¹IRAF is distributed by the National Optical Astronomy Observatories, which are operated by the Association of Universities for Research in Astronomy, Inc., under cooperative agreement with the National Science Foundation.

2.1.2 Previously published spectra from these campaigns

We also included in our sample the G and K dwarfs observed in the two other observing campaigns from that same time period and analysed in previous publications ([Barrado y Navascués et al., 2001a](#); [Anthony-Twarog et al., 2018](#)). Although these authors address the Li–rotation connection, they rely on rotation velocities, which are affected by the uncertainty in the rotation inclination angle, in contrast to the analysis provided in this work, which relies on measurements of rotation periods.

[Barrado y Navascués et al. \(2001a\)](#) observed 76 candidate members of M35 selected from the photometric survey of the cluster of [Barrado y Navascués et al. \(2001c\)](#). [Anthony-Twarog et al. \(2018\)](#) acquired spectra of 85 stars, 77 of which had preliminary radial velocities (RVs) consistent with membership; the other eight were selected based on their positions in a color–magnitude diagram (CMD). Table 2.2 shows further details of both campaigns.

There is no overlap between the objects analysed in the aforementioned studies, but a few of them were also observed in 1999 December and 2001 February. Fifteen of the spectra presented in this work are for stars also observed by [Barrado y Navascués et al. \(2001a\)](#), and five are also included in [Anthony-Twarog et al. \(2018\)](#).

2.1.3 Other Hydra surveys of M35

[Jeffries et al. \(2021\)](#) employed Hydra to observe 342 candidate members of M35 selected from the catalogs of [Bouy et al. \(2015\)](#), [Meibom et al. \(2009\)](#), and [Libralato et al. \(2016\)](#). [Jeffries et al. \(2021\)](#) rejected 100 of these stars because they considered them non-members of the cluster, found no rotation periods for them, or these objects exhibited a poor fit when analysed with the Virtual Observatory Spectral Energy Distribution (SED) Analyser (VOSA; [Bayo et al., 2008, 2017](#)). Because we developed our own set of membership criteria and have a different set of rotation period measurements for our analysis, we have incorporated these 100 discarded stars into our sample (ten were observed as part of our program).

On the other hand, the 242 stars that were analyzed by [Jeffries et al. \(2021\)](#) have not been

Table 2.2: Summary of our M35 sample in terms of the origin of the data. All the sources indicated in this table have been observed with the Hydra multifiber spectrograph.

Campaign	Number of Sources	Authors
1998 January	76	Barrado y Navascués et al. (2001a)
1999 December	76	This Work
2001 February	89	This Work
2001 March	85	Anthony-Twarog et al. (2018)
2017 November	100	Jeffries et al. (2021)

included in our sample for re-analysis. Instead, we incorporated the Jeffries et al. (2021) results for these stars into our analysis in Section 2.5. It is worth mentioning that 115 of these stars are included in Barrado y Navascués et al. (2001a), Anthony-Twarog et al. (2018), or the Hydra campaigns presented in this work.

2.1.4 The complete sample

As shown in Table 2.2, our sample includes 76 stars taken from Barrado y Navascués et al. (2001a), 85 taken from Anthony-Twarog et al. (2018), 100 taken from Jeffries et al. (2021), and 165 stars added by this study. As there are 30 objects in common between the campaigns analysed in this work and the ones presented in Barrado y Navascués et al. (2001a), Anthony-Twarog et al. (2018), and Jeffries et al. (2021), our final sample is composed of 396 unique G and K candidate members of M35 with Li measurements. The complete sample is presented in Table 2.3.

2.2 Revisiting the membership and multiplicity of stars in our sample

2.2.1 An initial membership selection based on Bouy et al. (2015) and our own proper-motion analysis

Using TOPCAT (Taylor, 2005), we cross-matched our 396 stars with the *Gaia* Data Release 3 (DR3; Gaia Collaboration et al., 2023), obtaining astrometry and photometry for 395 candidate members (see the CMD in the top panel, Figure 2.1). We also cross-matched our catalog with that

Table 2.3: Cross-identification numbers, coordinates, and observation campaigns for the complete sample presented in this work. Our sample is composed of 396 stars. Columns α and δ indicate the coordinates employed for the pointing. For the stars that have a counterpart in [Anthony-Twarog et al. \(2018\)](#) and/or [Jeffries et al. \(2021\)](#), we have also included the corresponding IDs in these papers. This table is only partially presented. Its complete version is available in [Appendix A](#).

ID ^(a)	α (2000) hh:mm:ss	δ (2000) dd:mm:ss	α (2000) deg	δ (2000) deg	Campaign	AT18 ^(b) ID	Je21 ^(c) ID
5076	06:08:52.9	+24:17:20	92.22042	24.28889	2001 Mar	16010	–
5081	06:09:26.200	+24:29:03.0	92.35917	24.48417	1998 Jan	–	–
7117	–	–	92.22672	24.05225	2017 Nov	–	J06085441+2403081
7036	06:09:00.7	+24:35:53	92.25292	24.59806	2001 Feb	–	–
5373	06:08:49.270	+24:15:33.30	92.20529	24.25925	1999 Dec	–	–
...		

Notes. As the 20 objects in common between the campaigns analysed in this work and the ones presented in [Barrado y Navascués et al. \(2001a\)](#) and [Anthony-Twarog et al. \(2018\)](#) are shown as different rows with the same identification number, the table includes 416 rows. ^(a)Object IDs between 5000 and 7000 are taken from [Barrado y Navascués et al. \(2001c\)](#). The stars not found in that catalog have been labelled with numbers between 7000 and 8000. ^(b)AT18 is [Anthony-Twarog et al. \(2018\)](#). ^(c)Je21 is [Jeffries et al. \(2021\)](#).

of [Bouy et al. \(2015\)](#), as these authors provided an extensive membership analysis for M35. We found counterpart for 373 stars in that work.

We then used Clusterix 2.0, a Spanish Virtual Observatory tool ([Balaguer-Núñez et al., 2020](#)), to assign membership probabilities to our candidates based on their *Gaia* Early Data Release 3 (EDR3; [Gaia Collaboration et al., 2021](#)) proper motions.² After selecting a region of the sky including M35 and a region free of cluster members, Clusterix 2.0 uses a non-parametric method to distinguish the proper-motion distribution of the cluster members and that of the field stars. In this process, the number of cluster members, N_c , is estimated, and the membership probability of each star in the selected regions is computed.

Clusterix 2.0 returns a file that includes, for each star considered, the *Gaia* EDR3 photometry and astrometry and a membership probability. In addition, the N_c stars with the highest membership probabilities are flagged as members of the cluster. We removed from this preliminary list of candidate members around half of them due to the large uncertainties in the photometry and/or astrometry measured for those stars, or because their parallaxes and/or proper motions were very

²Clusterix 2.0 does not yet include DR3 proper motions.

different from those of M35 (Gaia Collaboration et al., 2018a).

We then combined the membership probabilities of Bouy et al. (2015) with those derived by Clusterix 2.0 to classify each star as a non-member, a possible non-member, a possible member, or a probable member.

We flagged as non-members stars whose membership probabilities were below 50% in Bouy et al. (2015) and that were also rejected as members after running Clusterix 2.0. In addition, visual inspection of the cluster CMDs allowed us to identify 16 stars as photometric non-members. The stars that had a counterpart in either Bouy et al. (2015) or Clusterix 2.0, but not in both, and whose membership probabilities did not meet our requirements, were classified as possible non-members, as were stars that did not have a counterpart in either of them.

We classified as possible members the stars that were considered members by Bouy et al. (2015), that is, their membership probabilities were $\geq 50\%$, or after running Clusterix 2.0, but not by both. Finally, we classified as probable members the stars that met both requirements.

In this manner, we identified 101 stars in our original sample of 396 as non-members (26%), 44 stars as possible non-members (11%), 129 stars as possible members (32%), and 122 as probable members (31%) of M35. In our catalog, presented in Table 2.4, we use the labels *NM*, *CMD NM*, *NM?*, *Poss*, and *Prob* to indicate these membership categories.

2.2.2 Measuring radial velocities and distinguishing between single and binary stars in our sample

We employed iSpec (Blanco-Cuaresma et al., 2014; Blanco-Cuaresma, 2019) to measure radial velocities (RVs) for the M35 candidate members observed during the 1999 December and 2001 February campaigns. First, each spectrum was transformed to the solar barycentric reference frame. We then derived the RV by cross-correlating the spectrum with a solar mask covering the wavelength range 372–926 nm. We obtained eight measurements of the RV for the M35 candidates observed in 1999 and five measurements for those observed in 2001.

We used these RVs to distinguish between spectroscopic binaries and probable single stars by employing an approach similar to that of Leiner et al. (2015). The standard deviation in RV (e) for

each star was compared with the maximum and minimum single-measurement precision in RV calculated by iSpec for that star ($max(i)$ and $min(i)$, respectively).

The stars whose ratios $e/max(i)$ and $e/min(i)$ were both <4 were considered single, while those whose standard deviation in RV was clearly above the single-measurement precision derived for any of their spectra were classified as SBs. The M35 candidates with $e/max(i) < 4$ but $e/min(i) \geq 4$ were classified as having an unknown multiplicity.

In addition, the average RV of each single star was calculated to distinguish between single members and single non-members of the cluster. We considered single members those stars whose average RVs fall within the interval $[V_{rad} - 3\sigma, V_{rad} + 3\sigma]$, where V_{rad} and σ were taken from [Gaia Collaboration et al. \(2018a\)](#): $V_{rad} = -7.70 \text{ km s}^{-1}$; $\sigma = 0.27 \text{ km s}^{-1}$.

We added a “-” symbol to the membership labels employed for the non-members and possible non-members in our sample that were also considered single non-members based on their RVs. Conversely, we added a “+” to the membership labels for the possible and probable members whose RVs indicate that they are single members of M35.

Besides this, *Gaia* DR3 provides an astrometric criterion for distinguishing between single and binary members of the cluster. The *Gaia* Renormalised Unit Weight Error (RUWE) is expected to be $\lesssim 1.0$ for sources when the single-star model gives a good fit to the astrometric observations, and previous studies have found that larger RUWE values imply that the objects are unresolved binaries in wide orbits (e.g., [Deacon & Kraus, 2020](#); [Ziegler et al., 2020](#); [Kervella et al., 2022](#)). Accordingly, we flagged as wide binaries the 41 stars in our sample whose $RUWE > 1.2$.

We also took advantage of the membership classification published in [Barrado y Navascués et al. \(2001a\)](#) for the 76 M35 candidate members observed by these authors. After analyzing the RVs they measured, these authors split their sample into single members (39 stars), spectroscopic binary members (13), and non-members (24). We employed these labels for the part of the sample taken from that work but we kept the classification described in the previous section for the 15 stars observed in 1999 December and 2001 February that are included in [Barrado y Navascués et al. \(2001a\)](#). Six of these 15 dwarfs are members of M35.

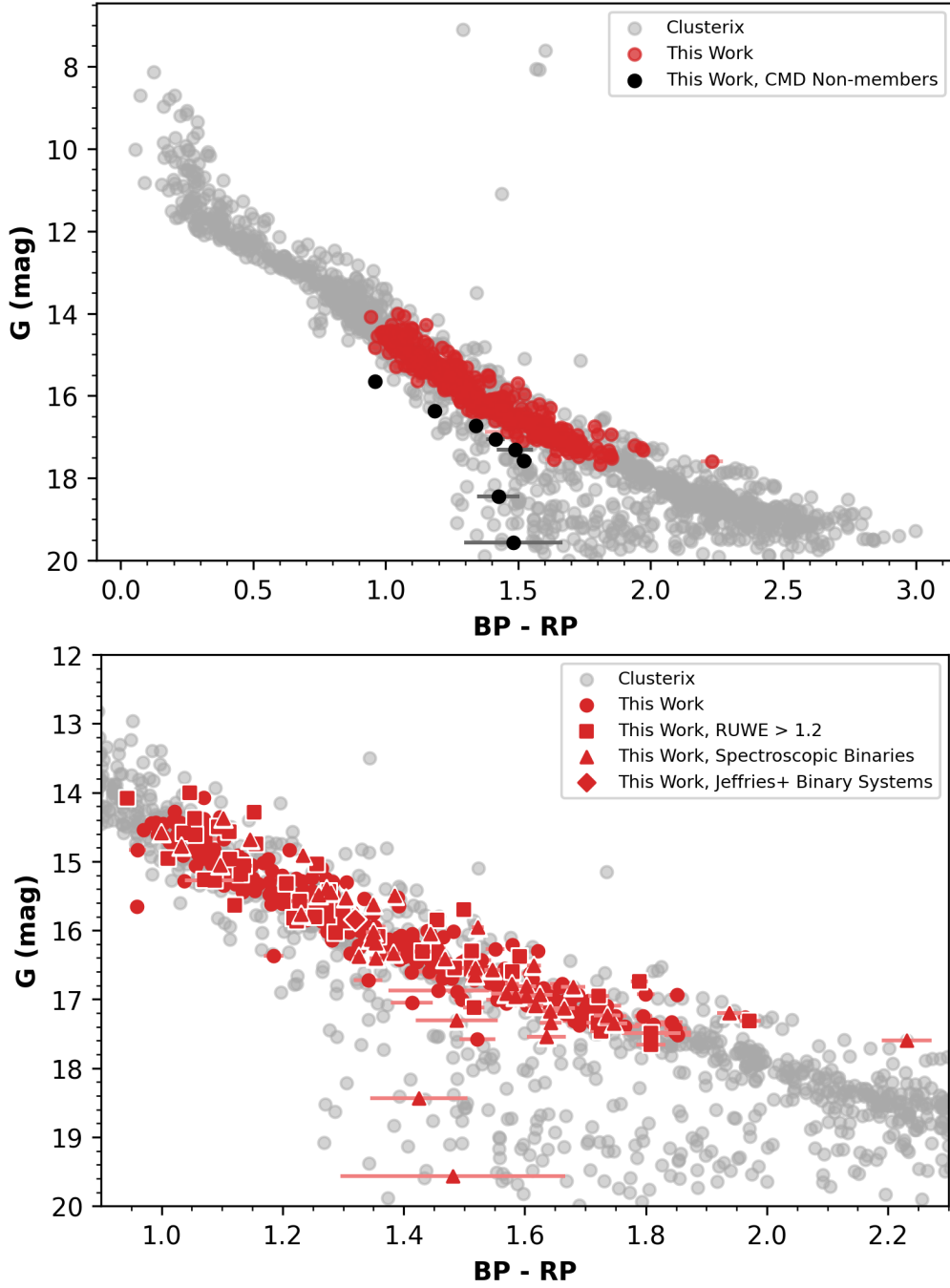


Figure 2.1: *Gaia DR3 CMD for M35. Top*—The grey points represent stars in the vicinity of M35 that Clusterix 2.0 classified as cluster members. We have carried out a subsequent analysis removing some stars whose parallaxes and/or proper motions were very different from those of M35 (*Gaia Collaboration et al., 2018a*). Candidate members of the cluster in our sample are shown in red, while the black circles are stars whose photometry suggests they are not members of M35. We used optical and infrared photometry published in *Bouy et al. (2015)* to classify eight other photometric outliers as non-members. *Bottom*—A zoomed-in version of the CMD highlighting the multiple systems in our sample. The squares are potential wide binaries identified by Gaia, triangles are spectroscopic binaries, and diamonds are binary systems found by *Jeffries et al. (2021)*. Note that neither CMD has been corrected for reddening.

As a further verification of our membership scheme, we cross-matched our complete sample with the catalog of [Leiner et al. \(2015\)](#), finding counterparts for 174 of the 396 stars. Reassuringly, the 28 stars that we classify as single members that have counterparts in [Leiner et al. \(2015\)](#) are also M35 members in that work. We turned to the binary / single star classification provided by [Leiner et al. \(2015\)](#) only for the part of the sample taken from [Anthony-Twarog et al. \(2018\)](#) and the part recovered from [Jeffries et al. \(2021\)](#).

At the end of this process, we had the sample of 41 wide binaries determined from their RUWE values, and 46 more stars identified as spectroscopic binaries thanks to the RV analysis discussed. One more binary system in our sample was identified from checking the list of probable binary systems defined by [Jeffries et al. \(2021\)](#). In total, we therefore found that 88 of the 396 candidates members that composed our sample could be considered binaries. These 88 binaries are represented by squares, triangles, and diamonds in the CMD shown in the right panel of [Figure 2.1](#), and are indicated with binary flag = 1 in [Table 2.4](#).

2.2.3 Summary

As mentioned above, we removed 16 candidates from our sample after visual inspection of their position in several CMDs. Eighty-five other stars were discarded because the membership probabilities derived by [Bouy et al. \(2015\)](#) and the analysis carried out with Clusterix 2.0 both labeled them as non-members. Reassuringly, 28 of these 85 candidates (labeled with *NM-* in [Table 2.4](#)) have RVs incompatible with M35 membership. Similarly, 17 of the 44 stars classified as possible non-members have RVs incompatible with cluster membership. These 17 dwarfs are labeled with *NM?-* in [Table 2.4](#).

On the other hand, we identified 129 dwarfs as possible members. The RVs confirmed 61 of these candidates as cluster members (labeled with *Poss+* in [Table 2.4](#)). In addition, our sample includes 122 M35 probable members, of which 68 (labeled with *Prob+* in [Table 2.4](#)) are single stars with RVs consistent with that of the cluster. Hereafter, we refer to the combined list of 251 possible and probable members we obtained as members of M35. Forty-two of these stars are

Table 2.4: Membership class and binary status for the complete sample presented in this work. Our sample is composed of 396 stars. This table is only partially presented. Its complete version is available in Appendix A.

ID	RV Class ^(a)	RV Source ^(b)	Final Memb. Class	Binary Flag ^(c)
5076	SM	L15	Poss+	0
5081	SB1	B01	NM	1
7117	BM	L15	Prob	1
7036	SM	This Work	Prob+	0
5373	U	This Work	CMD NM	0
...

Notes. ^(a)*MEM* and *SM* account for single members; *NM* and *SN* account for single non-members; *SB*, *BLM*, *BLN*, *BM*, *BN*, *BU*, *SB1*, and *SB2* account for spectroscopic binaries; and *U* accounts for unknown multiplicity. ^(b)B01 is [Barrado y Navascués et al. \(2001a\)](#) and L15 is [Leiner et al. \(2015\)](#). ^(c)1 = likely binary, 0 = single star.

likely binaries.

2.3 Assembling our sample of rotation periods

We cross-matched our sample of 251 cluster members with the photometric surveys of [Meibom et al. \(2009\)](#), [Nardiello et al. \(2015\)](#), [Libralato et al. \(2016\)](#), and [Soares-Furtado et al. \(2020\)](#). In addition, new rotation periods were derived by analyzing the light curves obtained from Zwicky Transient Facility (ZTF; [Masci et al., 2019](#)) data. The main properties of these photometric surveys are shown in Table 2.5.

2.3.1 Rotation periods from the literature

Our primary source of rotation periods is the survey of [Meibom et al. \(2009\)](#), who mixed high-frequency observations over the course of about two weeks with low-frequency observations over nearly five months to measure periods for both fast and slow rotators in M35. By matching our catalog with that of [Meibom et al. \(2009\)](#), we collected periods for 109 stars in our sample. A similar choice was made by [Jeffries et al. \(2021\)](#), who chose the periods published in [Meibom et al. \(2009\)](#) instead of the ones derived by [Libralato et al. \(2016\)](#) when both were available

Table 2.5: Field of view, instrument characteristics, timespan, and cadence for the photometric surveys from which we obtained rotation periods for our sample. M09 is [Meibom et al. \(2009\)](#), SF20 is [Soares-Furtado et al. \(2020\)](#), N15 is [Nardiello et al. \(2015\)](#), and L16 is [Libralato et al. \(2016\)](#).

Authors	Telescope	Field of View	Plate scale (arcsec/pixel)	Timespan	Cadence
M09	WIYN 0.9 m (Kitt Peak Observatory)	$\approx 20.5' \times 20.5'$	0.62	16 / 143 ^(a) d	1 hr / 1 d
N15	Asiago 67/92 cm Schmidt (OAPD)	$\approx 58' \times 38'$	0.86	≥ 10 d	3 min
L16	Kepler (K2)	$115^{\circ 2}$	3.98	≈ 31 d	1 min / 29 min ^(b)
SF20	Kepler (K2)	$115^{\circ 2}$	3.98	≈ 31 d	29 min
This Work	Samuel Oschin Telescope (Palomar Observatory; ZTF)	$47^{\circ 2}$	1.00	several yrs	1 - 2.5 d

Notes. ^(a)High-frequency (once per hr for 5–6 hrs per night) time-series photometric observations were taken over 16 nights and complemented with low-frequency (once per night) observations taken over 143 nights. ^(b)*Kepler* exposures are combined on board to create short-cadence timeseries (nine co-added exposures) or long-cadence timeseries (270 co-added exposures). See [Koch et al. \(2010\)](#) and references therein for a detailed description of the *Kepler* design.

because of the larger observing window of the former.

For those stars lacking periods in [Meibom et al. \(2009\)](#), we turned to the values derived from K2 light curves. From [Soares-Furtado et al. \(2020\)](#), we selected periods for the 31 stars classified as rotating with no blending. In addition, we adopted the period published for one star classified as indeterminate variable.

We have taken advantage of the periods not flagged as possible blends in [Libralato et al. \(2016, flags 0 and 30\)](#) to obtain rotation periods for 39 stars not included in [Soares-Furtado et al. \(2020\)](#). In addition, we recovered one period from [Libralato et al. \(2016\)](#) for a star classified in [Soares-Furtado et al. \(2020\)](#) as an eclipsing binary.

Finally, we obtained rotation periods for six stars from [Nardiello et al. \(2015\)](#). Two have no counterparts in [Meibom et al. \(2009\)](#), [Libralato et al. \(2016\)](#), [Soares-Furtado et al. \(2020\)](#); one has an invalid period ($P_{rot} = -99.0$) in [Libralato et al. \(2016\)](#); and three are considered blends in [Soares-Furtado et al. \(2020\)](#). As [Nardiello et al. \(2015\)](#) analysed light curves taken by an instrument whose plate scale is much smaller than *Kepler*'s, we considered that these light curves

were unlikely to be affected by blending and that these periods are reliable.

2.3.2 New rotational periods from ZTF light curves

ZTF has observed M35 regularly since 2018 March 25. Following [Curtis et al. \(2020\)](#), we extracted differential photometry from the archival ZTF imaging using nearby reference stars in the field. Although the resulting light curves are much sparser and more irregularly sampled than those from dedicated photometric surveys, they can still yield reliable period measurements. Our goal in analyzing these light curves was twofold: ZTF-derived periods can provide confirmation of periods in the literature, and ZTF light curves generally cover much longer timespans than those of other photometric surveys, and can therefore be used to measure periods for slower rotators in M35.

We inspected the light curves for each available season, computed Lomb–Scargle periodograms, and then recorded the period if it was significant and produced a convincing phase-folded light curve. In this manner, we measured periods for nine stars lacking periods in the literature, for one star classified as rotating with blending in [Soares-Furtado et al. \(2020\)](#), and for 37 stars with valid periods in the aforementioned surveys. For stars with periods in the literature, the average agreement between our measurements and the existing values is $<1\%$, and the differences are $\leq 10\%$ in all cases. We have chosen the periods derived from ZTF light curves for these 47 members of M35.

2.3.3 Final sample of M35 members with Li measurements and rotation periods

Combining the periods we derived and those collected from the literature, we obtained rotation periods for 197 of the 251 members of M35 observed with Hydra. [Table 2.6](#) provides the periods for these 197 stars.

Table 2.6: Rotation periods taken from the literature or derived from ZTF light curves for 197 M35 members. M09 is Meibom et al. (2009), SF20 is Soares-Furtado et al. (2020), N15 is Nardiello et al. (2015), and L16 is Libralato et al. (2016). This table is only partially presented. Its complete version is available in Appendix A.

ID	Prot (d) M09	Prot (d) SF20	Class ^(a) SF20	Subclass ^(b) SF20	Blend ^(c) SF20	Prot (d) L16	Flag ^(d) L16	Prot (d) N15	Type ^(e) N15	Prot (d) ZTF	Final Prot (d)
5483	–	–	–	–	–	0.48	1	0.48	Rot	0.48	0.48
7118	1.10	1.11	Rot.	RotVar	0	1.11	1	1.10	Rot	1.11	1.11
5356	–	–	–	–	–	–	–	–	–	7.01	7.01
5459	7.30	–	–	–	–	7.19	1	–	–	–	7.30
7076	–	2.44	Rot.	RotVar	0	–	–	–	–	–	2.44
...

Notes. ^(a)*Rotating* accounts for rotational variables, *Pulsating* for pulsating variables, *EB* for eclipsing binaries, and *Misc* for indeterminate variables. ^(b)*RotVar* accounts for rotational variables of indeterminate type, *GDor* for γ Doradus pulsators, *EB* for eclipsing binaries, and *Misc* for indeterminate variables. ^(c)0 = identified primary variable, 1 = ambiguous blend. ^(d)0 = high probability that it is a blend; 1 = candidate variable; 2 = difficult to classify; 30 = difficult to classify star that, by comparison with the literature, could be a possible blend; 31 = difficult to classify star for which a correspondence in the literature was found. ^(e)*Rot* are rotating stars, *EB* eclipsing binaries, *Long-Period* long-period variables, and *delta Sct* δ Scuti stars.

2.4 Analysis

2.4.1 Deriving effective temperatures and luminosities

We generated the SED of each star in our sample with VOSA (version 7.5; Bayo et al., 2008, 2017) using the photometry in Table 2.7, which was taken from Bouy et al. (2015) and Barrado y Navascués et al. (2001c). We also used VOSA to cross-match our sample with a number of catalogs, obtaining photometry in the PAN-STARRS/PS1 filters, Misc/APASS filters, WISE filters, INT/IPHAS filters, and Palomar/ZTF filters. Following an approach similar to that taken by Jeffries et al. (2021), we assumed a distance of 885 ± 80 pc for all the stars and a visual extinction in their direction of $A_V = 0.62$.

The dereddened SEDs obtained in this manner were compared with Kurucz model atmospheres (Castelli et al., 1997; Castelli & Kurucz, 2003), assuming $\log g = 4.5$ and a solar metallicity, to determine the luminosity and effective temperature that best fit each SED using a χ -squared minimisation method. The value of $\log g = 4.5$ is coherent with the assumed age of the cluster of ≈ 150 Myr and the spectral types studied. Figure 2.2 shows the Hertzsprung–Russell diagram

Table 2.7: Photometry uploaded to VOSA for the 251 members of M35 in our sample. This table is only partially presented. Its complete version is available in Appendix A.

ID	V ^(a)	Ic ^(b)	g ^(c)	r ^(c)	i ^(c)	z ^(c)	J ^(d)	H ^(d)	Ks ^(d)
5408	17.258	15.825	–	16.91±0.05	16.50±0.03	16.13±0.03	14.81±0.06	14.17±0.06	13.98±0.04
5087	14.652	13.743	15.07±0.05	14.58±0.13	14.15±0.11	14.08±0.03	13.15±0.02	12.82±0.02	12.68±0.02
5382	17.136	15.661	–	16.51±0.03	16.21±0.03	15.90±0.03	14.66±0.06	14.11±0.06	13.97±0.05
5194	15.756	14.607	16.29±0.05	15.41±0.05	15.10±0.03	14.88±0.03	13.76±0.03	13.27±0.03	13.18±0.03
7034	–	–	18.45±0.05	17.16±0.05	16.69±0.03	16.40±0.03	15.11±0.06	14.53±0.06	14.40±0.07
...

Notes. ^(a)Johnson V band magnitude taken from Barrado y Navascués et al. (2001c). ^(b)Cousins I band magnitude taken from Barrado y Navascués et al. (2001c). ^(c)SDSS magnitudes taken from Bouy et al. (2015). ^(d)2MASS magnitudes taken from Bouy et al. (2015).

(HRD) built with the astrophysical parameters obtained, which are listed in Table 2.9. As we could not obtain a reliable fit in VOSA for star number 7028, we excluded it from our study and focused on the remaining 250 cluster members.

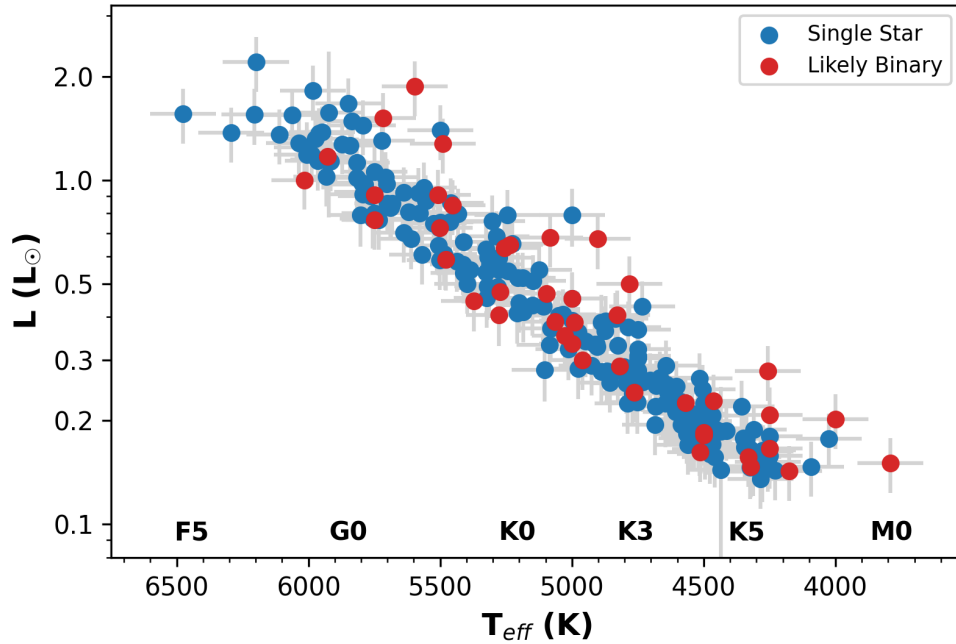


Figure 2.2: Positions in the HRD for the 250 members of M35 in our sample whose effective temperatures and bolometric luminosities were determined by SED fitting with VOSA. Red circles are likely binary systems, while blue circles are single stars.

2.4.2 Measuring equivalent widths and abundances

We used the iSpec software (Blanco-Cuaresma et al., 2014; Blanco-Cuaresma, 2019) to combine RV-corrected versions of the spectra collected during our 1999 and 2001 campaigns. This allowed us to obtain a single spectrum for each of the stars observed during each campaign with a signal-to-noise ratio (SNR) > 300 .

We also used iSpec to develop the pipeline to derive the EW(Li) and Li abundance for each star. First, we used the SPECTRUM radiative transfer code described in Gray & Corbally (1994), the MARCS model atmospheres (Gustafsson et al., 2008), and the *Gaia*–ESO survey line list (Heiter et al., 2021) to generate, for each star, a synthetic $R = 20\,000$ spectrum with solar metallicity, $\log g = 4.5$, and the effective temperature returned by VOSA. This process was repeated several times while modifying the rotational velocity until we found the $v \sin i$ that best fits the science spectrum.

Second, we determined the iron abundance for each star using 40 Fe lines between 645 nm and 680 nm together with the aforementioned stellar parameters. Once the rotational velocity and the Fe abundance have been determined, these parameters, together with the radiative transfer code, model atmospheres, and line list previously mentioned, were used to derive the EW of the Li doublet at 670.78 nm as well as the local thermodynamic equilibrium (LTE) Li abundance. Both quantities were measured three times for each star while modifying slightly the continuum value, and their uncertainties were calculated as the standard deviation of those measurements. Figure 2.3 shows a small region around the Li doublet for four stars of different spectral types and the synthetic spectra generated for them.

However, as the resolution of the spectra ($R \approx 20\,000$) is not high enough to separate the Li doublet at 670.78 nm and the Fe I line at 670.75 nm, both features are blended (see Figure 2.4, where a small region around the Li doublet is shown for four K stars). To remove the contribution of this iron line, we have tried two different approaches.

First, we built a synthetic spectrum employing a modified version of the *Gaia*–ESO line list where all the Li lines had been removed. The SNR estimated for the science spectrum was used to

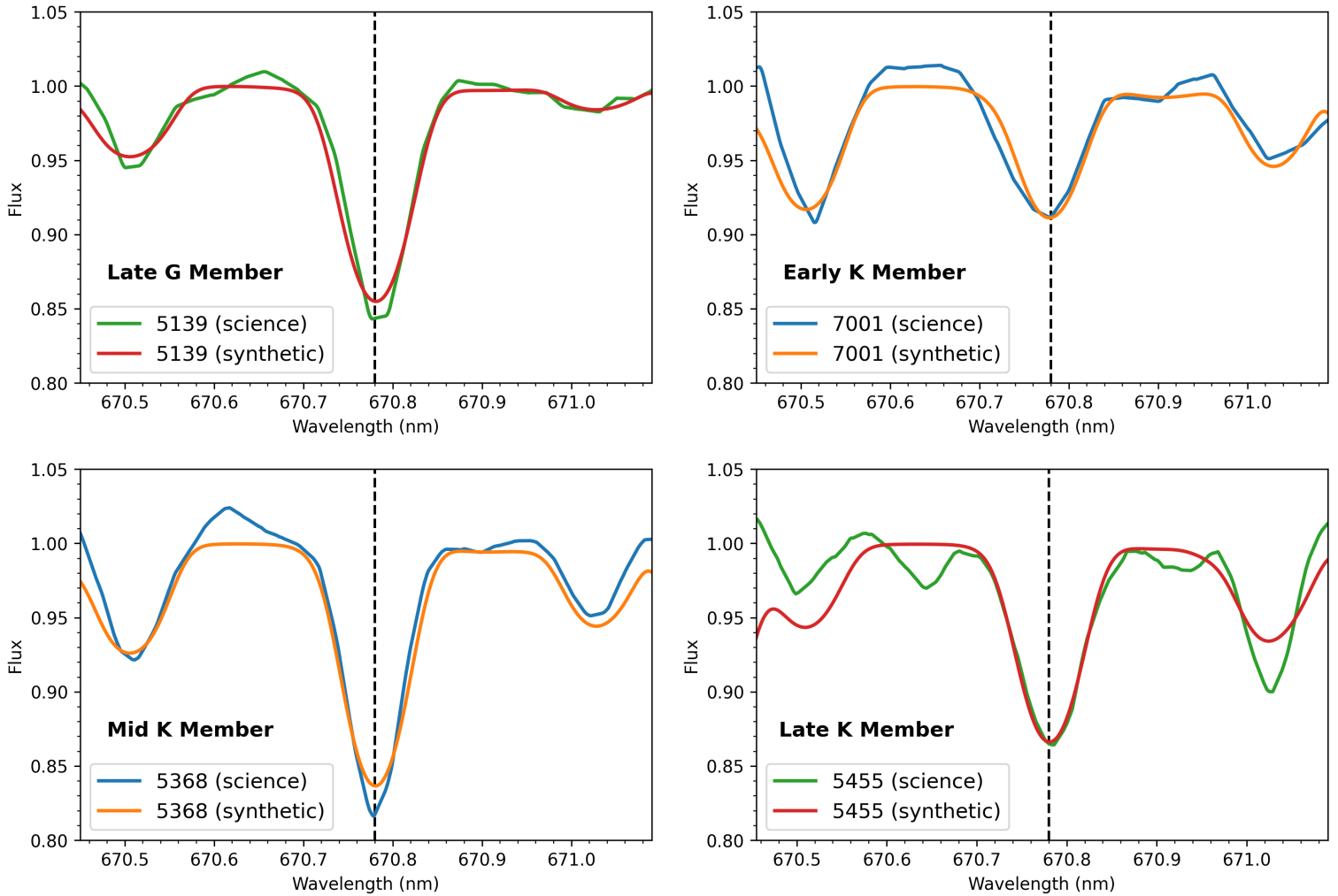


Figure 2.3: Science spectra and synthetic spectra for four M35 members of different spectral types, namely 5139, 7001, 5368, and 5455. The dashed black line shows the position of the Li doublet at 670.78 nm.

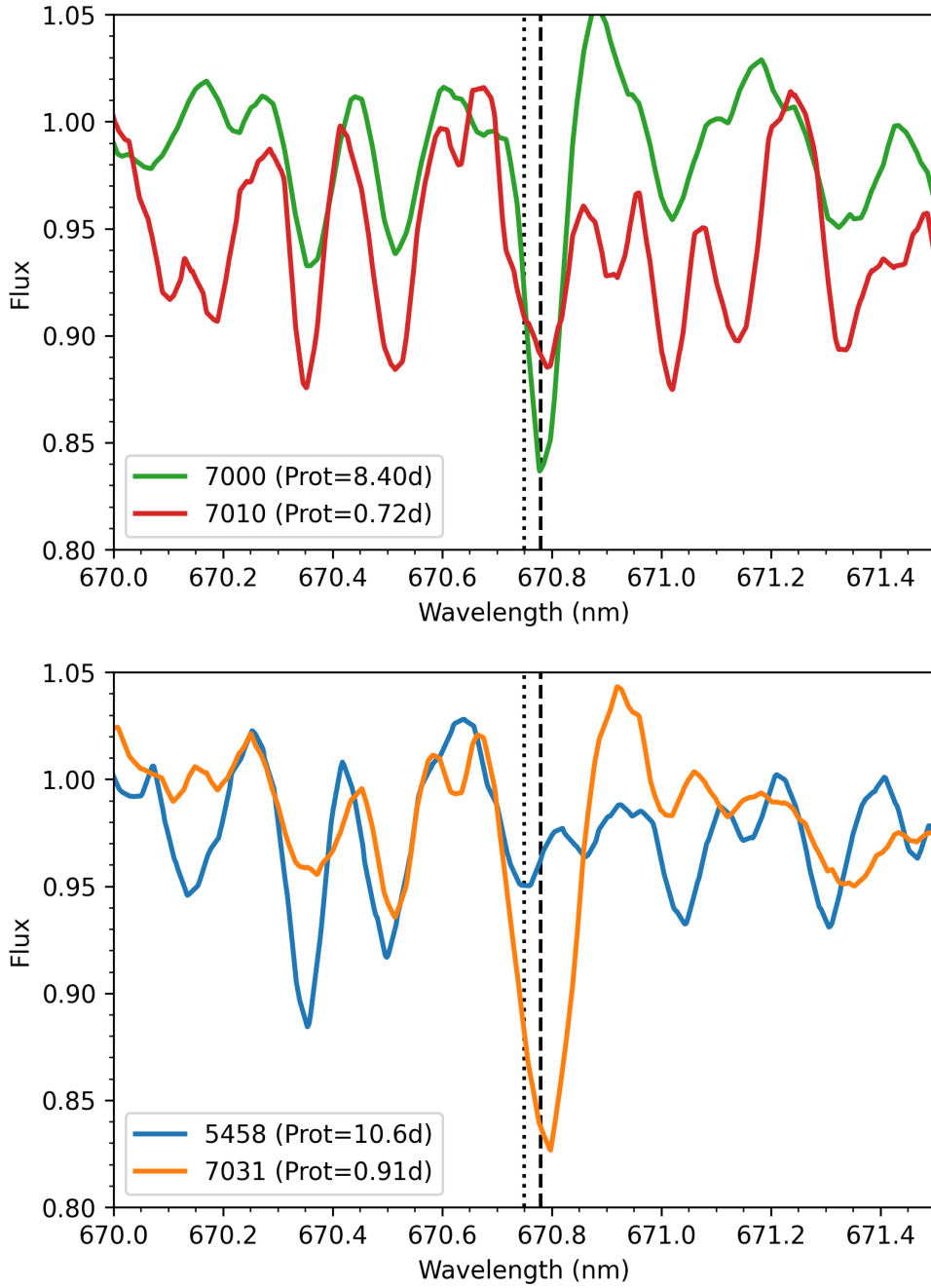


Figure 2.4: Blended feature around 670.78 nm for four K stars. **Top**— Small region of the spectrum for two mid K stars with different rotation periods. **Bottom**— Small region of the spectrum for two late K stars with different rotation periods. In both panels, the dashed black line shows the position of the Li doublet at 670.78 nm, while the dotted black line indicates the position of the Fe I line at 670.75 nm. Both features are blended independently of the spectral type and the rotation period of the star.

add errors to the synthetic one for each star. The EW corresponding to the Fe I line at 670.75 nm was then subtracted from the EW of the blend, resulting in a measurement of the EW of the Li doublet. The uncertainty in EW(Li) width was derived from the quadratic sum of the uncertainty in the blend and the uncertainty in the EW of the Fe I line.

Second, we followed the approach of [Arancibia-Silva et al. \(2020\)](#): we derived (B-V) colours for our stars from the dereddened *Gaia* (BP - RP) colours, and we applied the empirical relation derived in [Soderblom et al. \(1993b\)](#). To obtain intrinsic (B-V) colours for the targets observed in these campaigns we linearly interpolated through the [Pecaut & Mamajek \(2013\)](#) $(B-V)_0 - (BP-RP)_0$ relationship (see [Figure 2.5](#)). Finally, we calculated the contribution of the the Fe I line at 670.75 nm as in [Soderblom et al. \(1993b\)](#): $EW(Fe) = 20 (B-V)_0 - 3 \text{ m}\text{\AA}$.

The top panel on [Figure 2.6](#) shows the comparison between the Li EWs obtained by these two approaches. The median of the differences is around 10 mÅ, as indicated by the dotted black line, and the spread around this value is small.

The bottom panel of [Figure 2.6](#) shows the comparison between the Li EWs published in [Jeffries et al. \(2021\)](#) and the values obtained by employing the [Soderblom et al. \(1993b\)](#) relation. [Jeffries et al. \(2021\)](#) measured the Li EWs by comparing the science spectra with synthetic spectra without Li generated with the MOOG software ([Snedden et al., 2012](#)) and solar-metallicity Kurucz model atmospheres ([Kurucz, 1992](#)). The median of the differences is around 20 mÅ in this case, as indicated by the dotted black line, and the spread around this line is broader than the one shown in the top panel. Since the equivalent widths shown in the top panel have been derived from the same spectra, unlike the ones shown in the bottom panel, a broader spread in the latter is not surprising.

In [Figure 2.7](#), we plot the iron equivalent widths obtained from the [Soderblom et al. \(1993b\)](#) empirical relation and those measured in the synthetic spectra, confirming a $\approx 5 \text{ m}\text{\AA}$ difference between G0 and early K spectral types, which gets larger than 10 mÅ for stars cooler than $(BP-RP)_0 = 1.2$. Since [Soderblom et al. \(1993b\)](#) derived their relation from the spectra of inactive, old field stars with spectral types earlier than K3, a large difference for cooler dwarfs is not surprising. The smaller differences observed in hotter stars could have a methodological or an intrinsic origin.

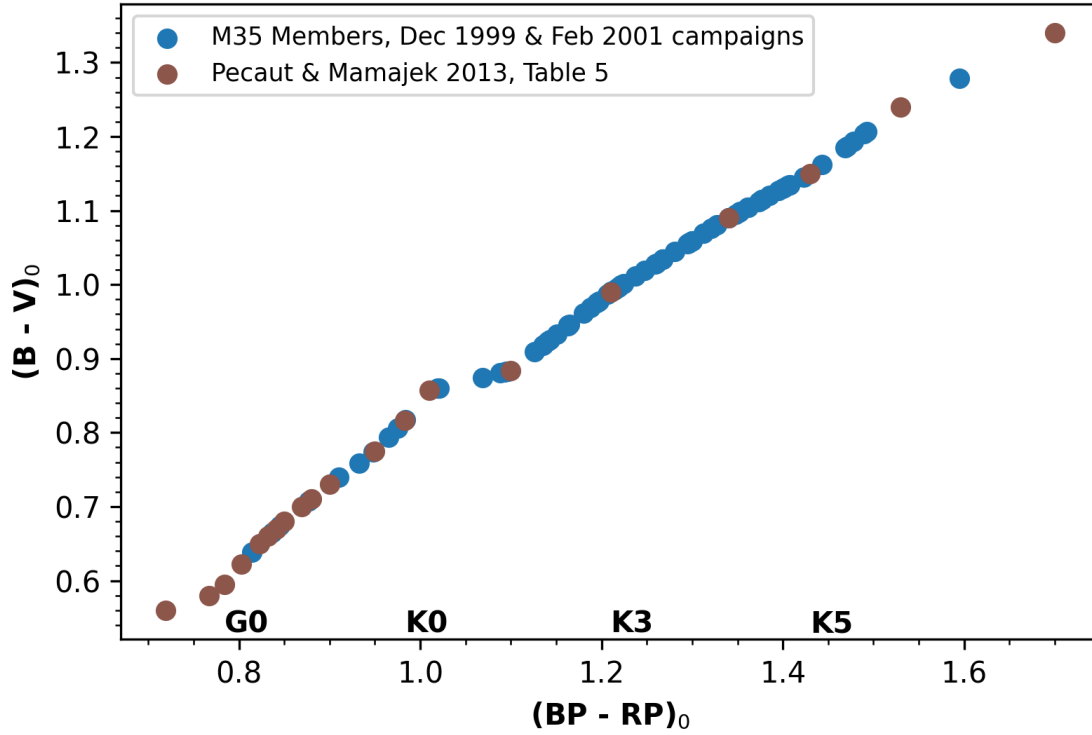


Figure 2.5: Equivalence between the intrinsic $(B-V)$ colours and the intrinsic Gaia colours. Brown circles have been taken from http://www.pas.rochester.edu/~emamajek/EEM_dwarf_UBVIJHK_colors_Teff.txt, where an updated version of the table shown in Pecaut & Mamajek (2013) is provided. Blue circles have been obtained by linear interpolation from the brown ones. The Gaia colours corresponding to M35 members have been dereddened using $E(BP - RP) = 0.415 A_V$, following Curtis et al. (2020).

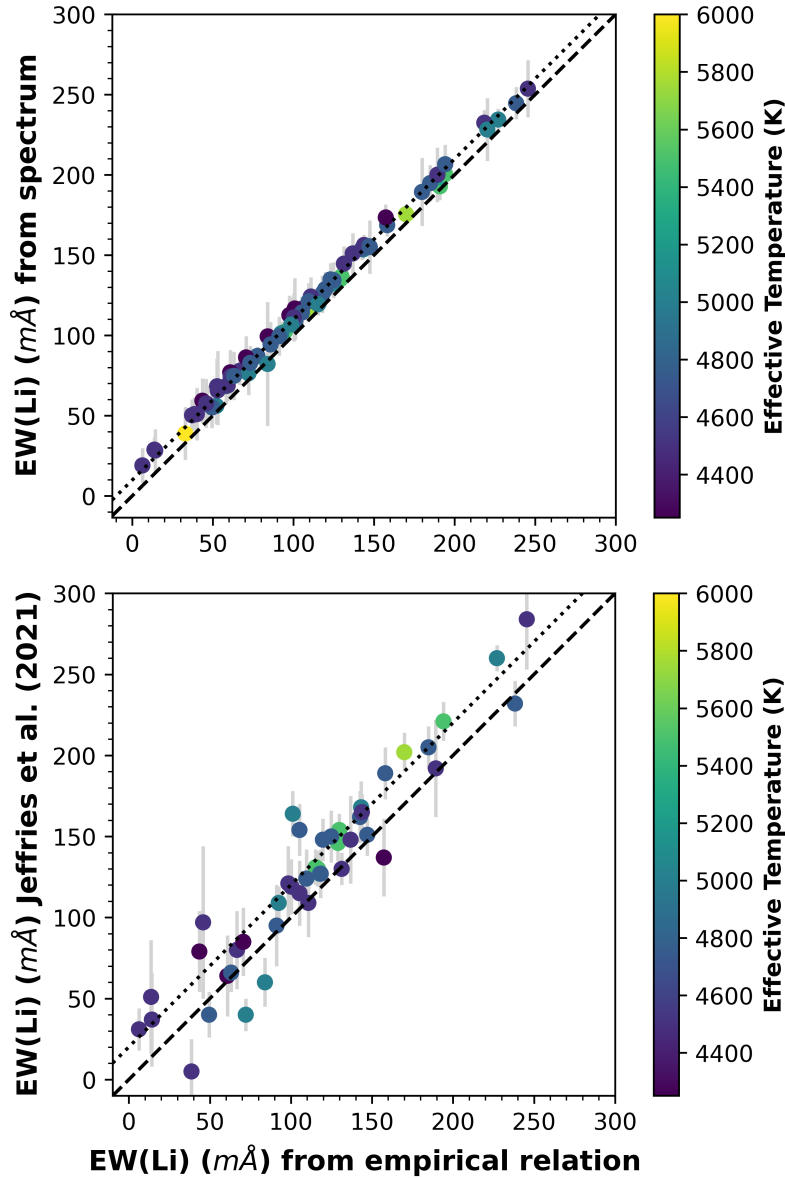


Figure 2.6: Comparisons between the Li EWs derived by applying the empirical relation published in [Soderblom et al. \(1993b\)](#) to the M35 spectra collected in 1999 December and 2001 February (*x* axes) and the EWs obtained by other methods for the same objects (*y* axes). **Top**—Comparison to Li EWs obtained using synthetic spectra without Li generated with the SPECTRUM code and MARCS model atmospheres. **Bottom**—Comparison to Li EWs published in [Jeffries et al. \(2021\)](#). In both panels, the dashed black line shows the one-to-one correspondence, while the dotted line indicates the median of the differences. The colour of each symbol indicates the effective temperature derived for the star. In both cases, the EWs indicated on the *y* axes are, on average, larger than the ones shown on the *x* axes.

It is possible that the empirical relation proposed by [Soderblom et al. \(1993b\)](#) takes into account fainter contributions from other elements different from iron that are not included in the synthetic spectra. However, given the completeness of the line list employed to generate the synthetic spectra, this explanation is unlikely. An alternative explanation could be that the [Soderblom et al. \(1993b\)](#) relation is useful for solar metallicity clusters, like the Pleiades, but overestimates the contribution of the Fe I line at 670.75 nm to the blended feature for subsolar metallicity clusters, such as M35. Consequently, we used the Li EWs obtained using synthetic spectra to remove the contribution of the Fe I line for our analysis.

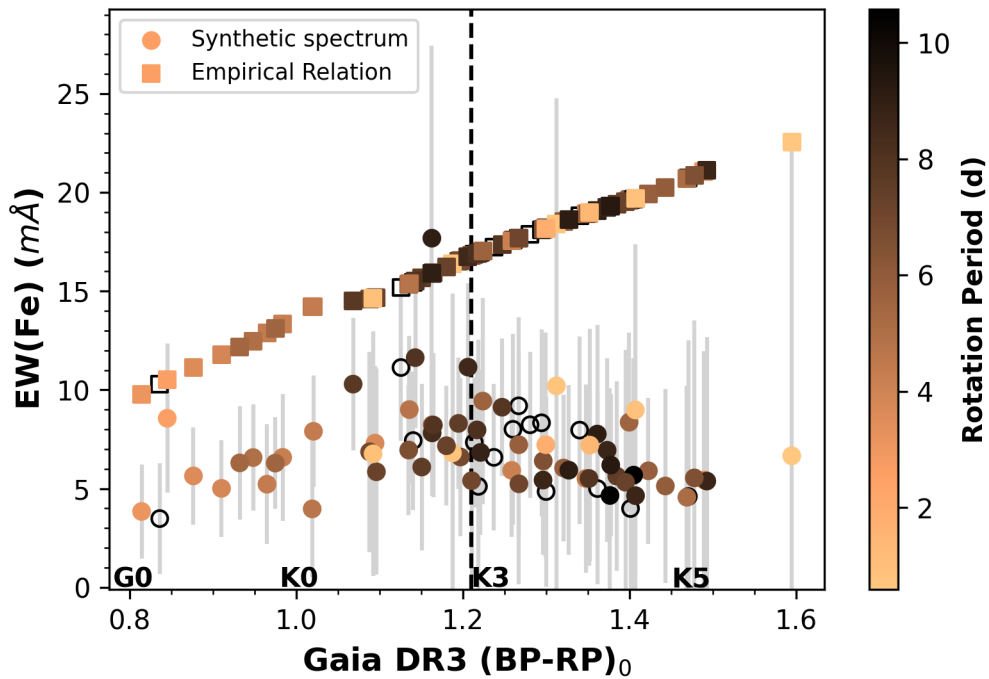


Figure 2.7: EWs measured for the Fe I line at 670.75 nm in the synthetic spectra and those derived from the empirical law proposed by [Soderblom et al. \(1993b\)](#). Gaia colours have been dereddened using $E(BP - RP) = 0.415 A_v$, following [Curtis et al. \(2020\)](#). The colour of each symbol indicates the rotation period of the star. The [Soderblom et al. \(1993b\)](#) relation was derived from spectra of stars on the left side of the vertical dashed line. The EWs obtained for stars on the right side of the line are therefore obtained by extrapolating that relation to a cooler range of temperatures.

Finally, we estimated the departures from LTE for the Li abundances derived from the non-LTE calculations published in [Lind et al. \(2009\)](#). To do so, we split our stars in bins of effective

temperature and linearly interpolated through Lind et al. (2009) non-LTE correction– $A(\text{Li})$ LTE relationship³ (see Figure 2.8).

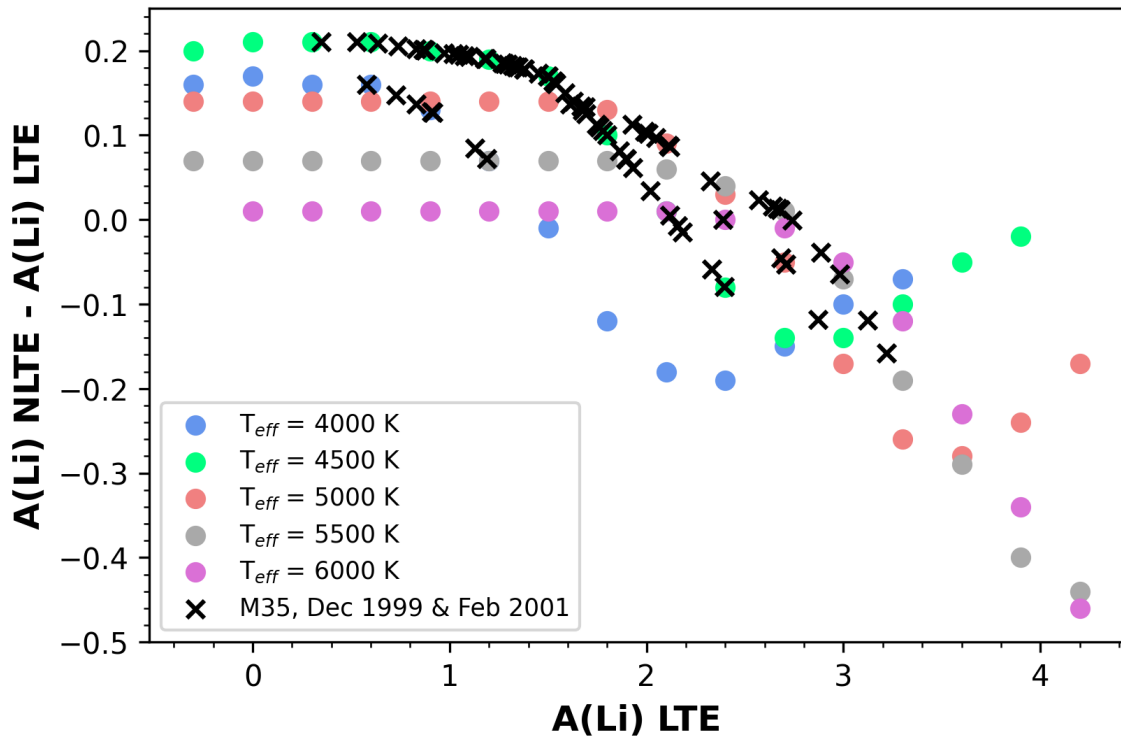


Figure 2.8: *non-LTE correction– $A(\text{Li})$ LTE relationship.* Circles indicate data taken from Lind et al. (2009), whereas the black crosses indicate the non-LTE corrections derived for the M35 members by linear interpolation. Circles of different colours indicate different effective temperatures.

Table 2.8 gives the derived Li EWs, the Fe EWs obtained with the two methods described above, as well as the LTE and non-LTE Li abundances for our stars.

2.5 Results

2.5.1 The metallicity of M35

Previous WIYN/Hydra spectroscopic studies of Li in M35 quoted different values for its metallicity. Barrado y Navascués et al. (2001a) derived $[\text{Fe}/\text{H}] = -0.21 \pm 0.10$ by measuring Fe EWs for

³We selected the rows in table 2 of Lind et al. (2009) for a solar metallicity and microturbulence $\xi_t = 1.0 \text{ km s}^{-1}$.

Table 2.8: Blended Li and Fe EWs, Fe EWs, Li EWs, and Li LTE and non-LTE abundances for the 110 members of M35 observed in 1999 December and 2001 February. This table is only partially presented. Its complete version is available in Appendix A.

ID	$EW(Li+Fe)$ (mÅ)	$EW(Fe)^{(a)}$ (mÅ)	$EW(Fe)^{(b)}$ (mÅ)	$EW(Li)^{(a)}$ (mÅ)	$A(Li)_{LTE}$	$A(Li)_{NLTE}$
5088	119.2±6.5	3.5±2.8	10.3	115.7±7.1	2.88±0.04	2.85
5103	201.4±7.6	8.6±3.8	10.5	192.9±8.5	2.98±0.03	2.92
5139	127.1±5.2	5.0±2.5	11.8	122.0±5.7	2.66±0.03	2.68
5148	181.1±4.7	5.6±2.5	11.1	175.5±5.3	3.22±0.03	3.06
5183	107.6±5.1	5.2±3.0	12.9	102.3±5.9	2.57±0.03	2.59
5295	≤14.3 ^(c)	–	–	–	–	–
...

Notes. ^(a)Value obtained from the synthetic spectrum without Li. ^(b)Value obtained from the empirical relation of [Soderblom et al. \(1993b\)](#). ^(c)Upper limit. Li abundances and Fe EWs are not provided for these cases.

a set of single G members of the cluster, whereas [Steinhauer & Deliyannis \(2004\)](#) set $[Fe/H] = -0.143 \pm 0.014$ when studying Li depletion in the cluster’s F dwarfs. On the other hand, [Anthony-Twarog et al. \(2018\)](#) measured the EW of the Ca I line at 671.77 nm and obtained results compatible with solar metallicity. [Jeffries et al. \(2021\)](#) assumed a solar metallicity for their analysis, but discussed the impact a lower metallicity could have on their results.

As discussed in §2.4.2, we used 40 iron lines to derive the abundance of this element for each of the M35 members observed in 1999 December and 2001 February. This list includes 38 Fe I transitions and two Fe II transitions. The results obtained for those single stars with the highest probability of belonging to M35 were employed to derive our own value for the metallicity for this cluster.

As shown in Figure 2.9, our results clearly point to a subsolar metallicity for M35. We have only considered the 13 hottest stars ($T_{eff} > 4500$ K) in the set previously described, obtaining an average metallicity of $[Fe/H] = -0.26 \pm 0.09$, where the standard deviation of the values has been used to indicate the uncertainty. This value is very similar to the metallicity obtained when the whole range of T_{eff} is considered, which is $[Fe/H] = -0.28 \pm 0.11$. Both results are fully consistent with the values published in [Barrado y Navascués et al. \(2001a\)](#) and [Steinhauer & Deliyannis](#)

(2004).

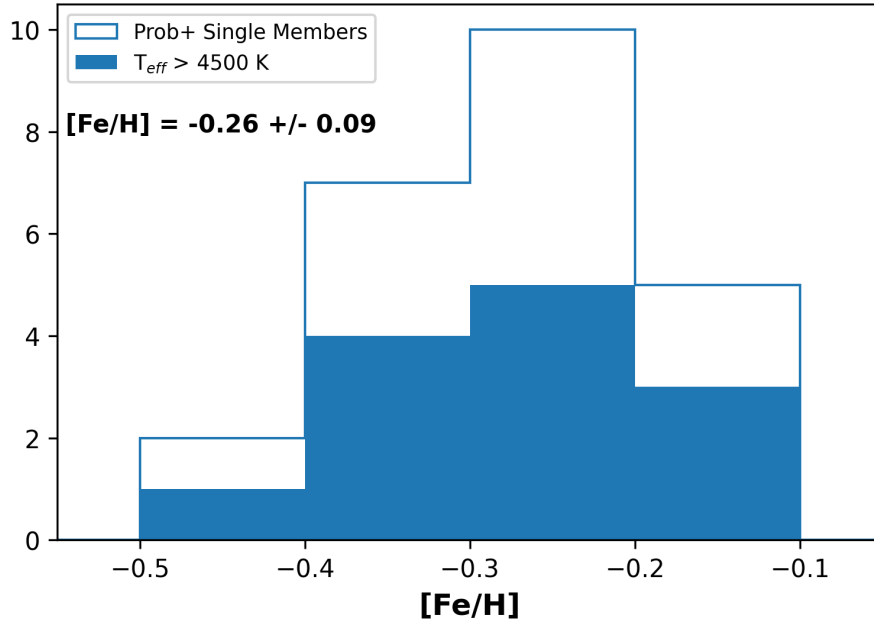


Figure 2.9: Metallicities obtained for the single stars observed in 1999 December and 2001 February that have the highest probability of belonging to M35 (Prob+ members). The unfilled histogram represents the distribution of metallicities obtained for all of them, whereas the filled histogram only includes the hottest stars in this sample. We used the values corresponding to the hottest ones to derive a metallicity of $[Fe/H] = -0.26 \pm 0.09$ for M35.

2.5.2 The Li-rotation connection in M35

Figure 2.10 is a color–period diagram in which we indicate the relative Li abundances of the stars in M35; the top panel includes all of the cluster members, whereas in the bottom panel we have removed candidate and known binary systems. Table 2.9 includes the stellar parameters, rotation periods, and Li EWs for these stars. The most striking result is that M35 fast rotators of G and K spectral types are Li-rich compared to slow rotators of similar effective temperature. This result is consistent with the pattern described in Barrado y Navascués et al. (2001a), Anthony-Twarog et al. (2018), and Jeffries et al. (2021) for the M35 open cluster, as well as with the trend found for other stellar associations of similar age such as Pleiades (Barrado et al., 2016; Bouvier et al., 2018) and younger associations (Bouvier, 2020).

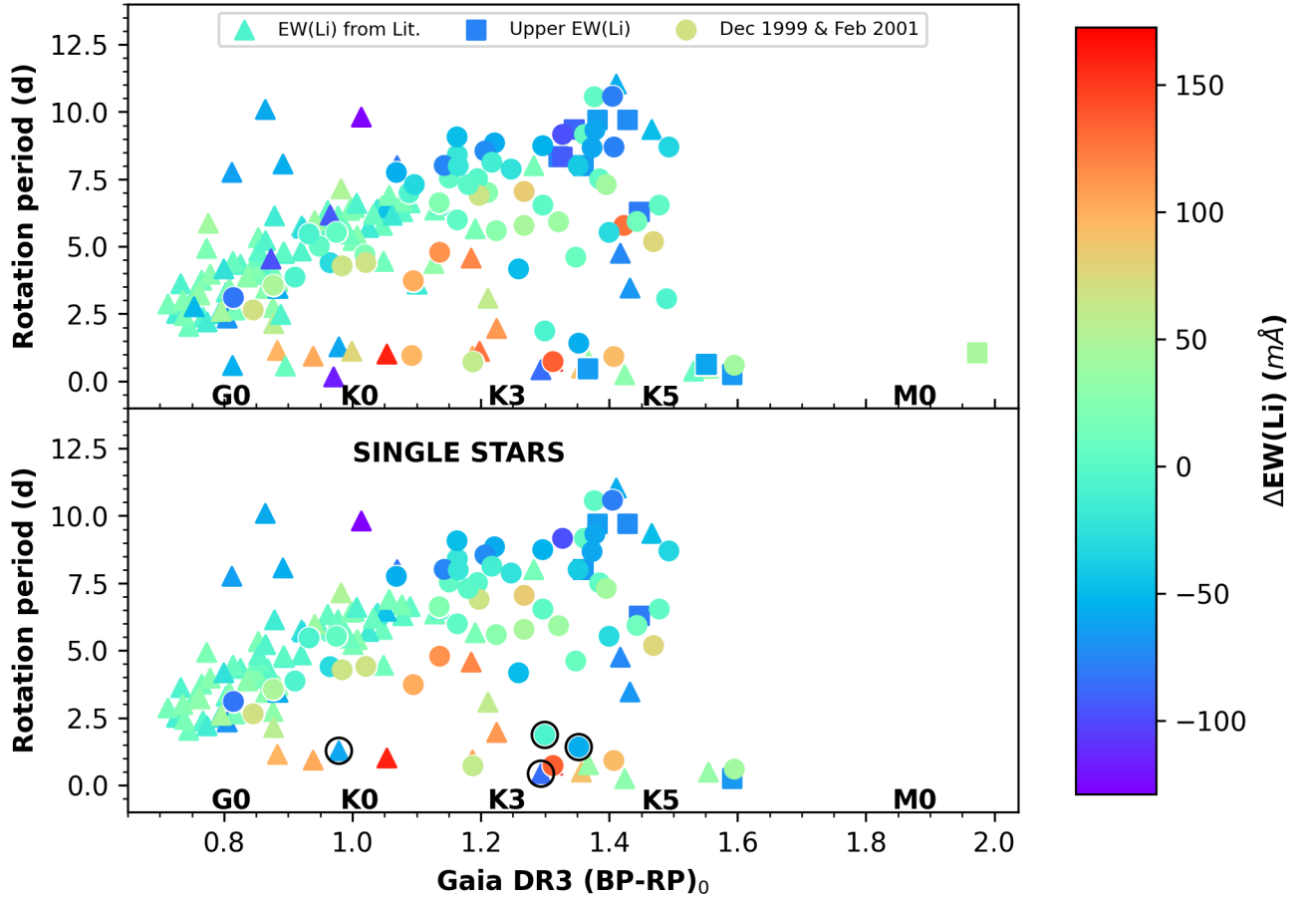


Figure 2.10: Distribution of rotation periods for the M35 members in our sample. The colour of each symbol indicates the deviation of the $EW(\text{Li})$ obtained for that star from a third order polynomial fit to $EW(\text{Li})$ vs. $(BP - RP)_0$. Circles indicate the M35 members observed in 1999 December and 2001 February whose Li EWs have been derived as discussed in section 2.4.2, while triangles are those M35 members whose Li EWs have been taken from [Barrado y Navascués et al. \(2001a\)](#), [Anthony-Twarog et al. \(2018\)](#), or [Jeffries et al. \(2021\)](#). Squares denote those stars observed in 1999 December and 2001 February for which we could only derive upper limits for the Li EWs. **Top**—Our complete set of M35 members with rotation periods. **Bottom**—Only those sources classified as single stars are shown. The four outliers that do not follow the general trend are circled in black.

Table 2.9: Rotation period, Li EW, effective temperature, luminosity, membership class and binary status for 250 M35 members. This table is only partially presented. Its complete version is available in Appendix A.

ID	Membership Class	Binary ^(a)	T_{eff} (K)	L (L_{\odot})	$EW(Li)$ (mÅ)	$EW(Li)$ ^(b) Source	Prot ^(c) (d)	Prot ^(d) Source
5408	Poss+	0	4500±125	0.21±0.04	291	B01	0.74	M09
5087	Poss+	0	6000±125	1.57±0.79	101.7	AT18	2.20	SF20
5382	Prob	0	4750±125	0.26±0.05	187	Je21	3.08	M09
5194	Poss	1	5000±125	0.68±0.12	153.6	This Work	4.70	M09
7034	Prob	0	4500±125	0.16±0.03	≤ 29.9	This Work	9.71	M09
5107	Poss+	0	6000±125	1.38±0.26	94	B01	2.51	This Work
...

Notes. ^(a)1 = likely binary, 0 = single star. ^(b)B01 is [Barrado y Navascués et al. \(2001a\)](#), AT18 is [Anthony-Twarog et al. \(2018\)](#), and Je21 is [Jeffries et al. \(2021\)](#). ^(c)-99 = No rotation period available for this source. ^(d)M09 is [Meibom et al. \(2009\)](#), SF20 is [Soares-Furtado et al. \(2020\)](#), N15 is [Nardiello et al. \(2015\)](#), and L16 is [Libralato et al. \(2016\)](#).

Few studies have addressed the influence of a stellar companion on the Li abundance. [Martín et al. \(2002\)](#) studied the abundance of this element in wide binaries with solar-type twin components, finding large differences between the components for a significant part of the sample. [Barrado y Navascués & Stauffer \(1996\)](#) demonstrated that tidally locked binaries in the Hyades open cluster are richer in Li in comparison with single stars. In addition, [Barrado y Navascués et al. \(1997\)](#) observed Li overabundances in chromospherically active binaries with respect to single stars. In our case, it is worth highlighting that the difference in Li EWs between fast and slow G and K rotators is more evident in the bottom panel of Figure 2.10, where multiple systems are not included. A similar fact is pointed out by [Beck et al. \(2017\)](#) from a sample of 18 solar-analogue stars.

The M0 fast rotator shown in the top panel deserves special attention. This star is a spectroscopic binary with identification number 5517 which was observed in 1999 December. We have measured $EW(Li) \leq 24.1$ mÅ for this object, which is a value very similar to the EWs derived by [Bouvier et al. \(2018\)](#) and [Barrado et al. \(2016\)](#) for Pleiades members of similar spectral type and rotation period. Thus, at least for M35 age, it seems that fast rotation is not enough for preserving Li in the atmosphere of an early M dwarf.

Four outliers, which are circled in the bottom panel of Figure 2.10, do not follow the trend

described above. The hottest, whose Li EW has been taken from [Anthony-Twarog et al. \(2018\)](#), has the identification number 5181 (46015 in [Anthony-Twarog et al., 2018](#)). Its rotation period has been taken from [Meibom et al. \(2009\)](#), but very similar periods are considered ambiguous blends in [Soares-Furtado et al. \(2020\)](#) and [Libralato et al. \(2016\)](#), so the rotation period of this source may be different from the one we have assigned it in [Table 2.6](#). This source is also considered as an outlier in [Anthony-Twarog et al. \(2018\)](#) (see section 4 of that work).

Two fast rotators, 7049 and 7053, observed in 1999 December and 2001 February have Li EWs that are surprisingly low. The membership of star 7049 is doubtful since both the probability provided by Clusterix 2.0 and the radial velocity measured for this star indicate it does not belong to M35. Consequently, the membership probability assigned in [Bouy et al. \(2015\)](#) to this source may be optimistic. By contrast, star 7053 has the highest probability of belonging to M35. However, only [Meibom et al. \(2009\)](#) provides rotation period for this star, and comparing their result with those of others is therefore not possible. Both sources were studied by [Jeffries et al. \(2021\)](#), who obtained Li EWs compatible with the ones shown in [Table 2.8](#).

Finally, the equivalent width of the remaining outlier, star 5290, has been taken from [Jeffries et al. \(2021\)](#). In contrast to the other sources, there is no reason to think that the rotation period assigned to this star is mistaken, nor that it is not member of M35. Follow-up observations of this star are needed to understand the reason why it is Li-poor in comparison with the other fast rotators. In any case, it is clear that the aforementioned connection between Li and rotation holds.

2.5.3 Comparison with other clusters

We have included in [Figure 2.11](#) and [Figure 2.12](#) the single stars studied by [Jeffries et al. \(2021\)](#) that do not have counterparts in our sample (top panels), as well as equivalent data for the Pleiades for comparison (bottom panels). [Galindo-Guil et al. \(2022\)](#) recently provided a robust value of $127.4^{+6.3}_{-10}$ Myr for the age of the Pleiades by employing the LDB technique described in [Barrado \(2016\)](#), [Soderblom et al. \(2014\)](#), [Rebolo et al. \(1992, 1996\)](#), and [Stauffer et al. \(1998, 1999\)](#). Although the age of M35 is affected by a much higher uncertainty, given the values provided by

Jeffries et al. (2021) and Anthony-Twarog et al. (2018) (140 ± 15 Myr and 150 ± 25 Myr, respectively) both clusters could be coeval. In fact, Abdelaziz et al. (2022) obtained an age of 126 Myr for M35 by using the Padova isochrones of Marigo et al. (2017) to fit the turnoff point in several color–magnitude diagrams. We assumed that the age of M35 is between 125 Myr and 175 Myr, the latter being the value provided by Barrado y Navascués et al. (2001a).

The metallicity of the Pleiades is very close to solar. Boesgaard & Friel (1990) derived $[\text{Fe}/\text{H}] = -0.034\pm 0.024$ from a sample of F dwarfs whereas Gebran & Monier (2008) obtained $[\text{Fe}/\text{H}] = 0.06\pm 0.02$. Given the metallicity derived for M35 by Barrado y Navascués et al. (2001a), Steinhauer & Deliyannis (2004), and this work, M35 is slightly metal poor in comparison with the Pleiades. Despite this difference in metal content and a possible difference in age, the trends shown in Figures 2.11 and 2.12 for M35 and the Pleiades are very similar. In both cases, fast rotators are richer in Li than slow rotators of the same spectral type. This connection is more evident for K stars than for G stars as the spread is larger in that range of effective temperatures.

We also compared our results for M35 to those for M34. Ianna & Schlemmer (1993) estimated an age of 250 Myr for M34 through isochrone fitting, whereas Meynet et al. (1993) derived an age of 178 Myr for this cluster employing the same technique. Schuler et al. (2003) derived $[\text{Fe}/\text{H}] = 0.07\pm 0.04$ from high resolution spectra of five G-K dwarf members of the cluster. Since M34 is older than M35 and has solar metallicity, as do the Pleiades, we have compared our sample of M35 single dwarfs of G-K spectral type with the one presented in Gondoin (2014) for M34 (Figure 2.13). Although the similarities between both distributions are more evident in Figure 2.12, as the Pleiades sample is more similar in size to that for M35, a similar trend can be observed for M34 K dwarfs: the fast rotators are richer in Li than the slow ones.

To statistically compare the Li measurements collected for the three clusters, we have performed Kolmogorov-Smirnov tests between them (Hodges, 1958). The purpose of this test is to verify whether two samples (in this case, the Li EWs collected) were taken from the same continuous distribution. As fast rotators exhibit abnormally high Li EWs, we only considered stars with rotation periods >2 d. We also excluded binaries and stars with upper limits of $\text{EW}(\text{Li})$. Figure

2.14 shows the empirical distribution functions obtained for each of the 1000 tests performed between the Li EWs sample corresponding to M35 and the samples corresponding to the Pleiades and M34. The median of the p-values obtained in both cases (shown in the panels of the figure) do not allow us to rule out the possibility that the three samples come from the same continuous distribution, implying a clear similarity between them. On the other hand, the median of the p-values obtained when we compared the Pleiades sample and the M34 sample in the same way is higher, indicating a larger difference between the Li distributions of these two clusters.

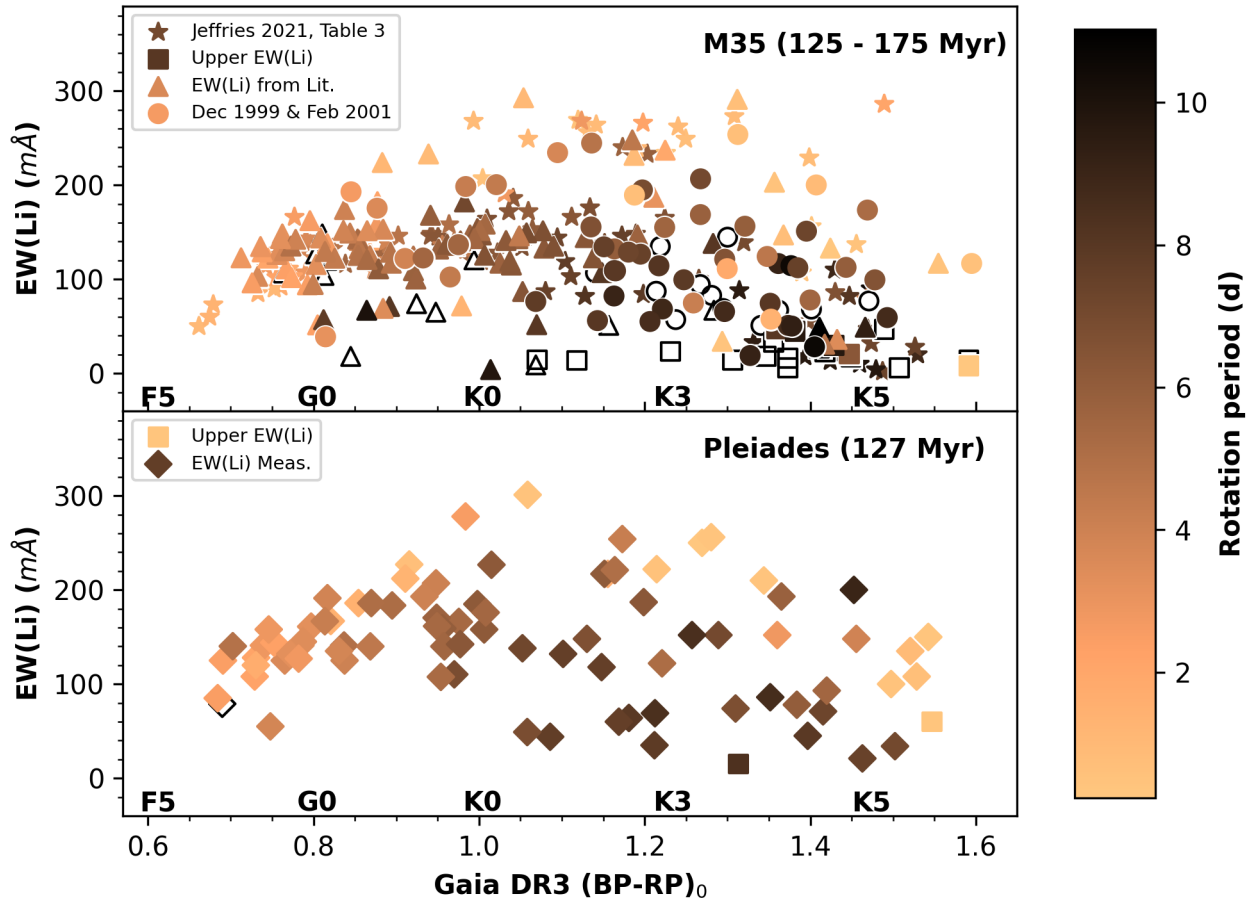


Figure 2.11: Li EWs vs. Gaia colours for single members of M35 and the Pleiades. The symbols are colour-coded by the rotation period of the star. The empty symbols are M35 members without a measure rotation period. **Top**—M35 single stars. Circles, triangles, and squares have the same meaning as in Figure 2.10. We use star symbols to represent the single stars analysed by [Jeffries et al. \(2021\)](#) that do not have counterparts in our sample. **Bottom**—Pleiades single stars taken from [Barrado et al. \(2016\)](#) and [Bouvier et al. \(2018\)](#). Note that we have chosen the Li EWs and rotation periods published in [Bouvier et al. \(2018\)](#) for all of the stars that are included in both studies. We have only plotted those Pleiades members whose Gaia colours are within the range covered by the M35 sample shown in the top panel. Gaia colours have been dereddened following [Curtis et al. \(2020\)](#) with $A_V = 0.12$.

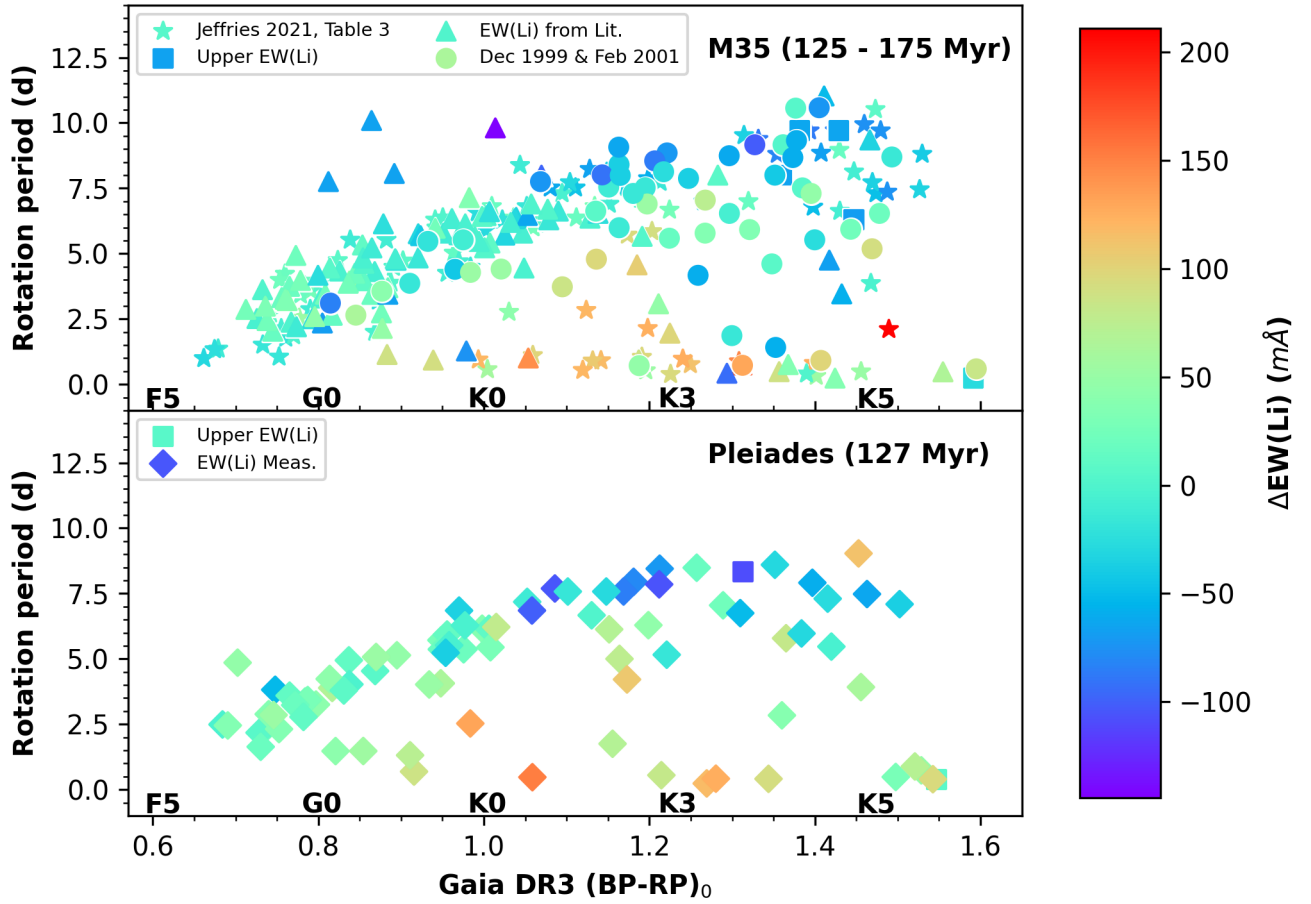


Figure 2.12: Rotation periods vs. Gaia colours for single members of M35 and the Pleiades. The colour of each symbol indicates the deviation of $EW(Li)$ from a third-order polynomial fit to $EW(Li)$ vs. $(BP - RP)_0$ for the M35 sample shown in the upper panel. **Top**— M35 single stars. Circles, triangles, and squares have the same meaning as in Figure 2.10 whereas stars account for the M35 single sources analysed in Jeffries et al. (2021) which do not have counterpart in our sample. **Bottom**— Pleiades single stars taken from Barrado et al. (2016) and Bouvier et al. (2018). Note that we have chosen the Li EWs and rotation periods published in Bouvier et al. (2018) for all the sources which have counterpart in both studies. We have only plotted those Pleiades members whose Gaia colours are within the range covered by the M35 sample shown on the top panel. Gaia colours have been dereddened following Curtis et al. (2020) with $A_V = 0.12$.

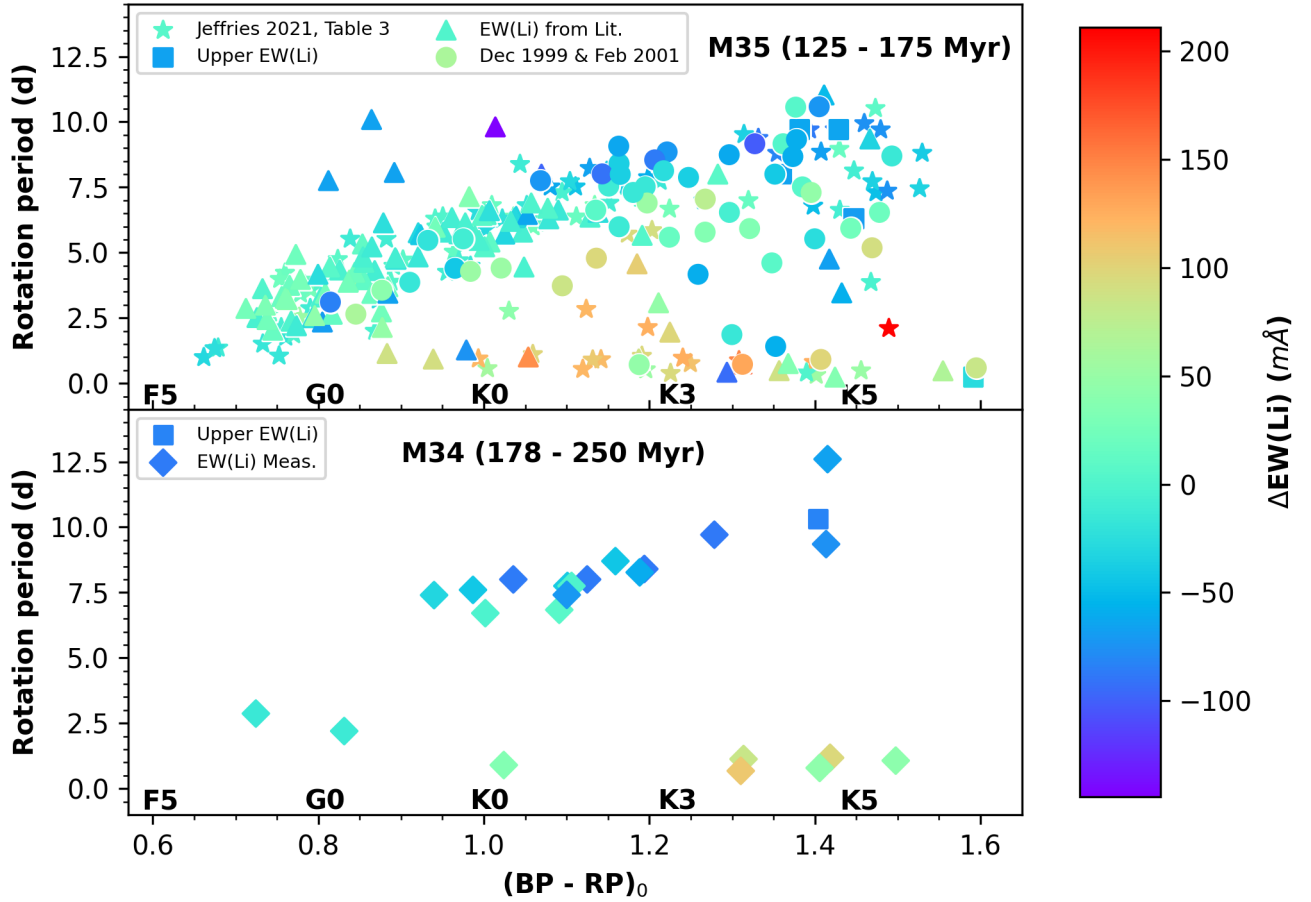


Figure 2.13: Rotation periods vs. Gaia colours for single members of M35 and M34. The colour of each symbol indicates the deviation of $EW(Li)$ from a third order polynomial fitted to $EW(Li)$ vs $(BP - RP)_0$ for the M35 sample shown in the upper plot. **Top**—M35 single stars. Circles, triangles, squares, and stars have the same meaning as in Figure 2.12. **Bottom**—M34 single stars from [Gondoin \(2014\)](#). Gaia colours have been dereddened following [Curtis et al. \(2020\)](#) with $A_V = 0.217$.

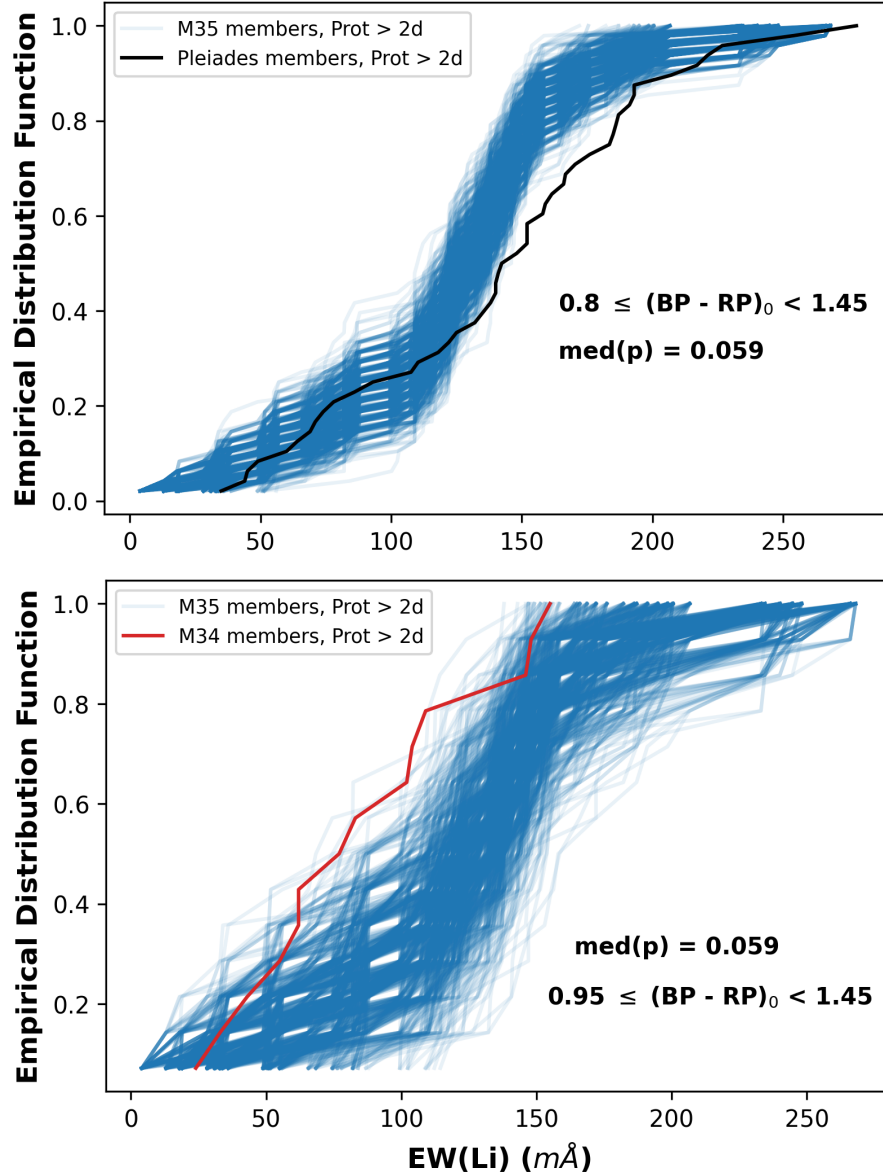


Figure 2.14: Empirical distribution functions obtained from 1000 Kolmogorov-Smirnov tests performed between the Li EWs sample corresponding to M35 and those of other clusters. **Top**—Pleiades Li EWs sample (see Figures 2.11 and 2.12). For each test we have randomly picked 48 Li EWs from the M35 sample (blue), that is, the size of the Pleiades sample, and compared them with the Pleiades sample (black). **Bottom**—M34 Li EWs sample (see Figure 2.13). For each test we have randomly picked 14 Li EWs from the M35 sample (blue), that is, the size of the M34 sample, and compared them with the latter (red). The range of Gaia colours employed in each case is written in each panel. We selected G and K stars for the comparison between M35 and the Pleiades, but only K stars in the comparison with M34 due to the few data available for this cluster.

Chapter 3

The effects of rotation and metallicity on the lithium depletion in 600 Myr open clusters

The Li distributions of open clusters with ages between 100 and 250 Myr are very similar even if they exhibit differences in metallicity of 0.2-0.3 dex (Cuenda-Muñoz et al., 2024). On the other hand, stellar rotation has a strong influence on Li depletion in G and K members of these clusters (Barrado y Navascués et al., 2001a; Gondoin, 2014; Barrado et al., 2016; Bouvier et al., 2018; Anthony-Twarog et al., 2018; Jeffries et al., 2021; Cuenda-Muñoz et al., 2024). Since stellar rotation and Li abundance change as these spectral types evolve in the MS, an intriguing issue is whether the effects of rotation and metallicity on Li depletion are similar in older OCs.

As we explained in Chapter 1, previous studies of Li in 600 Myr OCs focused mainly on Praesepe and the Hyades. The existence of some spread in the Li abundances of G and K dwarfs of this age was a matter of debate a few decades ago. Barrado y Navascués & Stauffer (1996) confirmed the Li overabundance of tidally locked binaries in the Hyades, but other works showed evidences that Praesepe close binaries do not follow the same pattern (see, for instance, Soderblom et al., 1993a). Furthermore, both clusters have roughly the same metallicity (Cummins et al., 2017) and few works have compared their Li distributions with OCs of similar ages but different metallicities.

To shed more light on this issue, we have obtained Li EWs and rotation periods for GK members of Praesepe and Coma Berenices. Although both OCs have roughly the same age (~600

Myr), the sparseness and low proper motion of the latter hamper the identification of its members (Singh et al., 2021). As a result, the few previous studies that have addressed the Li distribution of this cluster are affected by this limitation (see, for instance, Soderblom et al., 1990; Jeffries, 1999; Ford et al., 2001). Fortunately, *Gaia* data allow nowadays the identification of cluster members with better accuracy.

3.1 Assembling the sample

3.1.1 Target selection for Coma Berenices

We selected our targets from five catalogs of Coma Berenices members: Kraus & Hillenbrand (2007), Collier Cameron et al. (2009), Fürnkranz et al. (2019), Tang et al. (2019) and Pang et al. (2021). Kraus & Hillenbrand (2007) took advantage of archival data from SDSS, 2MASS, US-NOB1.0, and UCAC-2.0 surveys to identify 149 sources with membership probabilities $\geq 50\%$. On the other hand, Collier Cameron et al. (2009) provided rotation periods for 30 stars for which they derived membership probabilities $\geq 50\%$ from their proper motions and positions in a 2MASS CMD. Fürnkranz et al. (2019) and Tang et al. (2019) used *Gaia* Data Release 2 (DR2; Gaia Collaboration et al., 2018b) data to separate the population of the stellar association Group X from that of Coma Berenices. As a result, Fürnkranz et al. (2019) and Tang et al. (2019) identified 214 and 197 members of Coma Berenices, respectively. Finally, Pang et al. (2021) took advantage of *Gaia* Early Data Release 3 (EDR3; Gaia Collaboration et al., 2021) astrometry and kinematic data from the literature to identify members of different open clusters using an unsupervised machine-learning method. Pang et al. (2021) identified 158 Coma Berenices members in this way. After combining all these catalogs, we ended up with 339 unique members of Coma Berenices. It is worthy to mention that 91 and 16 of the members included in Kraus & Hillenbrand (2007) and Collier Cameron et al. (2009), respectively, are also included in some of the *Gaia*-based catalogs.

3.1.2 Target selection for Praesepe

In order to select Praesepe members for spectroscopic observations, we took advantage of the catalogs provided by [Cantat-Gaudin et al. \(2018\)](#) and [Rampalli et al. \(2021\)](#). In [Rampalli et al. \(2021\)](#) the list of Praesepe members presented in [Douglas et al. \(2014\)](#) was enriched with several catalogs that made use of Gaia DR2 data to distinguish between members and non-members of the cluster. On the other hand, [Cantat-Gaudin et al. \(2018\)](#) provided lists of members for a number of open clusters using Gaia DR2 data and an unsupervised membership assignment code. As a result, [Rampalli et al. \(2021\)](#) provided rotation periods for 1030 Praesepe members with membership probabilities $\geq 70\%$ while [Cantat-Gaudin et al. \(2018\)](#) identified 685 members with membership probabilities over that threshold. The catalog provided by [Rampalli et al. \(2021\)](#) includes 534 of the Praesepe members listed in [Cantat-Gaudin et al. \(2018\)](#). Consequently, our final catalog contains 1181 Praesepe members.

3.1.3 Spectroscopic observations

Between February 2022 and May 2023 we collected high resolution spectra for 22 Coma Berenices members selected from the aforementioned catalogs. In addition, 19 Praesepe members were observed between February 2022 and February 2024. We used the CAFE spectrograph ([Aceituno et al., 2013](#); [Lillo-Box et al., 2020](#)) located at the Calar Alto Astronomical Observatory, the FIES spectrograph ([Telting et al., 2014](#)) installed at the Nordic Optical Telescope (NOT), and the SOPHIE spectrograph ([Bouchy & Sophie Team, 2006](#); [Perruchot et al., 2008](#)) located at the Haute-Provence Observatory. All these facilities provide high resolution ($R \geq 40\,000$) spectra within a spectral range that includes the Li doublet at 670.78 nm. Table 3.1 shows the main characteristics of the facilities used. In addition, all of them are equipped with automatic data-reduction pipelines that provide the reduced spectra after each exposure.

The G and K stars that compose our samples exhibit a wide range of apparent V magnitudes: $9.8 \leq V \leq 12.6$ in the case of Coma Berenices and $9.9 \leq V \leq 12.0$ in the case of Praesepe. Consequently, only one exposure was required to obtain signal-to-noise ratios (SNRs) over 20 for

Table 3.1: *Facilities used and clusters observed in each observation campaign.*

Campaign	Clusters	Instrument	Telescope	Observatory	Spectral resolution	Spectral range (nm)
Feb 2022	Coma	SOPHIE	1.93 m	Haute-Provence	40 000	387 - 694
Feb 2022	Both	FIES	NOT	Roque de los Muchachos	46 000	370 - 830
Jun 2022	Coma	CAFE	2.2 m	Calar Alto	62 000	407 - 925
Jan 2023 - Feb 2023	Both	CAFE	2.2 m	Calar Alto	62 000	407 - 925
Apr 2023	Both	CAFE	2.2 m	Calar Alto	62 000	407 - 925
Apr 2023	Both	FIES	NOT	Roque de los Muchachos	46 000	370 - 830
May 2023	Coma	SOPHIE	1.93 m	Haute-Provence	40 000	387 - 694
Feb 2024	Praesepe	FIES	NOT	Roque de los Muchachos	46 000	370 - 830

the brightest targets, but we had to combine up to four exposures for the faintest ones to obtain SNRs over that threshold.

3.1.4 Archival spectra and data from the literature

In order to increase the size of our spectroscopic sample we searched for high resolution spectra for other Coma Berenices members in the archives of three spectrographs: ELODIE, ESPaDOs and SOPHIE. ELODIE ([Baranne et al., 1996](#)) was a cross-dispersed échelle spectrograph installed at the 1.93 m telescope of the Haute-Provence Observatory until August 2006, when it was decommissioned. The spectra provided by this instrument cover the wavelength range between 385 nm and 680 nm with a spectral resolution $R = 42\,000$. On the other hand, ESPaDOs ([Donati, 2003](#); [Moutou et al., 2015](#)) is a high-resolution échelle spectrograph and spectropolarimeter which provides spectra covering the wavelength range between 370 nm and 1050 nm. This instrument has two different spectroscopic modes, one of them (object+sky mode) provides a resolving power $R = 68\,000$ whereas the other one (object only mode) provides a resolving power $R = 81\,000$. We obtained spectra for five stars from the ELODIE archive ([Moultaka et al., 2004](#)), for four stars from the ESPaDOs archive ([Petit et al., 2014](#)), and for one more star from the SOPHIE archive.

Besides this, we also took advantage of previous studies of Li in Coma Berenices to increase the size of our sample. [Jeffries \(1999\)](#) reported Li abundances and EWs for 15 late F, G and K stars observed with the Intermediate Dispersion Spectrograph (IDS) installed at the Isaac Newton

Telescope. A few years later, [Ford et al. \(2001\)](#) took advantage of the proper motion study presented in [Odenkirchen et al. \(1998\)](#) to select candidate members for spectroscopic follow-up with the Isaac Newton Telescope and the William Herschel Telescope. As a result, [Ford et al. \(2001\)](#) provided Li abundances and EWs for 20 F, G and K stars. We have increased our sample with three stars analysed by [Ford et al. \(2001\)](#) and two analysed by [Jeffries \(1999\)](#).

To increase the size of our Praesepe sample we cross-matched the catalogs presented in [Rampalli et al. \(2021\)](#) and [Cantat-Gaudin et al. \(2018\)](#) with the stars analysed by [Cummings et al. \(2017\)](#). The authors of the latter work used the Hydra multi-object spectrograph on the WIYN 3.5 m telescope to observe a list of Praesepe candidate members selected from [Wang et al. \(1995\)](#). The Li abundances derived by them were supplemented with previously published results, obtaining a final sample of 110 Praesepe members with measurements of Li abundance. We added 36 of them to our Praesepe sample since they had counterpart in any of the aforementioned catalogs and we did not have spectra for them.

3.1.5 Multiple systems in our samples

In order to distinguish between single stars and multiple systems, we used TOPCAT ([Taylor, 2005](#)) to cross-match both samples with the *Gaia* Data Release 3 (DR3; [Gaia Collaboration et al., 2023](#)), obtaining photometry and astrometry for all the sources. The *Gaia* Renormalised Unit Weight Error (RUWE) is expected to be $\lesssim 1.0$ for sources when the single-star model gives a good fit to the astrometric observations, and previous studies have found that larger RUWE values imply that the objects are unresolved binaries in wide orbits (for instance, [Deacon & Kraus, 2020](#); [Ziegler et al., 2020](#); [Kervella et al., 2022](#)). Consequently, we flagged as wide binaries the stars with $\text{RUWE} > 1.2$, finding 16 wide binaries in our sample of Coma Berenices members and 25 in our sample of Praesepe members.

Besides this, we cross-matched our samples with the catalogs presented in [Mermilliod et al. \(2009\)](#). The authors of that paper studied membership and multiplicity for 1253 solar-type dwarfs in 13 open clusters, Praesepe and Coma Berenices among them. To do so, they obtained 6070

radial velocities during 19 years of observations at the Haute-Provence Observatory and 1130 during 13 years at ESO La Silla (Chile). We found that three stars in our sample of Coma Berenices members are flagged as spectroscopic binaries (SBs) in [Mermilliod et al. \(2009\)](#), two of them with $\text{RUWE} > 1.2$. In addition, 9 Praesepe members in our sample are flagged as SBs in that work, six of them with $\text{RUWE} > 1.2$.

Finally, after visual inspection of the color-magnitude diagrams (CMDs) of both clusters (see [Fig. 3.1](#)), we flagged as photometric binaries two Coma members and 12 Praesepe members. All of them exhibit G band magnitudes significantly lower those of single stars with similar *Gaia* ($BP - RP$) colors.

As a corollary, we have considered binaries 17 of the 37 stars that compose our sample of Coma Berenices members and 29 of the 55 stars that compose our sample of Praesepe members, that is, around half of the sample in both cases. The multiple systems found in the Coma Berenices sample are indicated in [Table 3.2](#). Accordingly, the multiple systems found in the Praesepe sample are indicated in [Table 3.3](#).

3.1.6 The final samples

We collected spectra for 22 Coma Berenices members during the observation campaigns described in [Table 3.1](#). In addition, we recovered spectra for five stars from the ELODIE archive, for four stars from the ESPaDOns archive, and for one star from the SOPHIE archive. Finally, we could obtain Li abundances and EWs for five more Coma Berenices members from [Jeffries \(1999\)](#) and [Ford et al. \(2001\)](#). To sum up, our spectroscopic sample of Coma Berenices is composed of 37 dwarfs that [Kraus & Hillenbrand \(2007\)](#), [Collier Cameron et al. \(2009\)](#), [Fürnkranz et al. \(2019\)](#), [Tang et al. \(2019\)](#) and/or [Pang et al. \(2021\)](#) considered members of the cluster. Reassuringly, all these sources exhibit *Gaia* DR3 parallaxes, proper motions, and positions coherent with cluster membership (M.A. Agüeros, private communication). Our sample of Coma Berenices members is presented in [Table 3.2](#), and the positions of these sources in a CMD built with *Gaia* DR3 photometry is shown on the top panel of [Fig. 3.1](#).

Table 3.2: Designations, coordinates, binary status, and source of the spectroscopic information for the Coma Berenices sample presented in this work. Our Coma Berenices sample is composed of 37 G and K dwarfs. This table is only partially presented. Its complete version is available in Appendix B.

ID	$\alpha(2000)$ hh:mm:ss	$\delta(2000)$ dd:mm:ss	EW(Li) source ^(a)	Wide Binary ^(b)	Spectroscopic Binary ^(b)	Photometric Binary ^(b)
2MASS J12083610+3106098	12:08:36.10	+31:06:09.76	SOPHIE	0	0	
AV 189	12:07:57.72	+25:35:11.39	CAFE	1	0	0
BD+20 2671	12:02:26.62	+20:07:22.75	FIES	0	0	0
BD+21 2335	11:36:51.71	+20:32:33.8	CAFE	0	0	0
BD+23 2472	12:33:20.01	+22:24:23.49	CAFE	1	0	0
BD+24 2462	12:27:20.69	+23:19:47.46	ESPADONS	0	0	0
...

Notes. ^(a)Some EWs were obtained during the observation campaigns shown in Table 3.1, some others from archival spectra, and the remaining ones were obtained from the literature. F01 is Ford et al. (2001) and J99 is Jeffries (1999). ^(b)1 = Yes, 0 = No.

Table 3.3: Designations, coordinates, binary status, and source of the spectroscopic information for the Praesepe sample presented in this work. Our Praesepe sample is composed of 55 G and K dwarfs. This table is only partially presented. Its complete version is available in Appendix C.

ID	$\alpha(2000)$ hh:mm:ss	$\delta(2000)$ dd:mm:ss	EW(Li) source ^(a)	Wide Binary ^(b)	Spectroscopic Binary ^(b)	Photometric Binary ^(b)
KW 325	08:40:41.90	+19:13:25.44	CAFE	1	1	0
KW 495	08:43:05.94	+19:26:15.29	CAFE	0	1	1
KW 466	08:42:32.26	+19:23:46.26	C17	0	1	0
KW 335	08:40:48.32	+19:55:18.91	C17	0	0	0
KW 182	08:39:30.42	+20:04:08.58	C17	0	1	1
...

Notes. ^(a)Some EWs were obtained from the spectra collected with the FIES spectrograph and the CAFE spectrograph, whereas others were obtained from the literature. C17 is Cummings et al. (2017). ^(b)1 = Yes, 0 = No.

On the other hand, we observed 19 Praesepe members selected from the catalogs provided by Cantat-Gaudin et al. (2018) and Rampalli et al. (2021) with the FIES spectrograph and the CAFE spectrograph. Beside this, we incorporated in our sample 36 dwarfs studied by Cummings et al. (2017) that have counterpart in, at least, one of those catalogs. As a result, our spectroscopic sample of Praesepe is composed of 55 stars. This sample is presented in Table 3.3, and the positions of these sources in a CMD built with *Gaia* DR3 photometry is shown on the bottom panel of Fig. 3.1.

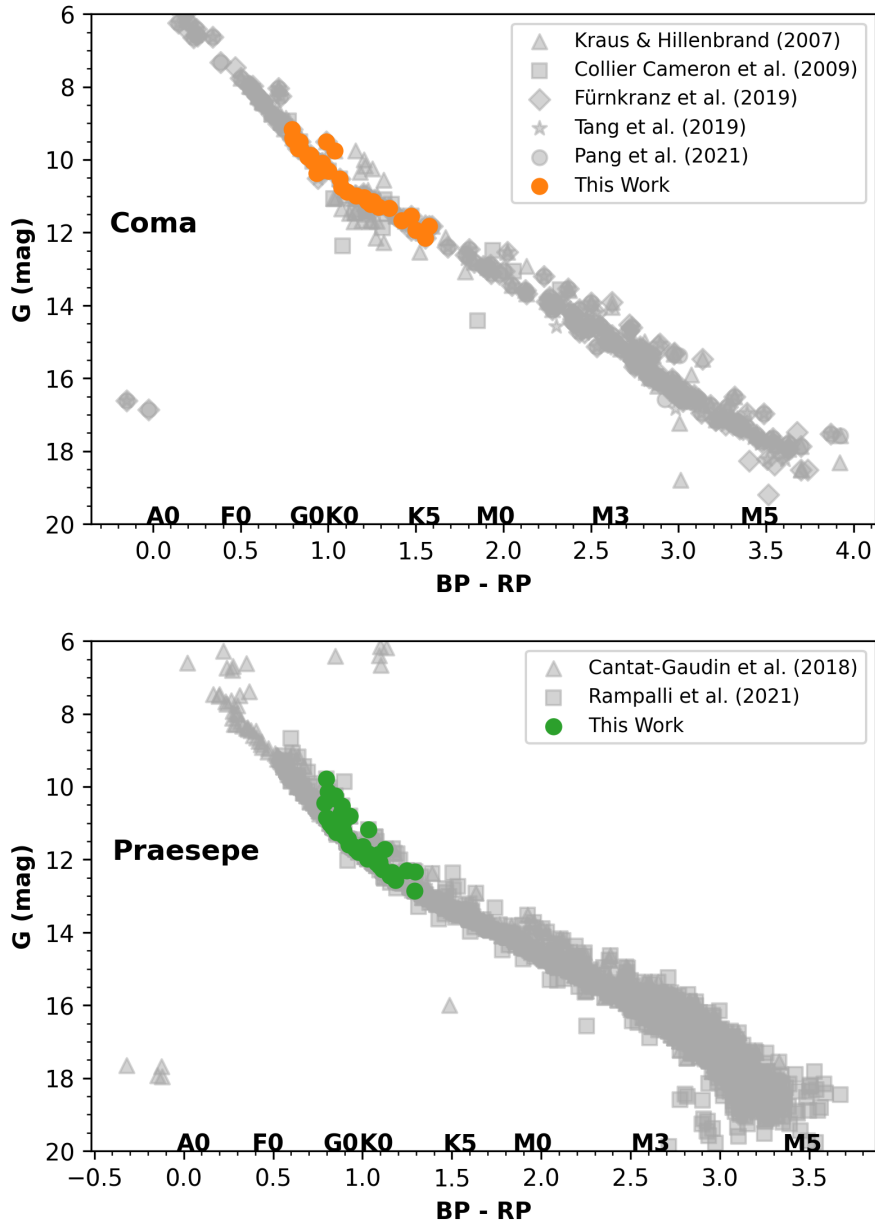


Figure 3.1: Gaia DR3 CMD for Coma and Praesepe. **Top**— The grey symbols represent the stars flagged as Coma members in the catalogs we have used to build our sample. Triangles indicate the cluster members listed in [Kraus & Hillenbrand \(2007\)](#), squares are members listed in [Collier Cameron et al. \(2009\)](#), diamonds are members listed in [Fürnkranz et al. \(2019\)](#), stars are members listed in [Tang et al. \(2019\)](#), and grey circles are members listed in [Pang et al. \(2021\)](#). The Coma members analysed in this work are represented by orange circles. **Bottom**—The grey symbols represent the stars flagged as Praesepe members in the catalogs we have used to build our sample. Triangles indicate the cluster members listed in [Cantat-Gaudin et al. \(2018\)](#) whereas squares are members listed in [Rampalli et al. \(2021\)](#). The Praesepe members studied in this work are represented by green circles. Neither CMD has been corrected for reddening.

3.2 Obtaining rotation periods

3.2.1 Coma Berenices

The Transiting Exoplanet Survey Satellite (TESS; [Ricker et al., 2015](#)) observed Coma Berenices in sectors S22, S23, S49, and S50, obtaining two-minute cadence photometry for stars included in the TESS Input Catalogue (TIC; [Stassun et al., 2018, 2019](#)). Since all the members in our sample are included in that catalog, we could obtain light curves (LCs) with a two-minute cadence for most of them. We inspected the LCs for each available sector independently, as well as all of them taken as a whole. In addition, we took into account both the Simple Aperture Photometry (SAP) flux and the Pre-search Data Conditioning SAP (PDCSAP) flux. We computed Lomb–Scargle periodograms and produced phase-folded LCs for each case. Finally, we recorded the most significant period for each source. Light curves, periodograms, and phase-folded LCs are available in [Appendix D](#).

Appart from the dedicated LCs, TESS also obtained photometry for all the objects in each field of view every 30 minutes during the primary mission and every 10 minutes in the extended one. As a result, it is possible to produce photometric LCs from these Full-Frame Images (FFIs) and compute Lomb-Scargle periodograms for them. [Table 3.4](#) shows the periods obtained from the dedicated LCs as well as the periods derived from the FFIs ([J.L. Curtis, private communication](#)). We obtained rotation periods from TESS FFIs for two sources lacking dedicated LCs and for one source for which we could not derive a reliable period from the dedicated photometry.

Finally, we also took into account the rotation periods available in the literature for our sample of Coma Berenices members. [Collier Cameron et al. \(2009\)](#) provided rotation periods for 30 F, G, and K members observed with the SuperWASP camera array in 2004 and/or 2007. In addition, [Terrien et al. \(2014\)](#) used Kilodegree Extremely Little Telescope photometry to measure rotation periods for eight F, G, and K cluster members. We found counterpart for 14 and three Coma Berenices members in [Collier Cameron et al. \(2009\)](#) and [Terrien et al. \(2014\)](#), respectively. The periods provided by those works are also included in [Table 3.4](#), but we have chosen the rotation periods obtained from TESS photometry for all the sources instead of the ones found in the

Table 3.4: Rotation periods obtained for 36 of the 37 Coma Berenices members that compose our sample. This table is only partially presented. Its complete version is available in Appendix B.

ID	TIC ID	Prot (d) TESS two-minute LCs	Prot (d) TESS FFIs	Prot (d) C09 ^(a)	Prot (d) T14	Final Prot (d)
StKM 1-980	138895417	6.84	–	–	–	6.84
TYC 1989-49-1	356702360	10.80	10.81	10.88	1.10	10.80
BD+20 2671	229655624	4.60	8.23	–	–	4.60
UCAC4 554-047403	3890292	12.90	12.41	–	–	12.90
BD+27 2130	393798833	–	9.07	–	8.81	9.07
...

Notes. C09 is [Collier Cameron et al. \(2009\)](#) and T14 is [Terrien et al. \(2014\)](#). ^(a) Periods suspected of being half the true period appear in parentheses in [Collier Cameron et al. \(2009\)](#).

literature.

We obtained rotation periods from TESS dedicated light curves and from TESS FFIs for 32 of 37 Coma Berenices members. The median of the differences between the rotations periods obtained from these two data sets is below 4%, but four sources exhibit differences over 50%, probably due to period aliases. We chose the periods obtained from dedicated light curves over the ones obtained from TESS FFIs for all these sources. In addition, we obtained a reliable period for StKM 1-980 from dedicated photometry but not from TESS FFIs. Despite our efforts, we could not obtain a reliable period for BD+27 2121 from TESS photometry and no counterpart was found in the literature for that star.

3.2.2 Praesepe

Our primary source of rotation periods for Praesepe members is the survey of [Rampalli et al. \(2021\)](#). The authors of that work obtained rotations periods from K2 light curves for 220 stars without previous determinations of rotation period and for 793 stars with rotation periods in previous photometric surveys. In addition, they enriched their sample with 17 sources whose rotation periods were obtained from ground-based facilities by previous studies.

Besides this, we cross-matched our Praesepe sample with the list of rotational variables provided by [Kovács et al. \(2014\)](#), who took advantage of photometric time series observations from

Table 3.5: Rotation periods obtained for the 55 Praesepe members that compose our sample. This table is only partially presented. Its complete version is available in Appendix C.

ID	Prot (d) R21	Prot (d) K14 ^(a)	Final Prot (d)
KW 3655	2.96	5.85	2.96
KW 495	4.73	–	4.73
TYC 1396-1240-1	–	9.20	9.20
KW 365	9.20	–	9.20
KW 367	3.21	6.04	3.21
...

Notes. R21 is Rampalli et al. (2021) and K14 is Kovács et al. (2014). ^(a) These periods have been calculated from the frequencies provided by Kovács et al. (2014) for the corresponding objects.

the Hungarian-made Automated Telescope Network to derive rotation periods for 180 F to K stars. We found in that work a counterpart for 12 of the 55 Praesepe members that compose our sample.

We chose the rotation periods obtained from Rampalli et al. (2021) for the 54 sources that have counterpart in Rampalli et al. (2021) and we turned to the period provided by Kovács et al. (2014) only in the case of TYC 1396-1240-1. Table 3.5 shows the rotation periods obtained for our Praesepe sample.

3.3 Analysis

3.3.1 Deriving effective temperatures and luminosities

We used VOSA (version 7.5; Bayo et al., 2008, 2017) to obtain effective temperatures and luminosities for the members of both clusters. To do so, we uploaded the *Gaia* DR3 photometry obtained for these sources and we cross-matched both samples with a number of photometric catalogs. We assumed negligible reddening for Coma Berenices (Taylor, 2006) and a visual extinction in the direction of Praesepe of $A_v = 0.034$, which is an intermediate value between $A_v = 0.032 \pm 0.017$ (Dias et al., 2021) and $A_v = 0.035 \pm 0.011$ (Douglas et al., 2019).

We compared the dereddened Spectral Energy Distributions (SEDs) obtained in this manner for both samples with Kurucz model atmospheres (Castelli et al., 1997; Castelli & Kurucz, 2003), assuming $\log g = 4.5$ and solar metallicity, to determine the effective temperature that best fit

each SED using a χ -squared minimisation method. To derive luminosities from the SEDs, we uploaded the distance of each source calculated from its *Gaia* DR3 parallax. For the two Praesepe members that have unreliable parallaxes in *Gaia* DR3 (namely KW 365 and KW 547), we assumed a distance of 184.72 ± 0.19 pc (Alfonso & García-Varela, 2023). Fig. 3.2 shows the Hertzsprung–Russell diagrams (HRDs) built with the astrophysical parameters obtained for Coma members (top panel) and Praesepe members (bottom panel). The effective temperatures and bolometric luminosities derived for Coma members are listed in Table 3.6, whereas Table 3.7 provides the same information for our Praesepe sample.

3.3.2 Measuring Li equivalent widths

We used iSpec (Blanco-Cuaresma et al., 2014; Blanco-Cuaresma, 2019) to obtain one single RV-corrected and continuum-normalized spectrum for each source from the spectra collected during the observational campaigns previously described and the archival spectra collected for part of the Coma members. First, we removed the continuum by fitting a spline function to each spectrum. For homogeneity, we degraded the resolution of all of them to $R = 40\,000$ and we cut the wavelength interval between 500 and 700 nm. After transforming all the spectra to the solar barycentric reference frame, we determined the radial velocity (RV) corresponding to each of them by cross-correlating the spectrum with a solar mask covering the wavelength range 372–926 nm. Finally, we corrected all the spectra from RV shift and we combined the spectra corresponding to the same source. The SNR estimated for the combined spectrum was used to add flux errors to its points.

We also used iSpec to develop the pipeline to derive the EW of the Li doublet at 670.78 nm for each star from the aforementioned spectra. For those cases where the Li doublet at 670.78 nm and the Fe I line at 670.75 nm were blended (see Fig. 3.3, where a small region around the Li doublet is shown for two Coma members), we used synthetic spectra without Li to remove the contribution from the latter as explained in Section 2.4.2. The Li EWs obtained for Coma Berenices members and Praesepe members are shown on Table 3.6 and Table 3.7, respectively.

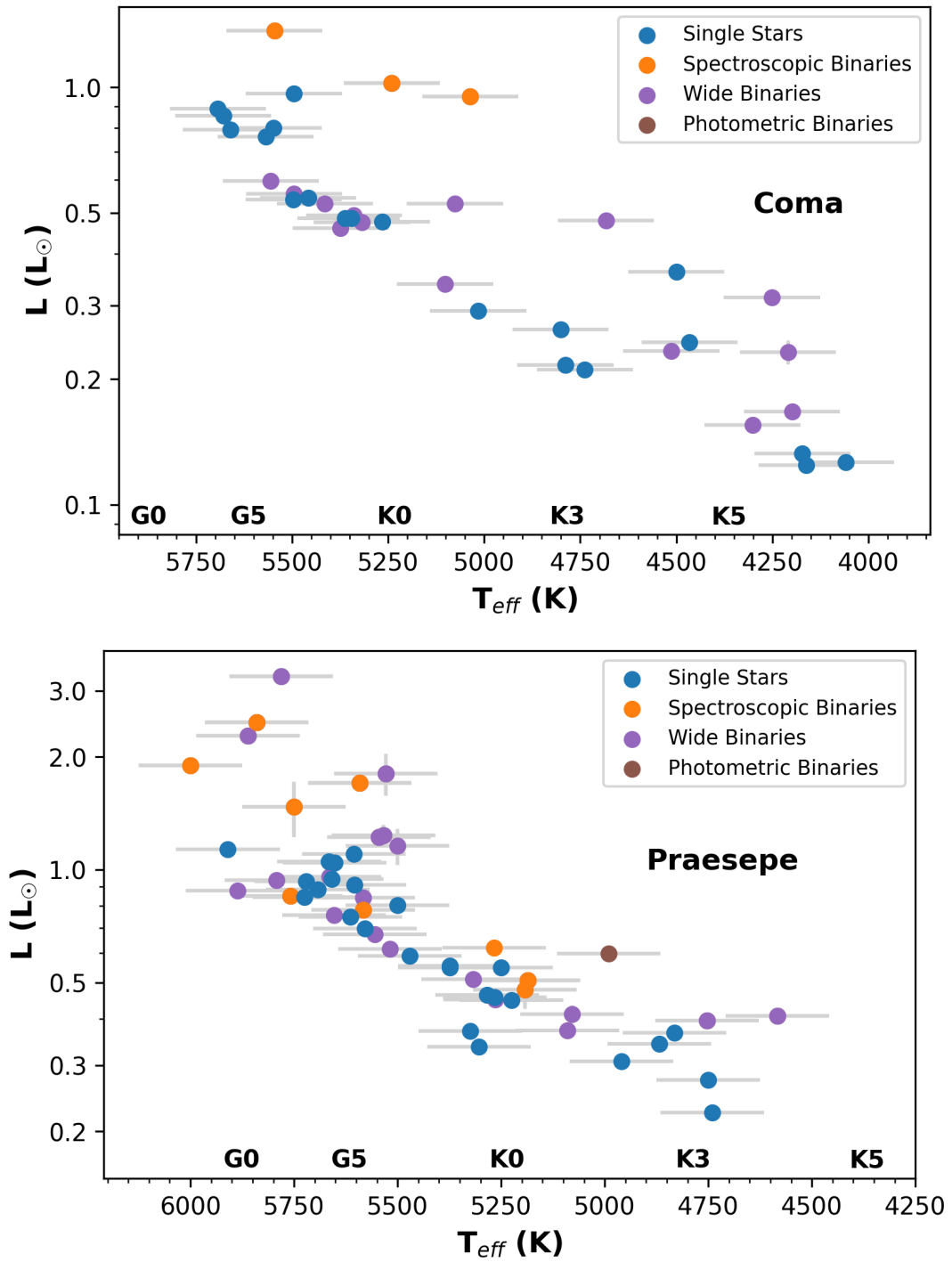


Figure 3.2: HRD for Coma and Praesepe. **Top**— Coma Berenices members. Blue circles are single stars, orange circles are spectroscopic binaries, purple circles are wide binaries, and brown circles are photometric binaries. **Bottom**— Praesepe members. Green circles are single stars, red circles are spectroscopic binaries, grey circles are wide binaries, and light blue circles are photometric binaries.

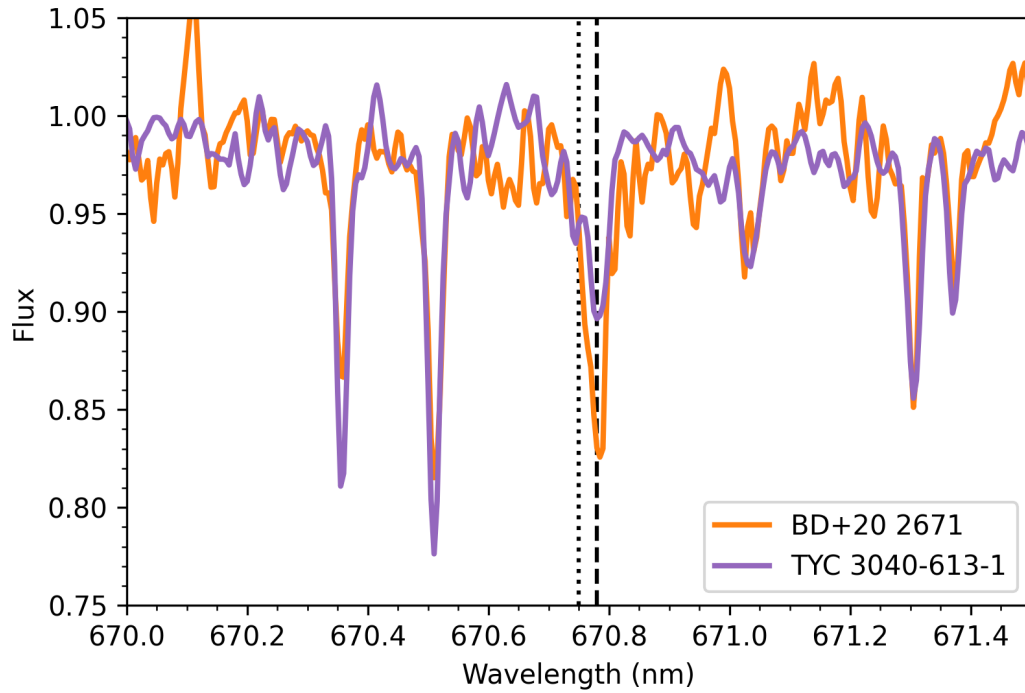


Figure 3.3: Spectral region around 670.78 nm for two Coma Berenices members, namely *BD+20 2671* and *TYC 3040-613-1*. The dashed black line shows the position of the Li doublet at 670.78 nm, while the dotted black line indicates the position of the Fe I line at 670.75 nm. Both features are blended in the spectrum of *BD+20 2671*, but they are resolved in the case of *TYC 3040-613-1*. Both spectra have similar SNR. A single spectrum was obtained for *BD+20 2671* with the FIES spectrograph, while three spectra were collected for *TYC 3040-613-1* using the CAFE spectrograph.

3.4 Results

3.4.1 Lithium distributions in Coma Berenices and Praesepe

Figure 3.4 is a color-period diagram (CPD) in which we indicate the Li EWs of the Coma Berenices members; the top panel includes all of the cluster members, whereas in the bottom panel we have removed binary systems. Table 3.6 lists the stellar parameters, rotation periods, and Li EWs for these stars.

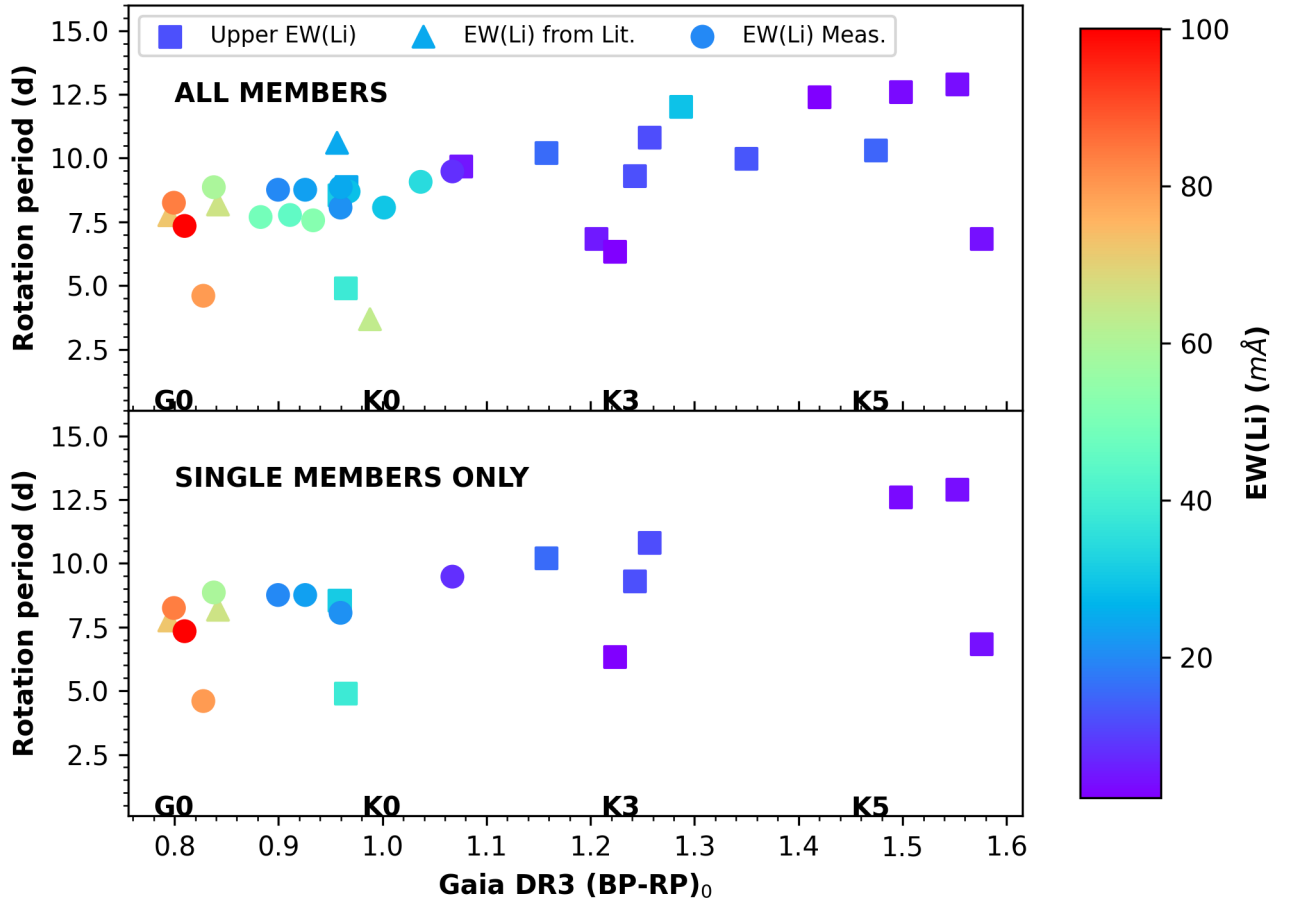


Figure 3.4: Distribution of rotation periods for our Coma Berenices sample as a function of color. The color of each symbol indicates the $EW(\text{Li})$ measured for the corresponding star. Circles represent Coma members whose EWs have been derived by us, while triangles represent stars whose EWs have been taken from *Ford et al. (2001)* or *Jeffries (1999)*. Squares denote those stars for which we could only derive upper limits for the Li EWs. **Top**—Our complete set of Coma members with rotation periods. **Bottom**—Only those sources classified as single stars are shown.

Table 3.6: *Li* EW, effective temperature, luminosity, and rotation period for the 37 Coma members that compose our sample. This table is only partially presented. Its complete version is available in Appendix B.

ID	T_{eff} (K)	σ_{Teff} (K)	L (L_{\odot})	σ_L (L_{\odot})	EW(Li) (mÅ)	$\sigma_{EW(Li)}$ (mÅ)	EW(Li) source ^(a)	Prot (d)
2MASS J12083610+3106098	4250	125	0.133	0.001	$\leq 3.4^{(b)}$	–	SOPHIE	12.6
TYC 1989-49-1	4750	125	0.211	0.001	$\leq 12.1^{(b)}$	–	CAFE	10.8
BD+20 2671	5750	125	0.793	0.003	79.5	35.3	FIES	4.6
BD+21 2335	5500	125	0.544	0.002	23.4	17.8	CAFE	8.76
BD+23 2472	5000	125	0.527	0.003	28.7	14.4	CAFE	8.69
...

Notes. ^(a) F01 is Ford et al. (2001) and J99 is Jeffries (1999). ^(b) Upper limit.

Unlike what has been observed in younger open clusters (see Bouvier, 2020, and references therein), Coma fast rotators are not richer in Li than slower rotators of similar effective temperatures. Only the K0 binary system with a rotation period below four days has clearly higher EW(Li) than slower rotators of similar color. This star has the ID BD+25 2511 and it is flagged as a double-lined binary in Mermilliod et al. (2009). The authors of that work measured an orbital period of 3.6 d for this star, the same value we derived. We found a possible explanation for the higher EW(Li) of this source in Barrado y Navascues & Stauffer (1996), who demonstrated that tidally locked binaries in the Hyades open cluster are richer in Li in comparison to single stars. On the other hand, the K3 binary system with a period around 7 d has the ID AV 189 and it is flagged as a wide binary. Consequently, it is not surprising that its EW(Li) is very similar to those of single stars of similar colors.

Only four single stars have rotation periods below seven days. The IDs of these sources are, from higher effective temperature to lower: BD+20 2671, TYC 1457-1029-1, UCAC4 561-053267, and StKM 1-980. The Li EWs of these fast rotators are very similar to the ones measured for slower rotators of similar colors, unlike what we observed for open clusters between 100 and 250 Myr. We found a possible explanation for this in the rotation periods derived from TESS light curves. The rotation periods obtained for the three hotter stars from TESS FFIs are between eight and ten days, that is, very similar values to the ones obtained for the rest of single stars in that range of effective temperatures. If the rotation periods derived from TESS dedicated light curves

Table 3.7: *Li* EW, effective temperature, luminosity, and rotation period for the 55 Praesepe members that compose our sample. This table is only partially presented. Its complete version is available in Appendix C.

ID	T_{eff} (K)	σ_{Teff} (K)	L (L_{\odot})	σ_L (L_{\odot})	EW(Li) (mÅ)	$\sigma_{EW(Li)}$ (mÅ)	EW(Li) source ^(a)	Prot (d)
TYC 1387-945-1	5750	125	1.044	0.011	46.7	19.3	CAFE	7.99
BD+18 2049	5750	125	0.944	0.006	53.4	40.9	CAFE	8.81
KW 365	5750	125	2.47	0.014	38.0	26.3	CAFE	9.2
KW 367	5500	125	1.705	0.029	$\leq 25.0^{(b)}$	–	FIES	3.21
KW 495	5750	125	3.284	0.074	43.1	27.6	CAFE	4.73
...

Notes. ^(a) C17 is Cummings et al. (2017). ^(b) Upper limit.

(the ones we assumed for this sample) were aliases of the true periods recovered from TESS FFIs, these stars would not be fast rotators but cluster members that have already transitioned to the I sequence (see Barnes, 2003). As previously mentioned, StKM 1-980 lacks a reliable period obtained from TESS FFIs, so we can not confirm nor deny that this star rotates slower than initially thought. In addition, we have not found rotation periods in the literature for any of these four sources.

Figure 3.5 is a CPD in which we indicate the Li EWs of Praesepe members; the top panel includes all cluster members, whereas in the bottom panel we have removed binary systems. Table 3.7 lists the stellar parameters, rotation periods, and Li EWs for these stars.

As noted above for Coma members, the Praesepe fast rotators are not richer in Li than slower stars of similar effective temperatures. Only the K0 binary system with a rotation period shorter than 2.5 days exhibits higher EW(Li) than slower rotators of similar colors. This star has the ID KW 1184 and it is flagged as a SB in Mermilliod et al. (2009). The authors of that work measured an orbital period of 1.2 d for this star, the same value obtained by Rampalli et al. (2021). Our conclusion is that the Coma member BD+25 2511 and the Praesepe member KW 1184 are tidally locked binaries that have retained more Li than single members of similar effective temperatures, like their twins in the Hyades open cluster. However, there are three SBs of G spectral type included in the top panel of the Fig. 3.5 that have rotation periods below 4.5 d but do not exhibit higher Li EWs than slower rotators of similar colors. These three stars are, from left to right, KW

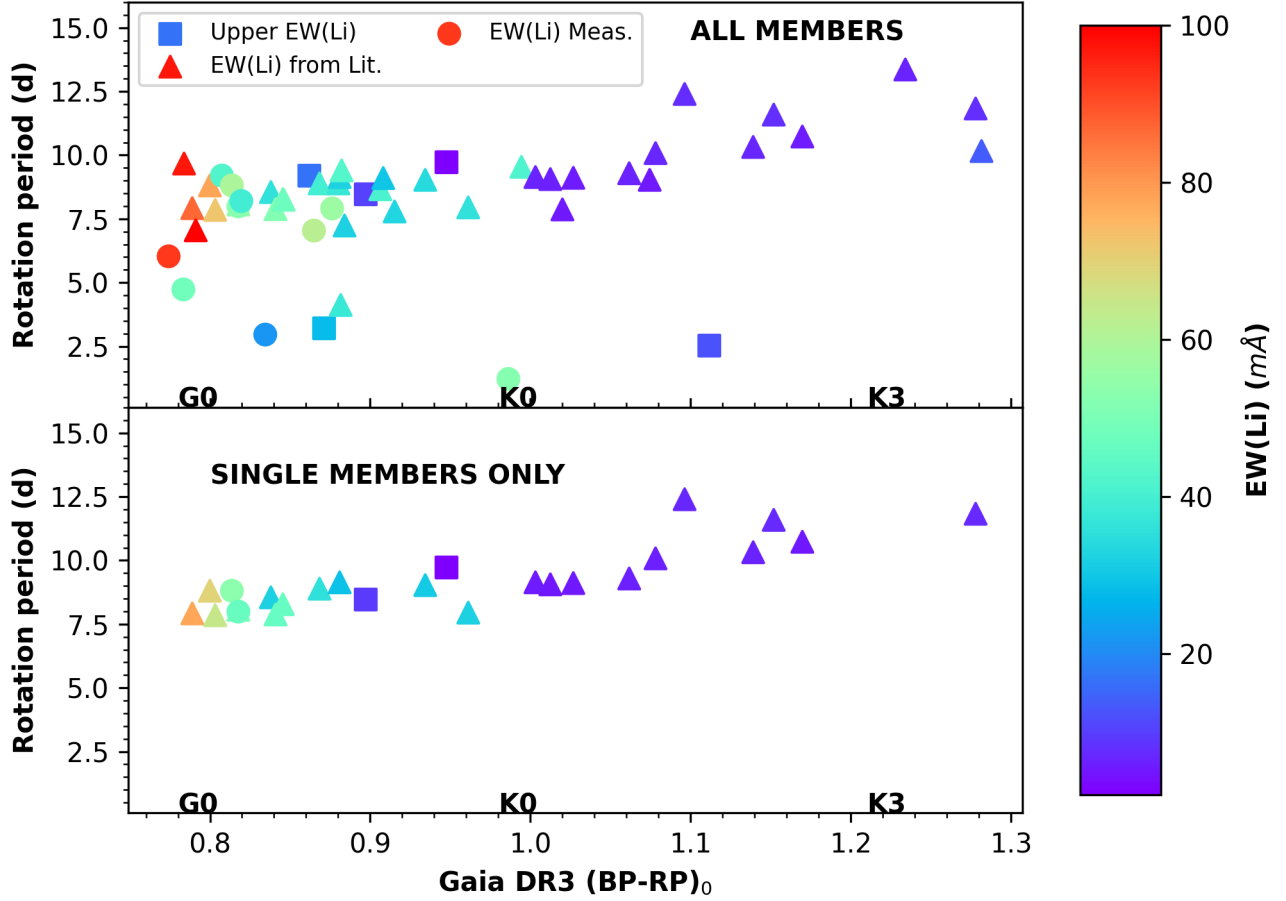


Figure 3.5: Distribution of rotation periods for our Praesepe sample as a function of color. The color of each symbol indicates the $EW(\text{Li})$ measured for the corresponding star. Circles represent Praesepe members whose EWs have been derived by us while triangles represent stars whose EWs have been taken from [Cummings et al. \(2017\)](#). Squares denote those stars for which we could only derive upper limits for the Li EWs . Gaia colors have been dereddened using $E(BP - RP) = 0.415 A_V$, following [Curtis et al. \(2020\)](#). **Top**—Our complete set of Praesepe members with rotation periods. **Bottom**—Only those sources classified as single stars are shown.

Table 3.8: *Metallicity determinations for Coma Berenices in previous spectroscopic studies.*

Authors	[Fe/H] (dex)	Spectral Types
Souto et al. (2021)	+0.04±0.02	G, K, and M
Heiter et al. (2014)	+0.00±0.08	F, G, and K
Gebran et al. (2008)	+0.07±0.09	F
Friel & Boesgaard (1992)	-0.052±0.026	F

3655, KW 367, and KW 434. [Mermilliod et al. \(2009\)](#) does not provide orbital period for KW 367 but the other two have orbital periods equal to their rotation periods, that is, they are also tidally locked binaries. On the other hand, as indicated in Table 3 of [Rampalli et al. \(2021\)](#), previous studies derived rotation periods of 5.85 d, 6.04 d, and 8.27 d for KW 3655, KW 367, and KW 434, respectively. If the latter periods were right, these stars would exhibit rotation rates and Li EWs similar to those of other Praesepe members of similar spectral types. The other binary of K spectral type shown in the top panel of Fig. 3.5 is the photometric binary KW 547.

All single stars in our Praesepe sample have rotation periods between 7.5 days and 12.5 days, that is, they have transitioned to the I sequence (see [Barnes, 2003](#)). Since Praesepe and Coma Berenices are coeval, this reinforces our hypothesis that the fast rotators included in the bottom panel of Fig. 3.4 have longer rotation periods than initially thought.

3.4.2 Comparison between them and with other clusters

Figure 3.6 shows a comparison between our Coma Berenices sample and the Pleiades. The latter is an extensively studied open cluster that has solar metallicity and an age of $127.4^{+6.3}_{-10}$ Myr ([Galindo-Guil et al., 2022](#)). On the other hand, previous studies indicate that the age of Coma is between 520 and 800 Myr ([Collier Cameron et al., 2009](#); [Fürnkranz et al., 2019](#); [Tang et al., 2019](#)). The average metallicity we have calculated for this cluster from the studies shown in Table 3.8 is $[Fe/H] = 0.01$, that is, solar metallicity. The gradual depletion of Li with time is evident in Fig. 3.6, which shows that the Pleiades members are richer in Li than Coma members of similar color.

As mentioned in Chapter 1, [Cummings et al. \(2017\)](#) derived very similar ages for Praesepe and the Hyades (670 ± 25 Myr and 635 ± 25 Myr, respectively), as well as similar metallicities

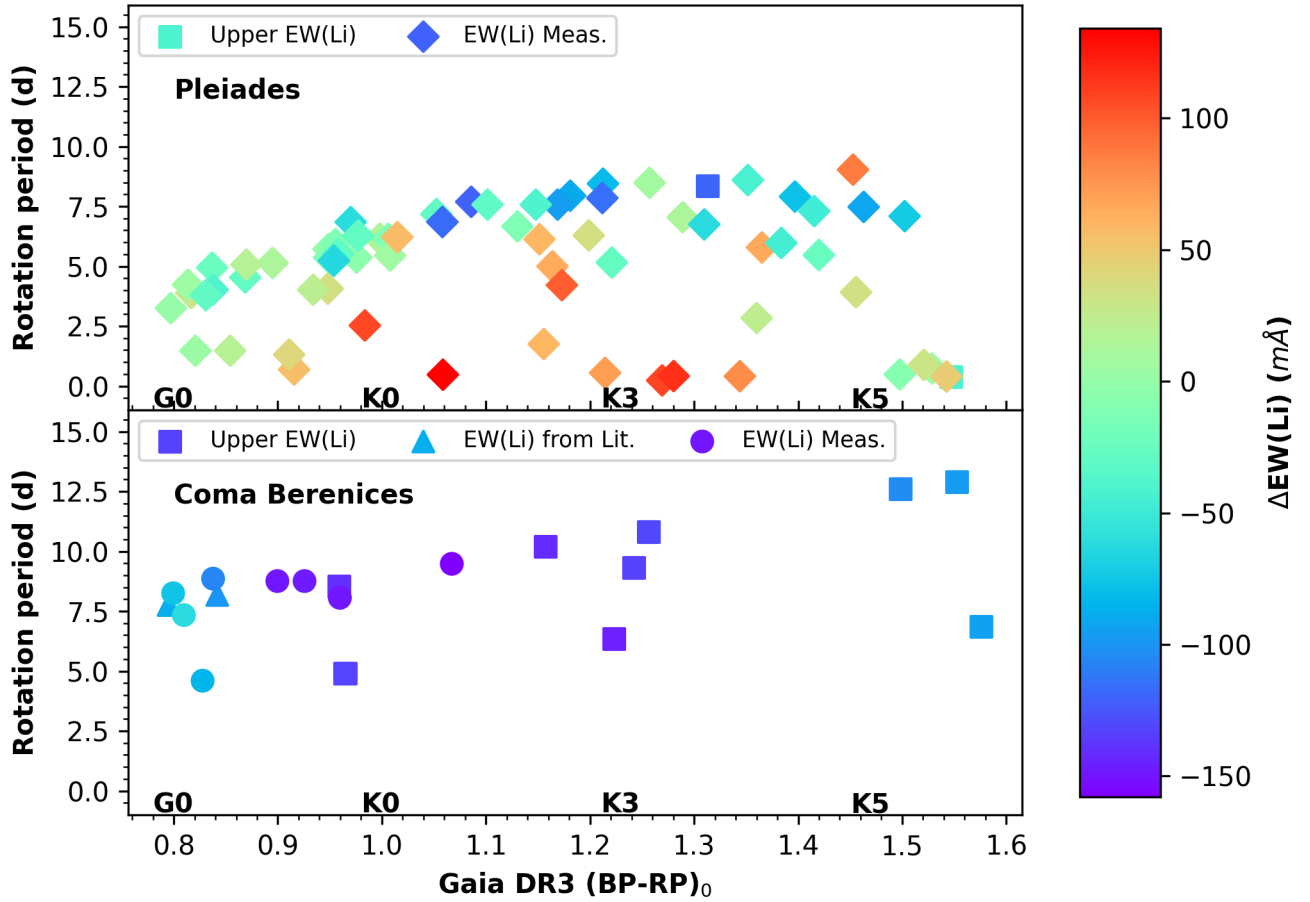


Figure 3.6: Rotation period vs. Gaia color for single members of Coma Berenices and the Pleiades. The color of each symbol indicates the deviation from a third-order polynomial fit to $EW(\text{Li})$ vs. $(BP-RP)_0$ for the Pleiades sample shown in the upper panel. **Top**—Pleiades single stars taken from [Barrado et al. \(2016\)](#) and [Bouvier et al. \(2018\)](#). Note that we have chosen the Li EWs and rotation periods published in [Bouvier et al. \(2018\)](#) for all the sources that have counterpart in both studies. We have only plotted those Pleiades members whose Gaia colors are within the range covered by the Coma sample shown in the bottom panel. Gaia colors were dereddened following [Curtis et al. \(2020\)](#) with $A_v = 0.12$. **Bottom**—Coma Berenices single stars. Circles, triangles, and squares have the same meaning as in [Fig. 3.4](#).

($[\text{Fe}/\text{H}] = 0.156 \pm 0.004$ and $[\text{Fe}/\text{H}] = 0.146 \pm 0.004$, respectively). In fact, previous estimations of the ages of these OCs place them inside the range previously provided for the age of Coma (see [Douglas et al., 2019](#)). Consequently, our sample of Coma Berenices allows us to compare the Li distribution of this cluster with those of Hyades and Praesepe, that is, two clusters of similar ages but 0.15 dex higher metallicity.

Figure 3.7 shows the Li EWs corresponding to our samples of Coma and Praesepe. To compare these distributions with that of the Hyades, we also included the Li EWs provided by [Cummings et al. \(2017\)](#) for members of that cluster. As we have shown that tidally locked binaries may exhibit abnormal Li EWs, we have not included SBs in Fig. 3.7. In addition, only the prime sample of Hyades members without spectroscopic evidence of contamination from a companion has been included. The Li EWs measured for K members of Coma and Praesepe are similar in the range where both samples overlap, that is, between $(BP-RP)_0 = 1.0$ and $(BP-RP)_0 = 1.3$. On the other hand, a subtle trend towards higher Li EWs for Coma members arises for $(BP-RP)_0 \leq 1.0$. As the three clusters are coeval, only the lower metallicity of Coma could explain this difference. Nevertheless, the Li EWs corresponding to Praesepe members and Hyades members are within the $\sigma_{EW(\text{Li})}$ estimated for Coma members.

To shed more light on this issue, we have performed Kolmogorov-Smirnov tests ([Hodges, 1958](#)) between our Coma sample and those corresponding to the other two clusters. The purpose of this test is to verify whether two samples (in this case, the Li EWs collected) were taken from the same continuous distribution. We only considered stars of G spectral type with concrete values of $EW(\text{Li})$, that is, not upper limits. We also excluded SBs for these tests. Figure 3.8 shows the empirical distribution functions obtained and the p-values derived in each case. From those p-values, we can not rule out the possibility that both samples come from the same continuous distribution. However, the relevance of the results obtained from these tests is limited due to the small sizes of the samples employed in the comparison: only 15 Coma members, 25 Praesepe members, and 23 Hyades members meet the aforementioned requirements.

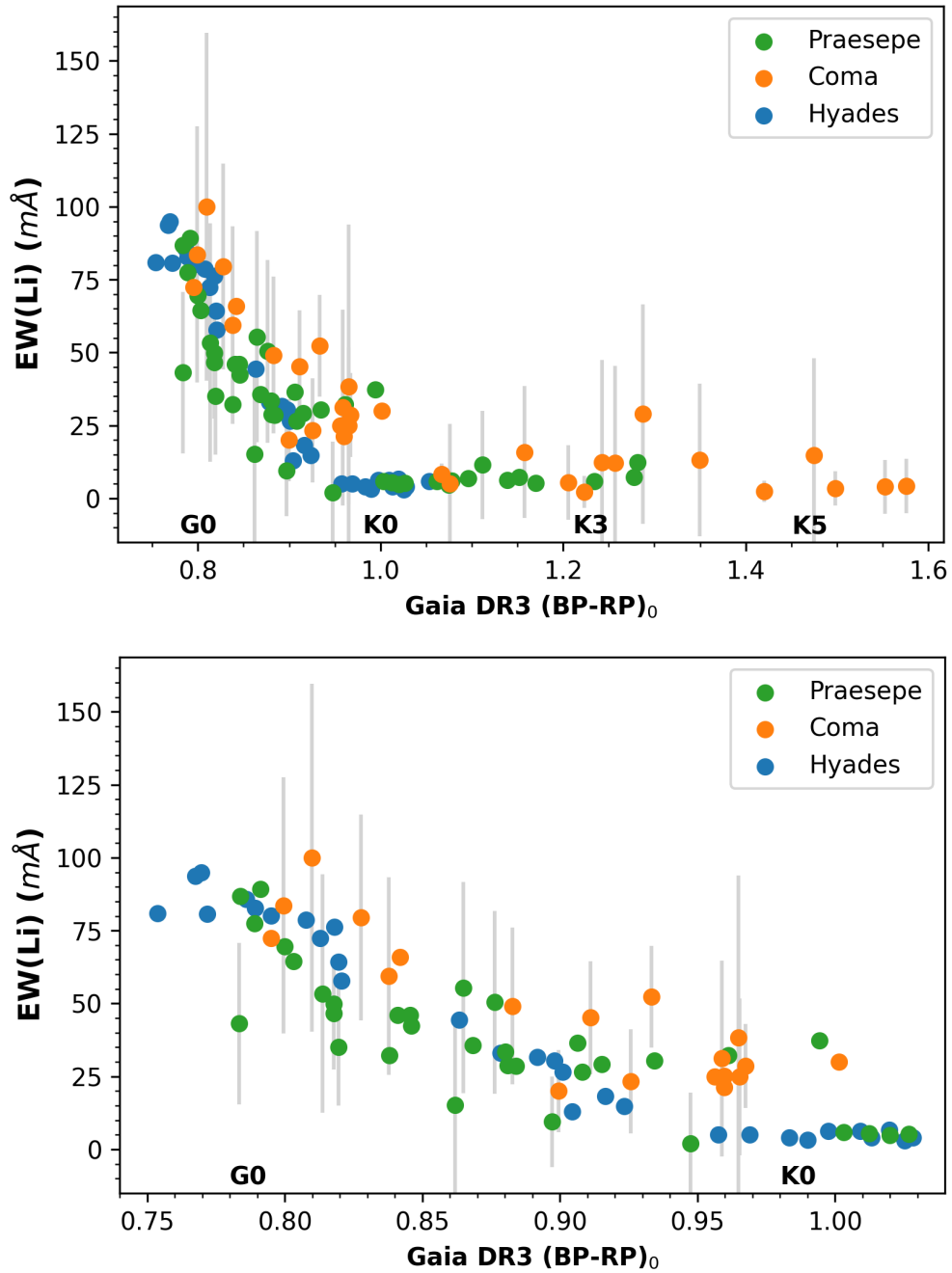


Figure 3.7: Distributions of Li EWs corresponding to Coma, Praesepe and Hyades. Coma members are indicated in orange, Praesepe members are indicated in green, and Hyades members are indicated in blue. Hyades Li EWs were taken from [Cummings et al. \(2017\)](#). SBs are not included in this figure. **Top**— G and K members of the three clusters. **Bottom**— Only G members are shown.

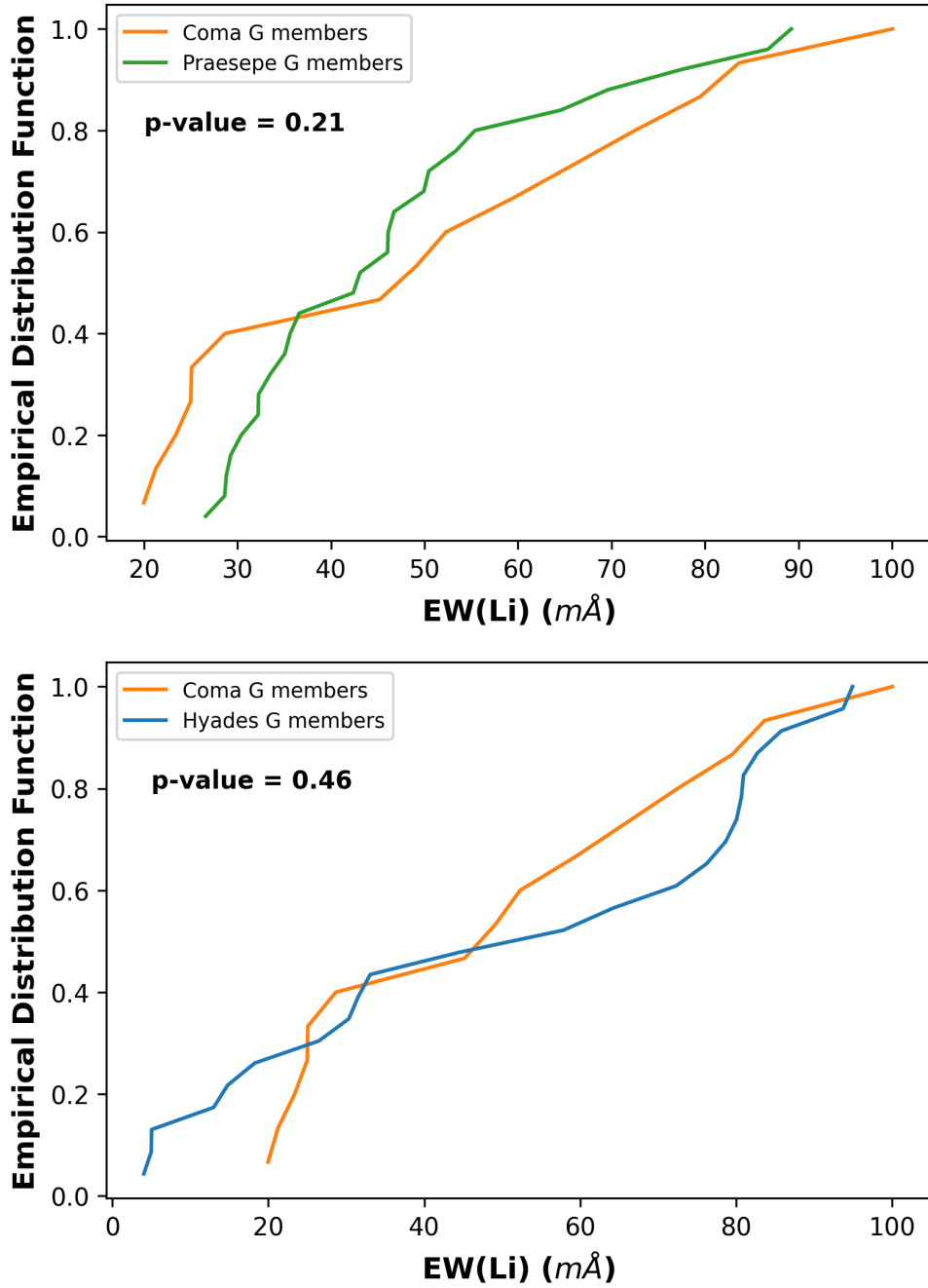


Figure 3.8: Empirical distribution functions obtained from the Kolmogorov-Smirnov tests performed between the Li EWs sample corresponding to Coma Berenices (orange) and those of other clusters. **Top**—Praesepe Li EWs sample (green). **Bottom**—Hyades Li EWs sample (blue) taken from Cummings et al. (2017). The p-values obtained are indicated in the panels. Only G stars with concrete Li EWs were used for these tests, that is, upper limits were excluded. We also excluded SBs for these tests.

Chapter 4

Summary and conclusions

This thesis aims at characterizing the effects of rotation and metallicity on the Li depletion of GK stars. To achieve this purpose, we collected spectra for several open clusters of different ages and metallicities, obtained their Li distributions, and compared them.

We collected a sample of 396 M35 members observed with the Hydra spectrograph of the 3.5-m telescope located at WYIN Observatory. We analysed the photometry, proper motions, and radial velocities of these sources, identifying 251 GK members of the cluster, 209 of which are single stars. In addition, we obtained rotation periods for 47 of these sources from ZTF light curves and we took advantage of previous photometric surveys, obtaining rotation periods for 197 M35 members in total.

We analyzed the spectra collected for 110 of our 251 M35 members, deriving iron abundances, Li EWs, and non-LTE Li abundances for them. From the iron abundances obtained for the most-probable single members with effective temperatures higher than 4500 K, we derived a metallicity $[\text{Fe}/\text{H}] = -0.26 \pm 0.09$ for M35. In other words, we discard that this cluster has solar metallicity. In addition, we found that the empirical law proposed in [Soderblom et al. \(1993b\)](#) for the Pleiades overestimates the equivalent width of the Fe I line at 670.75 nm by 5-15 mÅ for the range of effective temperatures analyzed. As a result, we conclude that the [Soderblom et al. \(1993b\)](#) empirical relation is not recommended for subsolar metallicity clusters.

We combined the Li EWs that we measured with data collected from previous studies, obtaining rotation periods and Li EWs for 257 single members of M35. This sample constitutes

the largest data set of this type built for this cluster. The Li-rotation connection found for this sample follows the trend observed in similar studies of M35 as well as with the trend found for other stellar associations: fast rotators are richer in Li than slower rotators of the same effective temperature.

Finally, we compared our sample with that for two open clusters with solar metallicity: the Pleiades, which is slightly younger than M35, and M34, which is slightly older. From the Kolmogorov-Smirnov tests performed, no significant statistical difference was observed between the Li EWs distribution for M35 and those for the other clusters. As a result, we conclude that a 0.2-0.3 dex difference in metallicity does not have an observable impact on the Li distributions of open clusters with ages between 100 Myr and 250 Myr.

During the course of this thesis, we observed GK members of Praesepe and Coma Berenices selected from previous catalogs of these clusters. The observations were carried out in eight campaigns between February 2022 and February 2024. As a result, we collected spectra for 22 Coma members and 19 Praesepe members with $R \geq 40\,000$. In addition, we took advantage of archival spectra obtained with spectrographs of similar resolutions. The Li EWs measured from the collected spectra were complemented with Li EWs from previous studies, obtaining a final sample of 37 Coma members and 55 Praesepe members. The former constitutes the largest sample of Li in Coma Berenices to date.

To obtain rotation periods for our sample of Coma members, we took advantage of the light curves collected by the TESS satellite. We computed periodograms from these light curves, obtaining convincing periods for 33 of 37 Coma members. In addition, rotation periods for three more Coma members were obtained from TESS FFIs. On the other hand, we cross-matched our Praesepe sample with previous photometric surveys, obtaining rotation periods for all the members of that cluster.

We studied the Li-rotation connection in these two clusters, without finding differences among the Li EWs of single stars of similar colors independently of their rotation periods. In the case of Coma, Li overabundance linked to fast rotation is only observed for one tidally locked binary of

K0 spectral type. Interestingly, we also found one Li-rich tidally-locked binary of K0 spectral type in the Praesepe sample. The Praesepe sample includes two fast-rotating tidally-locked binaries of G spectral types as well, but none of them exhibit abnormal Li EWs.

We compared the Li distributions of three coeval open clusters of roughly 600 Myr: Praesepe, Hyades and Coma Berenices. The first two have super-solar metallicities, and the metallicity of Coma is 0.15 dex lower. As expected, the Li distribution of our Praesepe sample mimics that of the Hyades in the range of effective temperatures studied. However, some evidence pointing to higher Li EWs for Coma members of G spectral type arises.

To sum up, there is a strong correlation between rotation and Li abundance for G and K dwarfs in open clusters with ages between 100 Myr and 250 Myr. Lithium depletion is hampered in fast rotators, which exhibit higher Li abundances than their slower counterparts as a result. However, the effect of metallicity is negligible in these associations, as clusters with different metallicities exhibit the same Li distributions. In other words, although the convective envelopes of more metallic stars are thicker, the higher rate of Li depletion of these stars does not have important effects on their Li surface abundances, at least in the ranges of age and metallicity studied in [Cuenda-Muñoz et al. \(2024\)](#). An alternative explanation is that metallicity does not condition the thickness of the convective envelope, but this contradicts the models proposed by [Dumont et al. \(2021\)](#).

On the other hand, single GK members of 600 Myr OCs do not exhibit the aforementioned Li-rotation connection. One possible explanation for this is that the Li-rotation link does not hold throughout the MS and, as a result, it is not observed in 600 Myr OCs. Taking into account previous studies and stellar models (see, for instance, [Dumont et al., 2021](#)), this scenario is unlikely. An alternative explanation is that the rotation periods derived for fast-rotating single members of Coma are aliases of the true periods, so they do not exhibit abnormal Li EWs because they are not fast rotators. This could also be the case for the fast-rotating SBs of G spectral type observed in Praesepe, as some previous studies derived longer rotation periods for them. In this scenario only tidally-locked binaries would maintain higher Li abundances and faster rotation velocities due to

the angular momentum transfer from the binary orbit to stellar rotation, which prevents the star from spinning down. The remaining members of these clusters would have transitioned to the I sequence at this age.

The effect of metallicity on Li depletion may be observable for G members of 600 Myr OCs, so lower metallicity clusters exhibit higher Li abundances, but the results obtained prevent us from stating stronger conclusions. If the overabundance of less metallic stars of G spectral type is confirmed in the future, this result will indicate that the gap in Li abundance between clusters of different metallicities gradually increases along the MS, as it is negligible at around 150 Myr but it can be observed in 600 Myr OCs.

In any case, the picture of the evolution of the Li-rotation connection along the MS is far from complete. More observations of OCs between 200 Myr and 600 Myr are required to confirm that the Li-rotation link holds throughout the MS. Besides this, further analysis of Li in OCs around 600 Myr is needed to confirm the aforementioned trend towards higher Li abundances in less metallic stars of G spectral type.

To finish this Chapter, I would like to quote a paragraph from [Soderblom et al. \(1993b\)](#), one of the works that opened this line of research more than 30 years ago:

The deeper reach of a new generation of telescopes and spectrographs will make it possible to pursue this kind of study in more distant open clusters. That means we can examine Li, rotation, and activity in somewhat older stars in order to more carefully delineate how these properties evolve during the early main-sequence lifetimes of solar-type stars and how they are interrelated. That also means we can sample other relevant properties such as metallicity to expand the regions of parameter space that are explored. And we will finally be able to test if the Pleiades is fully representative and typical of stars of its age and composition. Going to even younger clusters will show when and how the spread in N_{Li} develops—those are surely valuable clues to the mechanisms.

Nowadays, *Gaia* astrometry and photometry enable the identification of cluster members in the Milky Way with unprecedented accuracy. In addition, space missions such as *Kepler* or TESS and

ground-based facilities such as ZTF provide photometric light curves for thousands of stars. These two advantages are complemented with modern high-resolution spectrographs and dedicated software tools that simplify the chemical characterization of stars. As a result, studies similar to this one are finally disentangling the different factors that play a role on the lithium depletion, unveiling the evolution of this element in solar-type stars.

Bibliography

- Abdelaziz, A. E., Saad, S. M., Hendy, Y. H. M., Shokry, A., & Kamal, F. Y. 2022, *New A*, 92, 101727
- Aceituno, J., Sánchez, S. F., Grupp, F., et al. 2013, *A&A*, 552, A31
- Alfonso, J. & García-Varela, A. 2023, *A&A*, 677, A163
- Anthony-Twarog, B. J., Deliyannis, C. P., Harmer, D., et al. 2018, *AJ*, 156, 37
- Arancibia-Silva, J., Bouvier, J., Bayo, A., et al. 2020, *A&A*, 635, L13
- Balaguer-Núñez, L., López del Fresno, M., Solano, E., et al. 2020, *MNRAS*, 492, 5811
- Baranne, A., Queloz, D., Mayor, M., et al. 1996, *A&AS*, 119, 373
- Barnes, S. A. 2003, *ApJ*, 586, 464
- Barrado, D. 2016, in *EAS Publications Series*, Vol. 80-81, *EAS Publications Series*, ed. E. Moraux, Y. Lebreton, & C. Charbonnel, 115–175
- Barrado, D., Bouy, H., Bouvier, J., et al. 2016, *A&A*, 596, A113
- Barrado y Navascués, D. 1996, PhD thesis, Universidad Complutense de Madrid
- Barrado y Navascués, D., Deliyannis, C. P., & Stauffer, J. R. 2001a, *ApJ*, 549, 452
- Barrado y Navascués, D., Fernandez-Figueroa, M. J., Garcia Lopez, R. J., de Castro, E., & Cornide, M. 1997, *A&A*, 326, 780
- Barrado y Navascués, D., García López, R. J., Severino, G., & Gomez, M. T. 2001b, *A&A*, 371, 652
- Barrado y Navascués, D. & Stauffer, J. R. 1996, *A&A*, 310, 879
- Barrado y Navascués, D., Stauffer, J. R., Bouvier, J., & Martín, E. L. 2001c, *ApJ*, 546, 1006
- Baumann, P., Ramírez, I., Meléndez, J., Asplund, M., & Lind, K. 2010, *A&A*, 519, A87
- Bayo, A., Barrado, D., Allard, F., et al. 2017, *MNRAS*, 465, 760
- Bayo, A., Rodrigo, C., Barrado y Navascués, D., et al. 2008, *A&A*, 492, 277
- Beck, P. G., do Nascimento, J. D., J., Duarte, T., et al. 2017, *A&A*, 602, A63
- Bensby, T. & Lind, K. 2018, *A&A*, 615, A151
- Blanco-Cuaresma, S. 2019, *MNRAS*, 486, 2075

Blanco-Cuaresma, S., Soubiran, C., Heiter, U., & Jofré, P. 2014, *A&A*, 569, A111

Boesgaard, A. M. & Friel, E. D. 1990, *ApJ*, 351, 467

Boesgaard, A. M. & Tripicco, M. J. 1986, *ApJ*, 302, L49

Bouchy, F. & Sophie Team. 2006, in *Tenth Anniversary of 51 Peg-b: Status of and prospects for hot Jupiter studies*, ed. L. Arnold, F. Bouchy, & C. Moutou, 319–325

Bouvier, J. 2008, *A&A*, 489, L53

Bouvier, J. 2020, *Mem. Soc. Astron. It.*, 91, 39

Bouvier, J., Barrado, D., Moraux, E., et al. 2018, *A&A*, 613, A63

Bouvier, J., Lanzafame, A. C., Venuti, L., et al. 2016, *A&A*, 590, A78

Bouy, H., Bertin, E., Barrado, D., et al. 2015, *A&A*, 575, A120

Bovy, J. 2015, *ApJS*, 216, 29

Brewer, J. M. & Fischer, D. A. 2018, *ApJS*, 237, 38

Butler, R. P., Cohen, R. D., Duncan, D. K., & Marcy, G. W. 1987, *ApJ*, 319, L19

Cantat-Gaudin, T. & Anders, F. 2020, *A&A*, 633, A99

Cantat-Gaudin, T., Jordi, C., Vallenari, A., et al. 2018, *A&A*, 618, A93

Castelli, F., Gratton, R. G., & Kurucz, R. L. 1997, *A&A*, 318, 841

Castelli, F. & Kurucz, R. L. 2003, in *Modelling of Stellar Atmospheres*, ed. N. Piskunov, W. W. Weiss, & D. F. Gray, Vol. 210, A20

Castro, M., Vauclair, S., Richard, O., & Santos, N. C. 2009, *A&A*, 494, 663

Cautun, M., Benítez-Llambay, A., Deason, A. J., et al. 2020, *MNRAS*, 494, 4291

Chen, Y. Q. & Zhao, G. 2006, *AJ*, 131, 1816

Collier Cameron, A., Davidson, V. A., Hebb, L., et al. 2009, *MNRAS*, 400, 451

Cuenda-Muñoz, D., Barrado, D., Agüeros, M. A., Curtis, J. L., & Bouy, H. 2024, *A&A*, 687, A234

Cummings, J. D., Deliyannis, C. P., Maderak, R. M., & Steinhauer, A. 2017, *AJ*, 153, 128

Curtis, J. L., Agüeros, M. A., Matt, S. P., et al. 2020, *ApJ*, 904, 140

de la Reza, R., Chavero, C., Roca-Fàbrega, S., et al. 2023, *A&A*, 671, A136

Deacon, N. R. & Kraus, A. L. 2020, *MNRAS*, 496, 5176

Deal, M., Richard, O., & Vauclair, S. 2015, *A&A*, 584, A105

Dehnen, W. 2000, *AJ*, 119, 800

Delgado Mena, E., Bertrán de Lis, S., Adibekyan, V. Z., et al. 2015, *A&A*, 576, A69

Delgado Mena, E., Israelian, G., González Hernández, J. I., et al. 2014, *A&A*, 562, A92

Deliyannis, C. P. & Pinsonneault, M. H. 1997, *ApJ*, 488, 836

Dias, W. S., Monteiro, H., Moitinho, A., et al. 2021, *MNRAS*, 504, 356

Donati, J. F. 2003, in *Astronomical Society of the Pacific Conference Series*, Vol. 307, *Solar Polarization*, ed. J. Trujillo-Bueno & J. Sanchez Almeida, 41

Douglas, S. T., Agüeros, M. A., Covey, K. R., et al. 2014, *ApJ*, 795, 161

Douglas, S. T., Curtis, J. L., Agüeros, M. A., et al. 2019, *ApJ*, 879, 100

Dumont, T., Charbonnel, C., Palacios, A., & Borisov, S. 2021, *A&A*, 654, A46

Duncan, D. K. & Jones, B. F. 1983, *ApJ*, 271, 663

Ford, A., Jeffries, R. D., James, D. J., & Barnes, J. R. 2001, *A&A*, 369, 871

Friel, E. D. & Boesgaard, A. M. 1992, *ApJ*, 387, 170

Fu, X., Romano, D., Bragaglia, A., et al. 2018, *A&A*, 610, A38

Fürnkranz, V., Meingast, S., & Alves, J. 2019, *A&A*, 624, L11

Gaia Collaboration, Babusiaux, C., van Leeuwen, F., et al. 2018a, *A&A*, 616, A10

Gaia Collaboration, Brown, A. G. A., Vallenari, A., et al. 2018b, *A&A*, 616, A1

Gaia Collaboration, Brown, A. G. A., Vallenari, A., et al. 2021, *A&A*, 649, A1

Gaia Collaboration, Vallenari, A., Brown, A. G. A., et al. 2023, *A&A*, 674, A1

Galindo-Guil, F. J., Barrado, D., Bouy, H., et al. 2022, *A&A*, 664, A70

Gallet, F. & Bouvier, J. 2013, *A&A*, 556, A36

Gebran, M. & Monier, R. 2008, *A&A*, 483, 567

Gebran, M., Monier, R., & Richard, O. 2008, *A&A*, 479, 189

Ghezzi, L., Cunha, K., Smith, V. V., & de la Reza, R. 2010, *ApJ*, 724, 154

Gondoin, P. 2014, *A&A*, 566, A72

Gonzalez, G. & Laws, C. 2000, *AJ*, 119, 390

Gray, R. O. & Corbally, C. J. 1994, *AJ*, 107, 742

Guigliion, G., Chiappini, C., Romano, D., et al. 2019, *A&A*, 623, A99

Guigliion, G., de Laverny, P., Recio-Blanco, A., et al. 2016, *A&A*, 595, A18

Gustafsson, B., Edvardsson, B., Eriksson, K., et al. 2008, *A&A*, 486, 951

Gutiérrez Albarrán, M. L., Montes, D., Gómez Garrido, M., et al. 2020, *A&A*, 643, A71

Gutiérrez Albarrán, M. L., Montes, D., Tabernero, H. M., et al. 2024, *A&A*, 685, A83

Heiter, U., Lind, K., Bergemann, M., et al. 2021, *A&A*, 645, A106

Heiter, U., Soubiran, C., Netopil, M., & Paunzen, E. 2014, *A&A*, 561, A93

Herbig, G. H. 1965, *ApJ*, 141, 588

Hodges, J. L. 1958, *Arkiv for Matematik*, 3, 469

Ianna, P. A. & Schlemmer, D. M. 1993, *AJ*, 105, 209

Israelian, G., Delgado Mena, E., Santos, N. C., et al. 2009, *Nature*, 462, 189

Israelian, G., Santos, N. C., Mayor, M., & Rebolo, R. 2004, *A&A*, 414, 601

Jeffries, R. D. 1999, *MNRAS*, 304, 821

Jeffries, R. D., Jackson, R. J., Sun, Q., & Deliyannis, C. P. 2021, *MNRAS*, 500, 1158

Jeffries, R. D., Jackson, R. J., Wright, N. J., et al. 2023, *MNRAS*, 523, 802

Jeffries, R. D., Totten, E. J., Harmer, S., & Deliyannis, C. P. 2002, *MNRAS*, 336, 1109

Jones, B. F., Fischer, D., Shetrone, M., & Soderblom, D. R. 1997, *AJ*, 114, 352

Kervella, P., Arenou, F., & Thévenin, F. 2022, *A&A*, 657, A7

King, J. R. & Hiltgen, D. R. 1996, *PASP*, 108, 246

Koch, D. G., Borucki, W. J., Basri, G., et al. 2010, *ApJ*, 713, L79

Kovács, G., Hartman, J. D., Bakos, G. Á., et al. 2014, *MNRAS*, 442, 2081

Kraus, A. L. & Hillenbrand, L. A. 2007, *AJ*, 134, 2340

Kurucz, R. L. 1992, in *The Stellar Populations of Galaxies*, ed. B. Barbuy & A. Renzini, Vol. 149, 225

Leiner, E. M., Mathieu, R. D., Gosnell, N. M., & Geller, A. M. 2015, *AJ*, 150, 10

Libralato, M., Bedin, L. R., Nardiello, D., & Piotto, G. 2016, *MNRAS*, 456, 1137

Lillo-Box, J., Aceituno, J., Pedraz, S., et al. 2020, *MNRAS*, 491, 4496

Lind, K., Asplund, M., & Barklem, P. S. 2009, *A&A*, 503, 541

- Llorente de Andrés, F., Chavero, C., de la Reza, R., Roca-Fàbrega, S., & Cifuentes, C. 2021, *A&A*, 654, A137
- Llorente de Andrés, F., de la Reza, R., Cruz, P., et al. 2024, *A&A*, 684, A28
- Luck, R. E. & Heiter, U. 2006, *AJ*, 131, 3069
- Marigo, P., Girardi, L., Bressan, A., et al. 2017, *ApJ*, 835, 77
- Martín, E. L., Basri, G., Pavlenko, Y., & Lyubchik, Y. 2002, *ApJ*, 579, 437
- Martos, G., Meléndez, J., Rathsam, A., & Carvalho Silva, G. 2023, *MNRAS*, 522, 3217
- Masci, F. J., Laher, R. R., Rusholme, B., et al. 2019, *Publications of the Astronomical Society of the Pacific*, 131, 018003
- Meibom, S., Mathieu, R. D., & Stassun, K. G. 2009, *ApJ*, 695, 679
- Meléndez, J., Bedell, M., Bean, J. L., et al. 2017, *A&A*, 597, A34
- Mermilliod, J. C., Mayor, M., & Udry, S. 2009, *A&A*, 498, 949
- Meynet, G., Mermilliod, J. C., & Maeder, A. 1993, *A&AS*, 98, 477
- Mishenina, T. V., Soubiran, C., Kovtyukh, V. V., Katsova, M. M., & Livshits, M. A. 2012, *A&A*, 547, A106
- Moultaka, J., Ilovaisky, S. A., Prugniel, P., & Soubiran, C. 2004, *PASP*, 116, 693
- Moutou, C., Malo, L., Manset, N., Selliez-Vandernotte, L., & Desrochers, M. E. 2015, in *SF2A-2015: Proceedings of the Annual meeting of the French Society of Astronomy and Astrophysics*, ed. F. Martins, S. Boissier, V. Buat, L. Cambrésy, & P. Petit, 201–204
- Nardiello, D., Bedin, L. R., Nascimbeni, V., et al. 2015, *MNRAS*, 447, 3536
- Odenkirchen, M., Soubiran, C., & Colin, J. 1998, *New A*, 3, 583
- Pöder, S., Benito, M., Pata, J., et al. 2023, *A&A*, 676, A134
- Pang, X., Li, Y., Yu, Z., et al. 2021, *ApJ*, 912, 162
- Paxton, B., Bildsten, L., Dotter, A., et al. 2011, *ApJS*, 192, 3
- Paxton, B., Smolec, R., Schwab, J., et al. 2019, *ApJS*, 243, 10
- Pecaut, M. J. & Mamajek, E. E. 2013, *ApJS*, 208, 9
- Perruchot, S., Kohler, D., Bouchy, F., et al. 2008, in *Society of Photo-Optical Instrumentation Engineers (SPIE) Conference Series*, Vol. 7014, *Ground-based and Airborne Instrumentation for Astronomy II*, ed. I. S. McLean & M. M. Casali, 70140J
- Petit, P., Louge, T., Théado, S., et al. 2014, *PASP*, 126, 469

- Ramírez, I., Fish, J. R., Lambert, D. L., & Allende Prieto, C. 2012, *ApJ*, 756, 46
- Rampalli, R., Agüeros, M. A., Curtis, J. L., et al. 2021, *ApJ*, 921, 167
- Rebolo, R., Martin, E. L., Basri, G., Marcy, G. W., & Zapatero-Osorio, M. R. 1996, *ApJ*, 469, L53
- Rebolo, R., Martin, E. L., & Magazzu, A. 1992, *ApJ*, 389, L83
- Ricker, G. R., Winn, J. N., Vanderspek, R., et al. 2015, *Journal of Astronomical Telescopes, Instruments, and Systems*, 1, 014003
- Ryan, S. G. 2000, *MNRAS*, 316, L35
- Schuler, S. C., King, J. R., Fischer, D. A., Soderblom, D. R., & Jones, B. F. 2003, *AJ*, 125, 2085
- Sevilla, J., Behrard, A., & Fuller, J. 2022, *MNRAS*, 516, 3354
- Siess, L. & Livio, M. 1997, *ApJ*, 490, 785
- Singh, K., Rothstein, P., Curtis, J. L., Núñez, A., & Agüeros, M. A. 2021, *Research Notes of the American Astronomical Society*, 5, 84
- Skumanich, A. 1972, *ApJ*, 171, 565
- Snedden, C., Bean, J., Ivans, I., Lucatello, S., & Sobek, J. 2012, MOOG: LTE line analysis and spectrum synthesis, *Astrophysics Source Code Library*, record ascl:1202.009
- Soares-Furtado, M., Hartman, J. D., Bhatti, W., et al. 2020, *ApJS*, 246, 15
- Soderblom, D. R., Fedele, S. B., Jones, B. F., Stauffer, J. R., & Prosser, C. F. 1993a, *AJ*, 106, 1080
- Soderblom, D. R., Hillenbrand, L. A., Jeffries, R. D., Mamajek, E. E., & Naylor, T. 2014, in *Protostars and Planets VI*, ed. H. Beuther, R. S. Klessen, C. P. Dullemond, & T. Henning, 219–241
- Soderblom, D. R., Jones, B. F., Balachandran, S., et al. 1993b, *AJ*, 106, 1059
- Soderblom, D. R., Oey, M. S., Johnson, D. R. H., & Stone, R. P. S. 1990, *AJ*, 99, 595
- Somers, G. & Pinsonneault, M. H. 2014, *ApJ*, 790, 72
- Somers, G. & Pinsonneault, M. H. 2015, *MNRAS*, 449, 4131
- Souto, D., Cunha, K., & Smith, V. V. 2021, *ApJ*, 917, 11
- Spina, L., Sharma, P., Meléndez, J., et al. 2021, *Nature Astron.*, 5, 1163
- Stassun, K. G., Oelkers, R. J., Paegert, M., et al. 2019, *AJ*, 158, 138
- Stassun, K. G., Oelkers, R. J., Pepper, J., et al. 2018, *AJ*, 156, 102
- Stauffer, J. R., Barrado y Navascués, D., Bouvier, J., et al. 1999, *ApJ*, 527, 219

- Stauffer, J. R., Schultz, G., & Kirkpatrick, J. D. 1998, *ApJ*, 499, L199
- Steinhauer, A. & Deliyannis, C. P. 2004, *ApJ*, 614, L65
- Sun, Q., Deliyannis, C. P., Steinhauer, A., Anthony-Twarog, B. J., & Twarog, B. A. 2023, *ApJ*, 952, 71
- Takeda, Y., Honda, S., Kawanomoto, S., Ando, H., & Sakurai, T. 2010, *A&A*, 515, A93
- Tang, S.-Y., Pang, X., Yuan, Z., et al. 2019, *ApJ*, 877, 12
- Taylor, B. J. 2006, *AJ*, 132, 2453
- Taylor, M. B. 2005, in *Astronomical Society of the Pacific Conference Series*, Vol. 347, *Astronomical Data Analysis Software and Systems XIV*, ed. P. Shopbell, M. Britton, & R. Ebert, 29
- Telting, J. H., Avila, G., Buchhave, L., et al. 2014, *Astronomische Nachrichten*, 335, 41
- Terrien, R. C., Mahadevan, S., Deshpande, R., et al. 2014, *ApJ*, 782, 61
- Thorburn, J. A., Hobbs, L. M., Deliyannis, C. P., & Pinsonneault, M. H. 1993, *ApJ*, 415, 150
- Wang, J. J., Chen, L., Zhao, J. H., & Jiang, P. F. 1995, *A&AS*, 113, 419
- Zappala, R. R. 1972, *ApJ*, 172, 57
- Ziegler, C., Tokovinin, A., Briceño, C., et al. 2020, *AJ*, 159, 19

Acknowledgements

This research has been funded by grant No. PID2019-107061GB-C61 by the Spanish Ministry of Science and Innovation/State Agency of Research MCIN/AEI/10.13039/501100011033 and No. MDM-2017-0737 Unidad de Excelencia “María de Maeztu”- Centro de Astrobiología (INTA-CSIC). The author acknowledges financial support from a Erasmus+ grant co-funded by the European Commission and the Spanish Ministry of Education, Culture and Sport, and from a mobility grant funded by the Doctoral School of the Complutense University of Madrid.

Based on observations collected at the Centro Astronómico Hispano en Andalucía (CAHA) at Calar Alto, operated jointly by Junta de Andalucía and Consejo Superior de Investigaciones Científicas (IAA-CSIC). Based on observations made with the Nordic Optical Telescope, owned in collaboration by the University of Turku and Aarhus University, and operated jointly by Aarhus University, the University of Turku and the University of Oslo, representing Denmark, Finland and Norway, the University of Iceland and Stockholm University at the Observatorio del Roque de los Muchachos, La Palma, Spain, of the Instituto de Astrofísica de Canarias. Based on observations made at Observatoire de Haute-Provence (CNRS), France.

This work includes data collected by the TESS mission, which is funded by the NASA Science Mission directorate. We obtained these data from the Mikulski Archive for Space Telescopes (MAST). STScI is operated by the Association of Universities for Research in Astronomy, Inc., under NASA contract NAS5-26555. Support for MAST for non-HST data is provided by the NASA Office of Space Science via grant NNX09AF08G and by other grants and contracts.

Based on observations collected at the WIYN Observatory. The WIYN Observatory is a joint facility of the NSF’s National Optical-Infrared Astronomy Research Laboratory, Indiana University, the University of Wisconsin-Madison, Pennsylvania State University, the University of Missouri, the University of California-Irvine, and Purdue University. The astronomical community is honored to have the opportunity to conduct astronomical research on Iolkam Du’ag (Kitt Peak) in Arizona.

Based on observations obtained with the Samuel Oschin Telescope 48-inch and the 60-inch Telescope at the Palomar Observatory as part of the Zwicky Transient Facility project. ZTF is supported by the National Science Foundation under Grants No. AST-1440341 and AST-2034437 and a collaboration including current partners Caltech, IPAC, the Weizmann Institute for Science, the Oskar Klein Center at Stockholm University, the University of Maryland, Deutsches Elektronen-Synchrotron and Humboldt University, the TANGO Consortium of Taiwan, the University of Wisconsin at Milwaukee, Trinity College Dublin, Lawrence Livermore National Laboratories, IN2P3, University of Warwick, Ruhr University Bochum, Northwestern University and former partners the University of Washington, Los Alamos National Laboratories, and Lawrence Berkeley National Laboratories. Operations are conducted by COO, IPAC, and UW.

This work makes use of VOSA, maintained under the Spanish Virtual Observatory project funded by MCIN/AEI/10.13039/501100011033/ through grant PID2020-112949GB-I00. VOSA has been partially updated by using funding from the European Union's Horizon 2020 Research and Innovation Programme, under Grant Agreement n° 776403 (EXOPLANETS-A). Based on Clusterix 2.0 service at CAB (INTA-CSIC), the Tool for OPERations on Catalogues And Tables (TOPCAT) and the Image Reduction and Analysis Facility (IRAF). This work makes use of data from the European Space Agency (ESA) mission Gaia, processed by the Gaia Data Processing and Analysis Consortium (DPAC).

Appendix A

M35 tables

Electronic versions of all tables shown in this appendix are available at:

[https://vizier.cds.unistra.fr/viz-bin/VizieR?pm\\$-source=J/A+A/687/A234](https://vizier.cds.unistra.fr/viz-bin/VizieR?pm$-source=J/A+A/687/A234)

Table A.1: Cross-identification numbers, coordinates, and observation campaigns for the complete sample presented in this work.

ID	$\alpha(2000)$ hh:mm:ss	$\delta(2000)$ dd:mm:ss	$\alpha(2000)$ deg	$\delta(2000)$ deg	Campaign	AT18 ID	Je21 ID
5066			92.04135	24.4281	Nov_2017		J06080992+2425411
5076	06:08:52.9	+24:17:20	92.22042	24.28889	Mar_2001	16010	
5078			92.30182	24.41464	Nov_2017		J06091244+2424527
5081	6:09:26.200	24:29:03.0	92.35917	24.48417	Jan_1998		
5083	6:09:29.580	24:32:7.90	92.37325	24.53553	Dec_1999		
5087	06:09:29.5	+24:21:03	92.37292	24.35083	Mar_2001	18011	
5088	6:08:55.460	24:18:47.50	92.23108	24.31319	Dec_1999		
5089	6:09:10.230	24:31:44.8	92.29262	24.52911	Jan_1998		J06091027+2431443
5089	6:09:10.230	24:31:44.80	92.29262	24.52911	Dec_1999		J06091027+2431443
5094	06:09:05.0	+24:17:51	92.27083	24.2975	Mar_2001	13006	
5096	6:08:19.030	24:28:37.1	92.07929	24.47697	Jan_1998		
5097	06:08:25.4	+24:09:17	92.10583	24.15472	Mar_2001	22030	J06082549+2409174
5098	6:09:26.710	24:18:07.2	92.36129	24.302	Jan_1998		J06092672+2418063
5099	06:09:19.3	+24:19:08	92.33042	24.31889	Mar_2001	15007	
5103	6:09:19.600	24:31:57.6	92.33167	24.53267	Jan_1998		
5103	06:09:19.6	+24:31:58	92.33167	24.53278	Feb_2001		
5107	6:08:58.860	24:20:17.2	92.24525	24.33811	Jan_1998		J06085888+2420166
5111	6:08:10.460	24:15:50.70	92.04358	24.26408	Dec_1999		
5112	06:09:38.8	+24:19:42	92.41167	24.32833	Mar_2001	34015	
5113	6:08:47.580	24:12:04.2	92.19825	24.20117	Jan_1998		
5114	6:09:14.560	24:19:50.70	92.31067	24.33075	Dec_1999		
5116	6:08:40.600	24:15:58.4	92.16917	24.26622	Jan_1998		J06084064+2415577
5120	6:08:20.160	24:21:52.30	92.084	24.36453	Dec_1999		

Continuation of Table A.1

ID	$\alpha(2000)$ hh:mm:ss	$\delta(2000)$ dd:mm:ss	$\alpha(2000)$ deg	$\delta(2000)$ deg	Campaign	AT18 ID	Je21 ID
5121	06:09:10.2	+24:17:21	92.2925	24.28917	Mar_2001	16007	J06091020+2417215
5125	6:09:14.810	24:31:23.7	92.31171	24.52325	Jan_1998		
5126	6:09:36.270	24:27:08.9	92.40112	24.45247	Jan_1998		
5130	06:09:22.8	+24:23:48	92.345	24.39667	Mar_2001	21010	
5132	6:08:59.070	24:21:00.4	92.24612	24.35011	Jan_1998		
5132	6:08:59.070	24:21:0.40	92.24612	24.35011	Dec_1999		
5133	6:08:27.000	24:12:56.40	92.1125	24.21567	Dec_1999		
5135	6:08:52.220	24:23:28.6	92.21758	24.39128	Jan_1998		J06085223+2423282
5136	6:09:09.970	24:18:54.5	92.29154	24.31514	Jan_1998		
5136	6:09:9.970	24:18:54.50	92.29154	24.31514	Dec_1999		
5138	6:08:15.410	24:25:27.8	92.06421	24.42439	Jan_1998		J06081542+2425269
5139	6:09:0.080	24:18:15.20	92.25033	24.30422	Dec_1999		J06090010+2418146
5140	06:08:30.3	+24:26:28	92.12625	24.44111	Mar_2001	29021	J06083030+2426284
5141	6:08:48.550	24:10:29.0	92.20229	24.17472	Jan_1998		
5142	6:09:43.690	24:21:04.5	92.43204	24.35125	Jan_1998		
5144	6:09:28.520	24:15:32.1	92.36883	24.25892	Jan_1998		J06092852+2415312
5146	06:09:04.2	+24:12:42	92.2675	24.21167	Mar_2001	27016	J06090427+2412419
5148	6:08:29.610	24:16:24.80	92.12338	24.27356	Dec_1999		J06082965+2416240
5151	6:09:16.980	24:24:19.5	92.32075	24.40542	Jan_1998		
5152	06:08:33.1	+24:19:13	92.13792	24.32028	Mar_2001	26016	J06083318+2419132
5155			92.23644	24.1666	Nov_2017		J06085675+2409598
5156	6:09:38.950	24:14:1.20	92.41229	24.23367	Dec_1999		
5158			92.41636	24.43575	Nov_2017		J06093993+2426087
5159	6:09:33.840	24:14:59.9	92.391	24.24997	Jan_1998		
5162			92.41264	24.40681	Nov_2017		J06093903+2424245
5165	6:09:15.120	24:11:04.1	92.313	24.18447	Jan_1998		J06091512+2411035
5167	6:09:38.260	24:15:50.80	92.40942	24.26411	Dec_1999		
5174	6:08:10.430	24:24:24.7	92.04346	24.40686	Jan_1998		J06081045+2424237
5175			92.12279	24.26806	Nov_2017		J06082947+2416050
5176	6:08:56.400	24:27:10.9	92.235	24.45303	Jan_1998		J06085642+2427106
5178	6:09:10.840	24:19:46.3	92.29517	24.32953	Jan_1998		
5180	06:09:39.0	+24:16:44	92.4125	24.27889	Mar_2001	26017	J06093901+2416442
5181	06:09:28.7	+24:25:33	92.36958	24.42583	Mar_2001	46015	
5182	06:09:26.4	+24:15:13	92.36	24.25361	Mar_2001	36014	J06092648+2415136
5183	6:08:46.620	24:31:43.50	92.19425	24.52875	Dec_1999		
5184	6:09:20.740	24:19:55.2	92.33642	24.332	Jan_1998		
5186	6:08:42.970	24:26:34.50	92.17904	24.44292	Dec_1999		J06084297+2426341
5190	6:09:16.060	24:25:31.9	92.31692	24.42553	Jan_1998		
5192	6:08:24.170	24:12:23.2	92.10071	24.20644	Jan_1998		
5194	6:09:3.040	24:19:36.80	92.26267	24.32689	Dec_1999		J06090307+2419362
5194	6:09:03.040	24:19:36.8	92.26267	24.32689	Jan_1998		J06090307+2419362
5195	6:08:45.830	24:18:23.0	92.19096	24.30639	Jan_1998		J06084586+2418224

Continuation of Table A.1

ID	$\alpha(2000)$ hh:mm:ss	$\delta(2000)$ dd:mm:ss	$\alpha(2000)$ deg	$\delta(2000)$ deg	Campaign	AT18 ID	Je21 ID
5198			92.27664	24.44493	Nov_2017		J06090639+2426417
5200	6:08:12.180	24:31:20.60	92.05075	24.52239	Dec_1999		
5202	6:08:9.910	24:25:13.70	92.04129	24.42047	Dec_1999		
5203	6:09:19.6	+24:30:53	92.33167	24.51472	Mar_2001	42022	
5205	6:08:54.800	24:22:51.1	92.22833	24.38086	Jan_1998		
5206	6:09:5.590	24:22:32.60	92.27329	24.37572	Dec_1999		
5209	6:08:17.040	24:27:02.6	92.071	24.45072	Jan_1998		J06081704+2427019
5210	6:08:21.460	24:28:35.50	92.08942	24.47653	Dec_1999		
5213	6:08:52.690	24:09:41.00	92.21954	24.16139	Dec_1999		
5215	6:08:47.560	24:09:42.90	92.19817	24.16192	Dec_1999		J06084761+2409422
5216	6:08:32.690	24:27:18.9	92.13621	24.45525	Jan_1998		
5219	6:08:47.330	24:24:56.1	92.19721	24.41558	Jan_1998		
5220	6:08:12.010	24:21:27.60	92.05004	24.35767	Dec_1999		
5221	6:08:43.4	+24:16:07	92.18083	24.26861	Mar_2001	48015	J06084341+2416072
5222	6:09:13.7	+24:19:59	92.30708	24.33306	Mar_2001	8003	J06091371+2419595
5223	6:08:24.340	24:16:33.70	92.10142	24.27603	Dec_1999		
5227	6:09:5.370	24:12:18.60	92.27238	24.20517	Dec_1999		J06090539+2412180
5230	6:09:2.130	24:29:31.60	92.25888	24.49211	Dec_1999		J06090215+2429312
5231	6:08:52.710	24:24:44.9	92.21962	24.41247	Jan_1998		
5233	6:09:11.690	24:11:24.5	92.29871	24.19014	Jan_1998		J06091169+2411240
5235	6:08:59.030	24:18:25.6	92.24596	24.30711	Jan_1998		
5236	6:09:42.910	24:31:45.0	92.42879	24.52917	Jan_1998		
5240	6:08:55.3	+24:20:57	92.23042	24.34917	Mar_2001	23006	
5241	6:09:21.840	24:18:22.0	92.341	24.30611	Jan_1998		J06092185+2418212
5243	6:09:09.410	24:10:45.7	92.28921	24.17936	Jan_1998		
5243	6:09:9.410	24:10:45.70	92.28921	24.17936	Dec_1999		
5246	6:09:12.740	24:10:2.40	92.30308	24.16733	Dec_1999		
5257	6:09:06.460	24:18:00.3	92.27692	24.30008	Jan_1998		J06090648+2417596
5258	6:08:12.6	+24:19:36	92.0525	24.32667	Mar_2001	57026	J06081262+2419359
5259	6:08:41.0	+24:17:20	92.17083	24.28889	Mar_2001	42014	J06084106+2417206
5262	6:08:32.1	+24:20:36	92.13375	24.34333	Mar_2001	38017	J06083216+2420363
5263	6:09:14.070	24:13:37.5	92.30862	24.22708	Jan_1998		J06091408+2413367
5264	6:09:07.260	24:23:45.0	92.28025	24.39583	Jan_1998		J06090729+2423446
5265	6:09:22.9	+24:15:26	92.34542	24.25722	Mar_2001	50013	J06092291+2415263
5267	6:08:57.650	24:10:01.3	92.24021	24.16703	Jan_1998		J06085768+2410007
5268	6:09:26.480	24:20:47.20	92.36033	24.34644	Dec_1999		
5268	6:09:26.480	24:20:47.2	92.36033	24.34644	Jan_1998		
5273			92.28859	24.20445	Nov_2017		J06090926+2412160
5274	6:09:32.970	24:25:18.5	92.38738	24.42181	Jan_1998		J06093300+2425178
5278	6:09:38.5	+24:20:43	92.41042	24.34528	Mar_2001	58015	J06093859+2420427
5279	6:08:57.830	24:31:39.10	92.24096	24.52753	Dec_1999		
5281	6:08:29.8	+24:29:18	92.12417	24.48833	Mar_2001	52025	J06082982+2429178

Continuation of Table A.1

ID	$\alpha(2000)$ hh:mm:ss	$\delta(2000)$ dd:mm:ss	$\alpha(2000)$ deg	$\delta(2000)$ deg	Campaign	AT18 ID	Je21 ID
5283	6:09:26.320	24:23:20.30	92.35967	24.38897	Dec_1999		J06092635+2423196
5288	6:09:27.930	24:22:27.4	92.36638	24.37428	Jan_1998		J06092796+2422267
5289	6:09:29.170	24:21:52.1	92.37154	24.36447	Jan_1998		
5290			92.34139	24.51186	Nov_2017		J06092193+2430427
5292	6:09:13.470	24:21:46.8	92.30612	24.363	Jan_1998		
5293	6:09:06.460	24:21:30.8	92.27692	24.35856	Jan_1998		J06090649+2421303
5294	6:08:48.750	24:16:26.6	92.20312	24.27406	Jan_1998		J06084879+2416259
5295	6:09:19.660	24:12:28.70	92.33192	24.20797	Dec_1999		J06091966+2412280
5297	6:08:33.880	24:09:48.4	92.14117	24.16344	Jan_1998		
5297	6:08:33.880	24:09:48.40	92.14117	24.16344	Dec_1999		
5298			92.12848	24.37154	Nov_2017		J06083084+2422175
5299	6:08:49.620	24:14:40.1	92.20675	24.24447	Jan_1998		
5300			92.33686	24.19137	Nov_2017		J06092085+2411289
5302			92.15449	24.23357	Nov_2017		J06083708+2414008
5303	6:09:42.590	24:20:53.20	92.42746	24.34811	Dec_1999		
5304	6:09:31.420	24:15:21.90	92.38092	24.25608	Dec_1999		
5305	6:08:39.120	24:24:19.7	92.163	24.40547	Jan_1998		
5307	06:08:35.2	+24:17:15	92.14667	24.2875	Mar_2001	46017	J06083521+2417154
5308	06:09:32.0	+24:15:10	92.38333	24.25278	Mar_2001	40016	J06093201+2415101
5309	6:08:06.140	24:27:19.8	92.02558	24.4555	Jan_1998		
5312	6:08:10.950	24:26:34.10	92.04562	24.44281	Dec_1999		
5314	6:08:39.200	24:10:45.8	92.16333	24.17939	Jan_1998		
5316	6:09:26.760	24:27:55.50	92.3615	24.46542	Dec_1999		J06092680+2427549
5316	6:09:26.760	24:27:55.5	92.3615	24.46542	Jan_1998		J06092680+2427549
5317	6:08:22.260	24:15:03.3	92.09275	24.25092	Jan_1998		
5318	6:08:53.970	24:15:24.00	92.22488	24.25667	Dec_1999		
5323	6:09:10.620	24:28:4.30	92.29425	24.46786	Dec_1999		J06091065+2428039
5326	06:08:47.3	+24:30:25	92.19708	24.50694	Feb_2001		J06084739+2430249
5327	06:09:07.5	+24:31:52	92.28125	24.53111	Mar_2001	F1	J06090755+2431526
5332	6:08:55.970	24:25:11.5	92.23321	24.41986	Jan_1998		J06085599+2425111
5336			92.11154	24.49019	Nov_2017		J06082677+2429247
5337	06:09:38.8	+24:28:54	92.41167	24.48167	Feb_2001		
5338	06:08:45.6	+24:29:00	92.19	24.48333	Feb_2001	F4	
5338	06:08:45.6	+24:29:00	92.19	24.48333	Mar_2001	F4	
5339	6:09:16.290	24:18:37.3	92.31788	24.31036	Jan_1998		
5344	6:09:41.260	24:23:6.60	92.42192	24.38517	Dec_1999		
5345	6:08:58.330	24:14:22.2	92.24304	24.2395	Jan_1998		
5347	6:09:20.340	24:23:05.2	92.33475	24.38478	Jan_1998		J06092036+2423046
5350	6:09:41.770	24:14:59.9	92.42404	24.24997	Jan_1998		
5356	6:08:30.610	24:31:51.20	92.12754	24.53089	Dec_1999		J06083060+2431505
5357	6:08:40.610	24:25:40.4	92.16921	24.42789	Jan_1998		
5359	6:09:18.810	24:11:43.90	92.32838	24.19553	Dec_1999		

Continuation of Table A.1

ID	$\alpha(2000)$ hh:mm:ss	$\delta(2000)$ dd:mm:ss	$\alpha(2000)$ deg	$\delta(2000)$ deg	Campaign	AT18 ID	Je21 ID
5361	06:09:30.2	+24:23:14	92.37583	24.38722	Feb_2001		
5362	6:09:15.950	24:11:56.90	92.31646	24.19914	Dec_1999		
5366	06:09:28.4	+24:16:02	92.36833	24.26722	Feb_2001		
5368	06:08:25.8	+24:12:54	92.1075	24.215	Feb_2001		J06082585+2412538
5369	06:08:16.7	+24:26:27	92.06958	24.44083	Feb_2001		J06081678+2426268
5370			92.1772	24.39367	Nov_2017		J06084253+2423372
5373	6:08:49.270	24:15:33.30	92.20529	24.25925	Dec_1999		
5376	6:09:34.510	24:23:53.9	92.39379	24.39831	Jan_1998		
5378			92.06908	24.39039	Nov_2017		J06081658+2423254
5381	6:09:37.510	24:31:12.90	92.40629	24.52025	Dec_1999		
5382			92.06284	24.38779	Nov_2017		J06081508+2423160
5384	6:09:06.130	24:27:20.4	92.27554	24.45567	Jan_1998		
5386	6:08:10.020	24:27:30.70	92.04175	24.45853	Dec_1999		
5387	6:08:56.360	24:27:7.10	92.23483	24.45197	Dec_1999		
5388	6:08:48.250	24:17:59.8	92.20104	24.29994	Jan_1998		J06084828+2417591
5393	06:09:26.5	+24:20:39	92.36042	24.34417	Feb_2001		J06092651+2420393
5394	6:09:31.260	24:14:21.10	92.38025	24.23919	Dec_1999		
5395	6:08:12.800	24:19:49.70	92.05333	24.33047	Dec_1999		
5398	6:08:52.550	24:22:00.6	92.21896	24.36683	Jan_1998		
5398	6:08:52.550	24:22:0.60	92.21896	24.36683	Dec_1999		
5399	6:09:12.600	24:22:24.6	92.3025	24.3735	Jan_1998		J06091263+2422240
5399	6:09:12.600	24:22:24.60	92.3025	24.3735	Dec_1999		J06091263+2422240
5400	06:08:23.3	+24:15:20	92.09708	24.25556	Feb_2001		
5401	06:09:30.0	+24:32:08	92.375	24.53556	Feb_2001		
5402	6:09:14.690	24:18:9.30	92.31121	24.30258	Dec_1999		J06091471+2418085
5405	06:09:16.1	+24:18:03	92.31708	24.30083	Feb_2001		J06091610+2418033
5407	6:09:17.820	24:21:57.1	92.32425	24.36586	Jan_1998		
5407	6:09:17.820	24:21:57.10	92.32425	24.36586	Dec_1999		
5408	6:08:15.230	24:28:06.1	92.06346	24.46836	Jan_1998		J06081524+2428052
5409	06:08:46.5	+24:17:45	92.19375	24.29583	Feb_2001		
5410	6:08:23.370	24:23:55.9	92.09738	24.39886	Jan_1998		
5411	6:08:37.390	24:20:44.0	92.15579	24.34556	Jan_1998		J06083741+2420434
5413	06:09:05.6	+24:11:35	92.27333	24.19306	Feb_2001		J06090568+2411355
5415	6:09:38.260	24:16:34.80	92.40942	24.27633	Dec_1999		
5418	06:09:44.4	+24:17:32	92.435	24.29222	Feb_2001	F7	J06094442+2417318
5418	06:09:44.4	+24:17:32	92.435	24.29222	Mar_2001	F7	J06094442+2417318
5419	6:08:43.410	24:20:28.5	92.18088	24.34125	Jan_1998		
5421	6:08:39.410	24:17:12.20	92.16421	24.28672	Dec_1999		
5426	6:08:26.870	24:09:30.40	92.11196	24.15844	Dec_1999		
5428	6:09:16.850	24:14:23.80	92.32021	24.23994	Dec_1999		
5429			92.28536	24.41414	Nov_2017		J06090849+2424509
5431	6:08:23.880	24:13:53.40	92.0995	24.2315	Dec_1999		

Continuation of Table A.1

ID	$\alpha(2000)$ hh:mm:ss	$\delta(2000)$ dd:mm:ss	$\alpha(2000)$ deg	$\delta(2000)$ deg	Campaign	AT18 ID	Je21 ID
5432	6:09:23.670	24:31:56.3	92.34862	24.53231	Jan_1998		
5434	6:09:25.600	24:21:29.00	92.35667	24.35806	Dec_1999		
5436	06:09:36.8	+24:21:31	92.40333	24.35861	Feb_2001		J06093687+2421313
5437	6:09:23.580	24:26:19.2	92.34825	24.43867	Jan_1998		J06092361+2426187
5437	6:09:23.580	24:26:19.20	92.34825	24.43867	Dec_1999		J06092361+2426187
5438	06:08:16.1	+24:30:49	92.06708	24.51361	Feb_2001		J06081612+2430493
5440	6:09:11.440	24:25:24.50	92.29767	24.42347	Dec_1999		
5442			92.37198	24.47225	Nov_2017		J06092928+2428201
5445	06:08:32.8	+24:25:11	92.13667	24.41972	Feb_2001		
5446	06:08:39.7	+24:19:24	92.16542	24.32333	Feb_2001		J06083972+2419241
5447	6:08:19.620	24:20:51.90	92.08175	24.34775	Dec_1999		J06081964+2420511
5449	6:09:24.830	24:14:26.5	92.35346	24.24069	Jan_1998		
5449	6:09:24.830	24:14:26.50	92.35346	24.24069	Dec_1999		
5450	06:08:18.3	+24:10:48	92.07625	24.18	Feb_2001		J06081831+2410483
5452	6:08:12.610	24:23:21.60	92.05254	24.38933	Dec_1999		
5454	6:08:27.400	24:12:08.6	92.11417	24.20239	Jan_1998		
5454	6:08:27.400	24:12:8.60	92.11417	24.20239	Dec_1999		
5455	06:08:59.0	+24:15:16	92.24583	24.25444	Feb_2001		
5456	6:08:48.080	24:16:20.80	92.20033	24.27244	Dec_1999		
5458	06:08:24.0	+24:13:51	92.1	24.23083	Feb_2001		J06082405+2413516
5459	06:09:06.5	+24:31:26	92.27708	24.52389	Feb_2001		J06090654+2431260
5462	6:08:40.750	24:11:51.10	92.16979	24.19753	Dec_1999		J06084080+2411505
5463	06:08:37.8	+24:18:43	92.1575	24.31194	Mar_2001	F10	J06083785+2418429
5472	06:08:09.9	+24:21:56	92.04125	24.36556	Mar_2001	F9	J06080995+2421556
5476	6:09:22.510	24:27:56.20	92.34379	24.46561	Dec_1999		J06092254+2427558
5477			92.14568	24.34871	Nov_2017		J06083496+2420553
5479	06:08:46.9	+24:22:15	92.19542	24.37083	Feb_2001		
5481	6:08:57.200	24:15:53.90	92.23833	24.26497	Dec_1999		J06085723+2415532
5482	6:09:13.740	24:15:48.50	92.30725	24.26347	Dec_1999		
5483	06:08:44.7	+24:32:01	92.18625	24.53361	Mar_2001	F11	
5489	6:08:31.860	24:27:3.20	92.13275	24.45089	Dec_1999		
5493			92.25476	24.30016	Nov_2017		J06090114+2418006
5494	06:09:12.5	+24:10:14	92.30208	24.17056	Feb_2001		J06091259+2410139
5495	6:08:29.720	24:09:18.80	92.12383	24.15522	Dec_1999		
5497	6:08:26.020	24:26:53.30	92.10842	24.44814	Dec_1999		
5502	06:09:15.8	+24:13:57	92.31583	24.2325	Feb_2001		
5504	06:08:45.4	+24:12:41	92.18917	24.21139	Feb_2001		
5506	6:08:18.840	24:27:13.40	92.0785	24.45372	Dec_1999		
5508	06:08:44.9	+24:23:57	92.18708	24.39917	Feb_2001		J06084499+2423569
5516	6:09:5.030	24:30:44.50	92.27096	24.51236	Dec_1999		
5517	6:08:48.840	24:28:47.90	92.2035	24.47997	Dec_1999		
7000	06:07:40.8	+24:14:23	91.92	24.23972	Feb_2001		J06074081+2414234

Continuation of Table A.1

ID	$\alpha(2000)$ hh:mm:ss	$\delta(2000)$ dd:mm:ss	$\alpha(2000)$ deg	$\delta(2000)$ deg	Campaign	AT18 ID	Je21 ID
7001	06:09:18.8	+24:27:05	92.32833	24.45139	Feb_2001		J06091881+2427050
7002	06:09:27.7	+24:08:10	92.36542	24.13611	Feb_2001		J06092769+2408105
7003	06:08:41.3	+24:00:45	92.17208	24.0125	Feb_2001		
7004	06:09:49.4	+24:15:47	92.45583	24.26306	Feb_2001		J06094945+2415472
7005	06:09:51.6	+24:06:33	92.465	24.10917	Feb_2001		
7006	06:09:51.2	+24:10:02	92.46333	24.16722	Feb_2001		J06095127+2410018
7007	06:09:49.4	+24:25:04	92.45583	24.41778	Feb_2001		
7008	06:08:18.3	+24:33:40	92.07625	24.56111	Feb_2001		
7009	06:08:57.0	+24:17:04	92.2375	24.28444	Feb_2001		
7010	06:08:54.2	+24:09:01	92.22583	24.15028	Feb_2001		
7011	06:07:25.0	+24:22:30	91.85417	24.375	Feb_2001		
7012	06:09:58.1	+24:30:15	92.49208	24.50417	Feb_2001		
7013	06:09:54.7	+24:28:51	92.47792	24.48083	Feb_2001		
7014	06:09:53.3	+24:38:00	92.47208	24.63333	Feb_2001		J06095332+2437599
7015	06:10:22.2	+24:23:30	92.5925	24.39167	Feb_2001		J06102220+2423300
7016	06:08:55.5	+24:37:52	92.23125	24.63111	Feb_2001		
7017	06:08:06.0	+24:04:42	92.025	24.07833	Feb_2001		J06080602+2404419
7018	06:07:54.5	+24:35:50	91.97708	24.59722	Feb_2001		J06075455+2435499
7019	06:08:03.4	+24:34:10	92.01417	24.56944	Feb_2001		J06080337+2434101
7020	06:07:58.4	+24:19:40	91.99333	24.32778	Feb_2001		
7021	06:08:36.3	+24:06:23	92.15125	24.10639	Feb_2001		
7022	06:09:24.6	+24:37:03	92.3525	24.6175	Feb_2001		
7023	06:08:07.6	+24:03:17	92.03167	24.05472	Feb_2001		J06080763+2403166
7024	06:10:25.0	+24:07:30	92.60417	24.125	Feb_2001		
7025	06:10:19.4	+24:35:57	92.58083	24.59917	Feb_2001		
7026	06:09:45.7	+24:01:11	92.44042	24.01972	Feb_2001		
7027	06:09:39.8	+24:00:34	92.41583	24.00944	Feb_2001		
7028	06:09:17.9	+24:16:39	92.32458	24.2775	Feb_2001		
7029	06:07:49.7	+24:37:35	91.95708	24.62639	Feb_2001		
7030	06:10:14.2	+24:32:30	92.55917	24.54167	Feb_2001		J06101419+2432303
7031	06:08:04.6	+24:10:58	92.01917	24.18278	Feb_2001		J06080459+2410578
7032	06:09:24.5	+24:06:13	92.35208	24.10361	Feb_2001		J06092451+2406127
7033	06:07:23.5	+24:17:38	91.84792	24.29389	Feb_2001		
7034	06:07:49.0	+24:02:03	91.95417	24.03417	Feb_2001		
7035	06:07:34.4	+24:39:30	91.89333	24.65833	Feb_2001		
7036	06:09:00.7	+24:35:53	92.25292	24.59806	Feb_2001		
7037	06:07:52.2	+24:18:07	91.9675	24.30194	Feb_2001		
7038	06:07:42.9	+24:30:18	91.92875	24.505	Feb_2001		
7039	06:08:04.2	+24:40:00	92.0175	24.66667	Feb_2001		
7040	06:10:01.9	+24:07:17	92.50792	24.12139	Feb_2001		J06100196+2407172
7041	06:10:19.0	+24:19:45	92.57917	24.32917	Feb_2001		
7042	06:10:15.2	+24:28:59	92.56333	24.48306	Feb_2001		

Continuation of Table A.1

ID	$\alpha(2000)$ hh:mm:ss	$\delta(2000)$ dd:mm:ss	$\alpha(2000)$ deg	$\delta(2000)$ deg	Campaign	AT18 ID	Je21 ID
7043	06:08:53.7	+24:05:38	92.22375	24.09389	Feb_2001		
7044	06:09:55.1	+24:19:15	92.47958	24.32083	Feb_2001		
7045	06:07:53.6	+24:07:16	91.97333	24.12111	Feb_2001		
7046	06:07:47.5	+24:04:43	91.94792	24.07861	Feb_2001		
7047	06:08:32.1	+24:26:25	92.13375	24.44028	Feb_2001		J06083211+2426254
7048	06:07:53.7	+24:39:01	91.97375	24.65028	Feb_2001		
7049	06:08:25.0	+24:06:06	92.10417	24.10167	Feb_2001		J06082502+2406062
7050	06:10:18.7	+24:32:45	92.57792	24.54583	Feb_2001		J06101876+2432446
7051	06:09:49.4	+24:13:49	92.45583	24.23028	Feb_2001		
7052	06:07:25.5	+24:17:08	91.85625	24.28556	Feb_2001		
7053	06:08:53.3	+24:36:36	92.22208	24.61	Feb_2001		J06085330+2436363
7054	06:09:59.2	+24:35:55	92.49667	24.59861	Feb_2001		
7055	06:08:02.0	+24:26:47	92.00833	24.44639	Feb_2001		
7056	06:07:23.3	+24:08:51	91.84708	24.1475	Feb_2001		
7057	06:09:06.1	+24:05:40	92.27542	24.09444	Feb_2001		J06090617+2405398
7058	06:09:14.0	+24:38:47	92.30833	24.64639	Mar_2001	36037	
7059	06:09:29.7	+24:17:47	92.37375	24.29639	Mar_2001	36012	
7060	06:09:40.2	+24:01:17	92.4175	24.02139	Mar_2001	100042	J06094028+2401167
7061	06:09:51.2	+24:29:30	92.46333	24.49167	Mar_2001	64027	
7062	06:09:54.5	+24:18:20	92.47708	24.30556	Mar_2001	F3	J06095453+2418197
7063	06:09:15.7	+24:30:48	92.31542	24.51333	Mar_2001	34022	J06091570+2430486
7064	06:07:28.7	+24:13:40	91.86958	24.22778	Mar_2001	36048	
7065	06:10:00.6	+24:12:34	92.5025	24.20944	Mar_2001	51029	J06100068+2412339
7066	06:08:27.7	+24:33:12	92.11542	24.55333	Mar_2001	55032	
7067	06:09:43.4	+24:24:34	92.43083	24.40944	Mar_2001	29019	
7068	06:08:25.7	+24:38:42	92.10708	24.645	Mar_2001	38042	
7069	06:08:49.2	+24:05:50	92.205	24.09722	Mar_2001	F2	J06084923+2405504
7070	06:10:14.2	+24:25:23	92.55917	24.42306	Mar_2001	32032	J06101420+2425235
7071	06:09:29.2	+24:00:43	92.37167	24.01194	Mar_2001	49041	J06092920+2400423
7072	06:10:02.0	+24:28:29	92.50833	24.47472	Mar_2001	45030	
7073	06:09:47.4	+24:32:20	92.4475	24.53889	Mar_2001	31030	
7074	06:10:10.5	+24:24:14	92.54375	24.40389	Mar_2001	32030	J06101053+2424144
7075	06:09:03.0	+24:34:56	92.2625	24.58222	Mar_2001	52030	J06090307+2434565
7076	06:08:20.8	+24:27:18	92.08667	24.455	Mar_2001	31026	
7077	06:08:01.9	+24:30:18	92.00792	24.505	Mar_2001	36036	
7078	06:08:33.3	+24:05:34	92.13875	24.09278	Mar_2001	71034	J06083329+2405335
7079	06:08:19.8	+24:05:03	92.0825	24.08417	Mar_2001	57038	J06081984+2405023
7080	06:09:11.8	+24:26:16	92.29917	24.43778	Mar_2001	24012	J06091186+2426162
7081	06:10:07.6	+24:36:29	92.53167	24.60806	Mar_2001	86043	
7082	06:07:37.1	+24:14:33	91.90458	24.2425	Mar_2001	35043	J06073713+2414334
7083	06:08:50.4	+24:36:58	92.21	24.61611	Mar_2001	33034	
7084	06:09:31.2	+24:07:03	92.38	24.1175	Mar_2001	38029	J06093123+2407027

Continuation of Table A.1

ID	$\alpha(2000)$ hh:mm:ss	$\delta(2000)$ dd:mm:ss	$\alpha(2000)$ deg	$\delta(2000)$ deg	Campaign	AT18 ID	Je21 ID
7085	06:08:07.9	+24:32:58	92.03292	24.54944	Mar_2001	38037	
7086	06:09:55.7	+24:30:16	92.48208	24.50444	Mar_2001	46030	
7087	06:08:34.4	+24:08:14	92.14333	24.13722	Mar_2001	66029	J06083446+2408140
7088	06:07:30.7	+24:24:29	91.87792	24.40806	Mar_2001	56045	
7089	06:07:37.9	+24:19:09	91.90792	24.31917	Mar_2001	62041	
7090	06:10:14.3	+24:15:24	92.55958	24.25667	Mar_2001	62033	J06101431+2415236
7091	06:07:44.4	+24:30:26	91.935	24.50722	Mar_2001	32043	
7092	06:10:07.8	+24:28:11	92.5325	24.46972	Mar_2001	84032	
7093	06:08:59.5	+24:10:24	92.24792	24.17333	Mar_2001	56021	
7094	06:10:04.7	+24:17:35	92.51958	24.29306	Mar_2001	34027	J06100471+2417347
7095	06:09:34.4	+24:02:53	92.39333	24.04806	Mar_2001	59038	J06093447+2402526
7096	06:07:26.1	+24:26:24	91.85875	24.44	Mar_2001	32048	
7097	06:08:24.7	+24:04:41	92.10292	24.07806	Mar_2001	31038	
7098	06:09:31.3	+24:24:52	92.38042	24.41444	Mar_2001	34014	
7099	06:10:11.1	+24:14:02	92.54625	24.23389	Mar_2001	40032	J06101116+2414016
7100	06:09:54.4	+24:15:05	92.47667	24.25139	Mar_2001	41024	J06095447+2415052
7101	06:08:58.3	+24:37:44	92.24292	24.62889	Mar_2001	50035	
7102	06:07:36.4	+24:28:13	91.90167	24.47028	Mar_2001	43045	J06073642+2428130
7103	06:07:41.9	+24:32:43	91.92458	24.54528	Mar_2001	36047	
7104	06:10:10.3	+24:16:38	92.54292	24.27722	Mar_2001	61030	J06101031+2416384
7105	06:09:20.2	+24:06:21	92.33417	24.10583	Mar_2001	32029	
7106	06:07:30.5	+24:11:26	91.87708	24.19056	Mar_2001	38048	
7107	06:08:57.4	+23:59:36	92.23917	23.99333	Feb_2001	F5	
7107	06:08:57.4	+23:59:36	92.23917	23.99333	Mar_2001	F5	
7108	06:10:25.9	+24:22:24	92.60792	24.37333	Feb_2001	F6	
7108	06:10:25.9	+24:22:24	92.60792	24.37333	Mar_2001	F6	
7109	06:08:55.6	+24:13:49	92.23167	24.23028	Feb_2001	F8	J06085568+2413485
7109	06:08:55.6	+24:13:49	92.23167	24.23028	Mar_2001	F8	J06085568+2413485
7110	06:08:36.0	+24:15:34	92.15	24.25944	Mar_2001	61018	J06083600+2415341
7111			92.1034	23.98861	Nov_2017		J06082482+2359190
7112			92.48857	24.17101	Nov_2017		J06095726+2410157
7113			92.04814	24.12456	Nov_2017		J06081155+2407284
7114			92.39227	24.30253	Nov_2017		J06093414+2418091
7115			92.07397	24.20708	Nov_2017		J06081775+2412255
7116			92.65257	24.2283	Nov_2017		J06103662+2413419
7117			92.22672	24.05225	Nov_2017		J06085441+2403081
7118			92.26049	24.33108	Nov_2017		J06090252+2419519
7119			92.54566	24.32609	Nov_2017		J06101096+2419339
7120			92.12011	24.0422	Nov_2017		J06082883+2402319
7121			92.3306	23.8811	Nov_2017		J06091934+2352520
7122			92.4292	24.4569	Nov_2017		J06094301+2427249
7123			91.90672	23.96363	Nov_2017		J06073761+2357491

Continuation of Table A.1

ID	$\alpha(2000)$ hh:mm:ss	$\delta(2000)$ dd:mm:ss	$\alpha(2000)$ deg	$\delta(2000)$ deg	Campaign	AT18 ID	Je21 ID
7124			92.2602	24.2737	Nov_2017		J06090245+2416253
7125			92.02205	24.17374	Nov_2017		J06080529+2410255
7126			91.85031	24.00613	Nov_2017		J06072407+2400221
7127			92.26279	24.33599	Nov_2017		J06090307+2420096
7128			92.53687	24.30311	Nov_2017		J06100885+2418112
7129			92.47439	24.13714	Nov_2017		J06095385+2408137
7131			92.5756	24.21353	Nov_2017		J06101814+2412487
7132			92.37632	23.9885	Nov_2017		J06093032+2359186
7133			92.13139	24.20272	Nov_2017		J06083153+2412098
7134			92.09569	23.94637	Nov_2017		J06082297+2356469
7135			92.50779	24.09718	Nov_2017		J06100187+2405498
7136			92.25208	24.19996	Nov_2017		J06090050+2411599
7137			91.7909	24.17444	Nov_2017		J06070982+2410280
7138			92.27633	24.28476	Nov_2017		J06090632+2417051
7139			92.0397	24.09726	Nov_2017		J06080953+2405501
7140			92.45873	24.2745	Nov_2017		J06095009+2416282
7141			91.8406	24.10717	Nov_2017		J06072174+2406258
7142			92.0529	24.22798	Nov_2017		J06081269+2413407
7143			91.86508	24.27729	Nov_2017		J06072762+2416383
7144			92.24027	24.06565	Nov_2017		J06085767+2403563
7145			92.24643	24.28733	Nov_2017		J06085914+2417144
7146			92.25356	24.09685	Nov_2017		J06090085+2405487
7147			92.48284	24.27588	Nov_2017		J06095588+2416332
7148			92.51708	24.2151	Nov_2017		J06100410+2412544
7149			92.01683	24.13478	Nov_2017		J06080404+2408052
7150			91.86554	24.10601	Nov_2017		J06072773+2406216
7151			92.59129	24.15151	Nov_2017		J06102191+2409054
7152			92.35348	24.10341	Nov_2017		J06092483+2406123
7153			92.43661	24.09334	Nov_2017		J06094479+2405360
7154			92.48128	24.29488	Nov_2017		J06095551+2417416
7155			92.58132	23.96162	Nov_2017		J06101952+2357418
7156			91.88801	24.36738	Nov_2017		J06073312+2422025
7157			92.47935	24.05935	Nov_2017		J06095504+2403336
7158			92.03756	23.97827	Nov_2017		J06080902+2358418
7159			92.53465	24.57555	Nov_2017		J06100832+2434320
7160			91.88902	24.09746	Nov_2017		J06073336+2405508
7161			91.92192	24.2168	Nov_2017		J06074126+2413005
7162			92.34134	24.59965	Nov_2017		J06092192+2435587
7163			91.85776	24.23577	Nov_2017		J06072586+2414088
7164			92.09017	24.11936	Nov_2017		J06082164+2407097
7165			92.25849	24.04462	Nov_2017		J06090204+2402406
7166			92.50901	24.57702	Nov_2017		J06100216+2434373

Continuation of Table A.1

ID	$\alpha(2000)$ hh:mm:ss	$\delta(2000)$ dd:mm:ss	$\alpha(2000)$ deg	$\delta(2000)$ deg	Campaign	AT18 ID	Je21 ID
7167			92.54872	24.11028	Nov_2017		J06101169+2406370
7168			91.77506	24.19088	Nov_2017		J06070601+2411272
7169			91.97367	24.08165	Nov_2017		J06075368+2404540
7170			92.04996	24.56578	Nov_2017		J06081199+2433568
7171			92.22197	24.47702	Nov_2017		J06085327+2428373
7172			92.42821	23.98807	Nov_2017		J06094277+2359170
7174			91.92543	23.97412	Nov_2017		J06074210+2358268
7175			92.07115	24.54934	Nov_2017		J06081708+2432576
7176			91.84116	24.39089	Nov_2017		J06072188+2423272
7177			92.52979	24.04875	Nov_2017		J06100715+2402555
7178			92.57871	24.48616	Nov_2017		J06101889+2429102
7179			92.05068	24.52207	Nov_2017		J06081216+2431194
7180			91.90614	24.15711	Nov_2017		J06073747+2409256
7181			91.8674	24.28946	Nov_2017		J06072818+2417220
7182			92.16356	24.17919	Nov_2017		J06083925+2410451

Table A.2: Membership class and binary status for the complete sample presented in this work.

ID	RV Class	RV Source	Final Membership Class	Binary Flag
5066	SM	L15	NM?	1
5076	SM	L15	Poss+	0
5078	SM	L15	Poss+	0
5081	SB1	B01	NM	1
5083	U	This Work	NM?	0
5087	SM	L15	Poss+	0
5088	SM	This Work	Poss+	1
5089	U	This Work	NM	0
5094	SM	L15	Poss+	0
5096	MEM	B01	Poss+	0
5097	SM	L15	Poss+	0
5098	MEM	B01	NM	0
5099	SM	L15	Poss+	0
5103	SN	This Work	Poss	0
5107	MEM	B01	Poss+	0
5111	SB	This Work	NM?	1
5112	SM	L15	Poss+	0
5113	SB1	B01	NM	1
5114	SN	This Work	Prob	0
5116	MEM	B01	Prob+	0
5120	SN	This Work	NM-	0
5121	SM	L15	Prob+	0
5125	MEM	B01	CMD_NM	0
5126	NM	B01	NM-	1
5130	SM	L15	Prob+	0
5132	U	This Work	NM	0
5133	SN	This Work	NM-	0
5135	MEM	B01	Poss+	0
5136	U	This Work	NM	0
5138	MEM	B01	NM?	0
5139	SM	This Work	Prob+	0
5140	SM	L15	Prob+	0
5141	NM	B01	NM-	0
5142	NM	B01	NM?-	0
5144	MEM	B01	Prob+	0
5146	SM	L15	Prob+	1
5148	SN	This Work	Poss	0
5151	SB1	B01	NM	1
5152	SM	L15	Poss+	0
5155	SN	L15	Poss	0
5156	SN	This Work	NM?-	0

Continuation of Table A.2

ID	RV Class	RV Source	Final Membership Class	Binary Flag
5158			Poss	1
5159	NM	B01	Poss	0
5162	SM	L15	Poss+	0
5165	MEM	B01	Prob+	0
5167	SN	This Work	NM?-	0
5174	MEM	B01	Poss+	0
5175	SN	L15	NM-	0
5176	MEM	B01	Prob+	0
5178	NM	B01	NM-	0
5180	SM	L15	Prob+	0
5181	SM	L15	Poss+	0
5182	SM	L15	Prob+	0
5183	U	This Work	Poss	0
5184	NM	B01	NM-	0
5186	U	This Work	Poss	1
5190	MEM	B01	NM?	0
5192	NM	B01	NM?-	0
5194	SN	This Work	Poss	1
5195	NM	B01	Poss	0
5198	BN	L15	Poss	1
5200	SN	This Work	NM?-	0
5202	U	This Work	NM	0
5203	SM	L15	NM	0
5205	NM	B01	NM-	0
5206	U	This Work	NM	0
5209	MEM	B01	Poss+	0
5210	SN	This Work	NM-	0
5213	SN	This Work	Prob	0
5215	SN	This Work	Prob	0
5216	NM	B01	NM-	0
5219	NM	B01	CMD_NM	0
5220	SN	This Work	NM?-	0
5221	SM	L15	Poss+	0
5222	SM	L15	Prob+	0
5223	SB	This Work	NM	1
5227	SM	This Work	Prob+	0
5230	U	This Work	Prob	0
5231	NM	B01	NM?-	1
5233	MEM	B01	Poss+	0
5235	MEM	B01	Poss+	0
5236	NM	B01	NM?-	0
5240	SM	L15	Poss+	0
5241	MEM	B01	Prob+	0

Continuation of Table A.2

ID	RV Class	RV Source	Final Membership Class	Binary Flag
5243	U	This Work	NM	0
5246	U	This Work	NM?	1
5257	MEM	B01	Poss+	0
5258	SM	L15	Prob+	0
5259	SM	L15	Prob+	0
5262	SM	L15	Prob+	0
5263	MEM	B01	Prob+	0
5264	NM	B01	NM-	0
5265	SM	L15	NM	0
5267	MEM	B01	Poss+	1
5268	SB	This Work	NM	1
5273	SN	L15	NM-	0
5274	MEM	B01	Prob+	1
5278	SM	L15	Poss+	0
5279	SB	This Work	NM	1
5281	SM	L15	NM	0
5283	SM	This Work	Poss+	0
5288	MEM	B01	Prob+	0
5289	MEM	B01	Prob+	0
5290	SM	L15	Poss+	0
5292	NM	B01	NM-	0
5293	MEM	B01	Poss+	0
5294	NM	B01	Poss	1
5295	SN	This Work	Poss	0
5297	SN	This Work	NM?-	0
5298	SN	L15	NM-	0
5299	NM	B01	Poss	0
5300	SM	L15	Poss+	0
5302	BLN	L15	Poss	1
5303	U	This Work	NM?	0
5304	U	This Work	NM	0
5305	NM	B01	NM-	0
5307	SM	L15	Prob+	1
5308	SM	L15	Prob+	0
5309	NM	B01	NM?-	0
5312	SN	This Work	NM?-	0
5314	NM	B01	NM?-	0
5316	SB	This Work	Poss	1
5317	MEM	B01	NM?	0
5318	U	This Work	CMD_NM	0
5323	SB	This Work	Prob	1
5326	SN	This Work	NM-	0
5327			Prob	0

Continuation of Table A.2

ID	RV Class	RV Source	Final Membership Class	Binary Flag
5332	MEM	B01	Poss+	0
5336			Poss	0
5337	SM	This Work	Prob+	0
5338	SN	This Work	NM-	1
5339	MEM	B01	Prob+	0
5344	SB	This Work	NM	1
5345	MEM	B01	Prob+	0
5347	NM	B01	Poss	0
5350	SB2	B01	NM?	1
5356	SB	This Work	Prob	1
5357	MEM	B01	Poss+	0
5359	SB	This Work	NM	1
5361	SN	This Work	Prob	0
5362	SB	This Work	NM	1
5366	SM	This Work	NM?	1
5368	SN	This Work	Prob	0
5369	SM	This Work	Prob+	0
5370			Prob	0
5373	U	This Work	CMD_NM	0
5376	MEM	B01	NM	0
5378			NM	1
5381	SB	This Work	NM?	1
5382			Prob	0
5384	NM	B01	NM-	0
5386	U	This Work	Prob	0
5387	SB	This Work	Prob	1
5388	MEM	B01	Prob+	0
5393	U	This Work	Prob	0
5394	U	This Work	NM?	1
5395	U	This Work	NM?	0
5398	SB	This Work	NM	1
5399	SB	This Work	Poss	1
5400	SM	This Work	Poss+	0
5401	SM	This Work	CMD_NM	0
5402	U	This Work	Prob	0
5405	U	This Work	Prob	0
5407	U	This Work	CMD_NM	0
5408	MEM	B01	Poss+	0
5409	SB	This Work	Poss	1
5410	MEM	B01	Poss+	0
5411	NM	B01	Prob	0
5413	U	This Work	Prob	0
5415	U	This Work	NM?	0

Continuation of Table A.2

ID	RV Class	RV Source	Final Membership Class	Binary Flag
5418	SM	This Work	Prob+	0
5419	MEM	B01	Poss+	0
5421	SB	This Work	NM	1
5426	SB	This Work	NM?	1
5428	U	This Work	Prob	0
5429			Prob	0
5431	SB	This Work	CMD_NM	1
5432	NM	B01	NM?-	0
5434	SB	This Work	CMD_NM	1
5436	U	This Work	Prob	0
5437	SB	This Work	Prob	1
5438	SM	This Work	Prob+	0
5440	SB	This Work	Prob	1
5442			NM	0
5445	SM	This Work	Prob+	0
5446	SN	This Work	Prob	0
5447	SB	This Work	Poss	1
5449	U	This Work	Prob	0
5450	SM	This Work	Prob+	0
5452	SB	This Work	NM?	1
5454	SB	This Work	NM?	1
5455	SM	This Work	Prob+	0
5456	U	This Work	Poss	0
5458	SM	This Work	Prob+	0
5459	SN	This Work	Poss	0
5462	SM	This Work	Prob+	0
5463			Prob	0
5472			Prob	0
5476	SB	This Work	Prob	1
5477			NM	0
5479	SN	This Work	Poss	0
5481	U	This Work	Prob	0
5482	U	This Work	Prob	1
5483			Poss	0
5489	U	This Work	Poss	0
5493			Poss	0
5494	U	This Work	Poss	0
5495	SB	This Work	NM?	1
5497	SB	This Work	NM	1
5502	SN	This Work	Prob	0
5504	SN	This Work	NM-	0
5506	U	This Work	Prob	0
5508	SB	This Work	Poss	1

Continuation of Table A.2

ID	RV Class	RV Source	Final Membership Class	Binary Flag
5516	SB	This Work	NM?	1
5517	SB	This Work	Prob	1
7000	SN	This Work	Prob	0
7001	SM	This Work	Prob+	0
7002	SM	This Work	Prob+	0
7003	U	This Work	Poss	0
7004	SM	This Work	Prob+	0
7005	SM	This Work	Prob+	0
7006	SM	This Work	Prob+	0
7007	SN	This Work	Poss	0
7008	SB	This Work	Poss	1
7009	U	This Work	Poss	0
7010	U	This Work	Prob	0
7011	SM	This Work	Poss+	0
7012	SN	This Work	Prob	0
7013	SN	This Work	Poss	0
7014	SM	This Work	Prob+	0
7015	SN	This Work	Prob	0
7016	SM	This Work	Poss+	0
7017	SM	This Work	Poss+	0
7018	SM	This Work	Prob+	0
7019	SM	This Work	Prob+	0
7020	SN	This Work	Poss	0
7021	SN	This Work	Poss	0
7022	SM	This Work	Poss+	0
7023	SN	This Work	Poss	0
7024	SN	This Work	NM-	0
7025	U	This Work	Poss	0
7026	SM	This Work	Poss+	0
7027	U	This Work	CMD_NM	0
7028	SN	This Work	Poss	0
7029	SB	This Work	Prob	1
7030	SM	This Work	Prob+	0
7031	SN	This Work	Prob	0
7032	SN	This Work	Poss	0
7033	SN	This Work	NM-	0
7034	SN	This Work	Prob	0
7035	SM	This Work	Prob+	0
7036	SM	This Work	Prob+	0
7037	SN	This Work	Prob	0
7038	SN	This Work	Poss	0
7039	SB	This Work	Prob	1
7040	SN	This Work	Prob	0

Continuation of Table A.2

ID	RV Class	RV Source	Final Membership Class	Binary Flag
7041	U	This Work	Poss	0
7042	SN	This Work	Poss	0
7043	SB	This Work	CMD_NM	1
7044	SM	This Work	Poss+	0
7045	SB	This Work	CMD_NM	1
7046	SN	This Work	Prob	0
7047	SN	This Work	Prob	0
7048	SN	This Work	Poss	0
7049	SN	This Work	Poss	0
7050	SM	This Work	Prob+	0
7051	SN	This Work	Prob	0
7052	SM	This Work	Poss+	0
7053	SM	This Work	Prob+	0
7054	SM	This Work	Prob+	0
7055	SB	This Work	Prob	1
7056	SN	This Work	Poss	0
7057	SN	This Work	Prob	0
7058	SM	L15	NM	0
7059	SM	L15	Poss+	0
7060	SM	L15	NM	0
7061	SM	L15	NM	0
7062			Prob	0
7063	SM	L15	Poss+	0
7064	SM	L15	Poss+	0
7065	SM	L15	NM	0
7066	SM	L15	NM	0
7067	SM	L15	Poss+	0
7068	SM	L15	Poss+	0
7069			Poss	0
7070	SM	L15	Poss+	0
7071	SM	L15	Poss+	0
7072	SM	L15	Poss+	0
7073	SM	L15	Prob+	0
7074	SM	L15	Prob+	0
7075	SM	L15	Poss+	0
7076	SM	L15	Poss+	0
7077	SM	L15	Poss+	0
7078	SM	L15	Poss+	0
7079	SM	L15	Prob+	0
7080	SM	L15	Poss+	0
7081	SM	L15	NM?	0
7082	SM	L15	Prob+	0
7083	SM	L15	NM	1

Continuation of Table A.2

ID	RV Class	RV Source	Final Membership Class	Binary Flag
7084	SM	L15	Prob+	0
7085	SM	L15	Poss+	0
7086	SM	L15	Prob+	0
7087	SM	L15	Prob+	0
7088	SM	L15	Prob+	0
7089	SM	L15	Prob+	0
7090	SM	L15	Poss+	0
7091	BM	L15	NM?	1
7092	SM	L15	Prob+	0
7093	SM	L15	NM	0
7094	SM	L15	Prob+	0
7095	SM	L15	Prob+	0
7096	SM	L15	NM?	1
7097	SM	L15	Poss+	0
7098	SM	L15	Poss+	0
7099	SM	L15	Prob+	0
7100	SM	L15	Prob+	1
7101	SM	L15	Prob+	0
7102	SM	L15	Prob+	0
7103	SM	L15	Prob+	0
7104	SM	L15	Prob+	0
7105	SM	L15	NM	0
7106	SM	L15	Prob+	0
7107	U	This Work	Poss	0
7108	SN	This Work	Prob	0
7109	U	This Work	CMD_NM	0
7110	SM	L15	Poss+	0
7111			Prob	0
7112	BLM	L15	Poss	1
7113	SN	L15	Poss	0
7114	SM	L15	Poss+	0
7115	SM	L15	Poss+	1
7116	SN	L15	Poss	0
7117	BM	L15	Prob	1
7118	BM	L15	Poss	1
7119			Prob	0
7120			Poss	1
7121			Prob	0
7122			Poss	1
7123			Poss	0
7124	SN	L15	Poss	0
7125			Poss	0
7126			Poss	1

Continuation of Table A.2

ID	RV Class	RV Source	Final Membership Class	Binary Flag
7127	BM	L15	Poss	1
7128			Poss	0
7129	BLN	L15	Poss	1
7131	SN	L15	Poss	0
7132			Poss	1
7133	SN	L15	Poss	0
7134	SN	L15	Poss	0
7135			Poss	1
7136	SM	L15	Poss+	1
7137			Poss	0
7138			Poss	1
7139	SN	L15	NM-	0
7140			NM?	1
7141			NM	0
7142	SM	L15	NM	0
7143	SN	L15	NM-	0
7144	SN	L15	NM?-	0
7145			NM	0
7146	SN	L15	NM-	0
7147			Poss	0
7148	SN	L15	NM-	0
7149			CMD_NM	0
7150			CMD_NM	0
7151			NM	0
7152			NM	0
7153			NM	0
7154			NM	0
7155			NM	0
7156	SN	L15	NM?-	1
7157			NM?	1
7158	SN	L15	NM-	0
7159	SM	L15	NM	0
7160	U	L15	NM	0
7161	SN	L15	NM?-	1
7162	SM	L15	NM?	1
7163	SN	L15	CMD_NM	0
7164			NM	0
7165			NM?	1
7166			NM	0
7167	SN	L15	NM-	0
7168			NM	0
7169	SN	L15	NM?-	1
7170	BLN	L15	NM	1

Continuation of Table A.2

ID	RV Class	RV Source	Final Membership Class	Binary Flag
7171			NM	0
7172			NM	0
7174			NM	0
7175	SN	L15	CMD_NM	0
7176			NM?	1
7177			NM	0
7178			NM	0
7179	BU	L15	NM	1
7180	BLN	L15	NM	1
7181			NM	0
7182	SN	L15	NM-	0

Table A.3: Rotation periods taken from the literature or derived from ZTF light curves for 197 M35 members.

ID	Prot (d) M09	Prot (d) SF20	Class SF20	Subclass SF20	Blend SF20	Prot (d) L16	Flag L16	Prot (d) N15	Type N15	Prot (d) ZTF	Final Prot (d)
5087		2.2	Rotating	RotVar	0	-99.0	1				2.2
5094						2.34	1				2.34
5096		3.6	Rotating	RotVar	0					3.62	3.62
5097		2.03	Rotating	RotVar	0	2.04	1				2.03
5103										2.65	2.65
5107		2.48	Rotating	RotVar	0	2.5	1	2.41	Rot	2.51	2.51
5114		3.11	Rotating	RotVar	0						3.11
5116						2.38	1	2.37	Rot		2.38
5121		3.3	Rotating	RotVar	0	3.28	31	3.19	Rot		3.3
5130		2.73	Rotating	RotVar	0	-99.0	1	2.61	Rot	2.64	2.64
5135	4.33	4.17	Rotating	RotVar	0	4.22	1	4.25	Rot	4.31	4.31
5139		3.86	Rotating	RotVar	0	3.78	1	65.26	Long-Period		3.86
5140	3.56	3.44	Rotating	RotVar	0	3.51	1	3.44	Rot	3.45	3.45
5144		2.73	Rotating	RotVar	0			6.13	Unknown		2.73
5146	3.99	3.96	Rotating	RotVar	1	-99.0	31	3.98	Rot		3.99
5148	3.56	3.3	Rotating	RotVar	0						3.56
5152	4.33	4.28	Rotating	RotVar	1						4.33
5158		5.66	Rotating	RotVar	1	-99.0	0	4.54	Rot		4.54
5162						-99.0	1	10.07	Rot	10.09	10.09
5165	6.14	5.46	Rotating	RotVar	1			5.97	Rot		6.14
5174	3.96									3.95	3.95
5176	4.74	4.8	Rotating	RotVar	1	4.83	31	4.98	Rot		4.74
5180	4.83	4.95	Rotating	RotVar	0	4.78	1	4.87	Rot		4.83
5181	1.27	1.27	Rotating	RotVar	1	-99.0	0	1.27	Rot		1.27
5182		4.8	Rotating	RotVar	0	4.68	2				4.8
5183	4.61							4.37	Rot	4.4	4.4
5186	5.41	5.28	Rotating	RotVar	0	5.25	1	4.31	Rot	5.01	5.01
5194	4.7					4.66	31				4.7
5198	4.65	4.95	Rotating	RotVar	0	4.69	1				4.65
5209	5.72	5.87	Rotating	RotVar	0					5.76	5.76
5213		4.28	Misc	Misc	0	4.45	1	275.32	Unknown		4.28
5215	5.47	5.46	Rotating	RotVar	0	5.47	1	4.5	Rot		5.47
5221	5.72					6.03	1				5.72
5222						5.36	1			5.4	5.4
5227	5.53	5.66	Rotating	RotVar	0	5.77	1				5.53
5230	4.41	4.17	Rotating	RotVar	0	4.17	1	4.12	Rot		4.41
5233	5.78	5.46	Rotating	RotVar	1	5.74	31	5.84	Rot		5.78
5235	5.78	0.86	Rotating	RotVar	1	-99.0	0	34.97	Long-Period		5.78
5241	5.65	5.66	Rotating	RotVar	0			5.69	Rot		5.65
5257		0.04	Misc	Misc	1			5.71	Rot		5.71

Continuation of Table A.3

ID	Prot (d) M09	Prot (d) SF20	Class SF20	Subclass SF20	Blend SF20	Prot (d) L16	Flag L16	Prot (d) N15	Type N15	Prot (d) ZTF	Final Prot (d)
5258		6.34	Rotating	RotVar	0	6.33	1	6.54	Rot		6.34
5259	6.14					6.41	1	5.94	Rot		6.14
5262	6.45	6.09	Rotating	RotVar	0	-99.0	0	5.87	Rot	6.42	6.42
5263	6.45	6.09	Rotating	RotVar	0			5.96	Rot		6.45
5267		6.34	Rotating	RotVar	0	6.41	1				6.34
5274	6.54							6.53	Rot	6.51	6.51
5278						6.33	1				6.33
5283	3.75							3.73	Rot	3.73	3.73
5288		6.34	Rotating	RotVar	0					6.39	6.39
5289	6.29										6.29
5290		0.42	Rotating	RotVar	0	0.42	1	0.42	Rot		0.42
5293	6.62	6.34	Rotating	RotVar	0	6.63	1				6.62
5302						16.27	1				16.27
5307		3.6	Rotating	RotVar	0						3.6
5308						6.69	1				6.69
5316	7.0	6.89	Rotating	RotVar	0	6.62	1				7.0
5323	7.3					7.26	31				7.3
5327						6.35	1				6.35
5332		5.66	Rotating	RotVar	0	7.64	1				5.66
5336	15.37					15.31	1				15.37
5337	5.99	6.89	Rotating	RotVar	0	7.41	1				5.99
5347		9.9	Rotating	RotVar	0						9.9
5356										7.01	7.01
5357						8.12	1				8.12
5368	7.52					7.26	1	7.5	Rot		7.52
5369	6.9					6.99	1	7.06	Rot		6.9
5370	4.57										4.57
5382	3.08					3.04	1	3.04	Rot		3.08
5388	8.0										8.0
5393	5.78	5.66	Rotating	RotVar	0	2.8	31	5.34	Rot		5.78
5399						8.34	1				8.34
5400	8.85					9.07	1				8.85
5405	5.92					5.82	1	62.04	Rot		5.92
5408	0.74							1.48	EB		0.74
5409	5.78					-99.0	0	3.15	Rot		5.78
5411	0.36					0.18	1	0.36	Rot		0.36
5413	0.73					0.73	1	0.73	EB		0.73
5418						9.16	1				9.16
5428		10.56	Rotating	RotVar	0						10.56
5429						0.48	2				0.48
5436						7.51	1				7.51
5437						8.32	1				8.32

Continuation of Table A.3

ID	Prot (d) M09	Prot (d) SF20	Class SF20	Subclass SF20	Blend SF20	Prot (d) L16	Flag L16	Prot (d) N15	Type N15	Prot (d) ZTF	Final Prot (d)
5438						4.66	31	4.59	Rot	4.61	4.61
5440	0.46					-99.0	0	0.46	Rot		0.46
5445	7.41					-99.0	1				7.41
5446	5.53					5.57	31				5.53
5447	9.35										9.35
5450						9.16	1				9.16
5455								5.93	Rot		5.93
5458						10.58	2				10.58
5459	7.3					7.19	1				7.3
5462	8.0					7.61	1	7.4	Rot		8.0
5463						11.03	1				11.03
5472						9.68	1				9.68
5476	8.7					9.57	1				8.7
5481	5.18							5.11	Rot		5.18
5482	0.62							0.62	Rot		0.62
5483						0.48	1	0.48	Rot	0.48	0.48
5489	0.24										0.24
5493	0.24					0.47	1	0.47	Rot		0.24
5494						6.29	2				6.29
5506								0.59	Rot		0.59
5508						3.06	1	3.05	Rot		3.06
5517						1.06	1				1.06
7000	8.4	6.89	Rotating	RotVar	0	7.2	1				8.4
7001	7.75					7.98	1				7.75
7002		7.55	Rotating	RotVar	0	7.39	1	7.54	Rot		7.55
7004	6.62	6.6	Rotating	RotVar	0	6.59	1				6.62
7006	8.7					8.83	1				8.7
7010	0.72					-99.0	0	0.72	Rot		0.72
7011						8.08	2			8.01	8.01
7012		6.89	Rotating	RotVar	1	6.97	1			6.8	6.8
7013						8.74	1				8.74
7014	6.54										6.54
7015						8.56	1			8.67	8.67
7017	8.55					8.87	31				8.55
7018	9.71										9.71
7019	8.13										8.13
7022										9.32	9.32
7023	4.79					4.77	1	4.6	Rot		4.79
7025	6.54										6.54
7030	7.88	7.92	Rotating	RotVar	0	3.91	1				7.88
7031	0.91					0.92	1	0.92	Rot		0.91
7032	8.85					8.96	31				8.85

Continuation of Table A.3

ID	Prot (d) M09	Prot (d) SF20	Class SF20	Subclass SF20	Blend SF20	Prot (d) L16	Flag L16	Prot (d) N15	Type N15	Prot (d) ZTF	Final Prot (d)
7034	9.71					-99.0	0	58.73	Long-Period		9.71
7036										7.99	7.99
7042	8.0	7.92	Rotating	RotVar	0	-99.0	0				8.0
7047		4.17	Rotating	RotVar	0	4.14	1				4.17
7049	1.86					1.86	1	1.87	Rot		1.86
7050	7.3	6.89	Rotating	RotVar	0						7.3
7051						7.05	31	7.09	Rot		7.05
7053	1.41										1.41
7055	0.95					-99.0	0	56.83	Long-Period		0.95
7057						9.07	1				9.07
7059						6.46	2				6.46
7062	0.93	0.93	Rotating	RotVar	0	0.93	31	0.93	Rot		0.93
7063		3.96	Rotating	RotVar	0	3.88	1	3.99	Rot		3.96
7064		2.52	Rotating	RotVar	0	-99.0	0	2.5	Rot		2.52
7067	5.47	4.95	Rotating	RotVar	0	4.94	31	4.89	Rot	5.33	5.33
7068										3.32	3.32
7069	8.0					8.21	1	9.26	Rot		8.0
7070	2.74	2.64	Rotating	RotVar	0	2.62	1	2.61	Rot	2.59	2.59
7071	3.72	3.86	Rotating	RotVar	0	3.77	1	3.82	Rot	3.75	3.75
7072										5.22	5.22
7073	3.69	3.77	Rotating	RotVar	1	1.83	1			3.69	3.69
7074	4.26					0.41	31			4.24	4.24
7075	6.9	5.87	Rotating	RotVar	0						6.9
7076		2.44	Rotating	RotVar	0						2.44
7077		3.11	Rotating	RotVar	0	3.12	1	3.19	Rot	3.2	3.2
7078	5.92	5.87	Rotating	RotVar	0	6.02	31	5.95	Rot	5.97	5.97
7079	1.14	1.13	Rotating	RotVar	0	1.13	1	1.14	Rot	1.14	1.14
7080	4.93	4.4	Rotating	RotVar	1	4.57	1				4.93
7082		3.86	Rotating	RotVar	0	3.76	1	3.73	Rot		3.86
7084	4.45	4.28	Rotating	RotVar	0	4.35	1	7.88	EB		4.45
7085	3.96									3.97	3.97
7086		5.46	Rotating	RotVar	0	5.53	1				5.46
7087	6.54	6.34	Rotating	RotVar	0	6.51	1			7.14	7.14
7088						4.58	1			4.63	4.63
7089		2.3	Misc	Misc	1	-99.0	1	2.14	Rot		2.14
7090	1.01	1.0	Rotating	RotVar	0	1.0	1	1.01	Unknown		1.01
7092	6.54	6.34	Rotating	RotVar	0	3.19	1	6.57	Rot		6.54
7094	4.83	5.28	Rotating	RotVar	0	5.14	1				4.83
7095	5.85					5.71	31			5.69	5.69
7097	2.85	2.88	Rotating	RotVar	0	2.86	1	2.87	Rot	2.86	2.86
7098		4.17	Rotating	RotVar	0						4.17
7099	3.44	3.44	Rotating	RotVar	0	3.47	1	3.46	Rot		3.44

Continuation of Table A.3

ID	Prot (d) M09	Prot (d) SF20	Class SF20	Subclass SF20	Blend SF20	Prot (d) L16	Flag L16	Prot (d) N15	Type N15	Prot (d) ZTF	Final Prot (d)
7100						6.16	1	5.99	Rot		6.16
7101										5.22	5.22
7102						3.25	2				3.25
7104						6.19	1				6.19
7106		2.99	Rotating	RotVar	0	3.0	1				2.99
7107	5.59	5.87	Rotating	RotVar	0	5.83	1				5.59
7110		6.6	Rotating	RotVar	0	6.65	1				6.6
7111						0.75	1	0.75	Rot	0.75	0.75
7112	4.37	4.28	Rotating	RotVar	0	4.43	31	4.35	Rot		4.37
7114	4.45	4.28	Rotating	RotVar	0	4.36	1				4.45
7115	1.11	0.46	Rotating	RotVar	0	0.46	1	0.46	Rot		1.11
7116						8.06	1				8.06
7117	6.03	6.09	Rotating	RotVar	0	6.06	1	4.55	Rot	5.86	5.86
7118	1.1	1.11	Rotating	RotVar	0	1.11	1	1.1	Rot	1.11	1.11
7119	9.35					8.62	1				9.35
7120		2.77	EB	EB	0	2.74	1			2.76	2.76
7121										0.93	0.93
7122	0.37					0.37	31	0.37	Rot		0.37
7124	7.75					0.88	31	3.96	Rot		7.75
7125						3.46	1	3.46	EB		3.46
7126										6.17	6.17
7127	2.48	2.6	Rotating	RotVar	0	2.59	1	62.04	Unknown		2.48
7131						9.81	1				9.81
7132						0.58	1				0.58
7133		3.44	Rotating	RotVar	0	3.56	1				3.44
7134						22.54	1				22.54
7135	0.16	0.32	EB	EB	0	0.16	1	0.32	EB	0.16	0.16
7136	0.56	0.56	Rotating	RotVar	0	0.56	31				0.56
7137						4.75	1				4.75
7138	6.45					6.83	1				6.45
7147		1.96	Rotating	RotVar	0	2.05	1	0.66	Rot		1.96

Table A.4: Photometry uploaded to VOSA for the 251 members of M35 in our sample.

ID	V	Ic	g	r	i	z	J	H	Ks
5076	14.514	13.597	14.9±0.05	14.29±0.03	14.06±0.11	13.94±0.03	13.0±0.02	12.71±0.02	12.59±0.02
5078	14.593	13.67		14.53±0.13	14.13±0.03	13.99±0.03	13.02±0.03	12.6±0.03	12.53±0.03
5087	14.652	13.743	15.07±0.05	14.58±0.13	14.15±0.11	14.08±0.03	13.15±0.02	12.82±0.02	12.68±0.02
5088	14.733	13.758	15.17±0.05	14.51±0.03	14.22±0.11	14.08±0.03	13.06±0.03	12.75±0.03	12.63±0.03
5094	14.737	13.785	15.16±0.05			14.14±0.03	13.18±0.02	12.78±0.02	12.75±0.02
5096	14.667	13.791		14.62±0.13	14.24±0.11	14.13±0.08	13.18±0.02	12.86±0.02	12.74±0.02
5097	14.686	13.792		14.44±0.03	14.25±0.11	14.11±0.03	13.18±0.02	12.85±0.02	12.74±0.02
5099	14.78	13.838	15.2±0.05	14.56±0.03	14.27±0.11	14.16±0.03	13.18±0.02	12.84±0.02	12.76±0.03
5103	14.737	13.856				15.38±0.08			
5107	14.812	13.885	15.25±0.05	14.56±0.03	14.3±0.11	14.2±0.03	13.27±0.02	12.93±0.02	12.81±0.02
5112	14.827	13.914	15.26±0.05	14.61±0.03	14.34±0.11	14.22±0.03	13.26±0.03	12.96±0.04	12.84±0.03
5114	14.888	13.932	15.32±0.05	14.67±0.03	14.42±0.11	14.28±0.03	13.3±0.02	12.97±0.02	12.87±0.03
5116	14.863	13.937	15.25±0.05	14.64±0.03	14.39±0.11	14.3±0.03	13.35±0.02	12.98±0.02	12.91±0.03
5121	14.925	13.971	15.34±0.05	14.7±0.03	14.44±0.11	14.3±0.03	13.32±0.03	12.95±0.02	12.89±0.04
5130	15.008	14.095	15.37±0.03	14.77±0.03	14.46±0.11	14.38±0.08	13.45±0.02	13.06±0.02	12.98±0.03
5135	15.126	14.148		14.9±0.03	14.62±0.03	14.46±0.03	13.51±0.02	13.14±0.03	13.03±0.02
5139	15.244	14.205	15.73±0.05	15.02±0.03	14.73±0.11	14.54±0.03	13.53±0.02	13.13±0.03	13.03±0.03
5140	15.129	14.207		14.89±0.03	14.66±0.03	14.53±0.03	13.54±0.02	13.2±0.03	13.14±0.03
5144	15.267	14.243	15.72±0.05	14.96±0.03	14.69±0.03	14.53±0.03	13.56±0.02	13.17±0.03	13.04±0.03
5146	15.293	14.25	15.78±0.05	15.04±0.05	14.78±0.11	14.59±0.03	13.58±0.03	13.22±0.03	13.08±0.03
5148	15.245	14.259	15.81±0.03	15.13±0.03	14.84±0.03	14.71±0.03	13.65±0.02	13.25±0.03	13.16±0.02
5152	15.302	14.348	15.72±0.05	15.02±0.05	14.78±0.03	14.64±0.03	13.69±0.02	13.33±0.03	13.22±0.03
5155	15.477	14.354	15.9±0.05	15.11±0.05	14.84±0.03	14.65±0.03	13.63±0.03	13.21±0.03	13.1±0.03
5158	15.389	14.403	15.8±0.03	15.16±0.03	14.84±0.03	14.67±0.03	13.68±0.02	13.3±0.02	13.17±0.03
5159	15.51	14.417	15.98±0.05	15.17±0.05	14.9±0.11	14.72±0.03	13.7±0.02	13.26±0.02	13.19±0.03
5162	15.388	14.422	15.81±0.03	15.15±0.03	14.88±0.03	14.72±0.03	13.77±0.02	13.31±0.03	13.24±0.03
5165	15.466	14.444	15.92±0.05	15.17±0.05	14.9±0.03	14.74±0.03	13.74±0.03	13.39±0.02	13.3±0.03
5174	15.47	14.497		15.16±0.03	14.91±0.03	14.82±0.08	13.78±0.02	13.4±0.03	13.25±0.03
5176	15.509	14.5		15.22±0.03	14.94±0.03	14.79±0.03	13.84±0.04	13.42±0.04	13.31±0.04
5180	15.565	14.525	16.1±0.05	15.24±0.05	15.01±0.03	14.84±0.03	13.87±0.02	13.44±0.02	13.32±0.03
5181	15.636	14.532		15.71±0.13	15.05±0.11	14.84±0.03	13.77±0.04	13.28±0.03	13.17±0.03
5182	15.524	14.532	15.99±0.05	15.21±0.05	14.96±0.03	14.82±0.03	13.86±0.02	13.43±0.02	13.37±0.03
5183	15.591	14.54		15.67±0.13	14.91±0.11	14.76±0.08			
5186	15.576	14.55		15.28±0.03	14.96±0.03	14.78±0.03	13.84±0.02	13.33±0.03	13.19±0.03
5194	15.756	14.607	16.29±0.05	15.4±0.05	15.1±0.03	14.88±0.03	13.76±0.03	13.27±0.03	13.18±0.03
5195	15.738	14.632	16.25±0.05	15.41±0.05	15.12±0.03	14.9±0.03	13.83±0.02	13.48±0.02	13.36±0.03
5198	15.786	14.649		15.48±0.03	15.15±0.03	14.96±0.08	13.93±0.03	13.45±0.03	13.33±0.03
5209	15.737	14.709		15.46±0.03	15.17±0.03	15.02±0.03	14.0±0.06	13.62±0.03	13.52±0.03
5213	15.821	14.719	16.21±0.05	15.46±0.05	15.2±0.03	14.98±0.031			
5215	15.803	14.721	16.27±0.05	15.44±0.05	15.21±0.03	15.02±0.031	14.0±0.03	13.56±0.03	13.44±0.03
5221	15.826	14.766	16.36±0.05	15.55±0.03	15.2±0.03	15.08±0.03	14.01±0.06	13.62±0.02	13.46±0.03

Continuation of Table A.4

ID	V	Ic	g	r	i	z	J	H	Ks
5222	15.867	14.769	16.4±0.05	15.56±0.05	15.27±0.03	15.08±0.03	14.02±0.02	13.57±0.02	13.49±0.03
5227	15.895	14.793		15.78±0.13	15.25±0.11	15.12±0.08	14.04±0.02	13.57±0.03	13.54±0.03
5230	15.852	14.8		15.48±0.03	15.16±0.03	14.98±0.03	14.02±0.02	13.49±0.02	13.38±0.03
5233	15.928	14.811		15.81±0.13	15.33±0.11	15.19±0.08			
5235	15.963	14.816			15.28±0.03	15.1±0.03			
5240	15.949	14.832	16.45±0.05	15.59±0.05	15.27±0.03	15.1±0.03	14.03±0.06	13.65±0.03	13.57±0.03
5241	15.931	14.832	16.46±0.05	15.59±0.05	15.3±0.03	15.12±0.03	14.03±0.06	13.62±0.03	13.57±0.03
5257	15.997	14.916	16.56±0.05	15.68±0.05	15.35±0.031	15.17±0.03	14.08±0.06	13.62±0.03	13.5±0.03
5258	15.994	14.929		15.68±0.05	15.41±0.03	15.25±0.03	14.2±0.06	13.75±0.03	13.62±0.03
5259	16.041	14.929	16.58±0.05	15.7±0.05	15.43±0.03	15.26±0.03	14.18±0.06	13.7±0.03	13.65±0.03
5262	16.07	14.952	16.59±0.05	15.72±0.05	15.44±0.03	15.24±0.03	14.18±0.06	13.74±0.03	13.62±0.03
5263	16.071	14.959	16.6±0.05	15.76±0.03	15.43±0.03	15.24±0.03	14.18±0.06	13.7±0.03	13.59±0.04
5267	16.108	14.968	16.61±0.05	15.76±0.05	15.48±0.11	15.29±0.031	14.17±0.06	13.69±NaN	13.61±0.04
5274	16.141	15.007	16.69±0.03	15.82±0.03	15.49±0.03	15.3±0.03	14.18±0.06	13.72±0.03	13.61±0.03
5278	16.169	15.045	16.73±0.05	15.83±0.05	15.52±0.031	15.23±0.031	14.24±0.06	13.8±0.03	13.63±0.04
5283	16.29	15.079	17.02±0.03	16.1±0.03	15.64±0.11	15.47±0.03	14.27±0.06	13.75±0.03	13.58±0.03
5288	16.255	15.111	16.8±0.03	15.93±0.03	15.55±0.03	15.36±0.03	14.23±0.06	13.85±0.03	13.71±0.03
5289	16.236	15.115	16.84±0.05	15.94±0.03	15.58±0.03	15.37±0.03	14.27±0.06	13.8±0.03	13.73±0.03
5290	16.44	15.123		16.2±0.03	15.74±0.03	15.42±0.03	14.17±0.06	13.58±0.03	13.48±0.03
5293	16.341	15.144	16.93±0.05	15.96±0.05	15.66±0.03	15.44±0.031	14.29±0.06	13.8±0.03	13.71±0.03
5294	16.308	15.145	16.8±0.05	15.95±0.05	15.58±0.033	15.35±0.031	14.19±0.06	13.84±0.03	13.74±0.04
5295	16.284	15.146	16.83±0.05	15.88±0.05	15.57±0.03	15.37±0.03	14.28±0.06	13.82±0.03	13.64±0.03
5299	16.424	15.183	17.03±0.05	16.02±0.05	15.68±0.03	15.44±0.03	14.29±0.06	13.74±0.03	13.64±0.04
5300	16.486	15.189	17.04±0.05	16.07±0.05	15.69±0.03	15.43±0.03	14.25±0.06	13.79±0.03	13.6±0.03
5302	16.452	15.206	17.07±0.05	16.02±0.05	15.64±0.03	15.41±0.03	14.25±0.06	13.75±0.03	13.6±0.03
5307	16.428	15.227	16.96±0.05	16.04±0.05	15.67±0.03	15.43±0.03	14.31±0.06	13.83±0.03	13.65±0.03
5308	16.408	15.231	16.94±0.05	16.0±0.05	15.69±0.11	15.47±0.031	14.42±0.06	13.96±0.04	13.74±0.04
5316	16.45	15.286		16.11±0.03	15.75±0.03	15.54±0.03	14.47±0.06	13.9±0.03	13.82±0.04
5323	16.535	15.343		16.17±0.03	15.82±0.03	15.6±0.08	14.48±0.06	14.0±0.04	13.86±0.04
5327	16.555	15.356		16.17±0.03	15.81±0.03	15.58±0.03	14.44±0.06	13.99±0.04	13.83±0.04
5332	16.694	15.428		16.37±0.03	15.95±0.03		14.48±0.06	14.03±0.06	13.8±0.04
5336	16.665	15.44		16.3±0.03	15.87±0.03	15.62±0.03	14.45±0.06	13.93±0.04	13.83±0.04
5337	16.639	15.442		16.46±0.13	15.85±0.03	15.6±0.03	14.53±0.03	13.96±0.03	13.91±0.04
5339	16.726	15.476	17.33±0.05	16.33±0.05	15.98±0.03	15.76±0.03	14.56±0.06	14.07±0.06	13.96±0.05
5345	16.893	15.514	17.5±0.05	16.78±0.131	16.1±0.11	15.75±0.031	14.55±0.06	13.88±0.03	13.76±0.04
5347	16.717	15.516	17.31±0.03	16.38±0.03	15.99±0.03	15.76±0.031	14.65±0.06	14.19±0.06	14.07±0.07
5356	16.855	15.549		16.41±0.03	15.98±0.03	15.73±0.03	14.6±0.06	14.08±0.06	13.91±0.04
5357	16.806	15.549		16.39±0.03	15.98±0.03	15.75±0.03	14.57±0.06	14.06±0.06	13.94±0.04
5361	16.9	15.564	17.5±0.03	16.49±0.03	16.03±0.03	15.8±0.03	14.56±0.06	14.06±0.06	13.9±0.04
5368	16.881	15.608	17.48±0.03	16.44±0.05	16.05±0.03	15.83±0.03	14.66±0.06	14.19±0.06	14.05±0.07
5369	17.041	15.614		16.61±0.03	16.18±0.03	15.9±0.031	14.71±0.06	14.15±0.06	14.04±0.07
5370	16.916	15.615		16.7±0.13	16.05±0.036	15.91±0.08	14.57±0.06	14.04±0.06	13.92±0.05
5382	17.136	15.661		16.51±0.032	16.21±0.03	15.9±0.03	14.66±0.06	14.11±0.06	13.97±0.05

Continuation of Table A.4

ID	V	Ic	g	r	i	z	J	H	Ks
5386	16.967	15.687		16.5±0.03	16.14±0.03	15.88±0.03	14.59±0.06	14.09±0.06	13.96±0.05
5387	17.007	15.698		16.58±0.03	16.16±0.03	15.79±0.033	14.68±0.06	14.12±0.06	13.95±0.04
5388	17.074	15.702	17.77±0.05	16.62±0.05	16.17±0.031	15.93±0.031	14.7±0.06	14.16±0.06	
5393	17.096	15.74	17.7±0.05	16.63±0.05	16.23±0.031	15.95±0.031	14.74±0.06	14.17±0.06	14.03±0.07
5399	17.223	15.781	17.92±0.031	16.77±0.03	16.31±0.11	16.02±0.031	14.76±0.06	14.2±0.06	14.04±0.07
5400	17.133	15.787	17.78±0.03	16.65±0.05	16.27±0.11	16.05±0.03	14.87±0.06	14.32±0.06	14.19±0.07
5402	17.158	15.794	17.95±0.05	16.76±0.05	16.38±0.03	16.11±0.031	14.84±0.06	14.3±0.06	14.13±0.07
5405	17.191	15.817	17.94±0.05	16.81±0.05	16.39±0.03	16.12±0.03	14.88±0.06	14.32±0.06	14.17±0.07
5408	17.258	15.825		16.91±0.05	16.5±0.03	16.13±0.031	14.81±0.06	14.17±0.06	13.98±0.04
5409	17.263	15.825	17.97±0.05	16.99±0.05	16.29±0.11	15.94±0.034	14.71±0.06	14.13±0.06	13.9±0.04
5410	17.184	15.829		16.7±0.05	16.28±0.11	16.03±0.08	14.82±0.06	14.25±0.06	14.03±0.04
5411	17.335	15.833	17.99±0.05	16.83±0.05	16.38±0.11	16.0±0.03	14.72±0.06	14.14±0.06	13.87±0.04
5413	17.239	15.841	17.86±0.05	16.87±0.05	16.45±0.11	16.06±0.031	14.93±0.06	14.34±0.06	14.16±0.07
5418	17.358	15.888	18.14±0.05	16.92±0.05	16.44±0.03	16.12±0.031	14.91±0.06	14.31±0.06	14.12±0.07
5419	17.339	15.891	18.05±0.05	16.83±0.05	16.39±0.03	16.07±0.03	14.82±0.06	14.24±0.06	14.08±0.07
5428	17.448	15.96	18.08±0.05	16.92±0.05	16.51±0.03	16.22±0.03	15.01±0.06	14.35±0.06	14.2±0.07
5429	17.423	15.963		16.94±0.05	16.55±0.03	16.19±0.03	14.89±0.06	14.27±0.06	14.08±0.07
5436	17.37	15.988	18.09±0.05	16.89±0.05	16.42±0.033	16.13±0.031	14.93±0.06	14.33±0.06	14.15±0.07
5437	17.38	15.993		16.98±0.05	16.5±0.03	16.26±0.03	15.02±0.06	14.43±0.06	14.28±0.07
5438	17.364	15.996		16.98±0.05	16.44±0.03	16.17±0.03	14.98±0.06	14.39±0.06	14.21±0.07
5440	17.418	16.003		16.98±0.05	16.46±0.03	16.15±0.03	14.84±0.06	14.26±0.06	14.1±0.07
5445	17.541	16.027		16.96±0.05	16.55±0.03	16.29±0.08	14.98±0.06	14.4±0.06	14.24±0.07
5446	17.553	16.036	18.24±0.05	17.15±0.05	16.59±0.03	16.2±0.033	15.01±0.06	14.4±0.06	14.22±0.07
5447	17.45	16.037		16.97±0.05	16.52±0.03	16.24±0.03	15.01±0.06	14.43±0.06	14.28±0.07
5449	17.532	16.041	18.25±0.05	17.06±0.05	16.62±0.03	16.3±0.031	15.07±0.06	14.45±0.06	14.3±0.07
5450	17.535	16.041	18.26±0.03	16.98±0.05	16.57±0.03	16.29±0.031	15.09±0.06	14.5±0.06	14.36±0.07
5455	17.701	16.113	18.37±0.051	17.18±0.05	16.59±0.04	16.18±0.036	14.99±0.06	14.37±0.06	14.22±0.07
5456	17.953	16.114	18.8±0.05	17.38±0.05	16.69±0.035	16.16±0.036	14.98±0.06	14.34±0.06	14.11±0.07
5458	17.563	16.135		17.11±0.05	16.59±0.03	16.31±0.032	14.9±0.06	14.4±0.06	14.06±0.07
5459	17.654	16.141		17.12±0.03	16.6±0.03	16.29±0.031	14.97±0.06	14.38±0.06	14.22±0.07
5462	17.621	16.146	18.24±0.05	17.05±0.05	16.59±0.03	16.25±0.037	15.06±0.06	14.46±0.06	14.29±0.07
5463	17.712	16.153	18.52±0.05	17.24±0.05	16.71±0.031	16.38±0.031	15.1±0.06	14.48±0.06	14.32±0.07
5472	17.786	16.173		17.32±0.05	16.69±0.03	16.29±0.031	14.99±0.06	14.39±0.06	14.23±0.07
5476	17.624	16.19		17.12±0.05	16.65±0.03	16.34±0.031	15.06±0.06	14.44±0.06	14.33±0.07
5479	17.653	16.218		17.16±0.05	16.66±0.03	16.35±0.032	15.05±0.06	14.45±0.06	14.28±0.07
5481	17.774	16.229	18.38±0.05	17.19±0.05	16.72±0.03	16.39±0.031	15.0±0.06	14.4±0.06	14.24±0.07
5482	17.919	16.235	18.74±0.05	17.46±0.05	16.81±0.031	16.43±0.034	15.12±0.06	14.46±0.06	14.25±0.07
5483	17.904	16.24		17.42±0.03	16.84±0.03	16.43±0.03	15.1±0.06	14.42±0.06	14.21±0.07
5489	17.823	16.271		17.45±0.05	16.39±0.036	16.41±0.08	15.1±0.06	14.49±0.06	14.32±0.07
5493	17.967	16.294	18.61±0.05	17.39±0.05	16.88±0.03	16.49±0.032	15.14±0.06	14.53±0.06	14.38±0.07
5494	17.94	16.295	18.63±0.05	17.28±0.05	16.75±0.11	16.41±0.034	15.2±0.06	14.56±0.06	14.39±0.07
5502	17.921	16.327	18.68±0.05	17.35±0.05	16.83±0.031	16.5±0.031	15.23±0.06	14.6±0.06	14.43±0.07
5506	17.98	16.346		17.52±0.05	16.94±0.031	16.55±0.031	15.18±0.06	14.55±0.06	14.4±0.07

Continuation of Table A.4

ID	V	Ic	g	r	i	z	J	H	Ks
5508	17.973	16.36		17.33±0.05	16.83±0.03	16.48±0.034	15.17±0.06	14.55±0.06	14.39±0.07
5517	18.443	16.399		17.82±0.05	16.96±0.03	16.42±0.03	15.02±0.06	14.34±0.06	14.09±0.07
7000			17.21±0.05	16.23±0.05	15.85±0.03	15.59±0.032	14.37±0.06	13.88±0.03	13.74±0.04
7001				16.19±0.03	15.85±0.03	15.64±0.03	14.5±0.06	14.02±0.06	13.93±0.04
7002			17.32±0.05	16.32±0.03	15.95±0.11	15.71±0.03	14.6±0.06	14.09±0.06	13.98±0.04
7003			18.23±0.05	17.06±0.05	16.63±0.113	16.26±0.035	15.08±0.06	14.49±0.06	14.38±0.07
7004			17.13±0.05	16.19±0.03	15.79±0.03	15.54±0.03	14.42±0.04	13.85±0.04	13.76±0.05
7005				17.39±0.05	16.9±0.03	16.44±0.037	15.18±0.06	14.53±0.06	14.35±0.07
7006			18.56±0.05	17.25±0.05	16.71±0.03	16.36±0.033	15.11±0.06	14.5±0.06	14.28±0.07
7007			18.09±0.03	16.91±0.05	16.47±0.03	16.17±0.031	14.9±0.06	14.34±0.06	14.15±0.07
7008				17.3±0.03	16.77±0.03	16.45±0.031	15.16±0.06	14.54±0.06	14.37±0.07
7009			17.65±0.05	16.52±0.05	16.17±0.11	15.78±0.037	14.31±0.06	13.82±0.03	13.68±0.04
7010			17.52±0.05	16.51±0.05	16.04±0.03	15.78±0.03	14.64±0.06	14.08±0.06	13.92±0.04
7011				16.36±0.03	15.99±0.03	15.78±0.03	14.62±0.06	14.1±NaN	13.97±NaN
7012				16.21±0.03	15.82±0.03	15.59±0.03	14.42±0.06	13.98±0.03	13.84±0.04
7013				16.75±0.05	16.31±0.03	16.05±0.03	14.82±0.06	14.23±0.06	14.04±0.07
7014				16.74±0.03	16.29±0.03	16.03±0.03	14.77±0.06	14.21±0.06	14.03±0.07
7015			18.24±0.031	16.99±0.05	16.52±0.03	16.2±0.032	14.93±0.06	14.34±0.06	14.2±0.07
7016				17.66±0.133	16.65±0.03	16.34±0.03	15.07±0.06	14.45±0.06	14.31±0.07
7017			17.8±0.05	16.66±0.05	16.28±0.03	16.02±0.03	14.82±0.06	14.31±0.06	14.2±0.07
7018				17.12±0.03	16.62±0.03	16.33±0.03	15.08±0.06	14.47±0.06	14.36±0.07
7019				16.53±0.03	16.12±0.03	15.9±0.03	14.72±0.06	14.18±0.06	14.05±0.07
7020			17.09±0.05	16.06±0.05	15.75±0.03	15.56±0.03	14.4±0.06	13.89±0.04	13.79±0.04
7021			18.21±0.05	17.0±0.05	16.53±0.03	16.22±0.031	14.94±0.06	14.34±0.06	14.16±0.07
7022				17.02±0.03	16.53±0.03	16.21±0.032	14.92±0.06	14.3±0.06	14.2±0.07
7023			17.41±0.05	16.48±0.05	16.09±0.03	15.85±0.03	14.69±0.06	14.16±0.06	14.06±0.07
7025				17.1±0.03	16.58±0.03	16.25±0.03	14.97±0.04	14.29±0.06	14.1±0.07
7026			17.51±0.05	16.42±0.05	16.04±0.03	15.79±0.03	14.71±0.03	14.06±0.06	13.96±0.04
7028			18.55±0.05	17.23±0.05		16.41±0.08			
7029				16.33±0.03	15.96±0.03	15.75±0.03	14.55±0.06	14.05±0.06	13.96±0.04
7030				16.51±0.03	16.12±0.03	15.88±0.03	14.63±0.06	14.06±0.06	13.96±0.04
7031			18.18±0.03	16.93±0.05	16.52±0.03	16.19±0.03	14.92±0.06	14.34±0.06	14.19±0.07
7032			18.53±0.05	17.25±0.05	16.76±0.11	16.48±0.032	15.15±0.06	14.55±0.06	14.38±0.07
7034			18.45±0.05	17.16±0.05	16.69±0.03	16.4±0.031	15.11±0.06	14.53±0.06	14.4±0.07
7035				16.8±0.03	16.35±0.03	16.08±0.03	14.8±0.06	14.24±0.06	14.15±0.07
7036				16.46±0.03	16.07±0.03	15.84±0.03	14.64±0.06	14.13±0.06	14.02±0.07
7037			17.87±0.05	16.68±0.05	16.2±0.11	15.83±0.035	14.69±0.06	14.11±0.06	13.94±0.05
7038				16.96±0.031	16.51±0.031	16.27±0.031	14.97±0.06	14.41±0.06	14.19±0.07
7039				17.19±0.03	16.67±0.03		15.05±0.06	14.43±0.06	14.27±0.07
7040			18.42±0.033	17.15±0.05	16.68±0.03	16.35±0.031	15.03±0.06	14.43±0.06	14.24±0.07
7041			17.93±0.035	16.91±0.05	16.46±0.03	16.13±0.036	14.85±0.06	14.3±0.06	14.12±0.07
7042			17.68±0.031	16.66±0.03	16.14±0.03	15.83±0.03	14.54±0.06	14.06±0.05	13.85±0.05
7044			18.71±0.05	17.45±0.05	16.87±0.03	16.5±0.031	15.2±0.06	14.55±0.06	14.36±0.07

Continuation of Table A.4

ID	V	Ic	g	r	i	z	J	H	Ks
7046			18.27±0.05	17.06±0.05	16.57±0.03	16.27±0.031	15.07±0.06	14.48±0.06	14.37±0.07
7047				16.9±0.13	16.33±0.03	16.05±0.032	14.8±0.06	14.25±0.06	14.1±0.07
7048				17.04±0.03	16.57±0.03	16.28±0.03	14.96±0.06	14.36±0.06	14.24±0.07
7049			17.98±0.05	16.81±0.05	16.35±0.03	16.1±0.031	14.86±0.06	14.31±0.06	14.15±0.07
7050				16.27±0.03	15.86±0.03	15.64±0.03	14.4±0.06	14.04±0.04	13.9±0.03
7051			17.82±0.03	16.73±0.03	16.25±0.03	15.96±0.03	14.7±0.06	14.14±0.06	13.99±0.05
7052			17.22±0.05	16.19±0.05	15.84±0.03	15.62±0.03	14.44±0.06	13.99±0.04	13.82±0.05
7053				17.12±0.03	16.5±0.032	16.29±0.031	15.06±0.06	14.45±0.06	14.3±0.07
7054				16.58±0.032	16.15±0.03		14.66±0.06	14.11±0.06	14.06±0.04
7055				16.11±0.03	15.72±0.03	15.54±0.08	14.29±0.06	13.77±0.03	13.64±0.04
7056			18.23±0.05	16.96±0.05	16.5±0.035	16.22±0.032	14.96±0.06	14.36±0.07	14.16±0.07
7057			17.41±0.05	16.39±0.05	16.06±0.03	15.83±0.03	14.65±0.06	14.14±0.06	14.02±0.07
7059			16.58±0.05	15.67±0.05	15.34±0.11	14.99±0.047			
7062			17.05±0.05	16.03±0.05	15.72±0.03	15.48±0.03	14.32±0.06	13.77±0.03	13.63±0.03
7063				15.05±0.03	14.78±0.03	14.64±0.03	13.68±0.02	13.23±0.03	13.22±0.03
7064			15.07±0.05	14.48±0.03	14.25±0.03	14.14±0.03	13.23±0.02	12.87±0.03	12.72±0.02
7067					14.94±0.11		13.86±0.02	13.45±0.03	13.35±0.03
7068				14.72±0.03	14.5±0.03		13.43±0.03	13.09±0.03	13.03±0.03
7069			17.12±0.05	16.19±0.05	15.9±0.03	15.68±0.03	14.56±0.06	14.09±0.06	13.9±0.04
7070			15.42±0.03	14.81±0.03	14.51±0.11	14.41±0.03	13.48±0.02	13.08±0.02	13.0±0.02
7071			15.45±0.05	14.78±0.03	14.55±0.03	14.43±0.03	13.5±0.02	13.17±0.03	13.09±0.03
7072			16.36±0.03	15.55±0.03	15.15±0.11	15.01±0.03	13.94±0.02	13.56±0.03	13.43±0.03
7073				15.06±0.03	14.77±0.03	14.61±0.03	13.61±0.03	13.25±0.03	13.13±0.03
7074			15.76±0.03	15.12±0.03	14.84±0.03	14.71±0.03	13.76±0.03	13.33±0.03	13.26±0.03
7075				15.74±0.03	15.38±0.03	15.16±0.03	14.09±0.06	13.59±0.03	13.47±0.03
7076					14.35±0.03	14.25±0.03	13.33±0.02	13.01±0.02	12.94±0.02
7077				14.74±0.03	14.52±0.03	14.41±0.03	13.47±0.02	13.14±0.03	13.04±0.02
7078			16.4±0.05	15.58±0.05	15.32±0.03	15.13±0.03	14.08±0.06	13.62±0.03	13.51±0.03
7079			16.22±0.05	15.46±0.05	15.1±0.03	14.95±0.03	13.94±0.02	13.49±0.03	13.39±0.03
7080				14.77±0.03	14.55±0.03	14.43±0.03	13.55±0.03	13.12±0.03	13.08±0.03
7082			15.74±0.05	15.0±0.03	14.77±0.03	14.62±0.03	13.65±0.02	13.28±0.02	13.18±0.03
7084				14.92±0.03	14.67±0.11	14.54±0.03	13.57±0.03	13.25±0.04	13.17±0.03
7085				15.1±0.13	14.72±0.11		13.57±0.02	13.26±0.03	13.17±0.03
7086				15.57±0.03	15.23±0.03	15.05±0.03	13.97±0.02	13.56±0.02	13.42±0.03
7087			16.65±0.05	15.79±0.05	15.49±0.03	15.32±0.03	14.26±0.06	13.82±0.03	13.67±0.04
7088				15.15±0.03	14.88±0.03	14.76±0.03	13.75±0.02	13.32±0.03	13.23±0.02
7089			15.87±0.05	15.13±0.05	14.89±0.03	14.73±0.03	13.74±0.02	13.3±0.03	13.22±0.02
7090			16.47±0.03	15.66±0.03	15.32±0.03	15.08±0.031	14.02±0.06	13.54±0.03	13.35±0.03
7092				16.12±0.03	15.72±0.03	15.48±0.03	14.27±0.06	13.82±0.03	13.71±0.03
7094			15.88±0.03	15.22±0.03	14.96±0.03	14.83±0.03	13.84±0.03	13.41±0.03	13.34±0.03
7095			16.23±0.05	15.38±0.05	15.14±0.03	14.98±0.03	13.97±0.03	13.58±0.03	13.41±0.03
7097			15.14±0.05			14.25±0.03	13.3±0.02	12.95±0.02	12.81±0.02
7098					14.7±0.11	14.58±0.08			

Continuation of Table A.4

ID	V	Ic	g	r	i	z	J	H	Ks
7099				14.99±0.03	14.69±0.03	14.56±0.03	13.56±0.02	13.19±0.03	13.03±0.03
7100			16.76±0.05	15.87±0.03	15.46±0.03	15.26±0.031	14.18±0.06	13.7±0.03	13.62±0.04
7101				15.34±0.03	15.06±0.03	14.92±0.03	13.9±0.02	13.52±0.03	13.4±0.03
7102				14.9±0.13	14.52±0.11	14.39±0.03	13.44±0.03	13.09±0.02	13.03±0.03
7103				14.97±0.03	14.72±0.03	14.59±0.03	13.62±0.02	13.21±0.02	13.15±0.02
7104			16.76±0.03	15.91±0.03	15.57±0.03	15.35±0.03	14.24±0.06	13.75±0.03	13.63±0.03
7106			15.2±0.05	14.6±0.03	14.38±0.03	14.28±0.03	13.34±0.02	13.02±0.03	12.94±0.02
7107			17.68±0.05	16.6±0.05	16.19±0.03	15.93±0.032	14.88±0.03	14.24±0.04	14.12±0.07
7108			18.17±0.03	17.07±0.05	16.49±0.032	16.22±0.031	14.97±0.06	14.37±0.06	14.22±0.07
7110			16.7±0.05	15.82±0.05	15.53±0.03	15.24±0.032	14.24±0.06	13.79±0.03	13.66±0.04
7111			18.15±0.05	16.98±0.05	16.5±0.03	16.17±0.031	14.86±0.04	14.27±0.04	14.15±0.05
7112			16.42±0.03	15.55±0.03	15.06±0.11	14.89±0.03	13.7±0.03	13.21±0.03	13.06±0.03
7113			16.9±0.03	15.99±0.03	15.63±0.03	15.44±0.03	14.32±0.06	13.79±0.03	13.66±0.04
7114			16.12±0.05	15.23±0.05	14.93±0.03	14.64±0.031	13.55±0.03	13.09±0.03	13.0±0.03
7115			15.88±0.03	15.09±0.03	14.74±0.03	14.53±0.03	13.4±0.02	12.89±0.02	12.75±0.02
7116			15.75±0.03	15.11±0.13	14.74±0.03	14.6±0.03	13.6±0.02	13.22±0.03	13.12±0.03
7117			15.41±0.05	14.77±0.03	14.5±0.11	14.4±0.03	13.43±0.02	13.03±0.02	12.92±0.03
7118			16.89±0.05	15.78±0.05	15.38±0.03	15.11±0.03	13.95±0.02	13.39±0.03	13.24±0.03
7119			18.47±0.03	17.15±0.05	16.67±0.03	16.38±0.031	15.09±0.06	14.48±0.06	14.31±0.07
7120			15.55±0.05	14.96±0.03	14.74±0.11		13.62±0.02	13.27±0.03	13.17±0.03
7121			16.31±0.05	15.62±0.05	15.26±0.11	15.15±0.03	14.03±0.03	13.48±0.03	13.39±0.03
7122				16.78±0.03	16.17±0.03	15.79±0.03	14.48±0.06	13.79±0.03	13.55±0.03
7123			16.2±0.05	15.42±0.05	15.11±0.03	14.96±0.03	13.89±0.03	13.5±0.03	13.34±0.03
7124			14.7±0.03	14.05±0.03	13.8±0.11	13.7±0.03	12.74±0.03	12.41±0.04	12.3±0.03
7125			18.62±0.033	17.39±0.05	16.85±0.11	16.53±0.034	15.22±0.06	14.6±0.06	14.33±0.07
7126			16.65±0.05	15.88±0.05	15.54±0.03	15.34±0.03	14.21±0.06	13.78±0.03	13.73±0.04
7127			15.43±0.05	14.73±0.03	14.42±0.11	14.25±0.03	13.18±0.02	12.8±0.03	12.69±0.03
7128			15.85±0.03	15.22±0.03	14.94±0.03	14.78±0.03	13.79±0.02	13.44±0.03	13.32±0.02
7129			16.28±0.05	15.44±0.05	15.11±0.03	14.9±0.03	13.87±0.02	13.49±0.03	13.35±0.02
7131			16.06±0.03	15.28±0.03	14.93±0.11	14.69±0.03	13.6±0.02	13.2±0.03	13.15±0.03
7132			15.91±0.05	15.23±0.05	15.0±0.03	14.83±0.03	13.8±0.02	13.41±0.03	13.37±0.02
7133			15.84±0.05	15.29±0.13	14.82±0.03	14.67±0.03	13.68±0.02	13.27±0.02	13.16±0.03
7134			16.09±0.05	15.24±0.05	14.95±0.03	14.8±0.03	13.74±0.02	13.22±0.03	13.17±0.03
7135				15.56±0.03	15.22±0.03	15.02±0.03	14.06±0.06	13.56±0.03	13.43±0.03
7136			15.01±0.05	14.3±0.03	14.0±0.11	13.82±0.03	12.81±0.02	12.44±0.02	12.29±0.02
7137			18.22±0.05	17.03±0.05	16.55±0.03	16.2±0.03	14.97±0.04	14.32±0.06	14.06±0.05
7138			18.58±0.05	17.21±0.05	16.54±0.03	16.13±0.031	14.77±0.06	14.08±0.06	13.82±0.04
7147			17.12±0.05	16.17±0.13	15.62±0.03	15.33±0.03	14.09±0.06	13.65±0.03	13.48±0.03

Table A.5: Blended Li and Fe EWs, Fe EWs, Li EWs, and Li LTE and non-LTE abundances for the 110 members of M35 observed in 1999 December and 2001 February.

ID	$EW(Li+Fe)$ (mÅ)	$EW(Fe)^{(a)}$ (mÅ)	$EW(Fe)^{(b)}$ (mÅ)	$EW(Li)^{(a)}$ (mÅ)	$A(Li)_{LTE}$	$A(Li)_{NLTE}$
5088	119.2±6.5	3.5±2.8	10.3	115.7±7.1	2.88±0.04	2.84
5103	201.4±7.6	8.6±3.8	10.5	192.8±8.5	2.98±0.03	2.92
5114	42.7±16.3	3.8±2.4	9.8	38.8±16.4	2.39±0.08	2.39
5139	127.0±5.1	5.0±2.5	11.8	122.0±5.7	2.66±0.02	2.68
5148	181.1±4.7	5.6±2.5	11.1	175.4±5.3	3.22±0.02	3.06
5183	107.6±5.1	5.2±3.0	12.9	102.3±5.9	2.57±0.03	2.59
5186	141.5±4.8	6.6±2.7	12.5	134.9±5.5	2.74±0.02	2.74
5194	157.5±4.8	4.0±3.5	14.2	153.5±5.9	2.32±0.03	2.37
5213	205.0±4.7	6.6±3.2	13.4	198.5±5.7	2.87±0.02	2.75
5215	128.9±5.1	6.3±2.9	12.2	122.6±5.9	2.64±0.02	2.66
5227	143.0±5.1	6.3±2.3	13.1	136.7±5.6	2.68±0.02	2.69
5230	208.4±4.7	7.9±2.8	14.2	200.5±5.5	3.12±0.03	3.0
5283	241.7±5.6	7.3±3.9	14.6	234.4±6.8	2.71±0.03	2.65
5295	≤14.3					
5316	132.5±10.4	6.9±5.1	14.6	125.6±11.6	2.11±0.05	2.2
5323	107.1±5.4	5.8±5.2	14.7	101.3±7.5	1.93±0.03	2.04
5337	140.4±5.1	8.2±3.4	15.9	132.2±6.1	2.12±0.02	2.21
5356	159.5±5.2	5.4±4.9	16.8	154.1±7.2	1.93±0.02	1.99
5361	94.5±4.6	7.3±3.3	16.9	87.2±5.6	1.53±0.02	1.69
5368	134.9±4.8	8.3±3.3	16.5	126.6±5.9	1.78±0.02	1.88
5369	201.4±10.5	6.6±4.0	16.6	194.8±11.2	2.12±0.04	2.12
5386	140.0±6.8	5.1±7.4	16.9	134.9±10.1	1.86±0.04	1.94
5387	76.7±5.9	8.0±4.8	17.6	68.7±7.6	1.3±0.04	1.48
5393	175.9±5.3	7.2±4.7	17.7	168.6±7.0	2.02±0.02	2.05
5399	≤41.0					
5400	75.2±10.3	6.8±4.2	17.0	68.4±11.2	1.38±0.07	1.56
5402	149.5±9.6	4.8±4.8	18.2	144.7±10.8	1.5±0.04	1.67
5405	162.3±5.1	6.0±3.7	18.5	156.3±6.3	1.53±0.02	1.69
5409	238.4±6.9	5.9±3.7	19.9	232.5±7.8	1.54±0.02	1.7
5413	263.9±10.3	10.2±14.6	18.4	253.7±17.8	2.18±0.07	2.17
5418	124.4±5.0	7.8±5.5	19.1	116.6±7.5	1.38±0.03	1.55
5428	119.1±5.7	4.7±5.4	19.3	114.4±7.9	1.28±0.02	1.46
5436	117.8±10.2	5.6±4.8	19.4	112.2±11.3	1.32±0.05	1.5
5437	≤23.6					
5438	129.7±11.1	5.5±4.8	18.9	124.2±12.1	1.35±0.04	1.53
5440	≤47.0					
5445	-99.0					
5446	86.3±7.4	8.4±4.5	19.6	77.9±8.7	1.08±0.05	1.27
5447	≤25.4					

Continuation of Table A.5

ID	$EW(Li+Fe)$ (mÅ)	$EW(Fe)^{(a)}$ (mÅ)	$EW(Fe)^{(b)}$ (mÅ)	$EW(Li)^{(a)}$ (mÅ)	$A(Li)_{LTE}$	$A(Li)_{NLTE}$
5449	72.3±16.5	4.0±5.4	19.6	68.3±17.3	0.87±0.12	1.07
5450	24.9±9.9	5.9±4.3	18.6	19.0±10.8	0.35±0.2	0.56
5455	117.7±11.1	5.1±4.9	20.2	112.6±12.1	0.91±0.05	1.04
5456	-99.0					
5458	33.9±11.9	5.7±5.9	19.7	28.2±13.3	0.53±0.17	0.74
5459	156.4±10.7	5.3±6.7	19.5	151.0±12.6	1.45±0.04	1.62
5462	≤47.4					
5476	33.4±3.8	4.6±6.8	19.7	28.8±7.8	0.64±0.07	0.85
5479	≤17.2					
5481	178.0±5.7	4.6±5.6	20.7	173.5±8.0	1.19±0.02	1.26
5482	≤21.1					
5489	≤7.9					
5494	≤20.5					
5502	≤46.5					
5506	123.4±9.9	6.7±16.1	22.6	116.7±18.9	1.13±0.07	1.21
5508	91.7±11.5	5.4±6.5	21.1	86.2±13.2	0.83±0.08	0.97
5517	≤24.1					
7000	117.0±9.6	7.8±3.2	15.9	109.2±10.1	2.01±0.05	2.11
7001	86.6±13.2	10.3±3.4	14.5	76.3±13.6	1.67±0.07	1.8
7002	140.5±10.4	6.1±4.2	15.7	134.4±11.2	1.76±0.04	1.87
7003	≤18.0					
7004	162.5±5.4	6.9±3.3	15.4	155.5±6.4	1.89±0.02	1.97
7005	≤14.5					
7006	64.6±11.8	5.4±7.3	21.1	59.3±13.9	0.58±0.08	0.74
7007	≤13.9					
7008	-99.0					
7009	91.1±9.9	8.2±3.7	17.9	82.8±10.6	1.5±0.06	1.67
7010	196.2±19.6	6.8±8.1	16.4	189.3±21.2	2.33±0.11	2.27
7011	67.7±10.8	11.6±3.6	15.5	56.0±11.4	1.61±0.07	1.75
7012	-99.0					
7013	71.1±7.1	5.4±3.8	18.1	65.7±8.1	0.97±0.05	1.17
7014	127.7±10.7	6.4±3.7	18.1	121.3±11.3	1.67±0.04	1.8
7015	57.9±9.1	6.9±4.7	19.2	51.0±10.2	0.88±0.08	1.08
7016	≤22.6					
7017	66.2±12.2	11.1±4.2	16.7	55.1±12.9	1.18±0.09	1.37
7018	≤44.7					
7019	122.2±9.4	8.0±3.4	16.9	114.2±10.0	1.69±0.04	1.82
7020	≤13.9					
7021	-99.0					
7022	56.4±9.1	6.2±3.6	19.3	50.2±9.8	0.87±0.08	1.07
7023	253.6±9.3	9.0±3.7	15.4	244.6±10.0	2.4±0.04	2.32
7025	104.9±9.0	5.5±8.0	20.9	99.3±12.0	0.92±0.06	1.04

Continuation of Table A.5

ID	$EW(Li+Fe)$ (mÅ)	$EW(Fe)^{(a)}$ (mÅ)	$EW(Fe)^{(b)}$ (mÅ)	$EW(Li)^{(a)}$ (mÅ)	$A(Li)_{LTE}$	$A(Li)_{NLTE}$
7026	63.7±11.2	6.6±3.7	17.2	57.1±11.8	1.19±0.07	1.38
7029	130.5±5.8	11.1±3.7	15.2	119.4±6.9	2.05±0.03	2.14
7030	108.5±11.6	9.1±3.5	17.4	99.4±12.1	1.59±0.05	1.74
7031	209.1±14.7	9.0±8.4	19.7	200.1±17.0	1.8±0.07	1.9
7032	-99.0					
7034	≤29.9					
7035	77.2±9.0	8.3±4.7	18.1	68.9±10.2	1.05±0.06	1.24
7036	117.1±11.2	8.2±3.7	15.9	108.9±11.8	1.63±0.05	1.77
7037	≤33.1					
7038	-99.0					
7039	≤36.4					
7040	81.5±11.5	4.6±7.9	20.7	76.9±14.0	0.73±0.07	0.87
7041	≤23.1					
7042	80.0±4.9	5.5±4.4	19.0	74.5±6.6	1.1±0.03	1.29
7044	≤5.8					
7046	72.2±22.6	5.0±4.9	19.1	67.2±23.1	0.74±0.12	0.94
7047	80.7±14.7	5.9±3.4	17.5	74.7±15.1	1.34±0.07	1.52
7048	≤27.0					
7049	118.5±13.9	7.2±5.7	18.2	111.2±15.0	1.27±0.06	1.45
7050	136.0±10.2	7.2±3.0	16.2	128.8±10.7	1.75±0.04	1.86
7051	211.9±11.0	5.2±5.1	17.7	206.6±12.1	2.16±0.04	2.15
7052	114.2±5.0	7.4±3.5	15.5	106.7±6.1	1.99±0.02	2.09
7053	64.8±14.1	7.2±5.9	19.0	57.6±15.3	1.02±0.09	1.21
7054	103.5±13.3	9.2±4.5	17.7	94.3±14.1	1.54±0.06	1.7
7055	235.0±18.5	6.8±6.2	14.6	228.2±19.5	2.68±0.12	2.64
7056	≤16.2					
7057	99.9±37.3	17.7±9.8	15.9	82.2±38.5	1.69±0.2	1.82
7107	164.5±15.8	9.4±5.2	17.0	155.0±16.6	1.9±0.06	1.97
7108	58.9±15.6	8.0±4.8	18.8	50.9±16.3	0.83±0.11	1.03

Table A.6: Rotation period, Li EW, effective temperature, luminosity, membership class and binary status for 250 M35 members.

ID	Membership Class	Binary	T_{eff} (K)	L (L_{\odot})	Limit flag on $EW(Li)$	$EW(Li)$ ($m\text{\AA}$)	$EW(Li)$ Source	Prot (d)	Prot Source
5076	Poss+	0	6000±125	1.82±0.33		106.6	AT18	-99.0	
5078	Poss+	0	5750±125	1.67±0.3		104.0	Je21	-99.0	
5087	Poss+	0	6000±125	1.57±0.79		101.7	AT18	2.2	SF20
5088	Poss+	1	5750±125	1.51±0.27		115.7	This Work	-99.0	
5094	Poss+	0	5750±125	1.49±0.27		51.5	AT18	2.34	L16
5096	Poss+	0	6500±125	1.56±0.28		103.0	B01	3.62	This Work
5097	Poss+	0	6000±125	1.55±0.28		122.4	AT18	2.03	SF20
5099	Poss+	0	5750±125	1.44±0.26		120.0	AT18	-99.0	
5103	Poss	0	5500±125	1.4±0.25		192.8	This Work	2.65	This Work
5107	Poss+	0	6000±125	1.38±0.26		94.0	B01	2.51	This Work
5112	Poss+	0	6000±125	1.37±0.25		126.9	AT18	-99.0	
5114	Prob	0	6000±125	1.28±0.24		38.8	This Work	3.11	SF20
5116	Prob+	0	6000±125	1.32±0.24		111.0	B01	2.38	L16
5121	Prob+	0	5750±125	1.26±0.23		115.6	AT18	3.3	SF20
5130	Prob+	0	5750±125	1.12±0.2		137.7	AT18	2.64	This Work
5135	Poss+	0	5750±125	1.02±0.18		125.0	B01	4.31	This Work
5139	Prob+	0	5500±125	0.95±0.17		122.0	This Work	3.86	SF20
5140	Prob+	0	5750±125	1.06±0.19		143.8	AT18	3.45	This Work
5144	Prob+	0	5750±125	0.97±0.18		157.0	B01	2.73	SF20
5146	Prob+	1	5500±125	0.91±0.16		139.8	AT18	3.99	M09
5148	Poss	0	5750±125	0.85±0.15		175.4	This Work	3.56	M09
5152	Poss+	0	5750±125	0.91±0.16		122.3	AT18	4.33	M09
5155	Poss	0	5500±125	0.86±0.16		74.0	Je21	-99.0	
5158	Poss	1	5500±125	0.84±0.15		28.0	Je21	4.54	N15
5159	Poss	0	5500±125	0.8±0.14	≤	-99.0	B01	-99.0	
5162	Poss+	0	5750±125	0.84±0.15		67.0	Je21	10.09	This Work
5165	Prob+	0	5500±125	0.8±0.15		111.0	B01	6.14	M09
5174	Poss+	0	5750±125	0.8±0.15		174.0	B01	3.95	This Work
5176	Prob+	0	5500±125	0.75±0.14		117.0	B01	4.74	M09
5180	Prob+	0	5500±125	0.73±0.13		124.6	AT18	4.83	M09
5181	Poss+	0	5250±125	0.69±0.12		71.6	AT18	1.27	M09
5182	Prob+	0	5500±125	0.75±0.14		128.6	AT18	4.8	SF20
5183	Poss	0	5500±125	0.76±0.14		102.3	This Work	4.4	This Work
5186	Poss	1	5500±125	0.73±0.13		134.9	This Work	5.01	This Work
5194	Poss	1	5000±125	0.68±0.12		153.5	This Work	4.7	M09
5195	Poss	0	5250±125	0.65±0.12	≤	-99.0	B01	-99.0	
5198	Poss	1	5250±125	0.63±0.12		-4.0	Je21	4.65	M09
5209	Poss+	0	5500±125	0.61±0.11		109.0	B01	5.76	This Work
5213	Prob	0	5250±125	0.63±0.11		198.5	This Work	4.28	SF20
5215	Prob	0	5500±125	0.61±0.11		122.6	This Work	5.47	M09

Continuation of Table A.6

ID	Membership Class	Binary	T_{eff} (K)	L (L_{\odot})	Limit flag on $EW(Li)$	$EW(Li)$ ($m\text{\AA}$)	$EW(Li)$ Source	Prot (d)	Prot Source
5221	Poss+	0	5500±125	0.58±0.11		135.9	AT18	5.72	M09
5222	Prob+	0	5250±125	0.57±0.1		158.5	AT18	5.4	This Work
5227	Prob+	0	5500±125	0.57±0.11		136.7	This Work	5.53	M09
5230	Prob	0	5500±125	0.59±0.11		200.5	This Work	4.41	M09
5233	Poss+	0	5500±125	0.54±0.1		132.0	B01	5.78	M09
5235	Poss+	0	5000±125	0.55±0.1		143.0	B01	5.78	M09
5240	Poss+	0	5250±125	0.55±0.1		120.6	AT18	-99.0	
5241	Prob+	0	5250±125	0.54±0.1		147.0	B01	5.65	M09
5257	Poss+	0	5250±125	0.52±0.09		117.0	B01	5.71	N15
5258	Prob+	0	5500±125	0.5±0.09		137.2	AT18	6.34	SF20
5259	Prob+	0	5250±125	0.49±0.1		140.7	AT18	6.14	M09
5262	Prob+	0	5250±125	0.48±0.09		153.8	AT18	6.42	This Work
5263	Prob+	0	5250±125	0.49±0.09		147.0	B01	6.45	M09
5267	Poss+	1	5250±125	0.47±0.09		155.0	B01	6.34	SF20
5274	Prob+	1	5000±125	0.45±0.09		166.0	B01	6.51	This Work
5278	Poss+	0	5000±125	0.45±0.08		119.2	AT18	6.33	L16
5283	Poss+	0	5000±125	0.41±0.07		234.4	This Work	3.73	This Work
5288	Prob+	0	5250±125	0.41±0.08		115.0	B01	6.39	This Work
5289	Prob+	0	5250±125	0.41±0.08		133.0	B01	6.29	M09
5290	Poss+	0	4750±125	0.37±0.07		34.0	Je21	0.42	SF20
5293	Poss+	0	5000±125	0.39±0.07		135.0	B01	6.62	M09
5294	Poss	1	5250±125	0.41±0.08	≤	-99.0	B01	-99.0	
5295	Poss	0	5000±125	0.43±0.08	≤	14.3	This Work	-99.0	
5299	Poss	0	5000±125	0.39±0.08	≤	-99.0	B01	-99.0	
5300	Poss+	0	4750±125	0.4±0.08		51.0	Je21	-99.0	
5302	Poss	1	4750±125	0.4±0.07		-9.0	Je21	16.27	L16
5307	Prob+	1	5000±125	0.39±0.07		114.9	AT18	3.6	SF20
5308	Prob+	0	5000±125	0.37±0.07		151.4	AT18	6.69	L16
5316	Poss	1	5000±125	0.35±0.06		125.6	This Work	7.0	M09
5323	Prob	1	5000±125	0.34±0.06		101.3	This Work	7.3	M09
5327	Prob	0	5000±125	0.34±0.06		144.2	AT18	6.35	L16
5332	Poss+	0	4750±125	0.31±0.06		147.0	B01	5.66	SF20
5336	Poss	0	4750±125	0.33±0.06		-27.0	Je21	15.37	M09
5337	Prob+	0	5000±125	0.33±0.06		132.2	This Work	5.99	M09
5339	Prob+	0	4750±125	0.3±0.06		65.0	B01	-99.0	
5345	Prob+	0	4750±125	0.29±0.05		211.0	B01	-99.0	
5347	Poss	0	5000±125	0.28±0.05	≤	-99.0	B01	9.9	SF20
5356	Prob	1	4750±125	0.29±0.05		154.1	This Work	7.01	This Work
5357	Poss+	0	5000±125	0.28±0.05		107.0	B01	8.12	L16
5361	Prob	0	4750±125	0.28±0.06		87.2	This Work	-99.0	
5368	Prob	0	4750±125	0.28±0.05		126.6	This Work	7.52	M09
5369	Prob+	0	4750±125	0.26±0.05		194.8	This Work	6.9	M09

Continuation of Table A.6

ID	Membership Class	Binary	T_{eff} (K)	L (L_{\odot})	Limit flag on $EW(Li)$	$EW(Li)$ ($m\text{\AA}$)	$EW(Li)$ Source	Prot (d)	Prot Source
5370	Prob	0	4750±125	0.26±0.05		248.0	Je21	4.57	M09
5382	Prob	0	4750±125	0.26±0.05		187.0	Je21	3.08	M09
5386	Prob	0	4750±125	0.26±0.05		134.9	This Work	-99.0	
5387	Prob	1	4750±125	0.24±0.04		68.7	This Work	-99.0	
5388	Prob+	0	4500±125	0.25±0.05		138.0	B01	8.0	M09
5393	Prob	0	4750±125	0.24±0.05		168.6	This Work	5.78	M09
5399	Poss	1	4500±125	0.23±0.04	≤	41.0	This Work	8.34	L16
5400	Poss+	0	4750±125	0.23±0.04		68.4	This Work	8.85	M09
5402	Prob	0	4500±125	0.22±0.04		144.7	This Work	-99.0	
5405	Prob	0	4500±125	0.21±0.04		156.3	This Work	5.92	M09
5408	Poss+	0	4500±125	0.21±0.04		291.0	B01	0.74	M09
5409	Poss	1	4500±125	0.23±0.04		232.5	This Work	5.78	M09
5410	Poss+	0	4500±125	0.22±0.04		67.0	B01	-99.0	
5411	Prob	0	4250±125	0.22±0.04	≤	-99.0	B01	0.36	M09
5413	Prob	0	4500±125	0.21±0.04		253.7	This Work	0.73	M09
5418	Prob+	0	4500±125	0.2±0.04		116.6	This Work	9.16	L16
5419	Poss+	0	4500±125	0.21±0.04	≤	6.0	B01	-99.0	
5428	Prob	0	4500±125	0.19±0.04		114.4	This Work	10.56	SF20
5429	Prob	0	4500±125	0.2±0.04		203.0	Je21	0.48	L16
5436	Prob	0	4500±125	0.2±0.04		112.2	This Work	7.51	L16
5437	Prob	1	4500±125	0.18±0.03	≤	23.6	This Work	8.32	L16
5438	Prob+	0	4500±125	0.19±0.04		124.2	This Work	4.61	This Work
5440	Prob	1	4250±125	0.21±0.04	≤	47.0	This Work	0.46	M09
5445	Prob+	0	4500±125	0.19±0.03	≤	-99.0	This Work	7.41	M09
5446	Prob	0	4500±125	0.18±0.03		77.9	This Work	5.53	M09
5447	Poss	1	4500±125	0.18±0.03	≤	25.4	This Work	9.35	M09
5449	Prob	0	4500±125	0.17±0.03		68.3	This Work	-99.0	
5450	Prob+	0	4500±125	0.18±0.04		19.0	This Work	9.16	L16
5455	Prob+	0	4250±125	0.18±0.04		112.6	This Work	5.93	N15
5456	Poss	0	4000±125	0.18±0.03	≤	-99.0	This Work	-99.0	
5458	Prob+	0	4500±125	0.17±0.03		28.2	This Work	10.58	L16
5459	Poss	0	4500±125	0.18±0.03		151.0	This Work	7.3	M09
5462	Prob+	0	4500±125	0.17±0.03	≤	47.4	This Work	8.0	M09
5463	Prob	0	4250±125	0.17±0.03		48.9	AT18	11.03	L16
5472	Prob	0	4250±125	0.16±0.03		0.0	AT18	9.68	L16
5476	Prob	1	4500±125	0.16±0.03		28.8	This Work	8.7	M09
5479	Poss	0	4250±125	0.18±0.03	≤	17.2	This Work	-99.0	
5481	Prob	0	4250±125	0.18±0.03		173.5	This Work	5.18	M09
5482	Prob	1	4250±125	0.14±0.03	≤	21.1	This Work	0.62	M09
5483	Poss	0	4250±125	0.15±0.03		116.9	AT18	0.48	This Work
5489	Poss	0	4000±125	0.15±0.03	≤	7.9	This Work	0.24	M09
5493	Poss	0	4500±125	0.14±0.11		133.0	Je21	0.24	M09

Continuation of Table A.6

ID	Membership Class	Binary	T_{eff} (K)	L (L_{\odot})	Limit flag on $EW(Li)$	$EW(Li)$ ($m\text{\AA}$)	$EW(Li)$ Source	Prot (d)	Prot Source
5494	Poss	0	4250±198	0.16±0.04	≤	20.5	This Work	6.29	L16
5502	Prob	0	4250±125	0.15±0.03	≤	46.5	This Work	-99.0	
5506	Prob	0	4250±125	0.14±0.02		116.7	This Work	0.59	N15
5508	Poss	1	4250±125	0.15±0.03		86.2	This Work	3.06	L16
5517	Prob	1	3750±125	0.15±0.03	≤	24.1	This Work	1.06	L16
7000	Prob	0	5000±125	0.33±0.06		109.2	This Work	8.4	M09
7001	Prob+	0	5000±125	0.33±0.06		76.3	This Work	7.75	M09
7002	Prob+	0	4750±125	0.31±0.07		134.4	This Work	7.55	SF20
7003	Poss	0	4500±125	0.17±0.03	≤	18.0	This Work	-99.0	
7004	Prob+	0	4750±125	0.36±0.07		155.5	This Work	6.62	M09
7005	Prob+	0	4250±125	0.14±0.03	≤	14.5	This Work	-99.0	
7006	Prob+	0	4250±125	0.16±0.03		59.3	This Work	8.7	M09
7007	Poss	0	4500±125	0.2±0.04	≤	13.9	This Work	-99.0	
7008	Poss	1	4250±125	0.16±0.03	≤	-99.0	This Work	-99.0	
7009	Poss	0	4750±125	0.27±0.05		82.8	This Work	-99.0	
7010	Prob	0	4750±125	0.29±0.06		189.3	This Work	0.72	M09
7011	Poss+	0	5000±125	0.29±0.05		56.0	This Work	8.01	This Work
7012	Prob	0	5000±125	0.34±0.07	≤	-99.0	This Work	6.8	This Work
7013	Poss	0	4500±125	0.23±0.04		65.7	This Work	8.74	L16
7014	Prob+	0	4750±133	0.22±0.06		121.3	This Work	6.54	M09
7015	Prob	0	4500±125	0.19±0.03		51.0	This Work	8.67	This Work
7016	Poss+	0	4500±125	0.17±0.03	≤	22.6	This Work	-99.0	
7017	Poss+	0	4750±125	0.22±0.04		55.1	This Work	8.55	M09
7018	Prob+	0	4500±125	0.17±0.03	≤	44.7	This Work	9.71	M09
7019	Prob+	0	4750±125	0.26±0.05		114.2	This Work	8.13	M09
7020	Poss	0	5000±125	0.36±0.07	≤	13.9	This Work	-99.0	
7021	Poss	0	4500±125	0.19±0.03	≤	-99.0	This Work	-99.0	
7022	Poss+	0	4500±125	0.19±0.04		50.2	This Work	9.32	This Work
7023	Poss	0	4750±125	0.28±0.06		244.6	This Work	4.79	M09
7025	Poss	0	4250±125	0.19±0.03		99.3	This Work	6.54	M09
7026	Poss+	0	4750±125	0.28±0.05		57.1	This Work	-99.0	
7029	Prob	1	5000±125	0.3±0.05		119.4	This Work	-99.0	
7030	Prob+	0	4750±125	0.26±0.05		99.4	This Work	7.88	M09
7031	Prob	0	4500±125	0.19±0.03		200.1	This Work	0.91	M09
7032	Poss	0	4250±125	0.16±0.03	≤	-99.0	This Work	8.85	M09
7034	Prob	0	4500±125	0.16±0.03	≤	29.9	This Work	9.71	M09
7035	Prob+	0	4500±125	0.22±0.04		68.9	This Work	-99.0	
7036	Prob+	0	4750±125	0.28±0.05		108.9	This Work	7.99	This Work
7037	Prob	0	4500±125	0.25±0.04	≤	33.1	This Work	-99.0	
7038	Poss	0	4500±125	0.18±0.03	≤	-99.0	This Work	-99.0	
7039	Prob	1	4250±125	0.17±0.03	≤	36.4	This Work	-99.0	
7040	Prob	0	4250±125	0.17±0.03		76.9	This Work	-99.0	

Continuation of Table A.6

ID	Membership Class	Binary	T_{eff} (K)	L (L_{\odot})	Limit flag on $EW(Li)$	$EW(Li)$ ($m\text{\AA}$)	$EW(Li)$ Source	Prot (d)	Prot Source
7041	Poss	0	4750±125	0.19±0.04	≤	23.1	This Work	-99.0	
7042	Poss	0	4500±125	0.27±0.05		74.5	This Work	8.0	M09
7044	Poss+	0	4250±125	0.14±0.03	≤	5.8	This Work	-99.0	
7046	Prob	0	4500±125	0.18±0.03		67.2	This Work	-99.0	
7047	Prob	0	4750±125	0.22±0.04		74.7	This Work	4.17	SF20
7048	Poss	0	4500±125	0.18±0.03	≤	27.0	This Work	-99.0	
7049	Poss	0	4500±125	0.21±0.04		111.2	This Work	1.86	M09
7050	Prob+	0	4750±125	0.32±0.06		128.8	This Work	7.3	M09
7051	Prob	0	4750±125	0.25±0.05		206.6	This Work	7.05	L16
7052	Poss+	0	5000±125	0.33±0.06		106.7	This Work	-99.0	
7053	Prob+	0	4500±125	0.17±0.03		57.6	This Work	1.41	M09
7054	Prob+	0	4750±125	0.25±0.05		94.3	This Work	-99.0	
7055	Prob	1	5000±125	0.39±0.07		228.2	This Work	0.95	M09
7056	Poss	0	4500±125	0.19±0.03	≤	16.2	This Work	-99.0	
7057	Prob	0	5000±125	0.28±0.05		82.2	This Work	9.07	L16
7059	Poss+	0	5250±125	0.54±0.1		86.9	AT18	6.46	L16
7062	Prob	0	4750±125	0.37±0.07		231.5	AT18	0.93	M09
7063	Poss+	0	5750±125	0.9±0.16		141.3	AT18	3.96	SF20
7064	Poss+	0	6250±125	1.55±0.29		96.1	AT18	2.52	SF20
7067	Poss+	0	5750±125	0.77±0.14		142.7	AT18	5.33	This Work
7068	Poss+	0	6000±125	1.24±0.23		126.3	AT18	3.32	This Work
7069	Poss	0	5000±125	0.32±0.06		51.7	AT18	8.0	M09
7070	Poss+	0	6000±125	1.14±0.21		162.2	AT18	2.59	This Work
7071	Poss+	0	6000±125	1.14±0.21		130.2	AT18	3.75	This Work
7072	Poss+	0	5250±125	0.59±0.11		151.7	AT18	5.22	This Work
7073	Prob+	0	5750±132	0.92±0.17		153.1	AT18	3.69	This Work
7074	Prob+	0	5750±125	0.86±0.16		149.0	AT18	4.24	This Work
7075	Poss+	0	5250±125	0.51±0.1		149.2	AT18	6.9	M09
7076	Poss+	0	5750±125	1.27±0.23		129.0	AT18	2.44	SF20
7077	Poss+	0	6000±125	1.19±0.21		148.1	AT18	3.2	This Work
7078	Poss+	0	5500±134	0.55±0.1		167.9	AT18	5.97	This Work
7079	Prob+	0	5500±125	0.67±0.12		223.9	AT18	1.14	This Work
7080	Poss+	0	6000±125	1.14±0.21		135.2	AT18	4.93	M09
7082	Prob+	0	5750±125	0.93±0.17		151.8	AT18	3.86	SF20
7084	Prob+	0	5750±125	1.02±0.18		129.4	AT18	4.45	M09
7085	Poss+	0	6000±125	1.02±0.19		142.3	AT18	3.97	This Work
7086	Prob+	0	5250±125	0.6±0.11		143.1	AT18	5.46	SF20
7087	Prob+	0	5250±125	0.45±0.08		182.1	AT18	7.14	This Work
7088	Prob+	0	5750±125	0.83±0.15		132.5	AT18	4.63	This Work
7089	Prob+	0	5500±125	0.81±0.15		182.4	AT18	2.14	N15
7090	Poss+	0	5250±125	0.52±0.09		292.7	AT18	1.01	M09
7092	Prob+	0	4750±125	0.39±0.07		122.7	AT18	6.54	M09

Continuation of Table A.6

ID	Membership Class	Binary	T_{eff} (K)	L (L_{\odot})	Limit flag on $EW(Li)$	$EW(Li)$ ($m\text{\AA}$)	$EW(Li)$ Source	Prot (d)	Prot Source
7094	Prob+	0	5750±125	0.77±0.14		125.2	AT18	4.83	M09
7095	Prob+	0	5500±125	0.65±0.12		100.2	AT18	5.69	This Work
7097	Poss+	0	6250±125	1.37±0.25		122.7	AT18	2.86	This Work
7098	Poss+	0	5750±125	1.3±0.24		94.3	AT18	4.17	SF20
7099	Prob+	0	5750±125	0.97±0.18		151.5	AT18	3.44	M09
7100	Prob+	1	5000±125	0.47±0.08		114.8	AT18	6.16	L16
7101	Prob+	0	5750±125	0.7±0.13		120.9	AT18	5.22	This Work
7102	Prob+	0	6000±125	1.19±0.21		143.2	AT18	3.25	L16
7103	Prob+	0	5750±125	0.98±0.18		148.1	AT18	-99.0	
7104	Prob+	0	5250±125	0.43±0.08		141.1	AT18	6.19	L16
7106	Prob+	0	6000±125	1.36±0.25		134.7	AT18	2.99	SF20
7107	Poss	0	4750±125	0.24±0.04		155.0	This Work	5.59	M09
7108	Prob	0	4500±125	0.18±0.03		50.9	This Work	-99.0	
7110	Poss+	0	5250±125	0.44±0.08		125.5	AT18	6.6	SF20
7111	Prob	0	4500±125	0.19±0.04		147.0	Je21	0.75	This Work
7112	Poss	1	5000±125	0.68±0.13		164.0	Je21	4.37	M09
7113	Poss	0	5000±125	0.4±0.07		9.0	Je21	-99.0	
7114	Poss+	0	5000±125	0.79±0.15		146.0	Je21	4.45	M09
7115	Poss+	1	5750±125	0.91±0.16		210.0	Je21	1.11	M09
7116	Poss	0	5500±125	0.92±0.17		71.0	Je21	8.06	L16
7117	Prob	1	6000±125	1.17±0.21		157.0	Je21	5.86	This Work
7118	Poss	1	4750±125	0.5±0.1		257.0	Je21	1.11	This Work
7119	Prob	0	4500±125	0.16±0.03		49.0	Je21	9.35	M09
7120	Poss	1	6000±125	1.0±0.18		62.0	Je21	2.76	This Work
7121	Prob	0	5500±125	0.59±0.11		233.0	Je21	0.93	This Work
7122	Poss	1	4250±125	0.28±0.05		93.0	Je21	0.37	M09
7123	Poss	0	5500±125	0.66±0.12		65.0	Je21	-99.0	
7124	Poss	0	6250±125	2.21±0.4		57.0	Je21	7.75	M09
7125	Poss	0	4250±125	0.15±0.03		36.0	Je21	3.46	L16
7126	Poss	1	5250±125	0.45±0.08		37.0	Je21	6.17	This Work
7127	Poss	1	5500±125	1.28±0.23		123.0	Je21	2.48	M09
7128	Poss	0	5750±125	0.79±0.15		18.0	Je21	-99.0	
7129	Poss	1	5250±125	0.65±0.12		33.0	Je21	-99.0	
7131	Poss	0	5250±125	0.79±0.14		4.0	Je21	9.81	L16
7132	Poss	1	5750±125	0.77±0.14		65.0	Je21	0.58	L16
7133	Poss	0	5500±125	0.87±0.16		69.0	Je21	3.44	SF20
7134	Poss	0	5250±125	0.76±0.14		-8.0	Je21	22.54	L16
7135	Poss	1	5500±125	0.59±0.11		14.0	Je21	0.16	This Work
7136	Poss+	1	5500±125	1.87±0.34		137.0	Je21	0.56	M09
7137	Poss	0	4500±125	0.19±0.03		31.0	Je21	4.75	L16
7138	Poss	1	4000±125	0.2±0.04		-0.0	Je21	6.45	M09
7147	Poss	0	4750±125	0.43±0.08		237.0	Je21	1.96	SF20

Appendix B

Coma Berenices tables

Table B.1: Designations, coordinates, binary status, and source of the spectroscopic information for the Coma Berenices sample presented in this work.

ID	$\alpha(2000)$ hh:mm:ss	$\delta(2000)$ dd:mm:ss	EW(Li) source	Wide Binary	Spectroscopic Binary	Photometric Binary
2MASS J12083610+3106098	12:08:36.10	+31:06:09.76	SOPHIE	0	0	0
AV 189	12:07:57.72	+25:35:11.39	CAFE	1	0	0
BD+20 2671	12:02:26.62	+20:07:22.75	FIES	0	0	0
BD+21 2335	11:36:51.71	+20:32:33.8	CAFE	0	0	0
BD+23 2472	12:33:20.01	+22:24:23.49	CAFE	1	0	0
BD+24 2462	12:27:20.69	+23:19:47.46	ESPADONS	0	0	0
BD+25 2455	12:04:23.28	+24:49:14.48	CAFE	0	0	0
BD+25 2511	12:29:40.92	+24:31:14.64	J99	0	1	1
BD+26 2342	12:24:05.73	+26:07:42.92	F01	1	0	0
BD+26 2362	12:33:42.12	+25:56:33.96	ESPADONS	1	0	0
BD+27 2121	12:23:41.83	+26:36:05.40	F01	1	1	0
BD+27 2130	12:26:05.47	+26:44:38.31	ELODIE	1	1	1
BD+27 2139	12:28:56.43	+26:32:57.40	ESPADONS	0	0	0
BD+28 2119	12:28:21.11	+28:02:26.09	ELODIE	1	0	0
BD+29 2215	11:48:37.70	+28:16:30.53	ESPADONS	1	0	0
BD+29 2290	12:27:48.30	+28:11:39.89	ELODIE	0	0	0
BD+29 2346	12:57:36.87	+28:58:44.73	CAFE	1	0	0
BD+31 2571	14:00:14.71	+30:56:49.77	CAFE	0	0	0
BD+36 2278	12:32:31.07	+35:19:52.31	ELODIE	0	0	0
HD 105863	12:11:07.38	+25:59:24.63	F01	0	0	0
HD 114400	13:09:55.26	+33:43:18.71	ELODIE	0	0	0
StKM 1-980	11:55:02.94	+24:15:41.16	SOPHIE	0	0	0
TYC 293-747-1	12:46:03.14	+04:52:08.16	CAFE	1	0	0

Continuation of Table B.1

ID	$\alpha(2000)$ hh:mm:ss	$\delta(2000)$ dd:mm:ss	EW(Li) source	Wide Binary	Spectroscopic Binary	Photometric Binary
TYC 1457-1029-1	13:10:46.80	+22:09:10.84	CAFE	0	0	0
TYC 1461-326-1	13:26:21.97	+17:35:13.64	CAFE	1	0	0
TYC 1978-964-1	11:07:33.96	+25:49:40.51	CAFE	0	0	0
TYC 1987-169-1	11:55:33.37	+29:43:41.72	CAFE	1	0	0
TYC 1988-920-1	12:11:35.16	+29:22:44.51	CAFE	0	0	0
TYC 1989-49-1	12:21:15.62	+26:09:14.05	CAFE	0	0	0
TYC 1991-1034-1	12:27:06.26	+26:50:44.50	J99	0	0	0
TYC 2004-745-1	13:39:18.35	+28:51:33.21	CAFE	1	0	0
TYC 2010-1021-1	14:19:18.28	+26:19:17.81	CAFE	0	0	0
TYC 3040-613-1	14:04:38.86	+43:40:43.41	CAFE	1	0	0
UCAC4 554-047403	11:24:13.46	+20:40:36.46	SOPHIE	0	0	0
UCAC4 561-053267	13:10:47.24	+22:09:08.28	SOPHIE	0	0	0
UCAC4 577-048376	12:49:00.42	+25:21:35.57	FIES	1	0	0
UCAC4 597-049432	13:18:41.66	+29:15:02.95	SOPHIE	1	0	0

Table B.2: Rotation periods obtained for our Coma Berenices sample.

ID	TIC ID	Prot (d) TESS two-minute LCs	Prot(d) TESS FFIs	Prot (d) C09	Prot (d) T14	Final Prot
BD+25 2511	328978508	3.68	3.54			3.68
BD+20 2671	229655624	4.6	8.23			4.6
TYC 1457-1029-1	98428123	4.89	9.37			4.89
UCAC4 561-053267	98428122	6.33	9.87			6.33
AV 189	4701976	6.84	10.28	10.28		6.84
StKM 1-980	138895417	6.84				6.84
BD+36 2278	138973933	7.34	7.56	7.69		7.34
TYC 1461-326-1	27225565	7.56	8.7			7.56
TYC 3040-613-1	198154025	7.69	7.79			7.69
HD 105863	4734708	7.76	7.62			7.76
BD+29 2346	359121291	7.77	7.76	7.94		7.77
BD+26 2362	406754901	8.06	8.45	8.38		8.06
BD+24 2462	135153201	8.06	8.9	9.05		8.06
TYC 1991-1034-1	393800469		8.18			8.18
HD 114400	166009976	8.25	8.24			8.25
BD+31 2571	166677206	8.53	9.14			8.53
BD+23 2472	159163098	8.69	8.47	8.33		8.69
BD+25 2455	4667622	8.76	8.9			8.76
BD+21 2335	198282535	8.76	8.8			8.76
BD+29 2290	393801140	8.86	8.87	8.65		8.86
BD+29 2215	307751624	8.86	9.12	9.43		8.86
BD+28 2119	393807209	8.86	8.69			8.86
BD+27 2130	393798833		9.07		8.81	9.07
TYC 2010-1021-1	156617016	9.3	10.3			9.3
TYC 1978-964-1	284019067	9.37	9.62			9.37
BD+27 2139	393808026	9.48	9.46	(4.79)	9.483	9.48
TYC 293-747-1	380673047		9.68			9.68
TYC 2004-745-1	159187561	9.98	10.39			9.98
TYC 1988-920-1	356685135	10.2	10.19	10.37		10.2
UCAC4 577-048376	160010638	10.3	12.18	12.27		10.3
BD+26 2342	285117524	10.6	8.7			10.6
TYC 1989-49-1	356702360	10.8	10.81	10.88	1.098	10.8
TYC 1987-169-1	138896513	12.0	11.27	11.55		12.0
UCAC4 597-049432	305835973	12.4	11.05			12.4
2MASS J12083610+3106098	139053408	12.6	11.45	11.92		12.6
UCAC4 554-047403	3890292	12.9	12.41			12.9

Table B.3: Li EW, effective temperature, luminosity, and rotation period for our Coma Berenices sample.

ID	T_{eff} (K)	σ_{Teff} (K)	L (L_{\odot})	σ_L (L_{\odot})	EW(Li) (mÅ)	$\sigma_{EW(Li)}$ (mÅ)	EW(Li) source	Prot (d)
2MASS J12083610+3106098	4250	125	0.133	0.001	≤ 3.4		SOPHIE	12.6
TYC 1989-49-1	4750	125	0.211	0.001	≤ 12.1		CAFE	10.8
BD+20 2671	5750	125	0.793	0.003	79.5	35.3	FIES	4.6
BD+21 2335	5500	125	0.544	0.002	23.4	17.8	CAFE	8.76
BD+23 2472	5000	125	0.527	0.003	28.7	14.4	CAFE	8.69
BD+24 2462	5250	125	0.476	0.001	21.2	1.8	ESPADONS	8.06
BD+25 2455	5500	125	0.539	0.002	20.0	14.1	CAFE	8.76
BD+26 2342	5250	125	0.476	0.002	25.0	1.0	F01	10.6
BD+26 2362	5250	125	0.461	0.008	30.0	1.8	ESPADONS	8.06
BD+27 2121	5500	125	1.366	0.015	49.7		F01	
BD+27 2130	5250	125	1.025	0.038	34.4	24.6	ELODIE	9.07
BD+27 2139	4500	125	0.361	0.001	8.3	3.7	ESPADONS	9.48
BD+28 2119	4750	125	0.479	0.001	≤ 24.8		ELODIE	8.86
BD+29 2215	5250	125	0.494	0.002	25.1	1.7	ESPADONS	8.86
BD+29 2290	5500	125	0.8	0.003	59.5	33.8	ELODIE	8.86
BD+29 2346	5500	125	0.556	0.006	45.2	19.3	CAFE	7.77
BD+31 2571	5250	125	0.485	0.001	≤ 31.2		CAFE	8.53
BD+36 2278	5750	125	0.855	0.003	100.0	59.6	ELODIE	7.34
TYC 1991-1034-1	5500	125	0.763	0.003	66.0		J99	8.18
AV 189	4250	125	0.314	0.007	≤ 5.6		CAFE	6.84
HD 105863	5500	125	0.967	0.004	72.5		F01	7.76
HD 114400	5750	125	0.888	0.002	83.7	43.9	ELODIE	8.25
StKM 1-980	4000	125	0.126	0.001	≤ 4.2		SOPHIE	6.84
TYC 293-747-1	5000	125	0.338	0.001	≤ 5.1		CAFE	9.68
TYC 1457-1029-1	5250	125	0.486	0.002	≤ 38.3		CAFE	4.89
TYC 1461-326-1	5500	125	0.526	0.003	52.3	17.5	CAFE	7.56
TYC 1978-964-1	5000	125	0.292	0.005			CAFE	9.37
TYC 1987-169-1	4500	125	0.233	0.003	≤ 28.9		CAFE	12.0
TYC 1988-920-1	4750	125	0.263	0.001	≤ 15.9		CAFE	10.2
TYC 2004-745-1	4250	125	0.232	0.015	≤ 13.1		CAFE	9.98
TYC 2010-1021-1	4750	125	0.216	0.001	≤ 12.4		CAFE	9.3
TYC 3040-613-1	5500	125	0.598	0.007	49.1	26.9	CAFE	7.69
UCAC4 554-047403	4250	125	0.125	0.004	≤ 4.0		SOPHIE	12.9
UCAC4 561-053267	4500	125	0.245	0.001	≤ 2.2		SOPHIE	6.33
UCAC4 577-048376	4250	125	0.155	0.001	≤ 14.9		FIES	10.3
UCAC4 597-049432	4250	125	0.167	0.001	≤ 2.4		SOPHIE	12.4
BD+25 2511	5000	125	0.952	0.003	63.6		J99	3.68

Appendix C

Praesepe tables

Table C.1: Designations, coordinates, binary status, and source of the spectroscopic information for the Praesepe sample presented in this work.

ID	$\alpha(2000)$ hh:mm:ss	$\delta(2000)$ dd:mm:ss	EW(Li) source	Wide Binary	Spectroscopic Binary	Photometric Binary
KW 325	08:40:41.90	+19:13:25.44	CAFE	1	1	0
KW 495	08:43:05.94	+19:26:15.29	CAFE	0	1	1
KW 466	08:42:32.26	+19:23:46.26	C17	0	1	0
KW 335	08:40:48.32	+19:55:18.91	C17	0	0	0
KW 182	08:39:30.42	+20:04:08.58	C17	0	1	1
KW 432	08:41:55.87	+19:41:22.85	C17	0	0	0
KW 301	08:40:27.44	+19:16:40.92	C17	0	0	0
KW 365	08:41:07.36	+19:04:16.38	CAFE	1	1	1
BD+18 2049	08:49:59.98	+18:21:54.03	CAFE	0	0	0
KW 58	08:37:52.09	+19:59:13.86	C17	0	0	0
TYC 1387-945-1	08:29:13.51	+19:28:47.99	CAFE	0	0	0
TYC 1398-2191-1	08:41:59.24	+20:55:07.16	FIES	0	1	0
KW 3655	08:48:01.74	+18:40:37.64	FIES	1	0	1
KW 23	08:37:11.49	+19:48:13.24	C17	0	0	0
KW 30	08:37:22.23	+20:10:37.24	C17	0	0	0
KW 326	08:40:42.48	+19:33:57.62	C17	0	0	0
KW 164	08:39:14.99	+20:12:38.78	C17	0	1	0
TYC 1396-1240-1	08:48:27.84	+18:20:43.90	FIES	0	1	0
KW 90	08:38:14.27	+19:21:55.37	CAFE	0	1	1
KW 488	08:43:00.55	+20:20:16.10	C17	0	0	0
KW 367	08:41:09.60	+19:51:18.66	FIES	1	1	1
TYC 1396-40-1	08:45:13.10	+19:41:12.80	CAFE	0	1	0
KW 336	08:40:47.61	+18:54:11.93	C17	0	1	0

Continuation of Table C.1

ID	$\alpha(2000)$ hh:mm:ss	$\delta(2000)$ dd:mm:ss	EW(Li) source	Wide Binary	Spectroscopic Binary	Photometric Binary
KW 304	08:40:31.84	+20:12:06.02	C17	0	0	0
KW 434	08:41:54.38	+19:15:26.59	C17	1	1	0
KW 368	08:41:10.31	+19:49:07.01	C17	1	1	0
KW 334	08:40:47.98	+19:39:32.16	C17	0	1	1
KW 309	08:40:31.69	+19:51:01.01	FIES	0	0	0
KW 476	08:42:42.50	+19:05:58.95	C17	0	1	0
KW 498	08:43:10.77	+19:31:34.64	C17	0	1	0
KW 257	08:40:06.36	+19:18:26.51	C17	0	1	1
KW 70	08:37:57.04	+19:14:10.37	C17	0	0	0
2MASS J08490670+1941113	08:49:06.71	+19:41:11.41	FIES	0	0	0
2MASS J08450735+2023418	08:45:07.35	+20:23:41.93	CAFE	0	0	0
KW 263	08:40:09.68	+19:37:17.10	C17	0	0	0
KW 1184	08:35:56.95	+20:49:34.73	CAFE	1	0	0
KW 430	08:41:51.99	+20:10:01.15	C17	0	1	0
KW 344	08:40:54.87	+19:56:06.64	C17	0	0	0
KW 349	08:40:56.69	+19:44:05.18	C17	0	0	0
KW 246	08:40:04.16	+19:47:04.01	CAFE	1	1	0
KW 448	08:42:11.50	+19:16:37.24	C17	0	1	0
KW 55	08:37:49.98	+19:53:28.88	CAFE	1	1	1
KW 313	08:40:33.46	+19:38:00.94	C17	0	0	0
KW 48	08:37:46.41	+19:35:57.47	C17	0	0	0
KW 79	08:38:07.58	+19:59:16.34	C17	0	1	0
KW 363	08:41:07.25	+19:26:48.90	C17	0	0	0
KW 529	08:43:38.81	+22:16:09.48	FIES	0	1	0
KW 172	08:39:21.85	+19:51:40.31	C17	0	0	0
KW 547	08:40:37.87	+18:42:00.31	FIES	0	0	1
KW 209	08:39:47.07	+19:49:39.44	C17	0	0	0
KW 198	08:39:38.37	+19:26:27.08	C17	0	0	0
KW 237	08:39:59.98	+19:34:40.48	C17	0	0	0
KW 183	08:39:29.40	+19:47:11.78	C17	0	1	1
KW 299	08:40:27.51	+19:39:19.77	C17	0	0	0
KW 272	08:40:15.71	+19:54:54.35	C17	0	1	1

Table C.2: Rotation periods obtained for our Praesepe sample.

ID	Prot (d) R21	Prot (d) K14	Final Prot (d)
2MASS J08450735+2023418	10.8		10.8
2MASS J08490670+1941113	9.73	9.72	9.73
BD+18 2049	8.81		8.81
KW 23	8.55		8.55
KW 30	7.88		7.88
KW 48	9.29		9.29
KW 58	8.06		8.06
KW 70	9.03		9.03
KW 79	9.03		9.03
KW 1184	1.22		1.22
KW 164	8.25		8.25
KW 172	12.4		12.4
KW 182	7.05		7.05
KW 183	13.36		13.36
KW 198	11.59		11.59
KW 209	10.32		10.32
KW 237	10.73		10.73
KW 246	10.44	10.39	10.44
KW 257	7.79		7.79
KW 263	7.95		7.95
KW 272	10.16		10.16
KW 299	11.83		11.83
KW 301	7.85		7.85
KW 304	9.14		9.14
KW 309	8.46	8.43	8.46
KW 313	9.11		9.11
KW 325	6.03	6.24	6.03
KW 326	8.28		8.28
KW 334	7.24		7.24
KW 335	7.92		7.92
KW 336	8.89		8.89
KW 344	9.14		9.14
KW 349	9.06		9.06
KW 363	10.08		10.08
KW 365	9.2		9.2
KW 3655	2.96	5.85	2.96
KW 367	3.21	6.04	3.21
KW 368	9.4		9.4

Continuation of Table C.2

ID	Prot (d) R21	Prot (d) K14	Final Prot (d)
KW 430	9.54		9.54
KW 432	8.81		8.81
KW 434	4.12		4.12
KW 448	7.87		7.87
KW 466	9.67		9.67
KW 476	8.66		8.66
KW 488	8.89		8.89
KW 495	4.73		4.73
KW 498	9.1		9.1
KW 529	9.06	8.96	9.06
KW 547	2.52		2.52
KW 55	6.84	7.14	6.84
KW 90	7.04	7.01	7.04
TYC 1387-945-1	7.99		7.99
TYC 1396-1240-1		9.19	9.2
TYC 1396-40-1	7.91	7.32	7.91
TYC 1398-2191-1	8.2	8.2	8.2

Table C.3: Li EW, effective temperature, luminosity, and rotation period for our Praesepe sample.

ID	T_{eff} (K)	σ_{Teff} (K)	L (L_{\odot})	σ_L (L_{\odot})	EW(Li) (mÅ)	$\sigma_{EW(Li)}$ (mÅ)	EW(Li) source	Prot (d)
TYC 1387-945-1	5750	125	1.044	0.011	46.7	19.3	CAFE	7.99
BD+18 2049	5750	125	0.944	0.006	53.4	40.9	CAFE	8.81
KW 365	5750	125	2.47	0.014	38.0	26.3	CAFE	9.2
KW 367	5500	125	1.705	0.029	≤ 25.0		FIES	3.21
KW 495	5750	125	3.284	0.074	43.1	27.6	CAFE	4.73
KW 55	5250	125	0.506	0.004			CAFE	6.84
KW 90	5500	125	1.807	0.232	55.4	36.2	CAFE	7.04
KW 309	5500	125	0.696	0.008	≤ 9.4		FIES	8.46
KW 325	5750	125	1.471	0.248	82.9	30.7	CAFE	6.03
KW 246	5250	125	0.478	0.052			CAFE	10.44
KW 1184	5250	125	0.619	0.005	46.7	32.0	CAFE	1.22
TYC 1398-2191-1	5750	125	0.939	0.01	35.1	20.1	FIES	8.2
TYC 1396-1240-1	5750	125	0.757	0.013	≤ 15.3		FIES	9.2
KW 529	5000	125	0.372	0.003			FIES	9.06
KW 547	5000	125	0.597	0.008	≤ 11.5		FIES	2.52
2MASS J08450735+2023418	5250	125	0.555	0.008			CAFE	10.8
TYC 1396-40-1	5500	125	1.157	0.13	50.5	31.4	CAFE	7.91
2MASS J08490670+1941113	5250	125	0.549	0.007	≤ 2.0		FIES	9.73
KW 23	5500	125	0.91	0.007	32.2		C17	8.55
KW 30	5750	125	0.845	0.009	46.0	1.8	C17	7.88
KW 48	5250	125	0.371	0.002	5.8		C17	9.29
KW 58	5750	125	0.932	0.009	49.9		C17	8.06
KW 70	5500	125	0.589	0.007	30.4		C17	9.03
KW 79	5000	125	0.411	0.022	4.8		C17	9.03
KW 164	5750	125	0.959	0.013	42.4		C17	8.25
KW 172	5250	125	0.336	0.002	6.8		C17	12.4
KW 182	5750	125	2.276	0.026	89.2		C17	7.05
KW 183	4750	125	0.395	0.012	5.9		C17	13.36
KW 198	4750	125	0.343	0.004	7.3		C17	11.59
KW 209	5000	125	0.308	0.007	6.3		C17	10.32
KW 237	4750	125	0.275	0.005	5.2		C17	10.73
KW 257	5500	125	1.223	0.02	29.3		C17	7.79
KW 263	5250	125	0.549	0.005	32.2	2.0	C17	7.95
KW 272	4500	125	0.406	0.013	12.4		C17	10.16
KW 299	4750	125	0.224	0.004	7.3		C17	11.83
KW 301	5750	125	1.053	0.018	64.6		C17	7.85
KW 304	5500	125	0.75	0.008	28.8		C17	9.14

Continuation of Table C.3

ID	T_{eff} (K)	σ_{Teff} (K)	L (L_{\odot})	σ_L (L_{\odot})	EW(Li) (mÅ)	$\sigma_{EW(Li)}$ (mÅ)	EW(Li) source	Prot (d)
KW 313	5250	125	0.449	0.004	5.3		C17	9.11
KW 326	5750	125	0.886	0.008	46.1	0.7	C17	8.28
KW 334	5500	125	1.235	0.082	28.6		C17	7.24
KW 335	6000	125	1.135	0.009	77.4	1.0	C17	7.92
KW 336	5500	125	0.842	0.015	33.5		C17	8.89
KW 344	5250	125	0.463	0.014	5.8		C17	9.14
KW 349	5250	125	0.456	0.01	5.4		C17	9.06
KW 363	4750	125	0.366	0.003	6.1		C17	10.08
KW 368	5500	125	0.78	0.016	38.3		C17	9.4
KW 430	5250	125	0.51	0.005	37.3	1.9	C17	9.54
KW 432	5500	125	1.101	0.008	69.6	1.3	C17	8.81
KW 434	5750	125	0.852	0.008	33.7	1.8	C17	4.12
KW 448	5250	125	0.45	0.003	4.9		C17	7.87
KW 466	6000	125	0.88	0.027	86.7	0.8	C17	9.67
KW 476	5500	125	0.672	0.009	36.6	2.2	C17	8.66
KW 488	5500	125	0.803	0.011	35.6		C17	8.89
KW 498	5500	125	0.615	0.007	26.6		C17	9.1
KW 3655	6000	125	1.897	0.013	19.6	17.3	FIES	2.96

Appendix D

Rotation periods derived from TESS light curves for Coma Berenices members

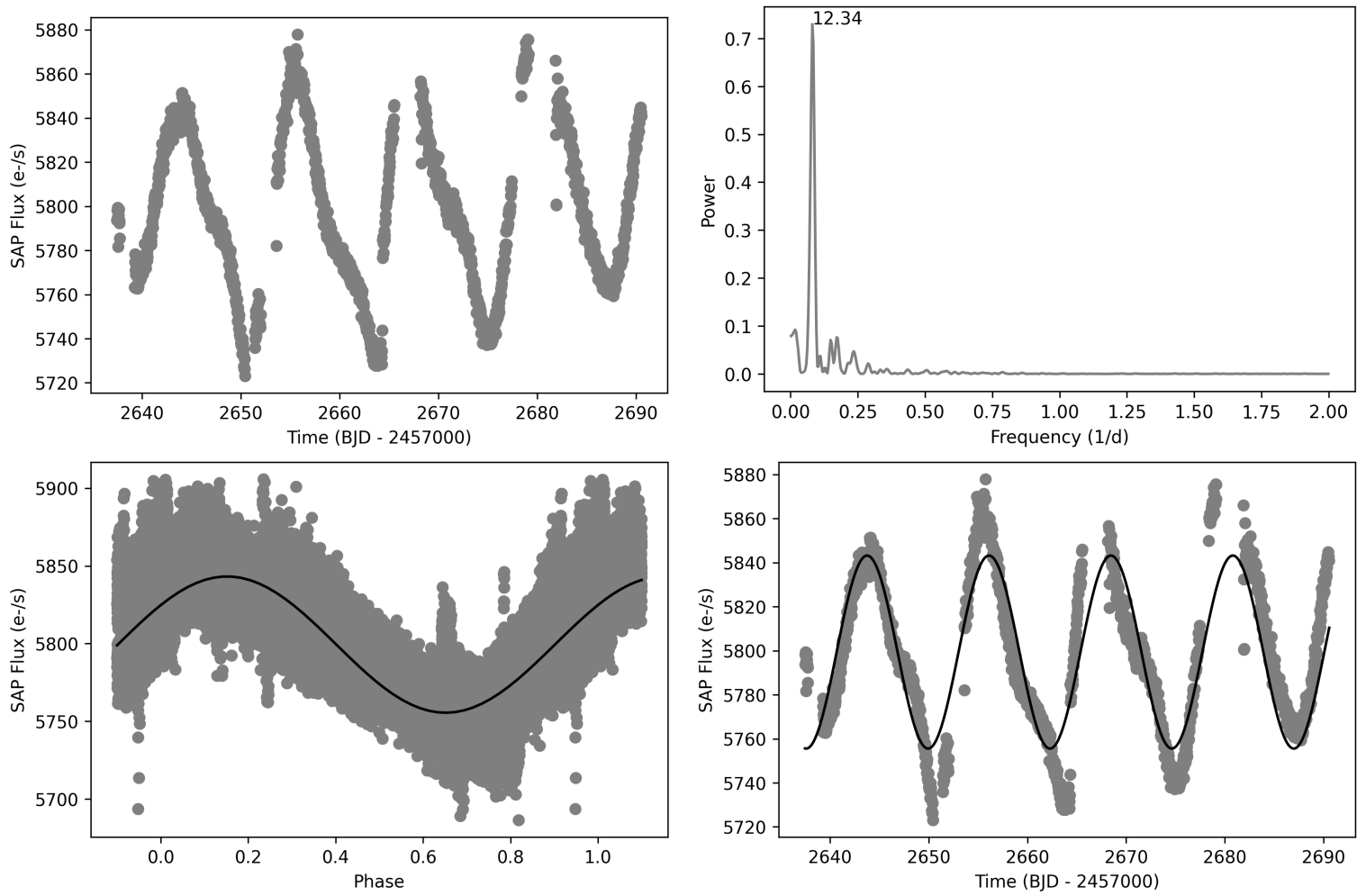


Figure D.1: UCAC4 597-049432. **Top-Left**— Photometry collected by TESS in sectors 49 and 50. **Top-Right**— Lomb-Scargle periodogram. **Bottom-Left**— Phase-folded light curve with period 12.4 d. **Bottom-Right**— 12.4 d period light curve plotted over TESS photometry.

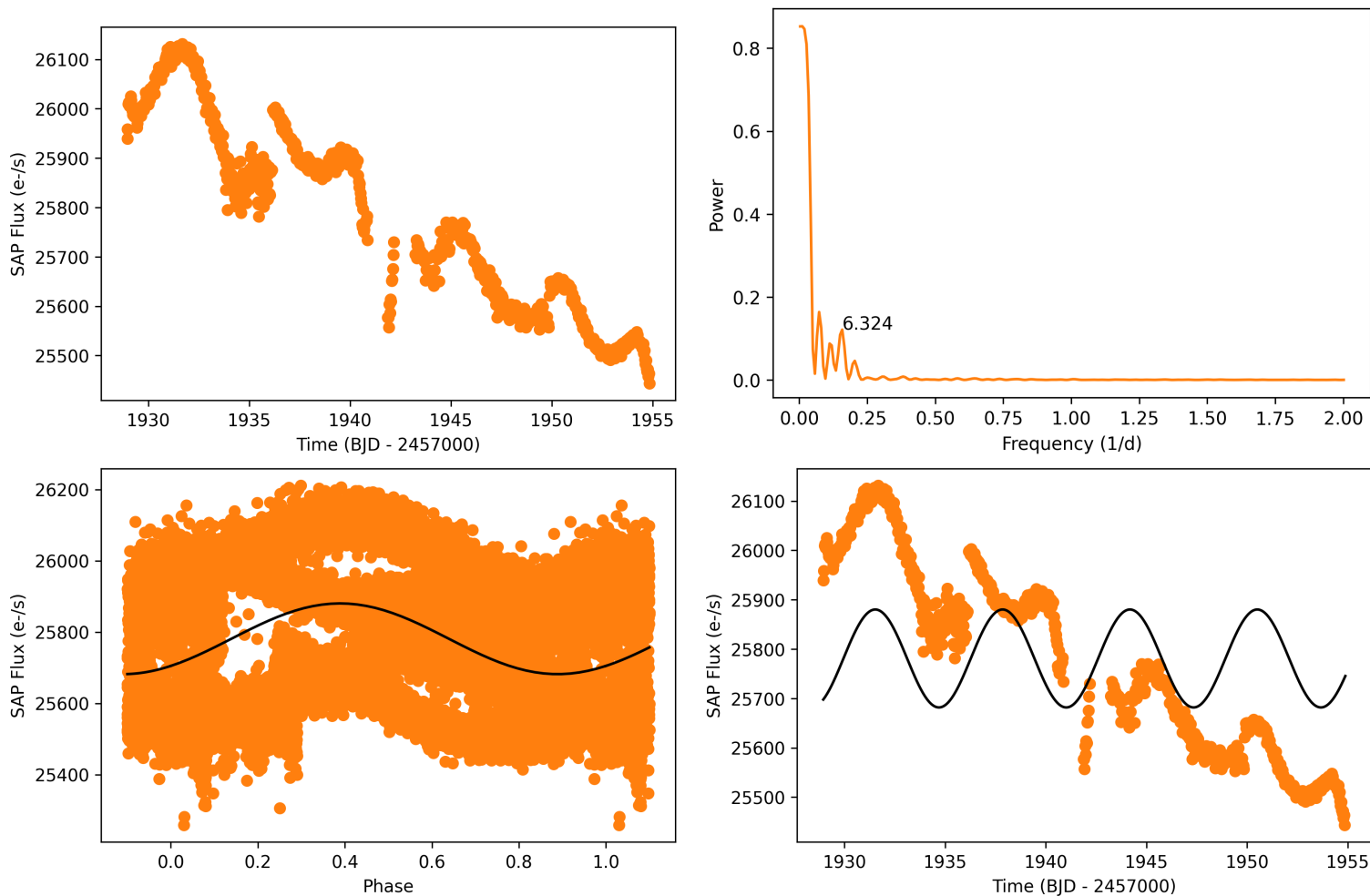


Figure D.2: UCAC4 561-053267. **Top-Left**— Photometry collected by TESS in sector 23. **Top-Right**— Lomb-Scargle periodogram. **Bottom-Left**— Phase-folded light curve with period 6.33 d. **Bottom-Right**— 6.33 d period light curve plotted over TESS photometry.

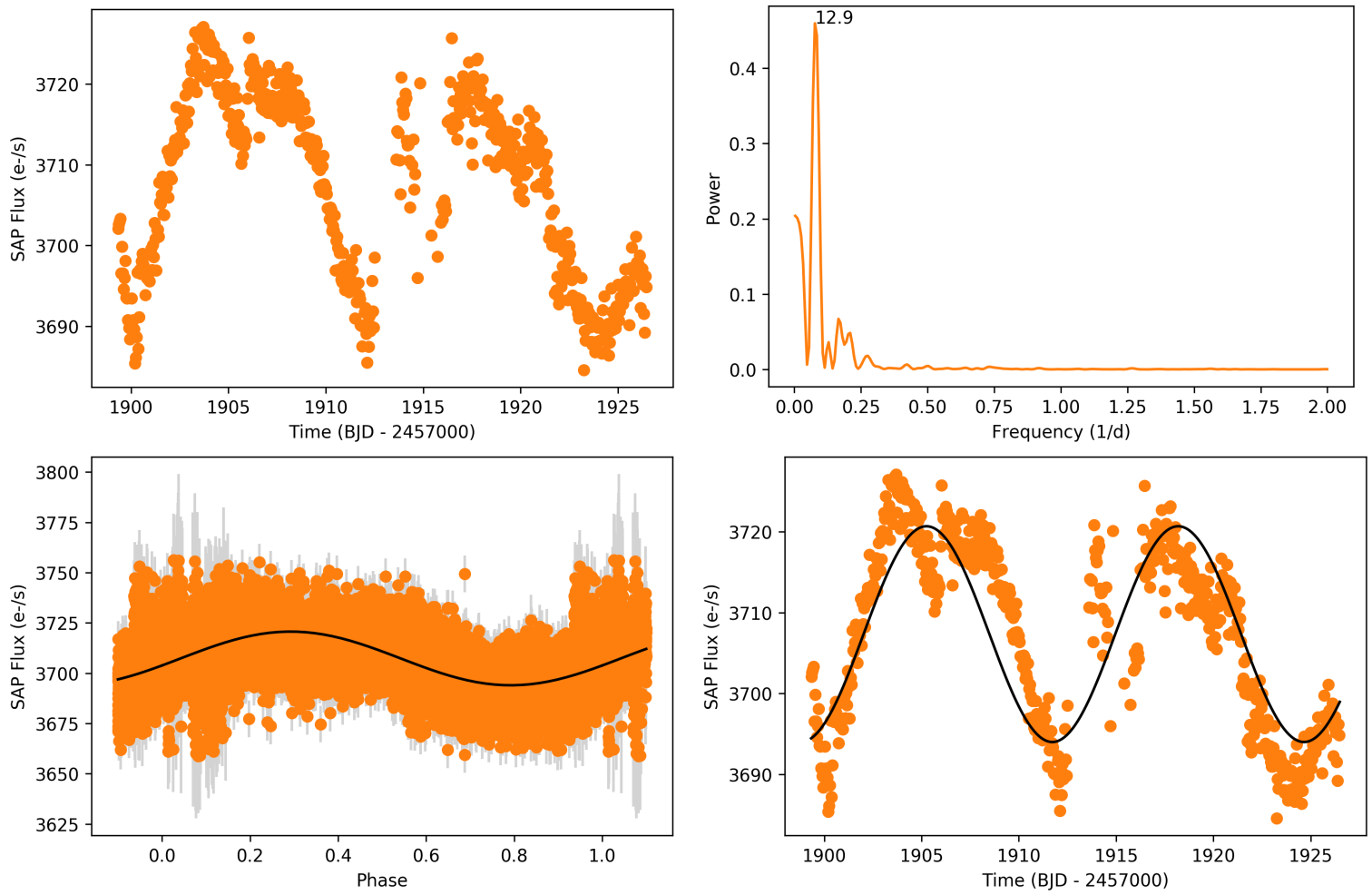


Figure D.3: UCAC4 554-047403. **Top-Left**— Photometry collected by TESS in sector 22. **Top-Right**— Lomb-Scargle periodogram. **Bottom-Left**— Phase-folded light curve with period 12.9 d. **Bottom-Right**— 12.9 d period light curve plotted over TESS photometry.

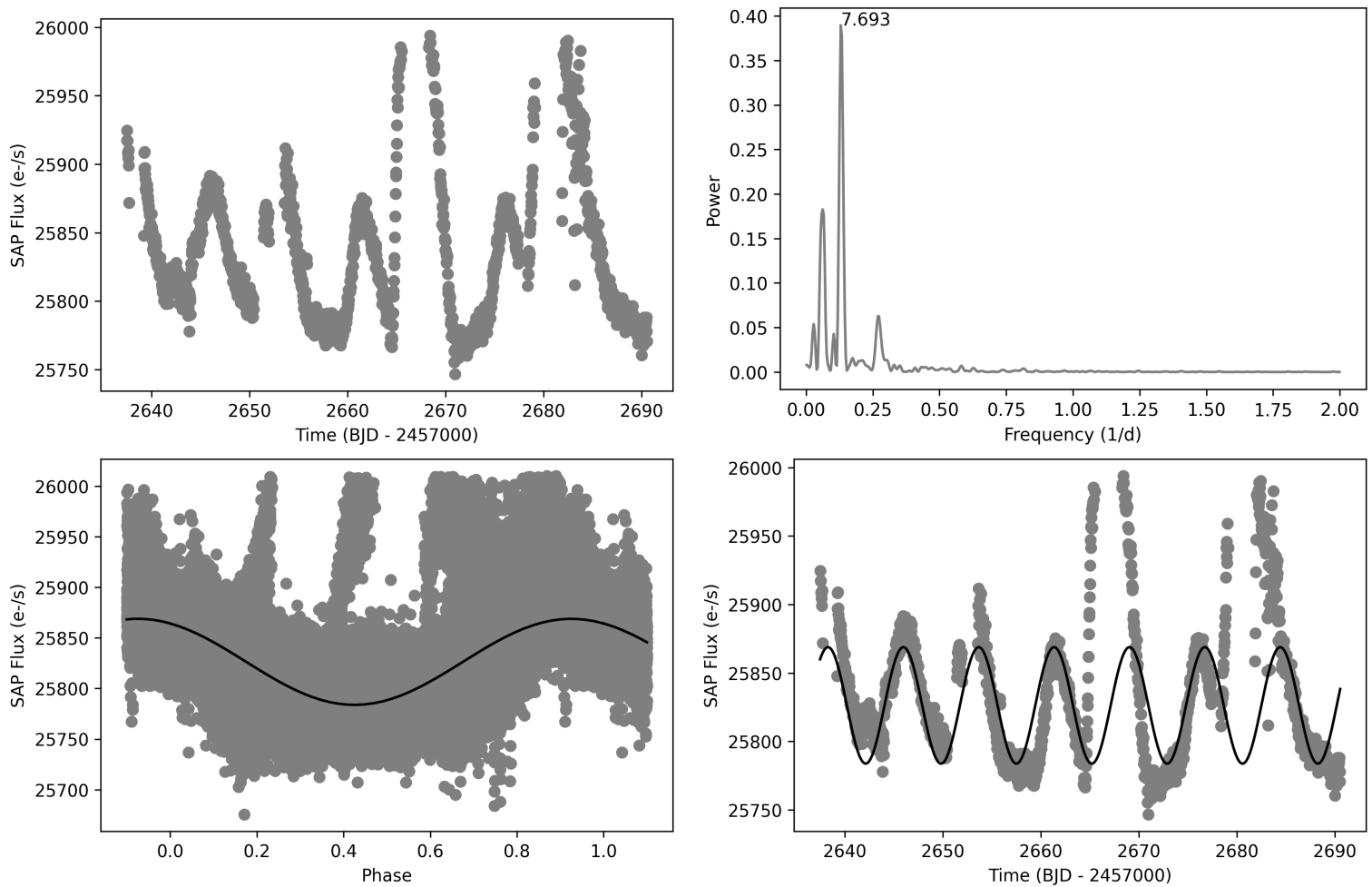


Figure D.4: TYC 3040-613-1. **Top-Left**— Photometry collected by TESS in sectors 49 and 50. **Top-Right**— Lomb-Scargle periodogram. **Bottom-Left**— Phase-folded light curve with period 7.69 d. **Bottom-Right**— 7.69 d period light curve plotted over TESS photometry.

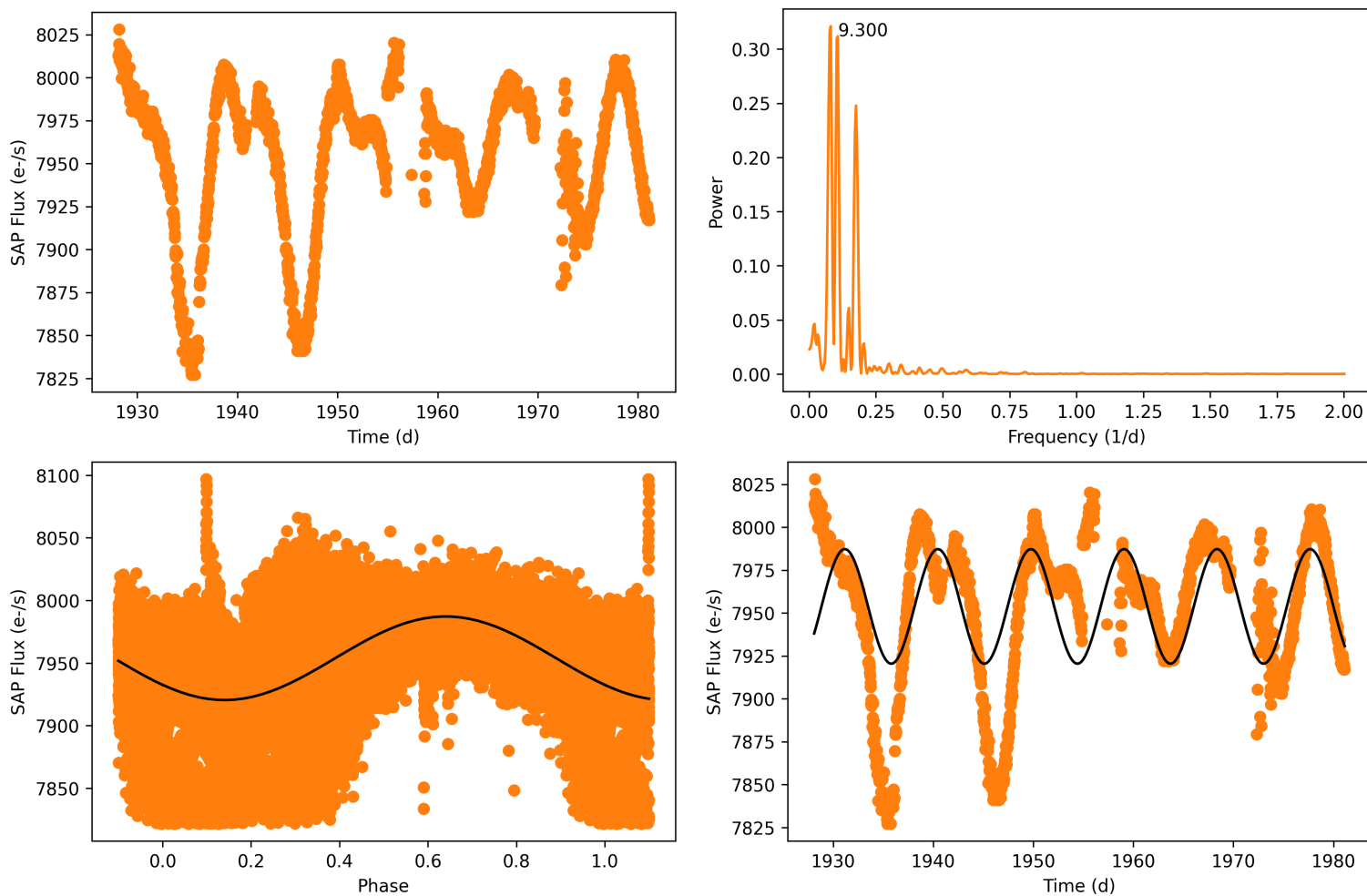


Figure D.5: TYC 2010-1021-1. **Top-Left**— Photometry collected by TESS in sectors 23 and 50. **Top-Right**— Lomb-Scargle periodogram. **Bottom-Left**— Phase-folded light curve with period 9.30 d. **Bottom-Right**— 9.30 d period light curve plotted over TESS photometry.

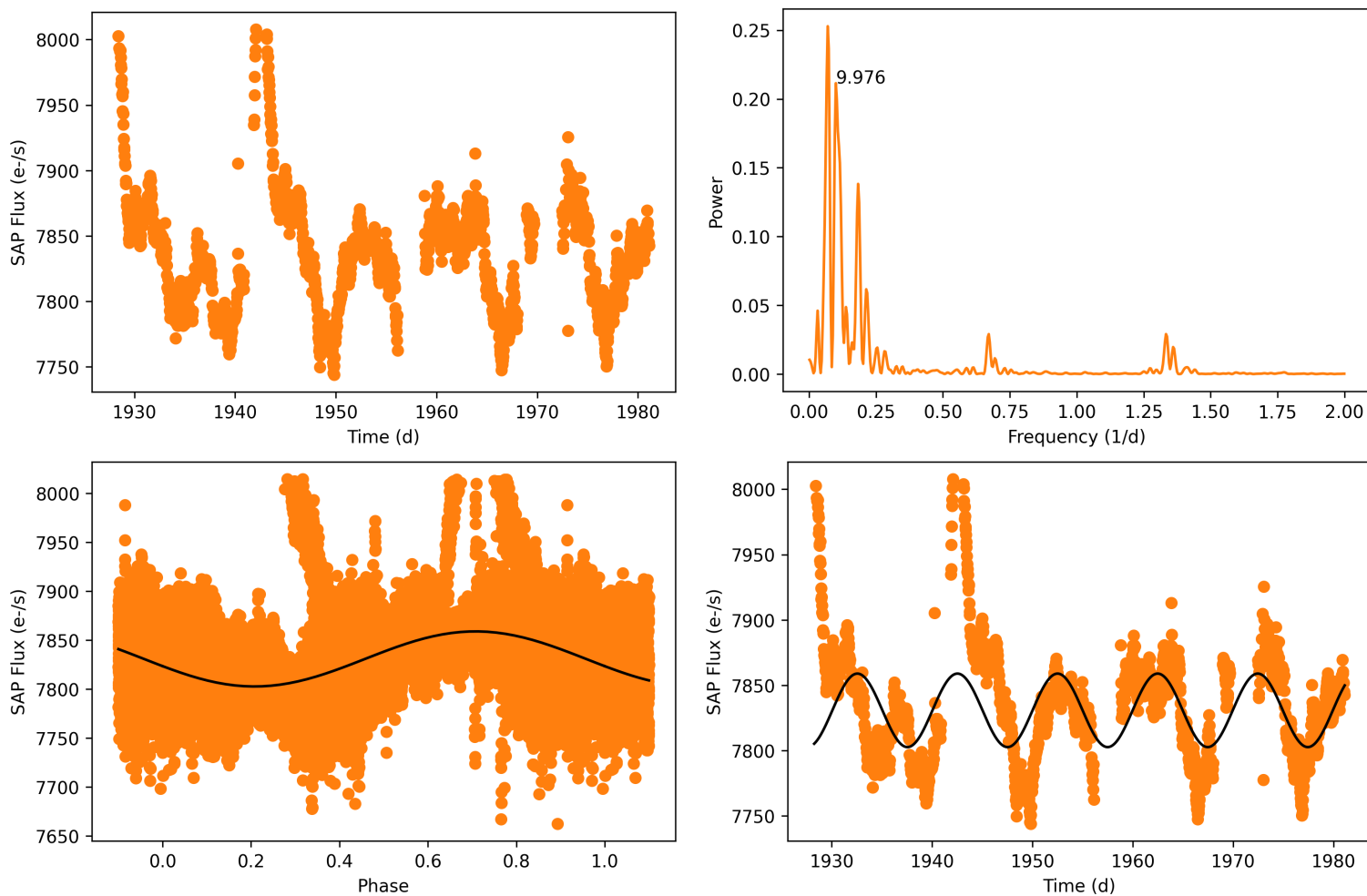


Figure D.6: TYC 2004-745-1. **Top-Left**— Photometry collected by TESS in sectors 23 and 50. **Top-Right**— Lomb-Scargle periodogram. **Bottom-Left**— Phase-folded light curve with period 9.98 d. **Bottom-Right**— 9.98 d period light curve plotted over TESS photometry.

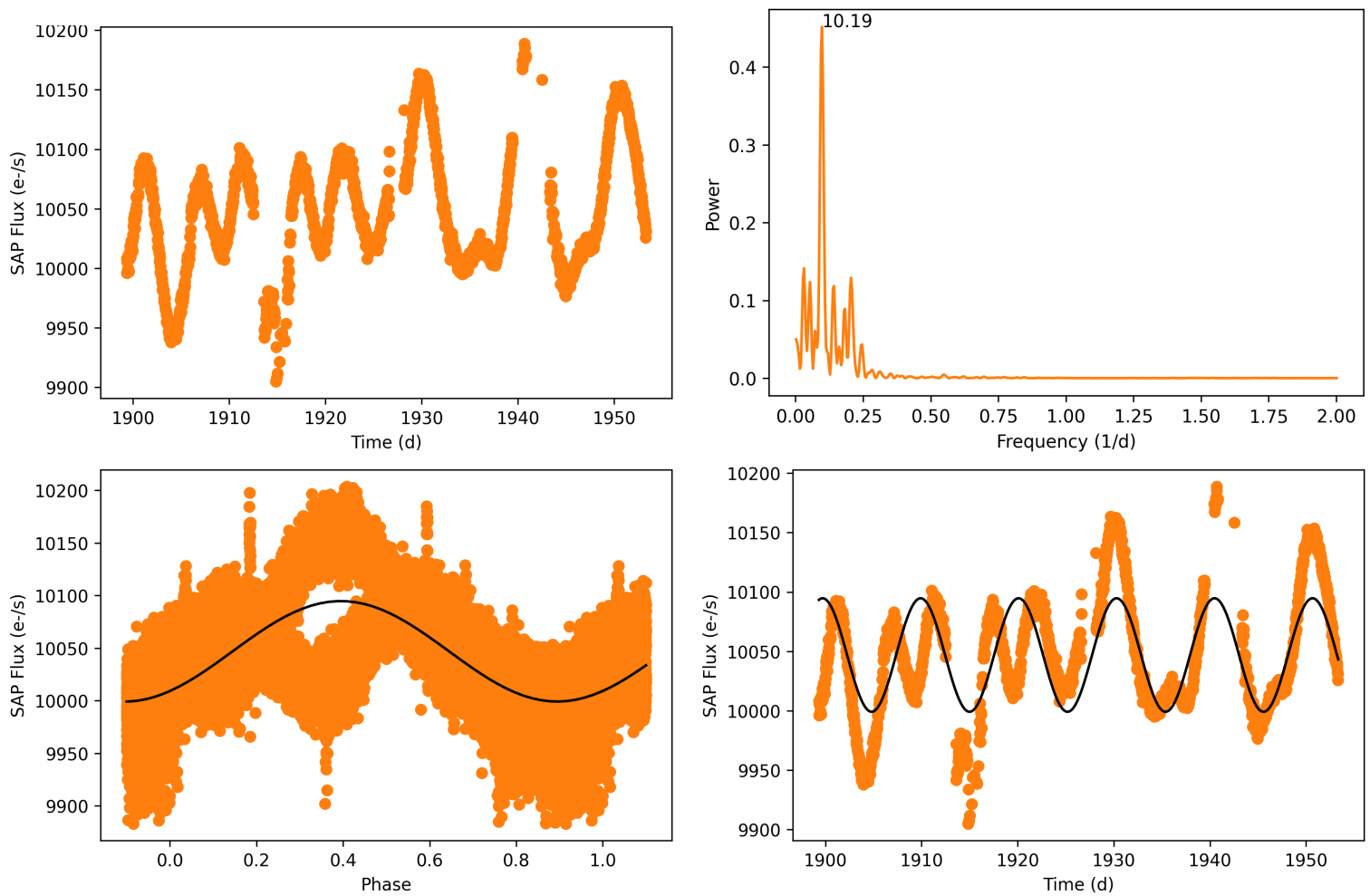


Figure D.7: TYC 1888-920-1. **Top-Left**— Photometry collected by TESS in sectors 22 and 49. **Top-Right**— Lomb-Scargle periodogram. **Bottom-Left**— Phase-folded light curve with period 10.2 d. **Bottom-Right**— 10.2 d period light curve plotted over TESS photometry.

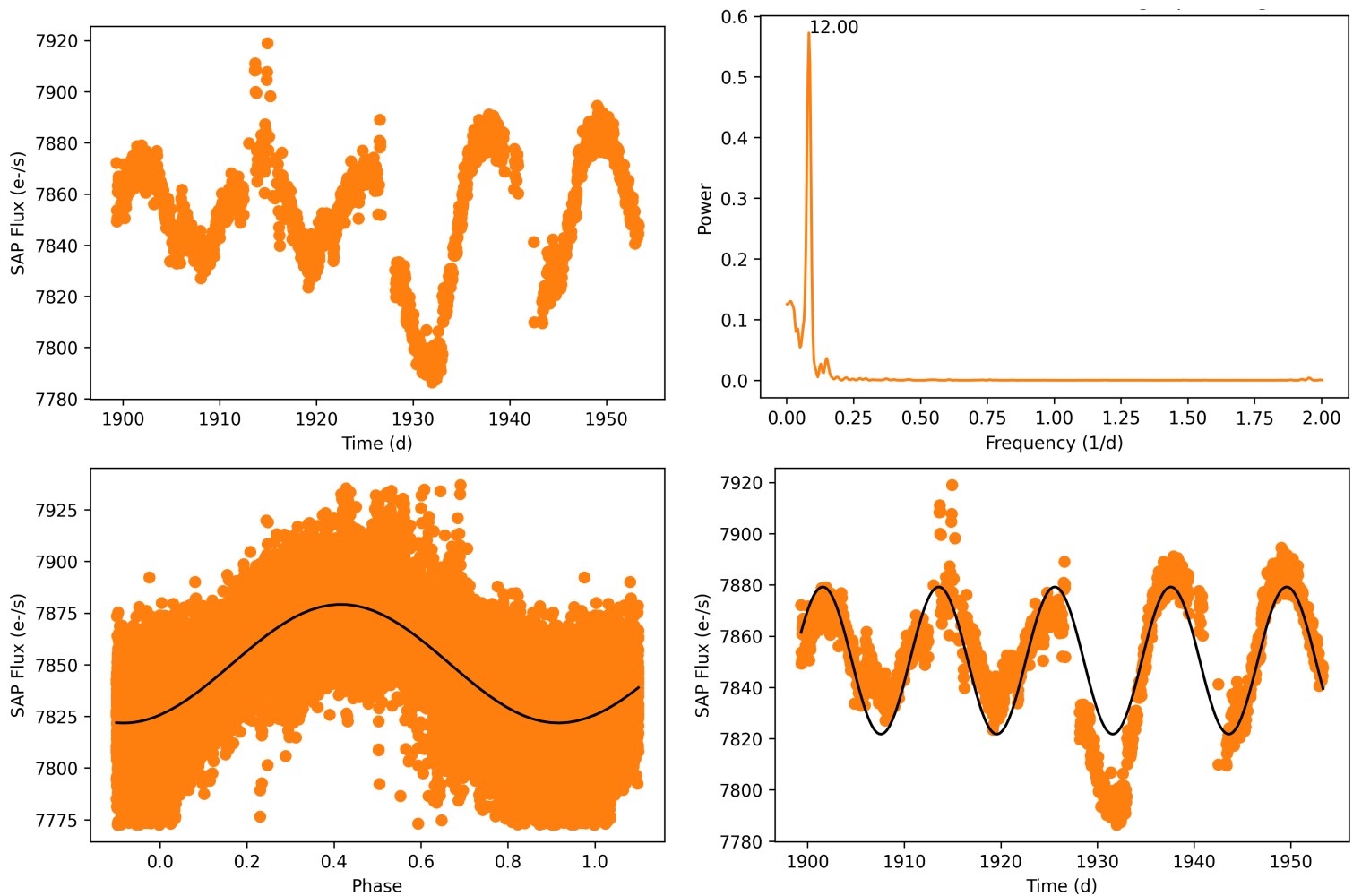


Figure D.8: TYC 1987-169-1. **Top-Left**— Photometry collected by TESS in sectors 22 and 49. **Top-Right**— Lomb-Scargle periodogram. **Bottom-Left**— Phase-folded light curve with period 12.0 d. **Bottom-Right**— 12.0 d period light curve plotted over TESS photometry.

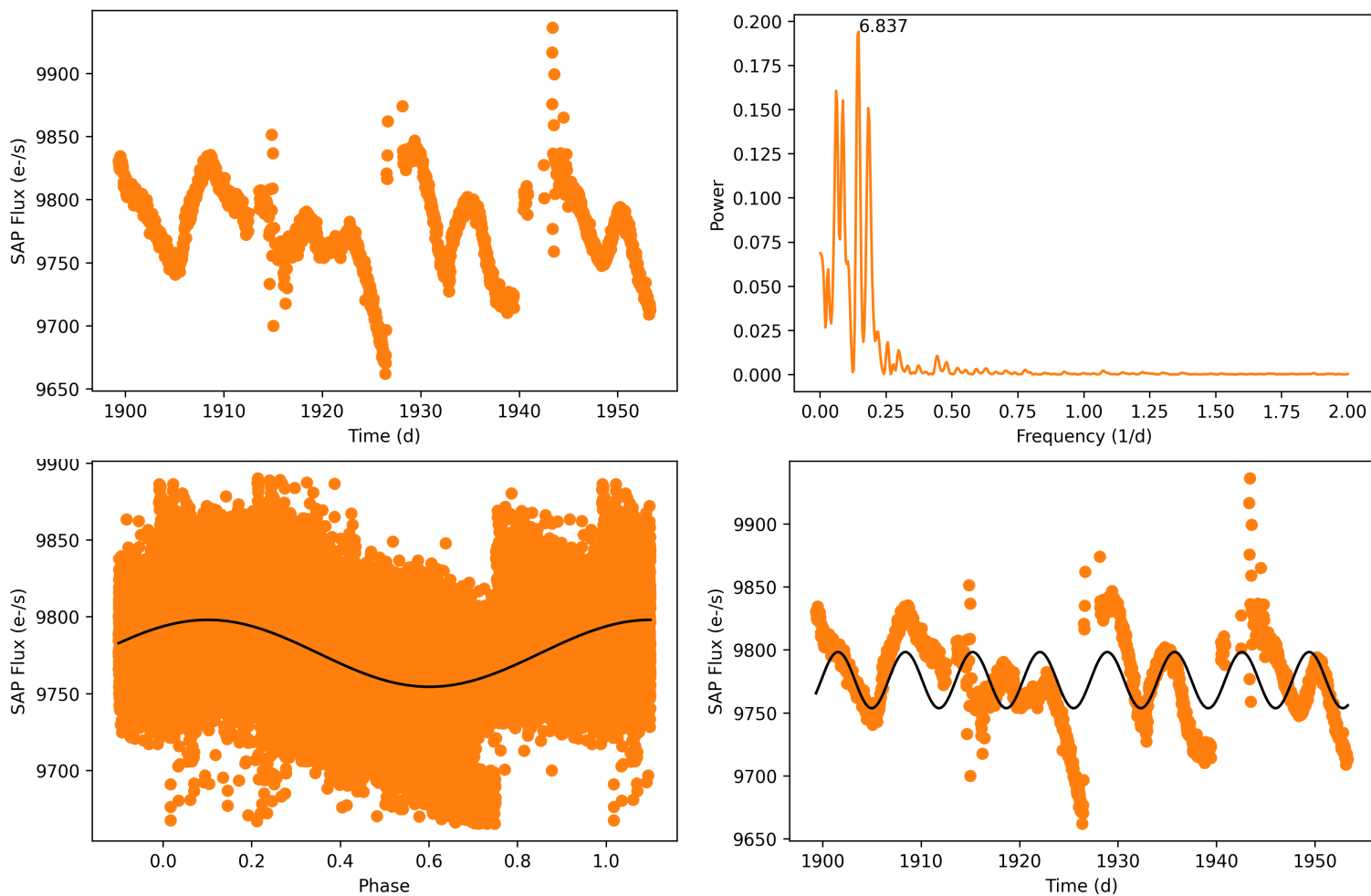


Figure D.9: AV 189. *Top-Left*— Photometry collected by TESS in sectors 22 and 49. *Top-Right*— Lomb-Scargle periodogram. *Bottom-Left*— Phase-folded light curve with period 6.84 d. *Bottom-Right*— 6.84 d period light curve plotted over TESS photometry.

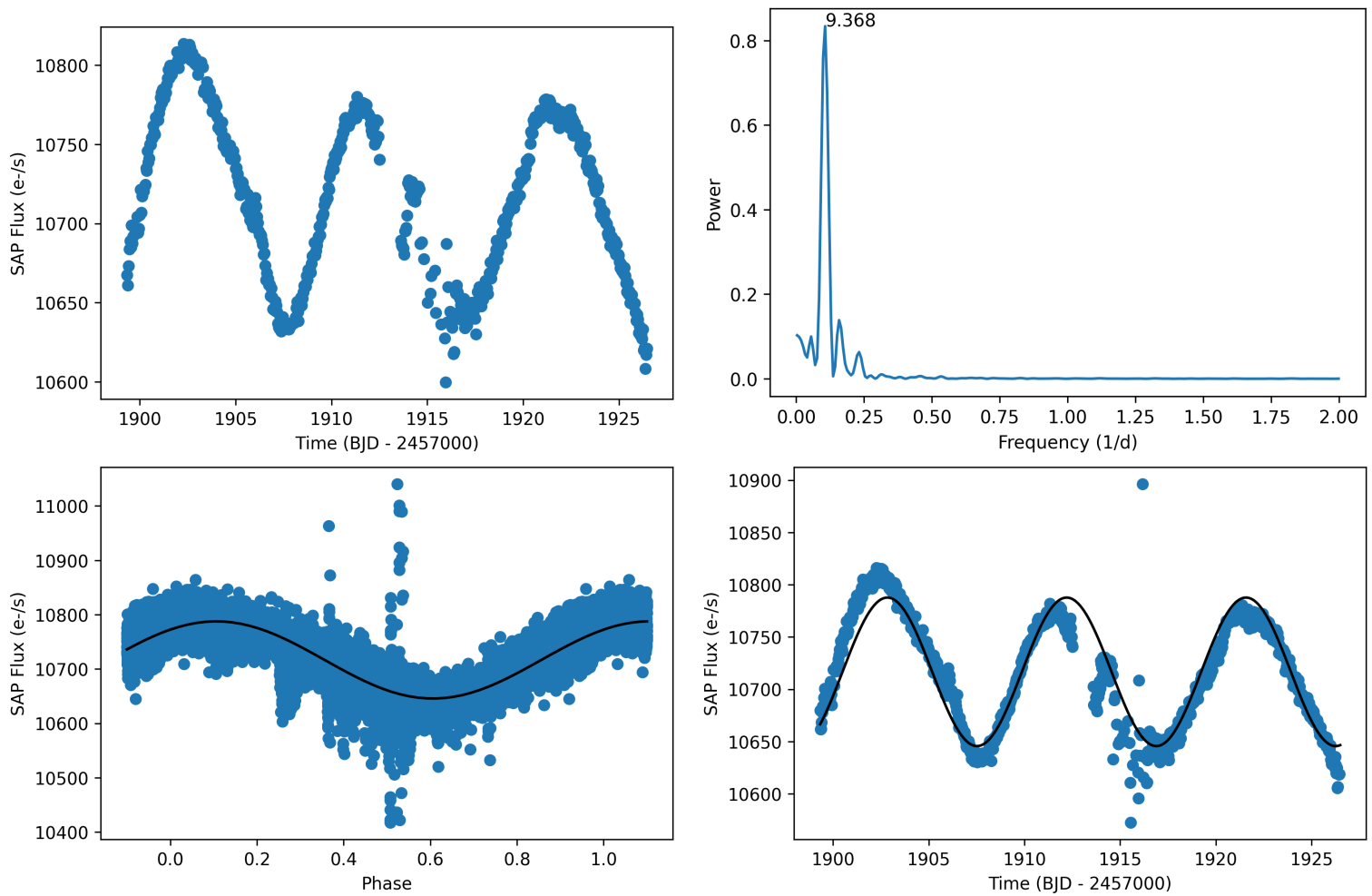


Figure D.10: TYC 1978-964-1. **Top-Left**— Photometry collected by TESS in sector 22. **Top-Right**— Lomb-Scargle periodogram. **Bottom-Left**— Phase-folded light curve with period 9.37 d. **Bottom-Right**— 9.37 d period light curve plotted over TESS photometry.

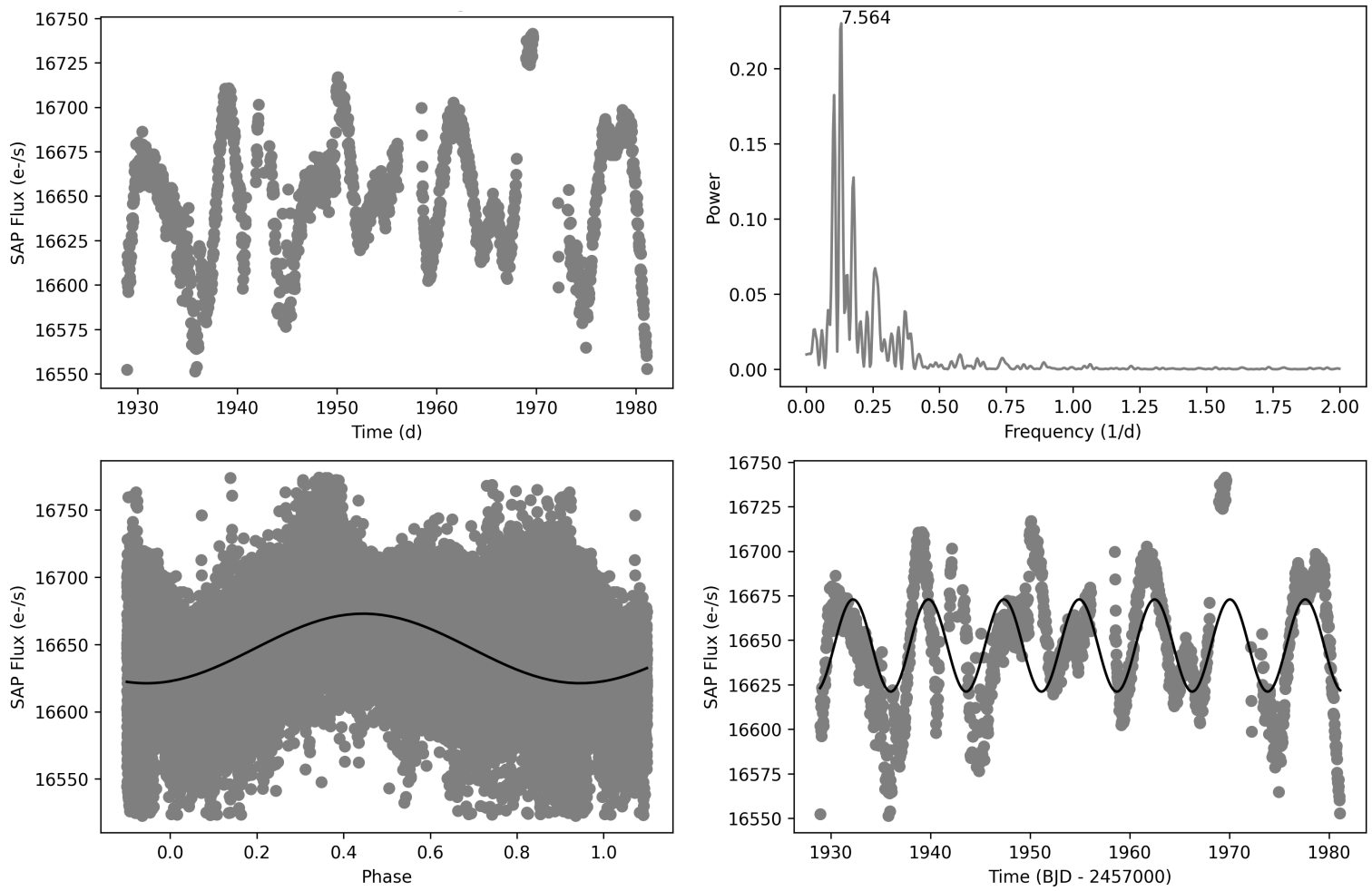


Figure D.11: *TYC 1461-326-1. Top-Left—* Photometry collected by TESS in sectors 23 and 50. *Top-Right—* Lomb-Scargle periodogram. *Bottom-Left—* Phase-folded light curve with period 7.56 d. *Bottom-Right—* 7.56 d period light curve plotted over TESS photometry.

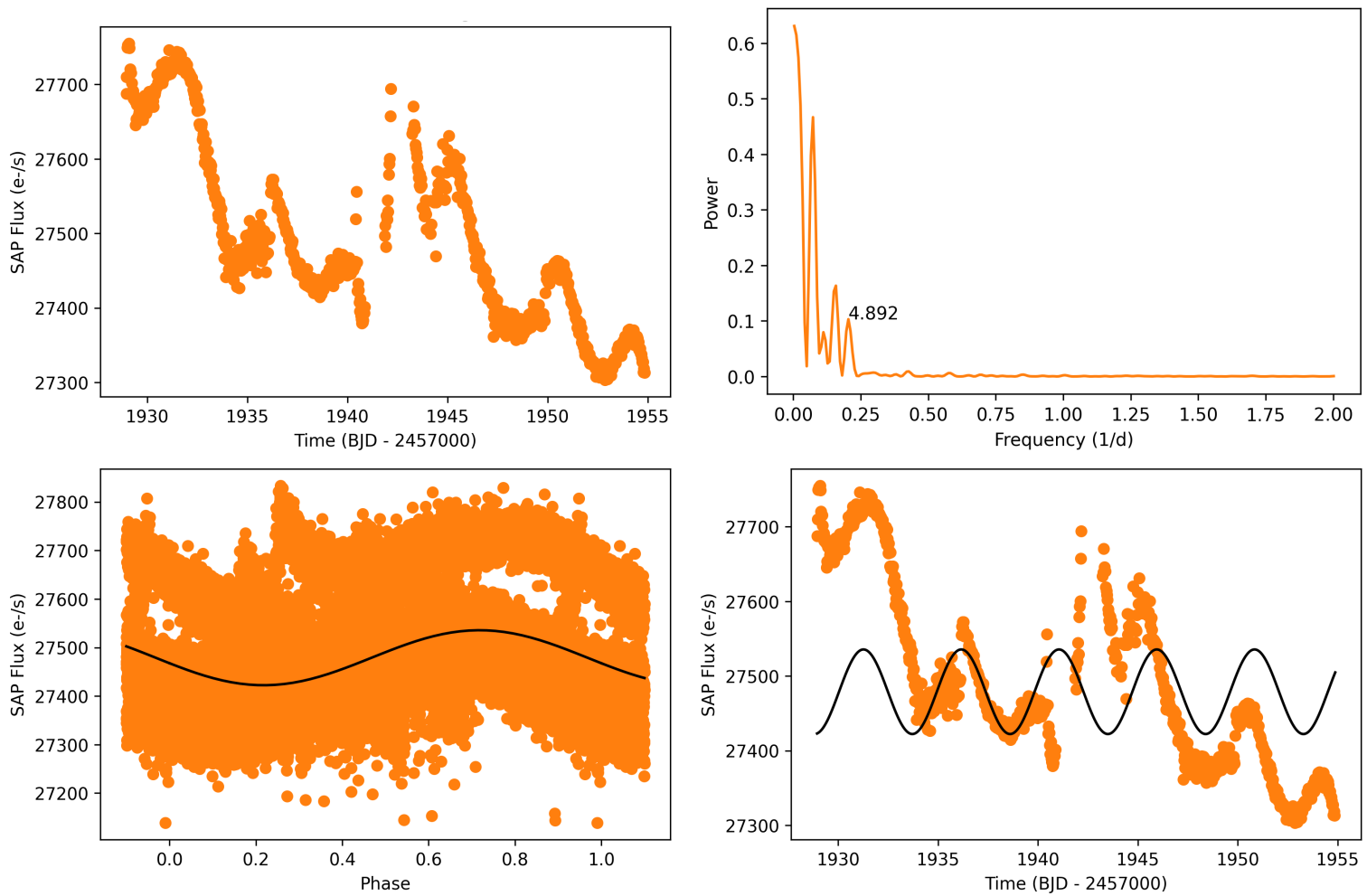


Figure D.12: TYC 1457-1029-1. **Top-Left**— Photometry collected by TESS in sector 23. **Top-Right**— Lomb-Scargle periodogram. **Bottom-Left**— Phase-folded light curve with period 4.89 d. **Bottom-Right**— 4.89 d period light curve plotted over TESS photometry.

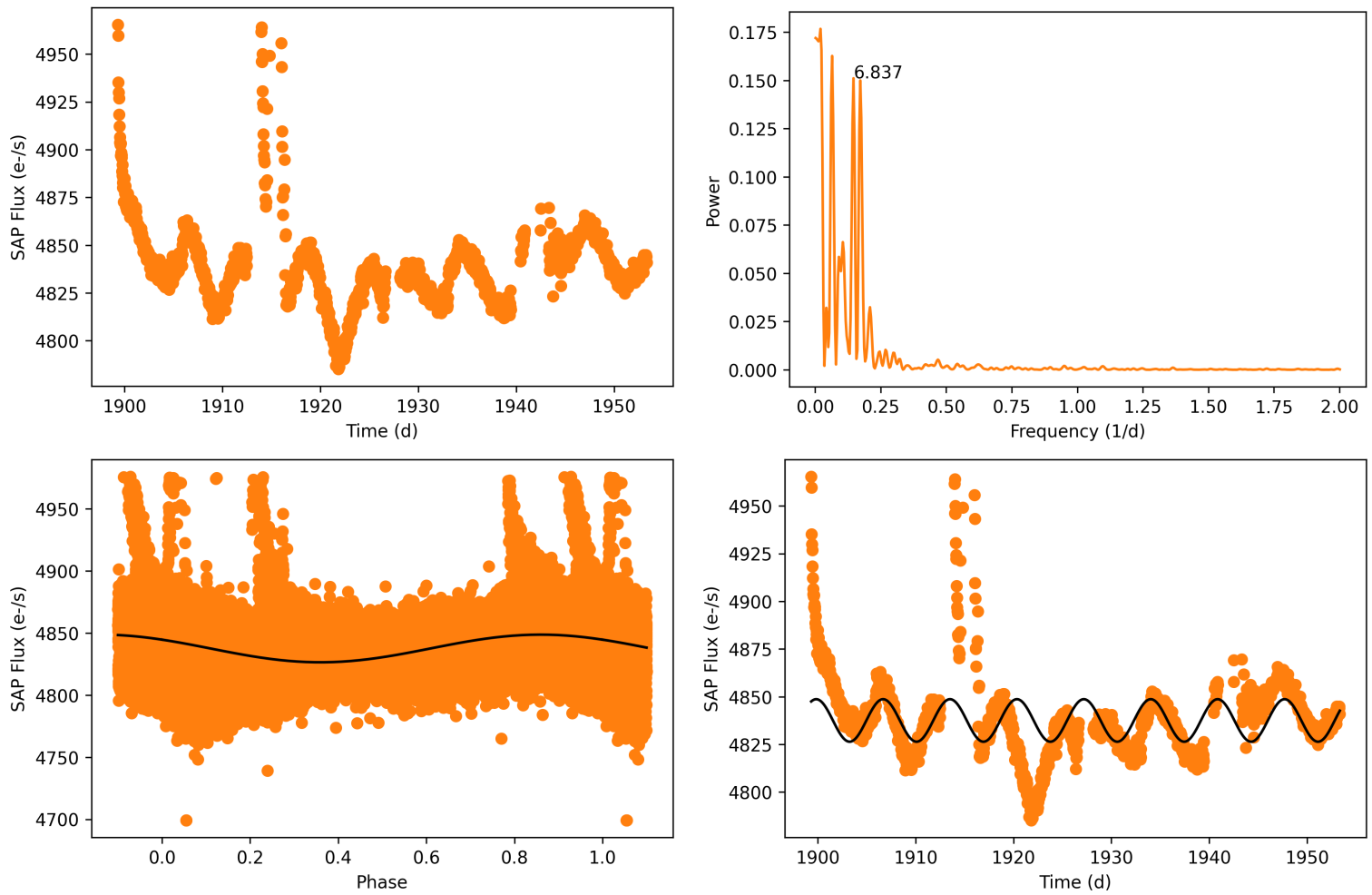


Figure D.13: *StKM 1-980. Top-Left*— Photometry collected by TESS in sectors 22 and 49. *Top-Right*— Lomb-Scargle periodogram. *Bottom-Left*— Phase-folded light curve with period 6.84 d. *Bottom-Right*— 6.84 d period light curve plotted over TESS photometry.

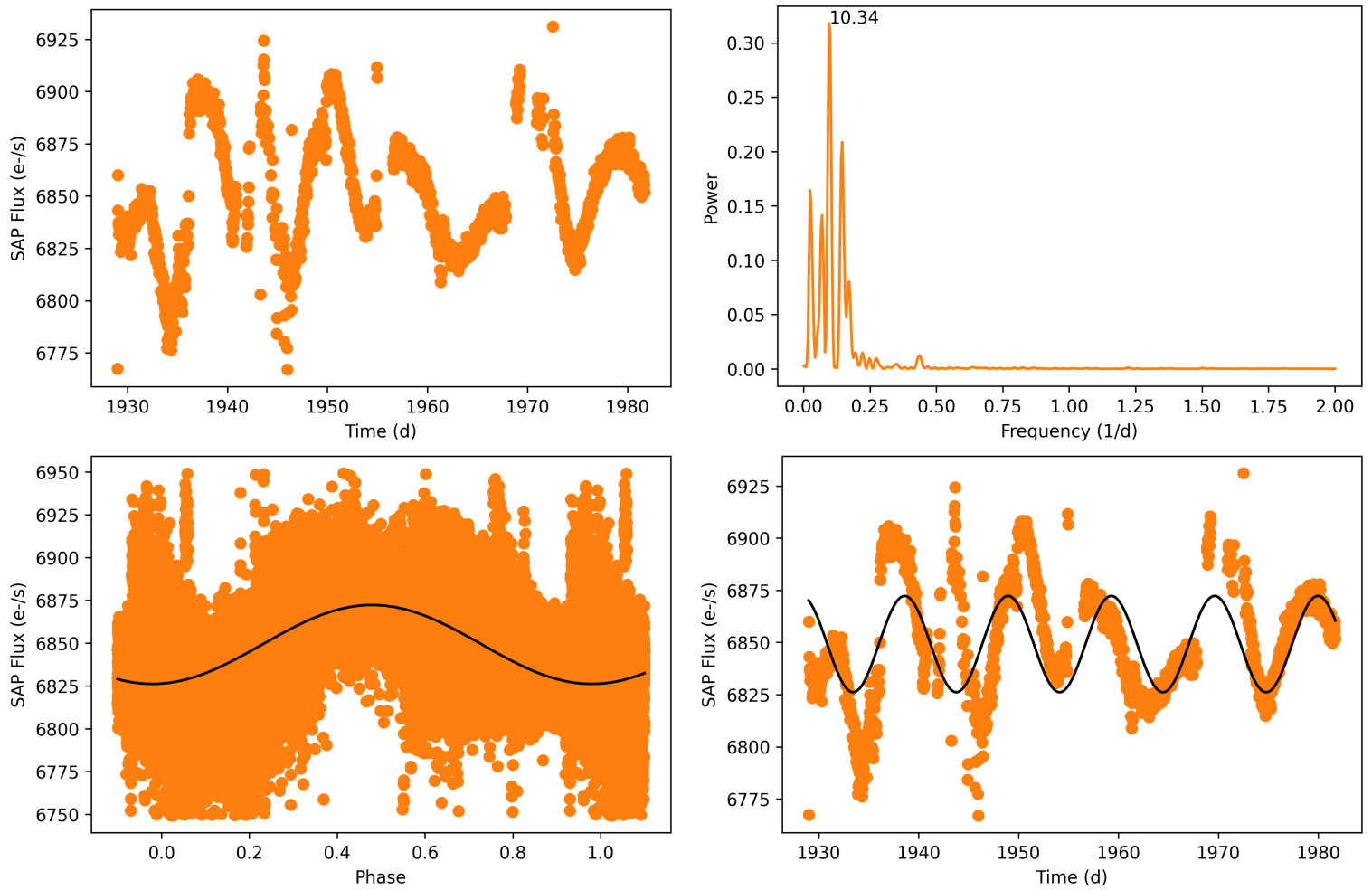


Figure D.14: UCAC4 577-048376. **Top-Left**— Photometry collected by TESS in sectors 23 and 49. **Top-Right**— Lomb-Scargle periodogram. **Bottom-Left**— Phase-folded light curve with period 10.3 d. **Bottom-Right**— 10.3 d period light curve plotted over TESS photometry.

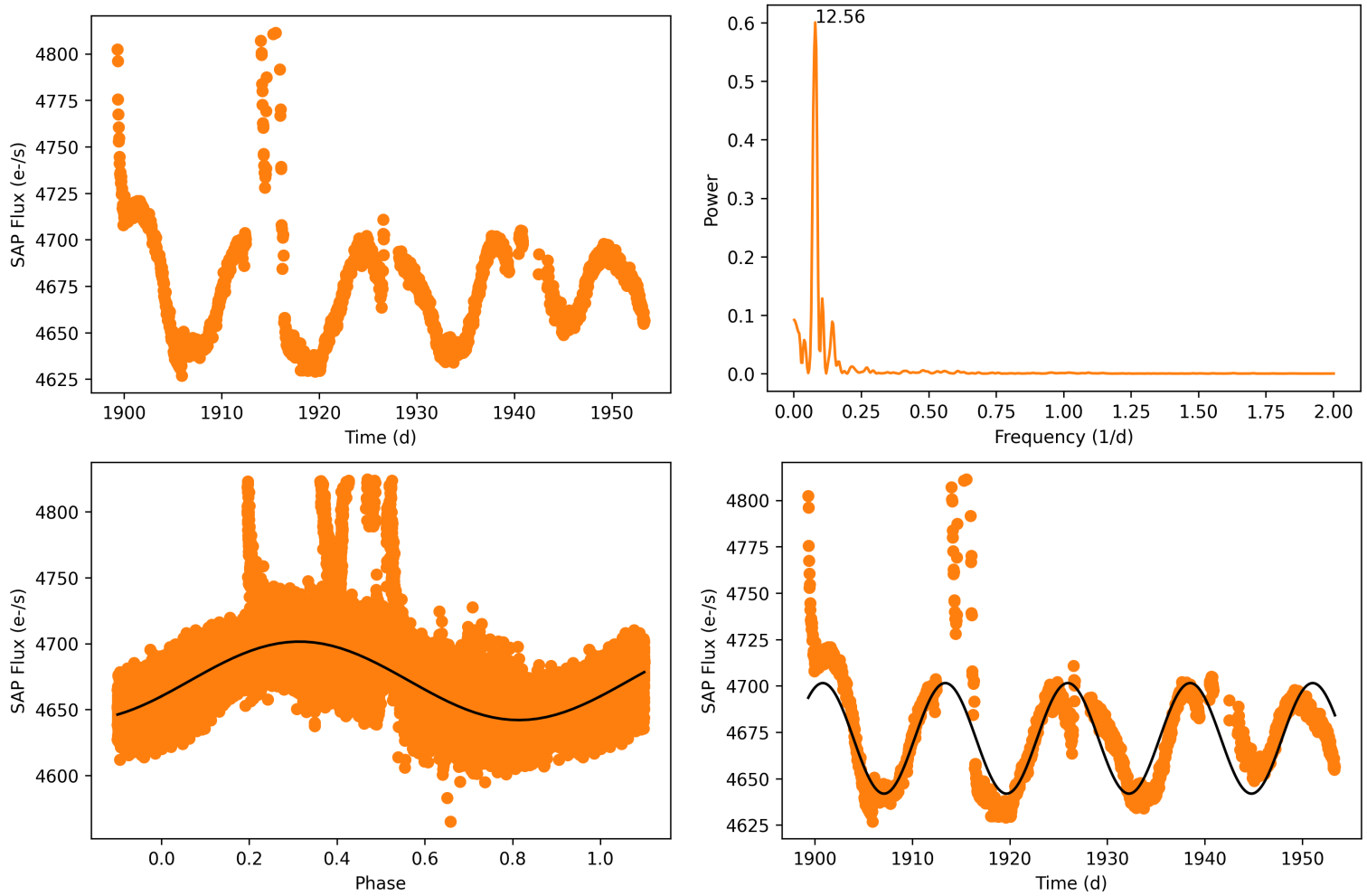


Figure D.15: *2MASS J12083610+3106098*. **Top-Left**— Photometry collected by TESS in sectors 22 and 49. **Top-Right**— Lomb-Scargle periodogram. **Bottom-Left**— Phase-folded light curve with period 12.6 d. **Bottom-Right**— 12.6 d period light curve plotted over TESS photometry.

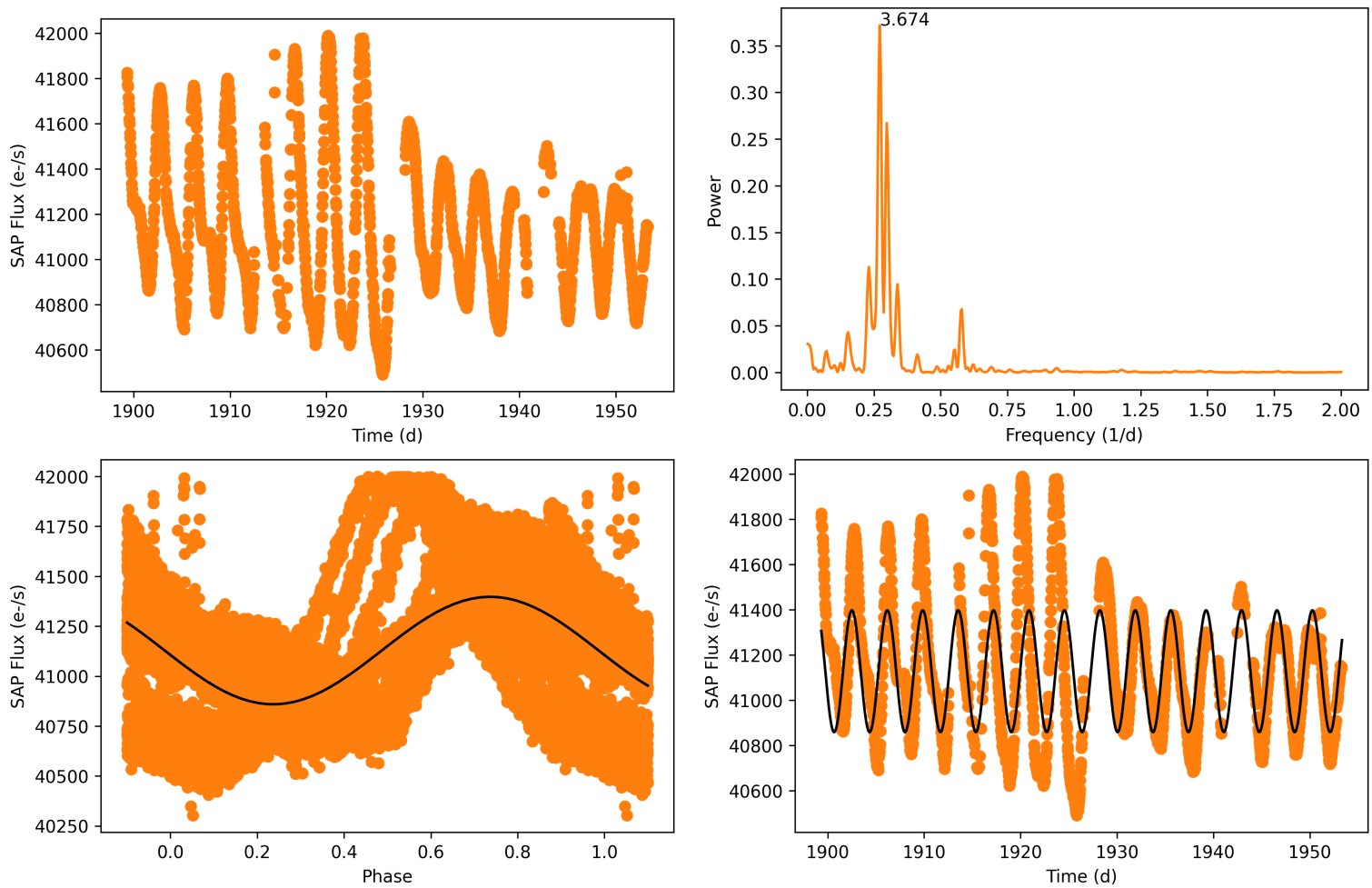


Figure D.16: *BD+25 2511. Top-Left— Photometry collected by TESS in sectors 22 and 49. Top-Right— Lomb-Scargle periodogram. Bottom-Left— Phase-folded light curve with period 3.68 d. Bottom-Right— 3.68 d period light curve plotted over TESS photometry.*

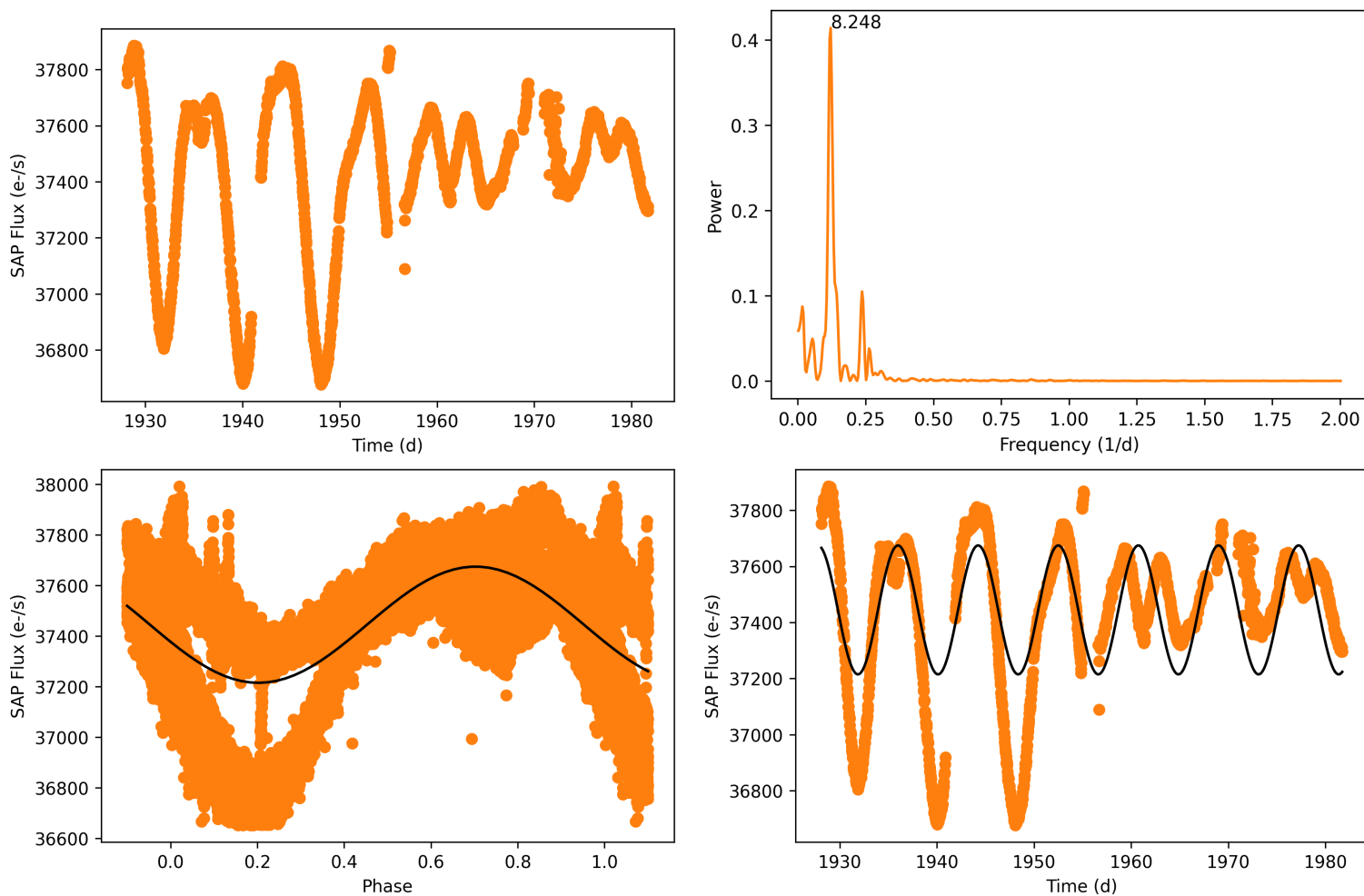


Figure D.17: *HD 114400. Top-Left— Photometry collected by TESS in sectors 23 and 49. Top-Right— Lomb-Scargle periodogram. Bottom-Left— Phase-folded light curve with period 8.25 d. Bottom-Right— 8.25 d period light curve plotted over TESS photometry.*

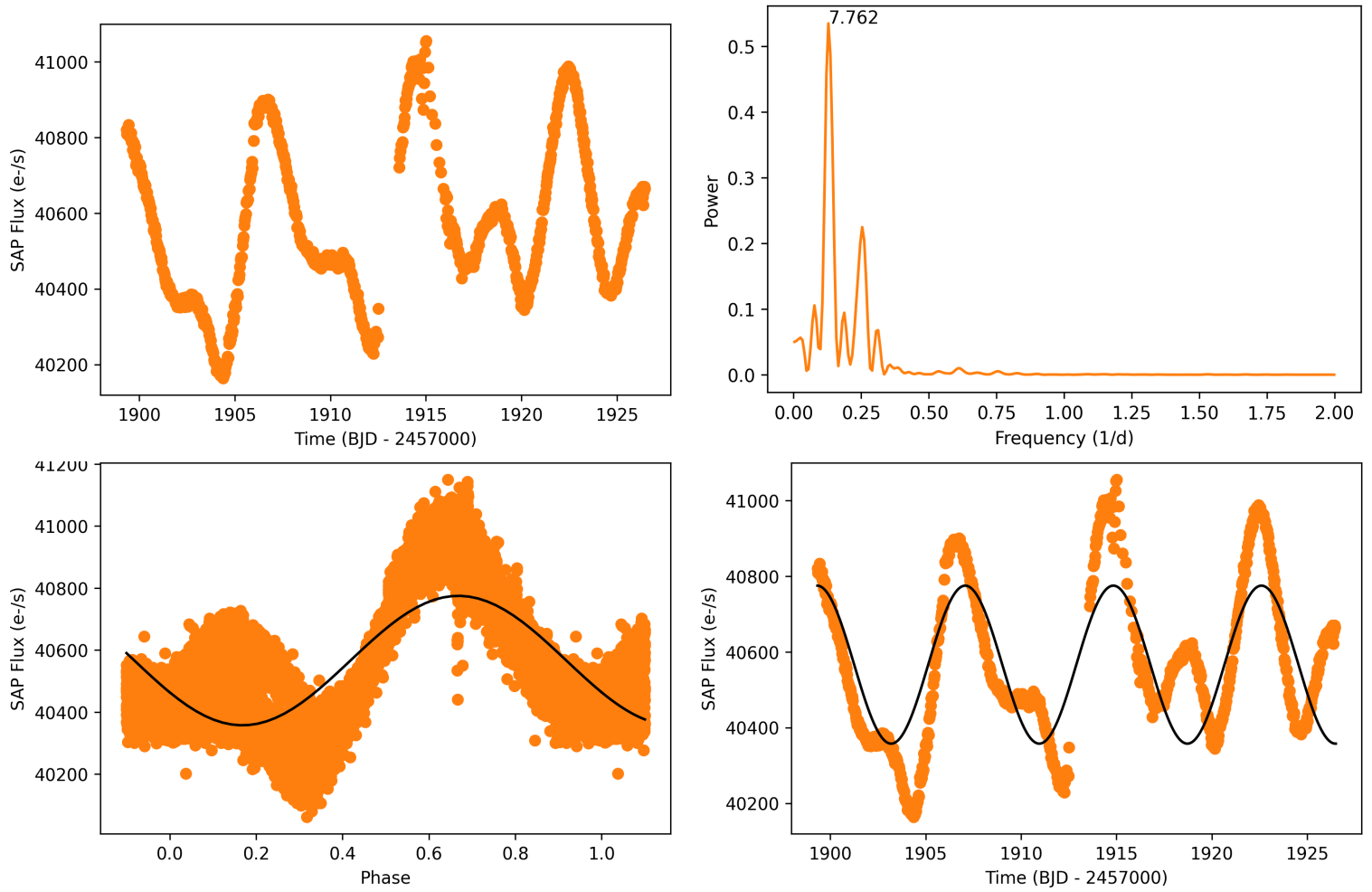


Figure D.18: *HD 105863*. **Top-Left**— Photometry collected by TESS in sector 22. **Top-Right**— Lomb-Scargle periodogram. **Bottom-Left**— Phase-folded light curve with period 7.76 d. **Bottom-Right**— 7.76 d period light curve plotted over TESS photometry.

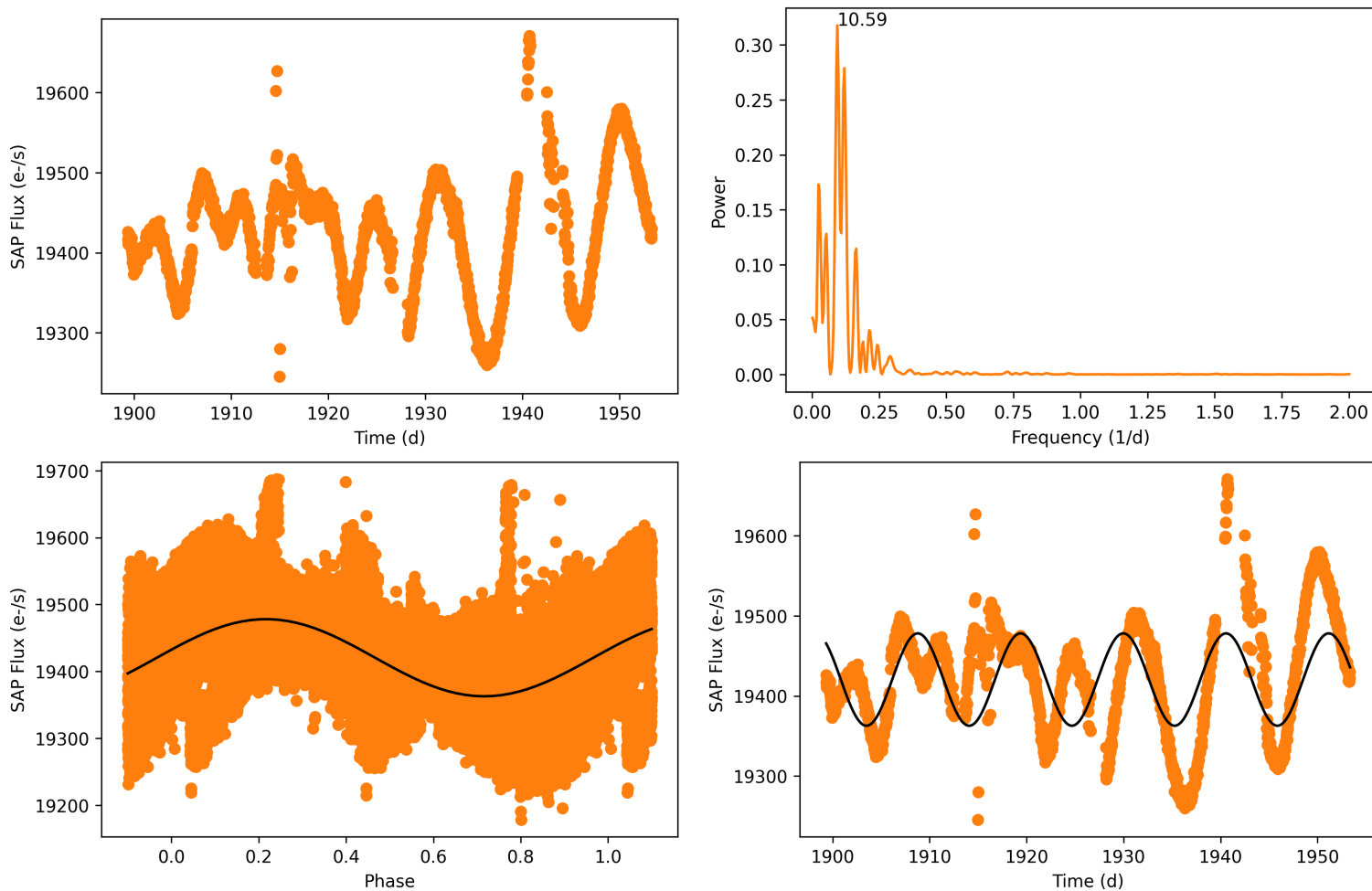


Figure D.19: *BD+26 2342. Top-Left— Photometry collected by TESS in sectors 22 and 49. Top-Right— Lomb-Scargle periodogram. Bottom-Left— Phase-folded light curve with period 10.6 d. Bottom-Right— 10.6 d period light curve plotted over TESS photometry.*

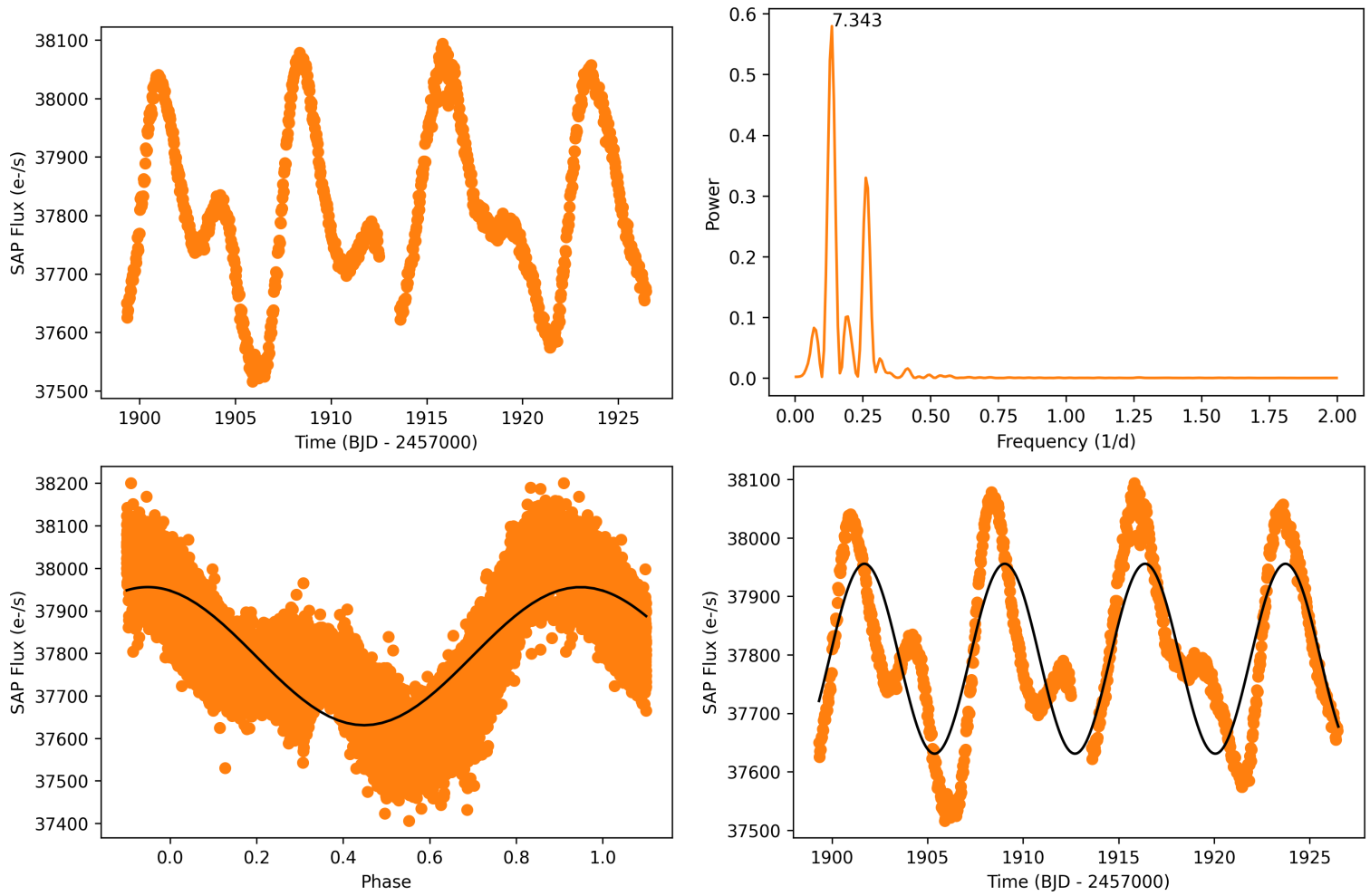


Figure D.20: *BD+36 2278. Top-Left—* Photometry collected by TESS in sector 22. *Top-Right—* Lomb-Scargle periodogram. *Bottom-Left—* Phase-folded light curve with period 7.34 d. *Bottom-Right—* 7.34 d period light curve plotted over TESS photometry.

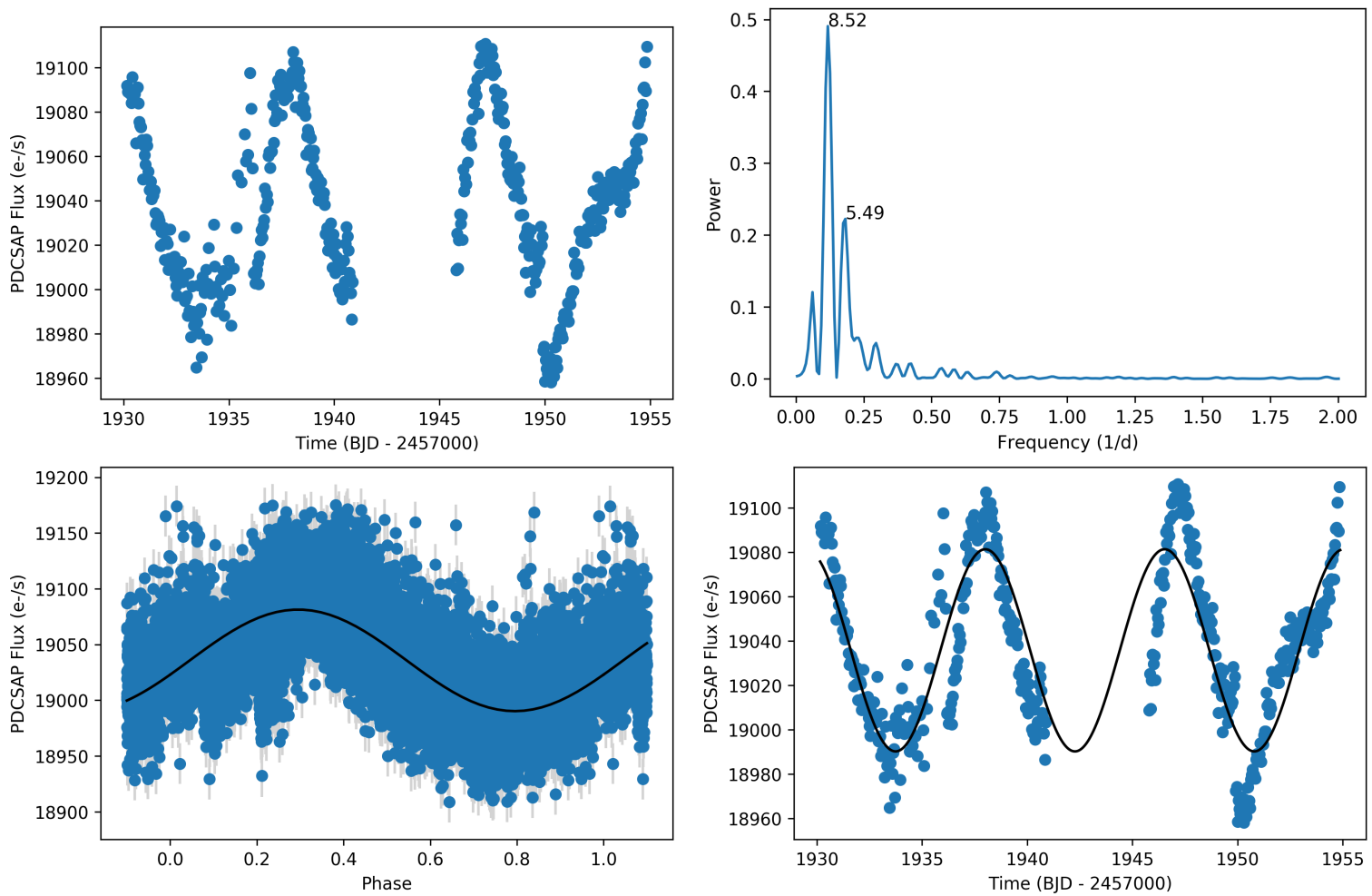


Figure D.21: *BD+31 2571. Top-Left— PDCSAP flux collected by TESS in sector 23. Top-Right— Lomb-Scargle periodogram. Bottom-Left— Phase-folded light curve with period 8.53 d. Bottom-Right— 8.53 d period light curve plotted over TESS photometry.*

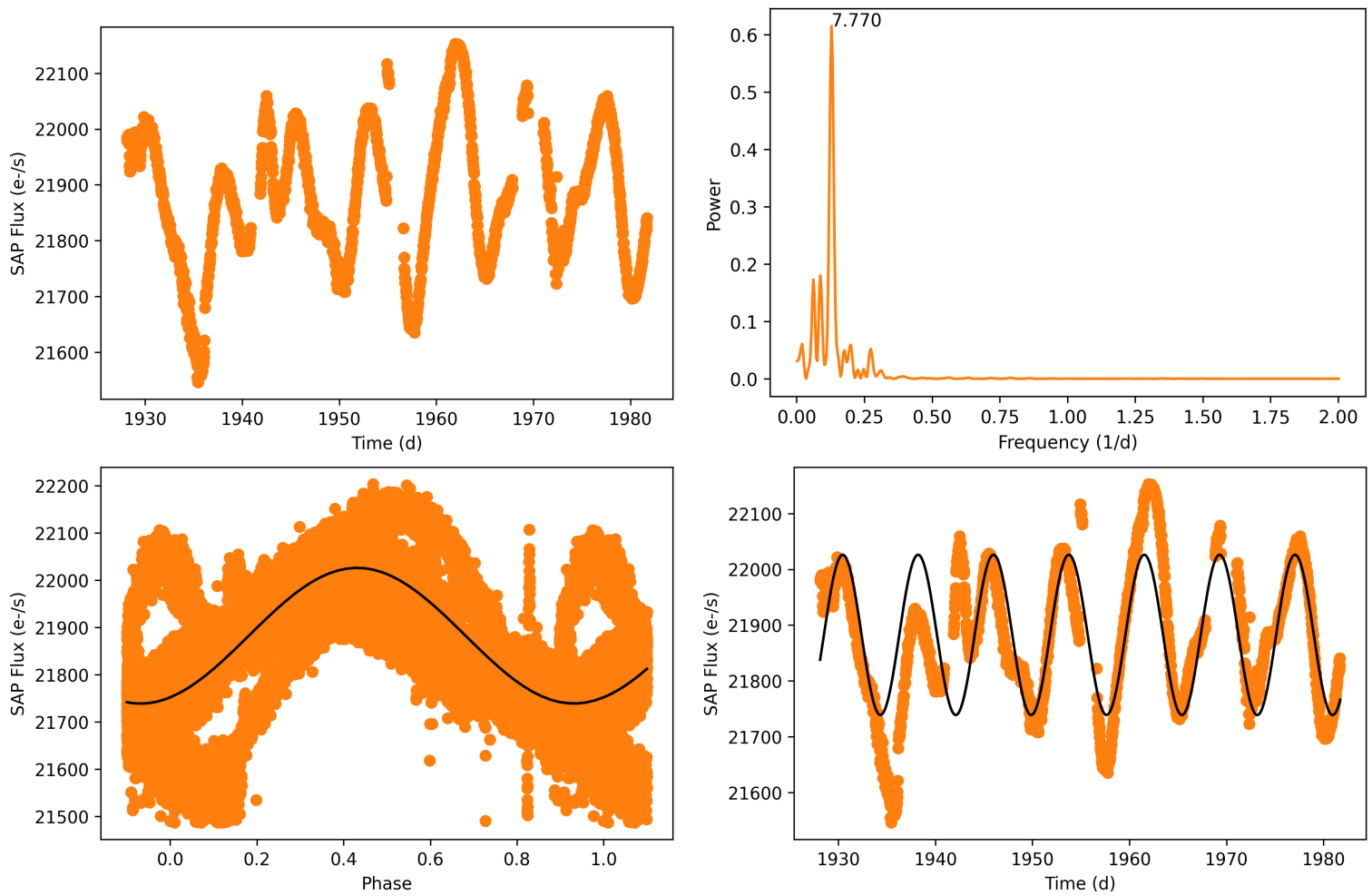


Figure D.22: *BD+29 2346. Top-Left—* Photometry collected by TESS in sectors 23 and 49. *Top-Right—* Lomb-Scargle periodogram. *Bottom-Left—* Phase-folded light curve with period 7.77 d. *Bottom-Right—* 7.77 d period light curve plotted over TESS photometry.

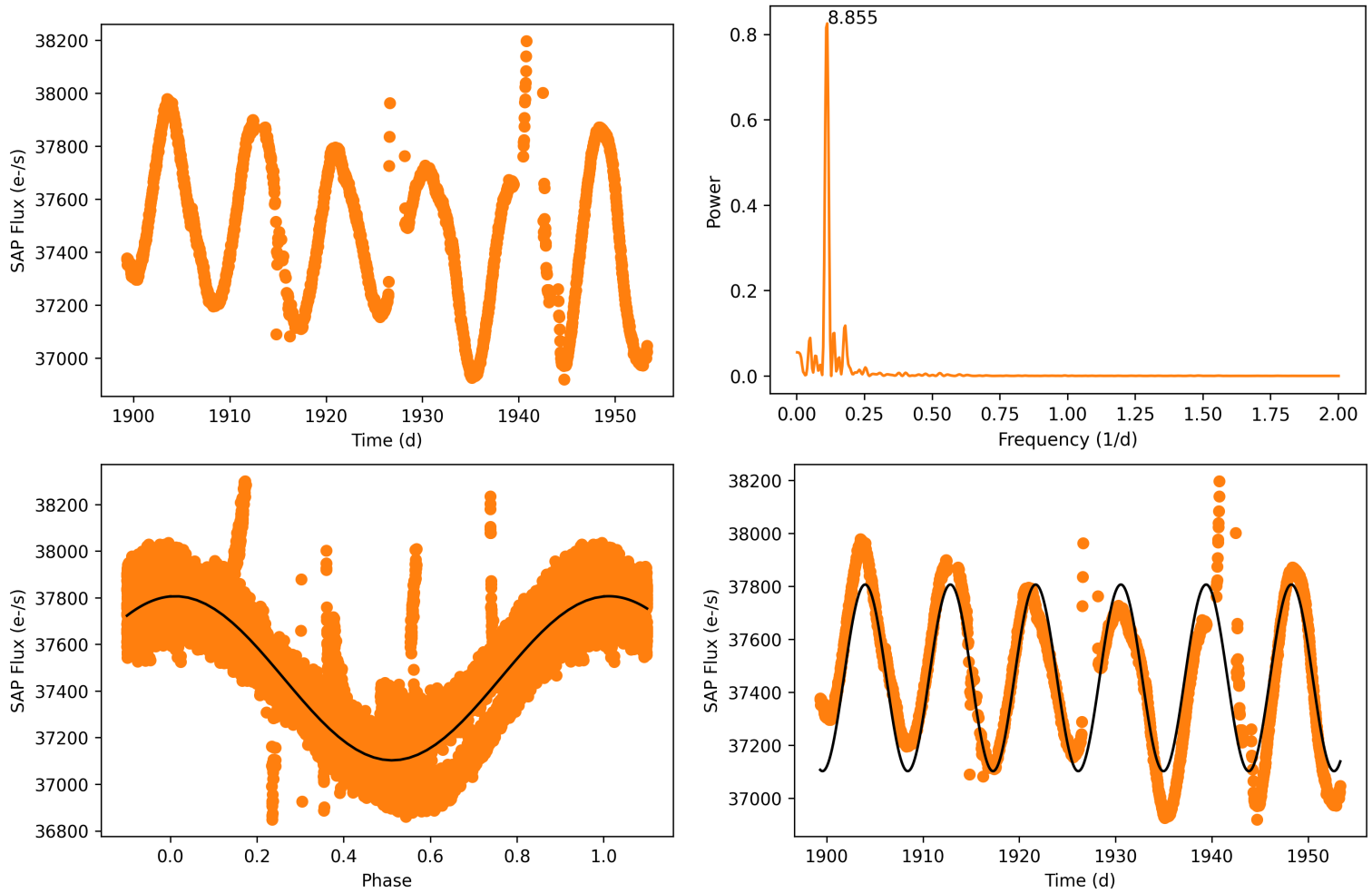


Figure D.23: *BD+29 2290. Top-Left— Photometry collected by TESS in sectors 22 and 49. Top-Right— Lomb-Scargle periodogram. Bottom-Left— Phase-folded light curve with period 8.86 d. Bottom-Right— 8.86 d period light curve plotted over TESS photometry.*

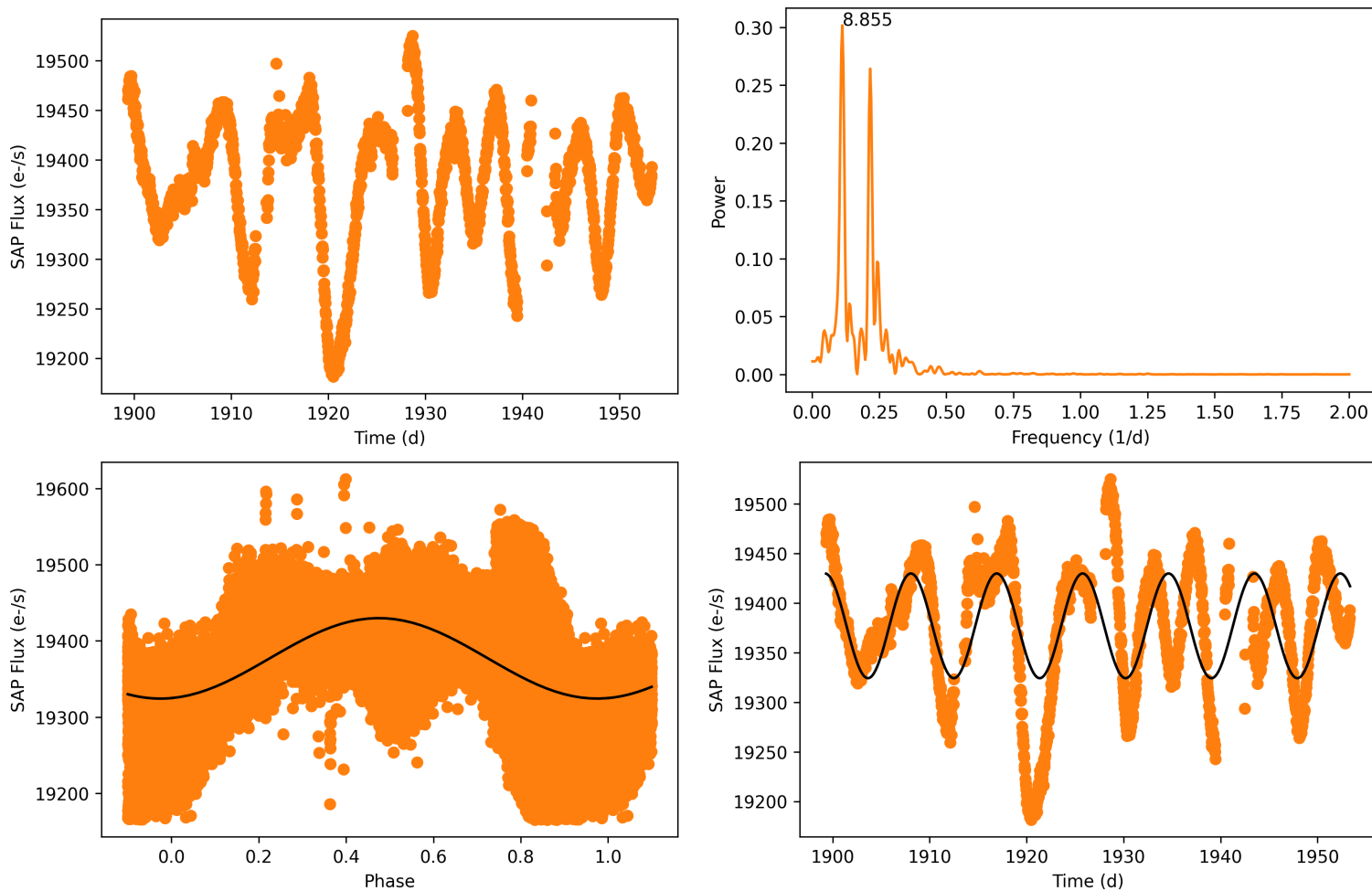


Figure D.24: *BD+29 2215. Top-Left— Photometry collected by TESS in sectors 22 and 49. Top-Right— Lomb-Scargle periodogram. Bottom-Left— Phase-folded light curve with period 8.86 d. Bottom-Right— 8.86 d period light curve plotted over TESS photometry.*

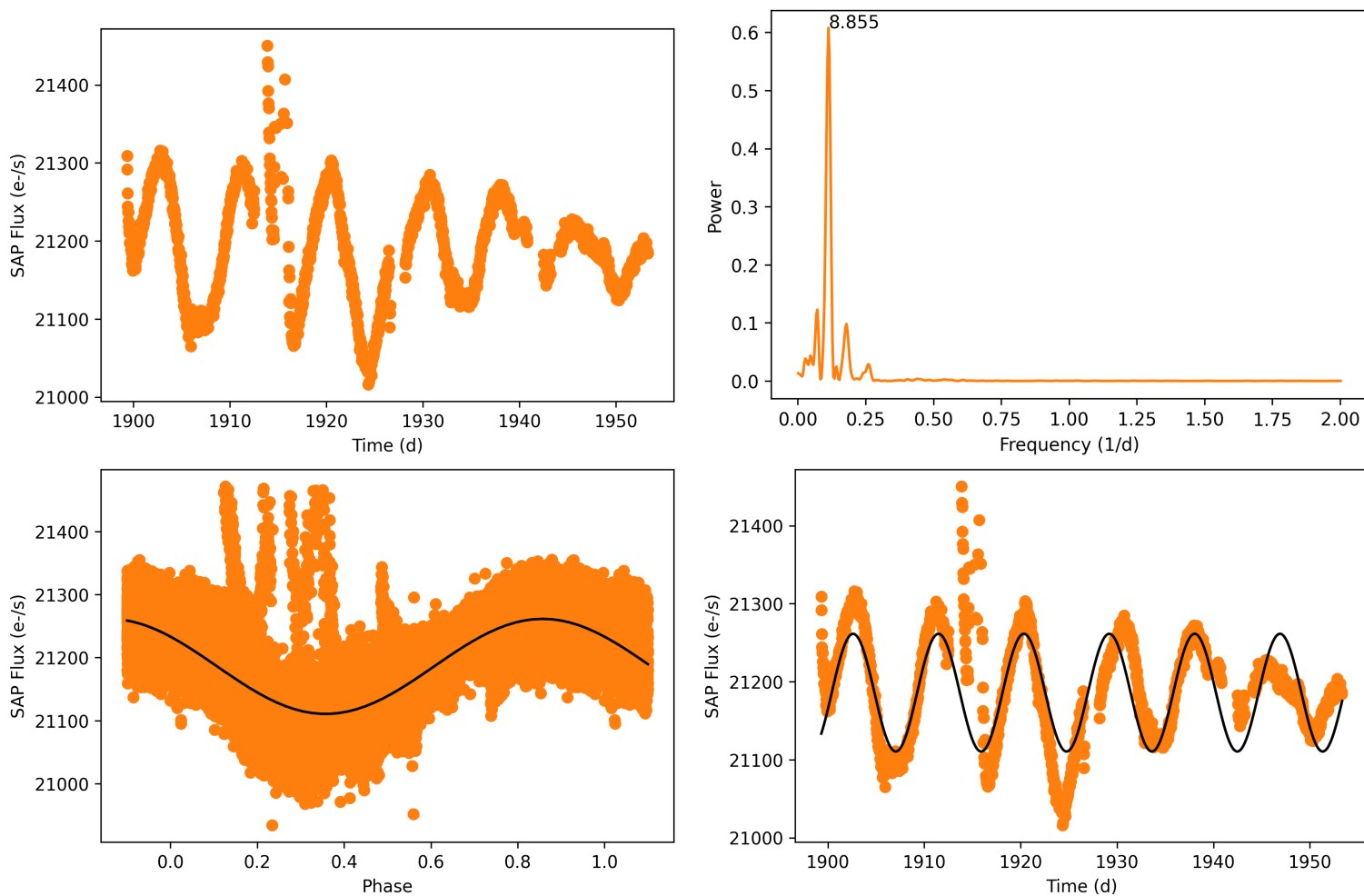


Figure D.25: *BD+28 2119. Top-Left—* Photometry collected by TESS in sectors 22 and 49. *Top-Right—* Lomb-Scargle periodogram. *Bottom-Left—* Phase-folded light curve with period 8.86 d. *Bottom-Right—* 8.86 d period light curve plotted over TESS photometry.

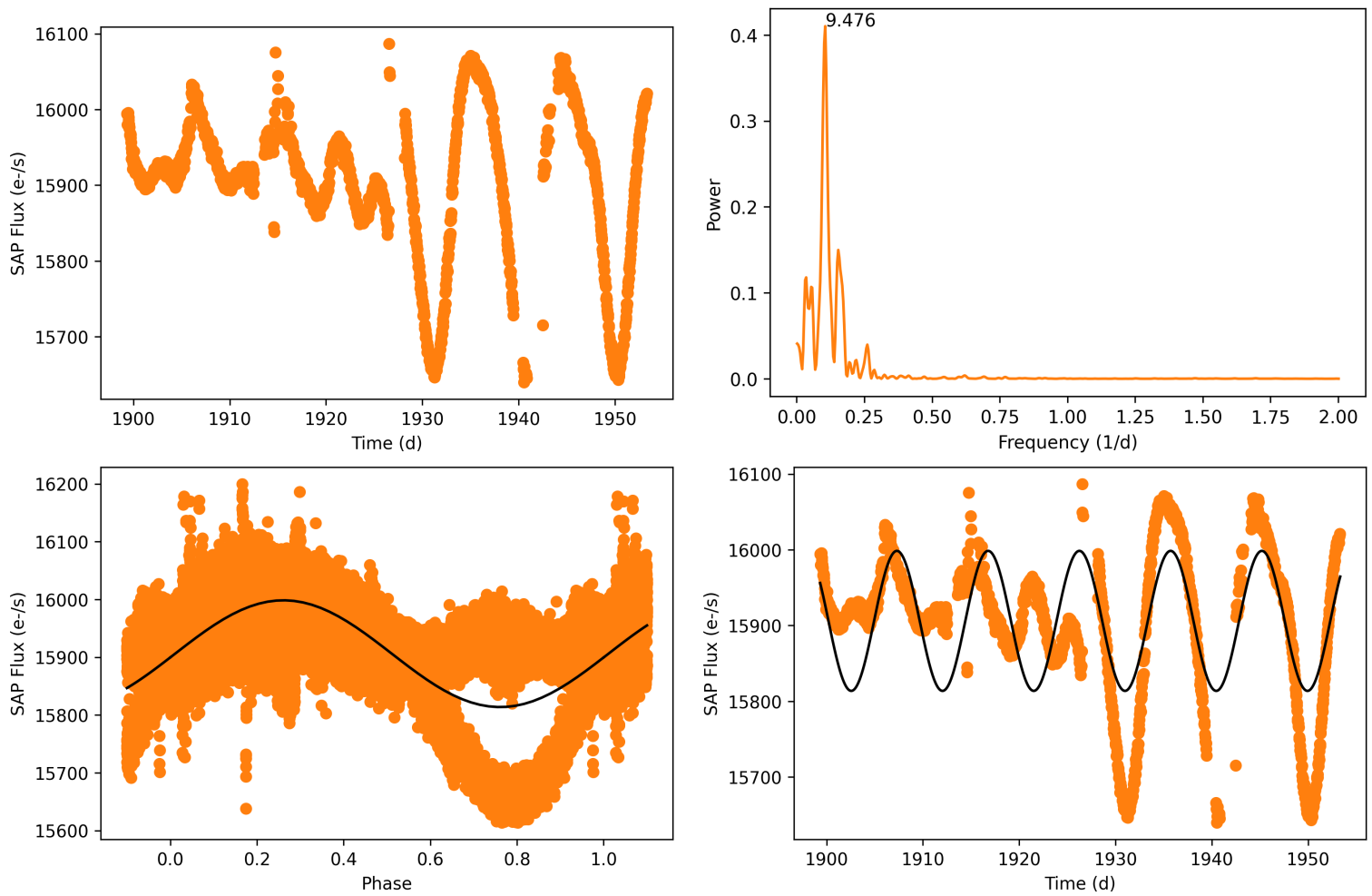


Figure D.26: *BD+27 2139. Top-Left*— Photometry collected by TESS in sectors 22 and 49. *Top-Right*— Lomb-Scargle periodogram. *Bottom-Left*— Phase-folded light curve with period 9.48 d. *Bottom-Right*— 9.48 d period light curve plotted over TESS photometry.

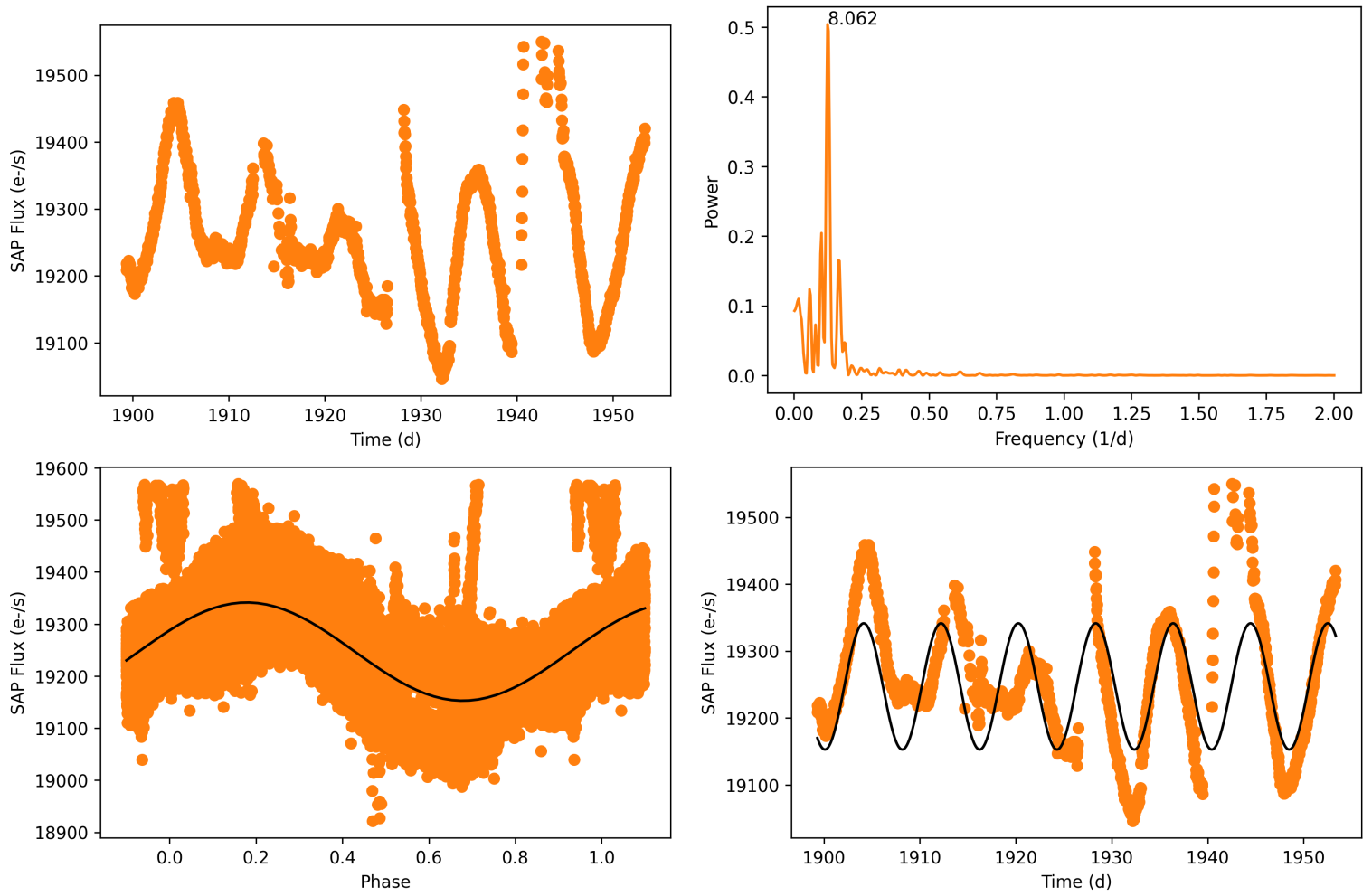


Figure D.27: *BD+26 2362. Top-Left—* Photometry collected by TESS in sectors 22 and 49. *Top-Right—* Lomb-Scargle periodogram. *Bottom-Left—* Phase-folded light curve with period 8.06 d. *Bottom-Right—* 8.06 d period light curve plotted over TESS photometry.

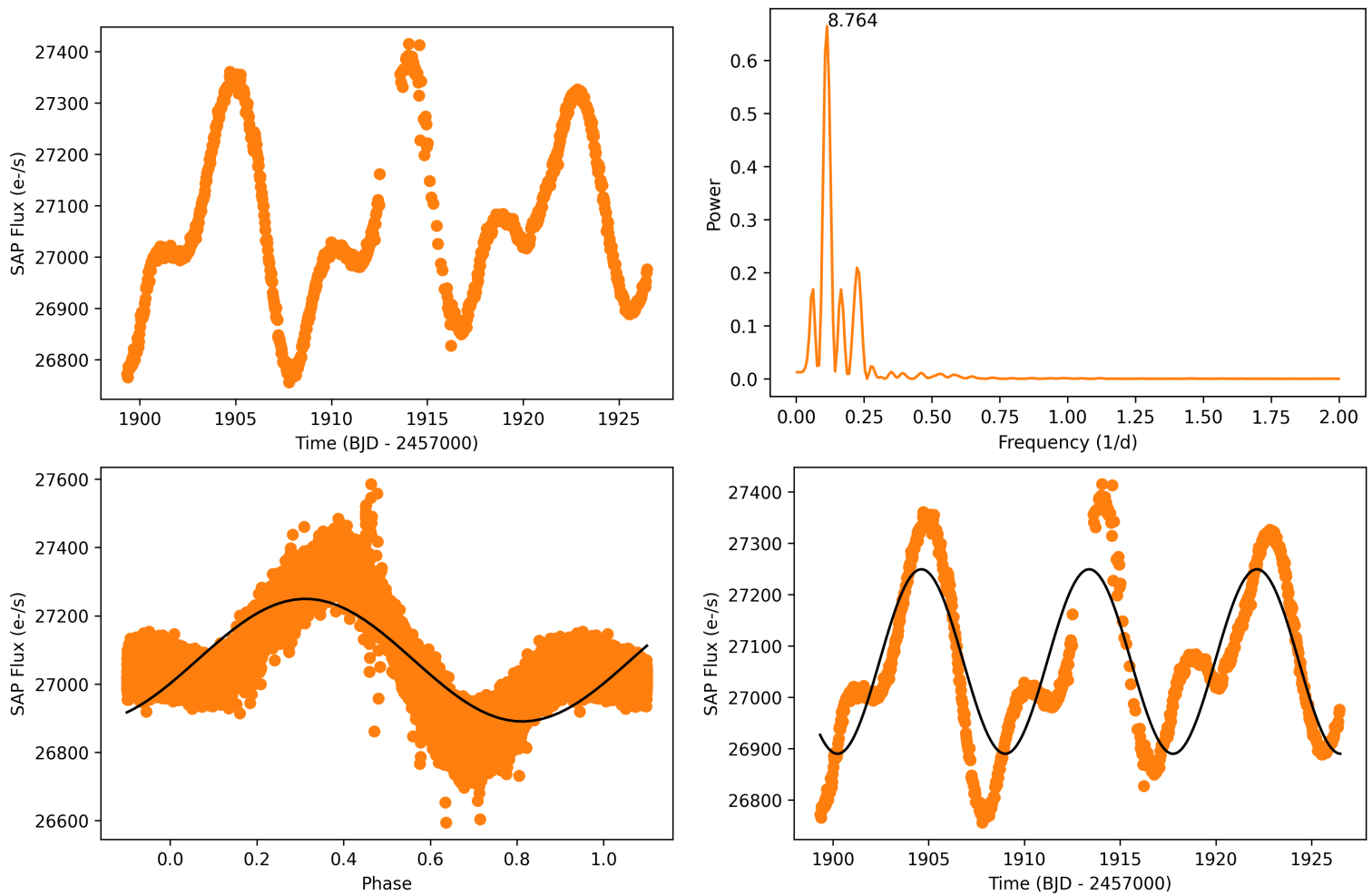


Figure D.28: *BD+25 2455. Top-Left—* Photometry collected by TESS in sector 22. *Top-Right—* Lomb-Scargle periodogram. *Bottom-Left—* Phase-folded light curve with period 8.76 d. *Bottom-Right—* 8.76 d period light curve plotted over TESS photometry.

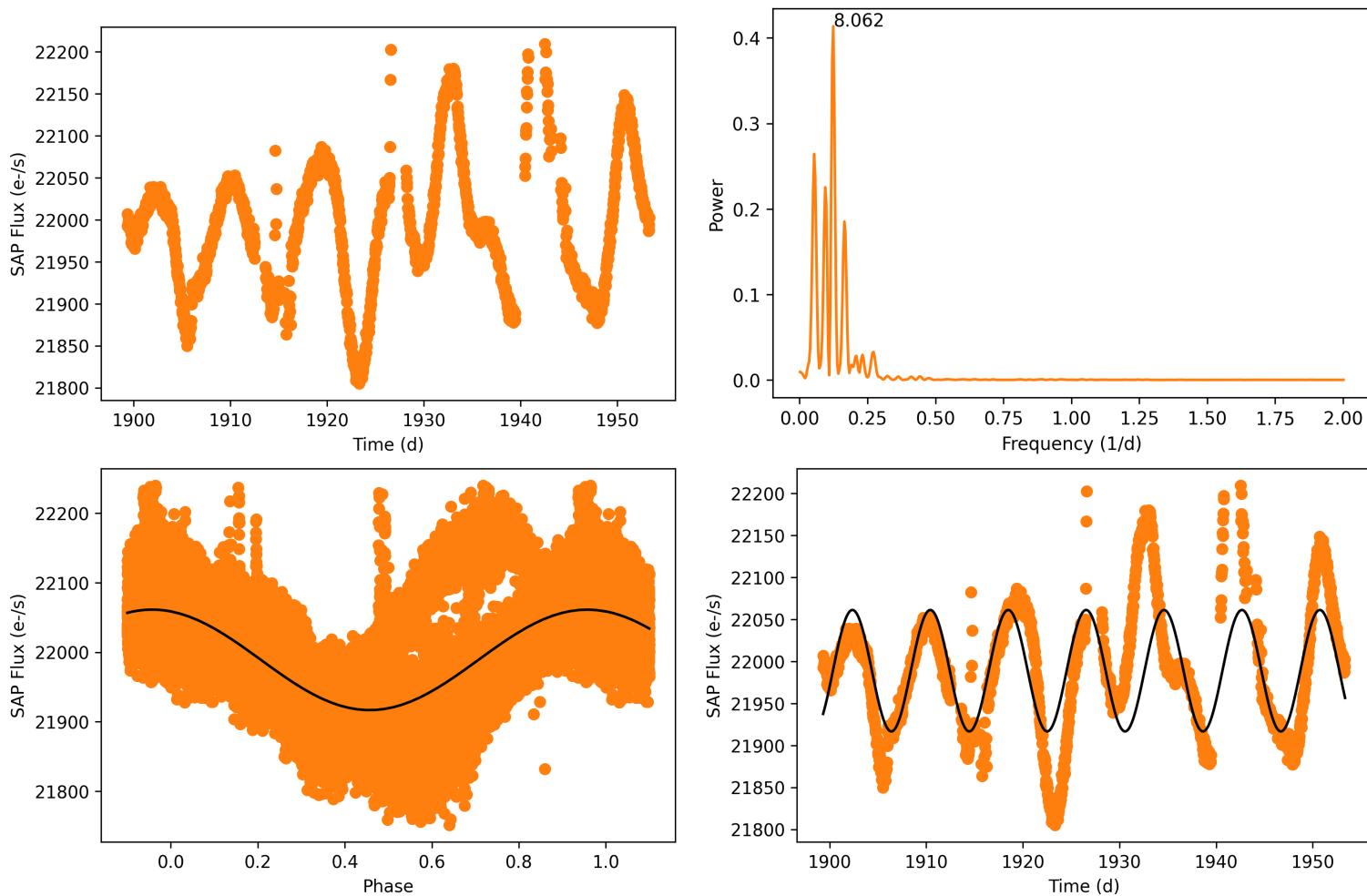


Figure D.29: *BD+24 2462. Top-Left— Photometry collected by TESS in sectors 22 and 49. Top-Right— Lomb-Scargle periodogram. Bottom-Left— Phase-folded light curve with period 8.06 d. Bottom-Right— 8.06 d period light curve plotted over TESS photometry.*

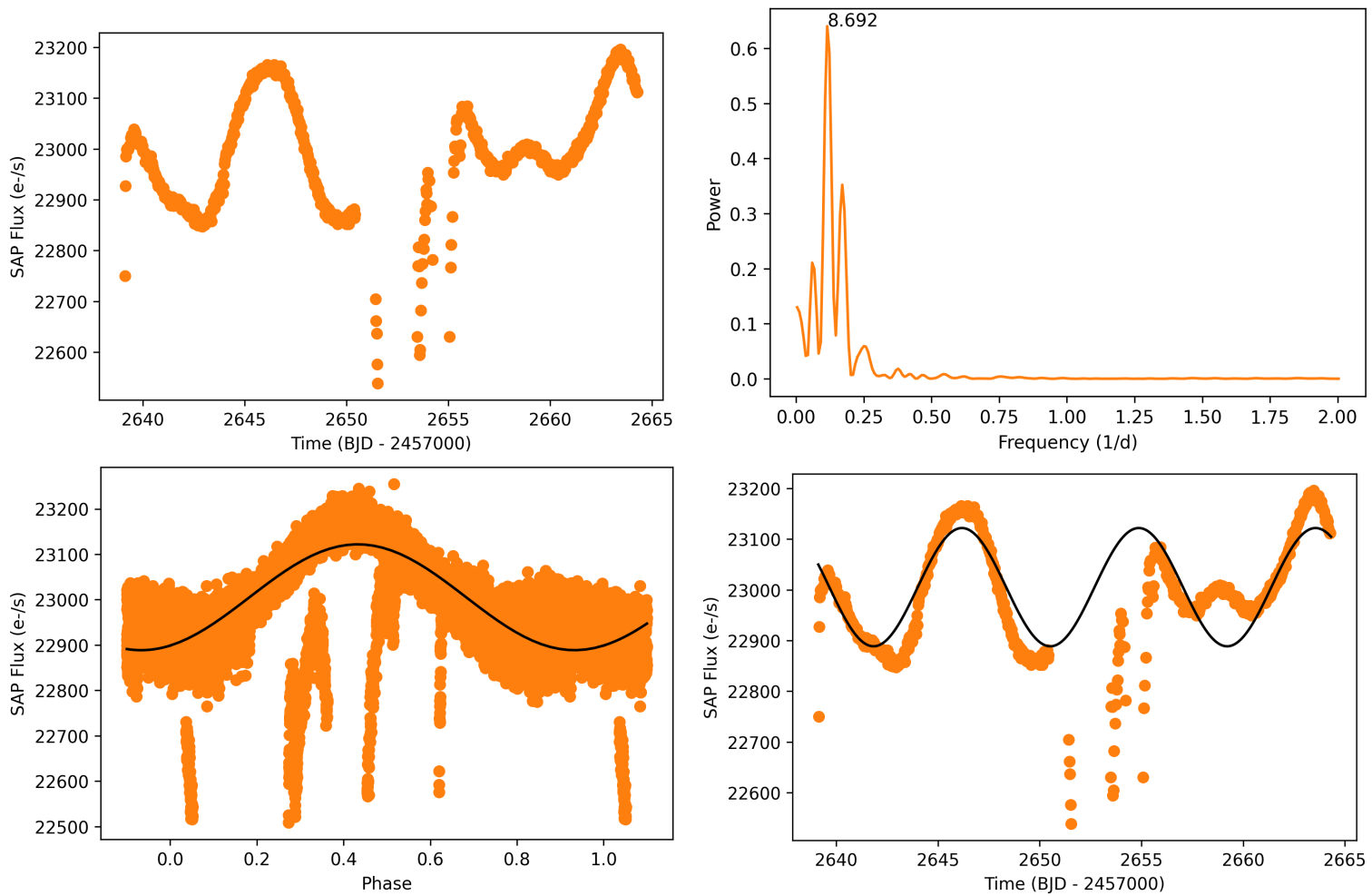


Figure D.30: *BD+23 2472. Top-Left—* Photometry collected by TESS in sector 49. *Top-Right—* Lomb-Scargle periodogram. *Bottom-Left—* Phase-folded light curve with period 8.69 d. *Bottom-Right—* 8.69 d period light curve plotted over TESS photometry.

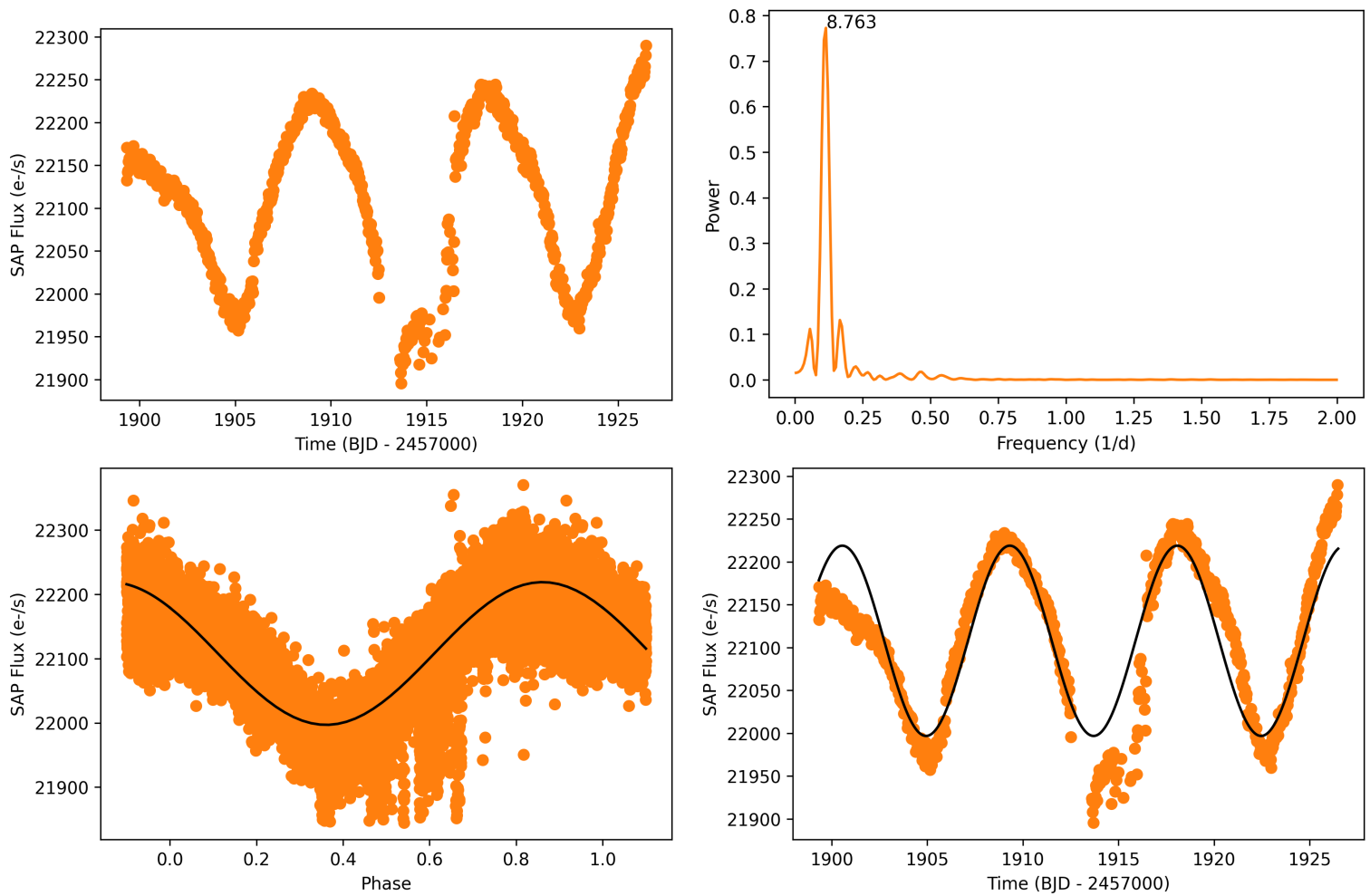


Figure D.31: *BD+21 2335*. **Top-Left**— Photometry collected by TESS in sector 22. **Top-Right**— Lomb-Scargle periodogram. **Bottom-Left**— Phase-folded light curve with period 8.76 d. **Bottom-Right**— 8.76 d period light curve plotted over TESS photometry.

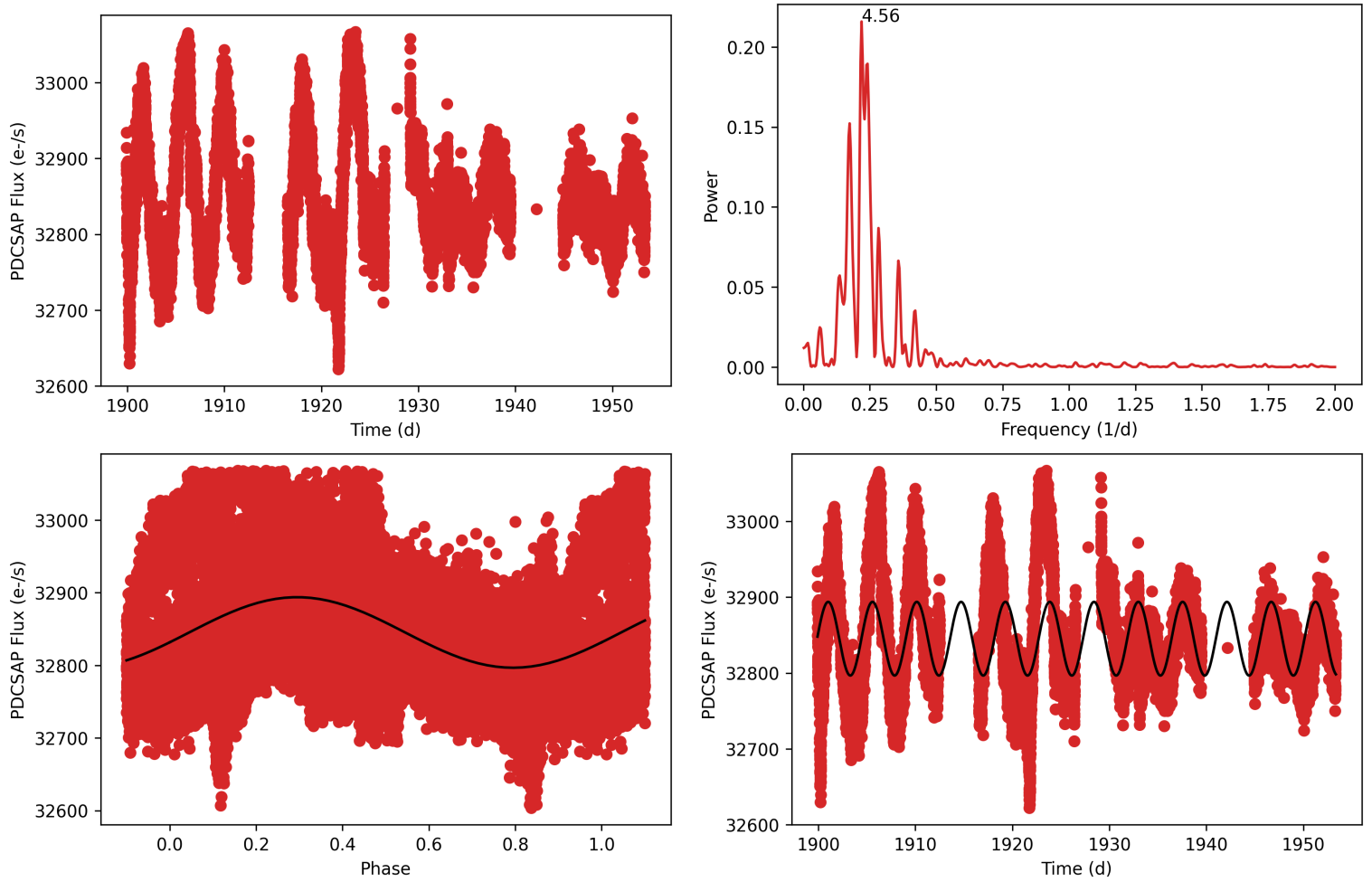


Figure D.32: *BD+20 2671*. **Top-Left**— PDCSAP flux collected by TESS in sectors 22 and 49. **Top-Right**— Lomb-Scargle periodogram. **Bottom-Left**— Phase-folded light curve with period 4.56 d. **Bottom-Right**— 4.56 d period light curve plotted over TESS photometry.

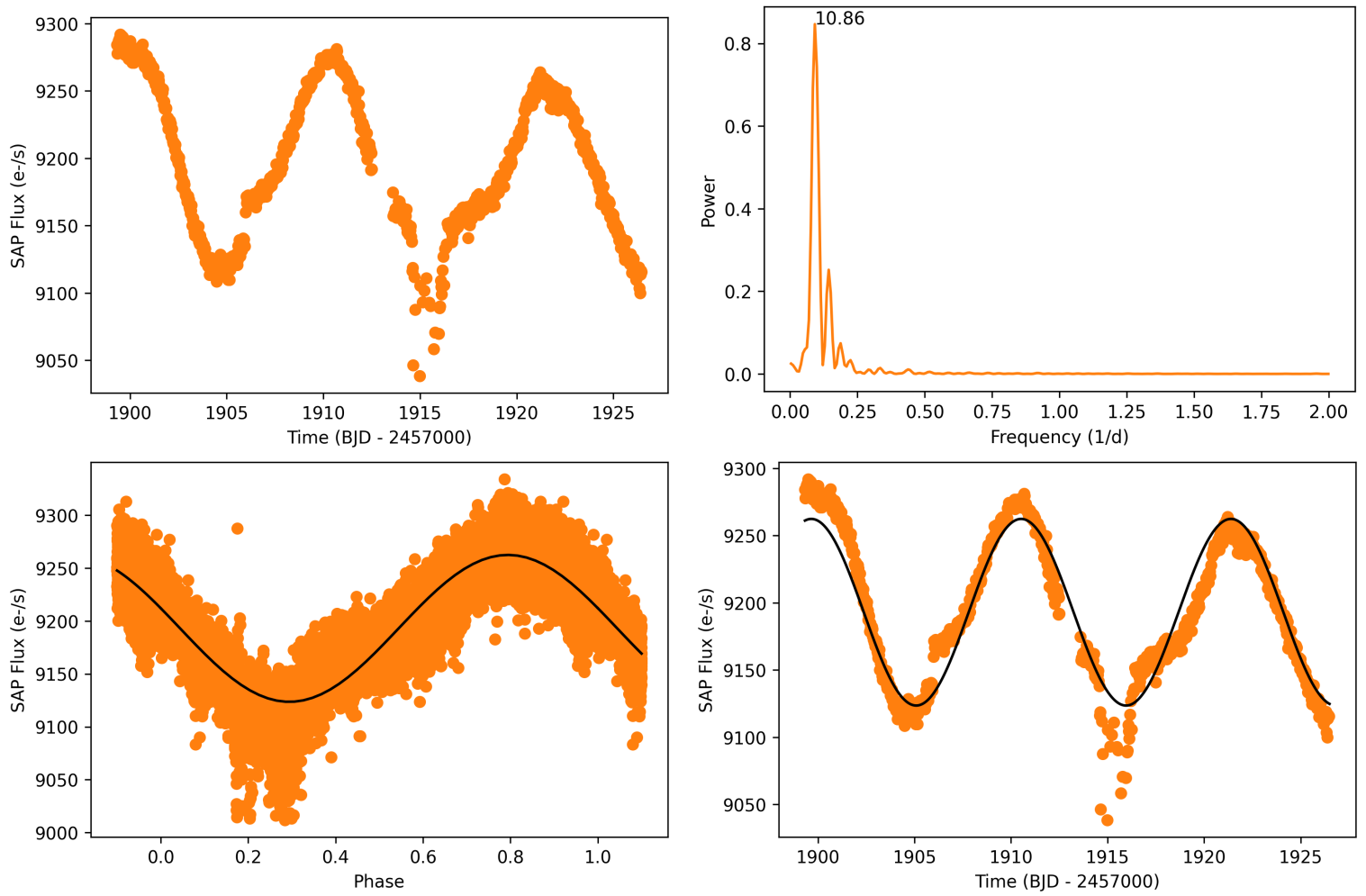


Figure D.33: *TYC 1989-49-1. Top-Left— Photometry collected by TESS in sector 22. Top-Right— Lomb-Scargle periodogram. Bottom-Left— Phase-folded light curve with period 10.9 d. Bottom-Right— 10.9 d period light curve plotted over TESS photometry.*

Appendix E

On the origin of high-metal lithium-poor stars

Several authors have observed stars with high metallicity and low lithium abundance in the solar neighborhood during the past decade (see, for instance, [Delgado Mena et al., 2015](#); [Guiglion et al., 2016](#); [Fu et al., 2018](#); [Bensby & Lind, 2018](#)). These observations have given rise to the appearance of different models that try to explain the existence of the aforementioned objects, that is, how these metal-rich objects have lost their lithium well below the value inherited from their natal cloud. In [Llorente de Andrés et al. \(2024\)](#) we took advantage of a homogeneous sample of 1332 field stars to test the Galactic migration model proposed by [Guiglion et al. \(2016, 2019\)](#). These authors proposed that these metal-rich dwarfs are old stars that came from the inner regions of the Galaxy. These stars would have depleted their lithium in their journey from their place of birth, which had a high metallicity, to their current position.

Sixteen of the 1332 stars that composed our sample were lithium-poor stars ($A(\text{Li}) < 1.0$ dex) with high metallicity ($[\text{Fe}/\text{H}] > 0.15$ dex) and ages above 8 Gyr. The ages of these sources were obtained from [Llorente de Andrés et al. \(2021\)](#). We chose the ages obtained by the authors of that work with the PARAM code when possible and we turned to the ages recovered from the literature when the former values were not available.

[Guiglion et al. \(2019\)](#) distinguished four populations in the $[\alpha/\text{Fe}]$ vs. $[\text{M}/\text{H}]$ plane: a thin-disk, a chemical thick-disk, a metal-rich α -rich population, and a super-metal-rich ($[\text{M}/\text{H}] > 0.2$

dex) solar- α population. In order to determine whether the aforementioned stars belong to the thin disk or the thick disk, we obtained the titanium abundance ($[\text{Ti}/\text{H}]$) for these objects from the literature. When the $[\text{Ti}/\text{H}]$ value was not available, we turned to the value of $[\alpha/\text{Fe}]$. The $[\text{Ti}/\text{Fe}]$ values derived for the test stars are lower than ~ 0.04 dex, chemically indicating that they belong to the thin disk (de la Reza et al., 2023).

To analyse the kinematics of the test stars we employed *galpy*, a Python package for Galactic dynamics calculations fully described in Bovy (2015). When a Galactic potential is selected, this tool can calculate the trajectory of a star in the Milky Way, taking its position, proper motion, radial velocity, and distance, as well as the distance to the Galactic centre from the Sun (R_0) and the circular velocity in that point (v_0) as inputs. The proper motions, radial velocities, and distances for our sample of high-metallicity Li-poor stars were taken from *Gaia* DR3 (Gaia Collaboration et al., 2023). Despite the plethora of data released in *Gaia* DR3, HD 73526 and Kepler-46 do not have radial velocities available in that source. We therefore turned to Gaia Collaboration et al. (2018b) and Brewer & Fischer (2018), respectively, to obtain this information. We employed three different potentials for our analysis: the potential described in Bovy (2015) (hereafter MW2014); the Galactic potential described in Cautun et al. (2020) (hereafter Cautun2020); and the MW2014 potential modified by adding the bar described in Dehnen (2000) (hereafter MW2014+DW). Because the results were similar in the three cases, we only discussed the results obtained with the MW2014+DW potential and the R_0 and v_0 taken from Pöder et al. (2023).

Table E.1 shows metallicities, ages, Li abundances, and the radial component of the galactocentric velocities (U) for our sample of 16 high-metallicity Li-poor stars, as well as the minimum and maximum distances to the Galactic centre and the orbit eccentricities derived from our analysis with *galpy*. In order to analyse this information, we have plotted in Fig E.1 the eccentricities obtained vs. the minimum distances to the Galactic centre. Stars with eccentricities higher than 0.22 get closer to the Galactic centre, but no clear trend is observed regarding the Li abundance: some stars with minimum distances to the Galactic centre over 7 kpc exhibit abundances below 0.3 dex, and so does a star that get closer to the Galactic centre than 5 kpc. In addition, the histogram

Table E.1: *High-metallicity Li-poor stars in our sample.*

Identifier	Age (Gyr)	[Fe/H]	A(Li)	U (km s ⁻¹)	R_{min} (kpc)	R_{max} (kpc)	e
HD115585	8.5±1.2	0.35	0.51	-50.14	4.47	8.49	0.31
HD117207	8.4±1.6	0.23	0.16	-33.4	7.73	8.88	0.07
HD134606	12.2±1.1	0.28	0.7	-20.98	7.47	8.34	0.06
HD166745	8.2±1.6	0.24	< 0.11	-7.61	4.32	8.22	0.31
HD190647	8.9±1.0	0.22	< 0.47	-32.37	5.35	8.33	0.22
HD22177	8.2±1.6	0.19	< 0.34	-8.89	5.07	8.28	0.24
HD64640	9.5±1.7	0.18	< 0.14	-23.83	7.52	8.45	0.06
HD73526	8.1±1.8	0.25	0.59	-78.91	6.85	10.41	0.21
HD102117	8.1±1.4	0.29	0.6	13.35	5.72	8.42	0.19
HD108874	12.3±1.0	0.23	0.58	44.91	7.34	10.81	0.19
HD145675	12.3±0.9	0.44	0.91	23.35	7.45	9.27	0.11
HD30306	8.4±1.7	0.17	< 0.48	5.0	8.21	11.91	0.18
HD45350	8.1±1.5	0.25	< 0.15	16.65	7.78	9.34	0.09
HD46375	10.0±1.4	0.24	0.73	9.22	7.60	8.73	0.07
HD76909	8.4±1.7	0.38	< 0.91	24.72	6.76	8.90	0.14
Kepler-46	10.5±1.2	0.172	0.39	258.74	7.42	8.50	0.07

Notes. Ages, metallicities, Li abundances, and the U component of the galactocentric velocities were taken from [Llorente de Andrés et al. \(2021\)](#). The minimum (R_{min}) and maximum (R_{max}) distance to the Galactic centre, and the orbit eccentricity (e), obtained with the MW2014+DW potential, are also listed for each object.

shown on Fig. [E.2](#) shows that the stars with higher eccentricities are associated with negative U values. Despite this, there are three stars with eccentricities below 0.10 that have $U < 0$: HD 117207, HD 134606, and HD 64640.

Among the Galactic chemical evolution models shown on Fig. 2 of [Guiglion et al. \(2019\)](#) only the model corresponding to the galactocentric bin centered at 2 kpc fits the ages and metallicities of the 16 test stars. However, most of the sample exhibits $R_{min} > 6$ kpc, and none of the test stars get closer to the Galactic centre than 4 kpc. As a result, we concluded that the test stars deviate from the chemical models proposed by [Guiglion et al. \(2019\)](#).

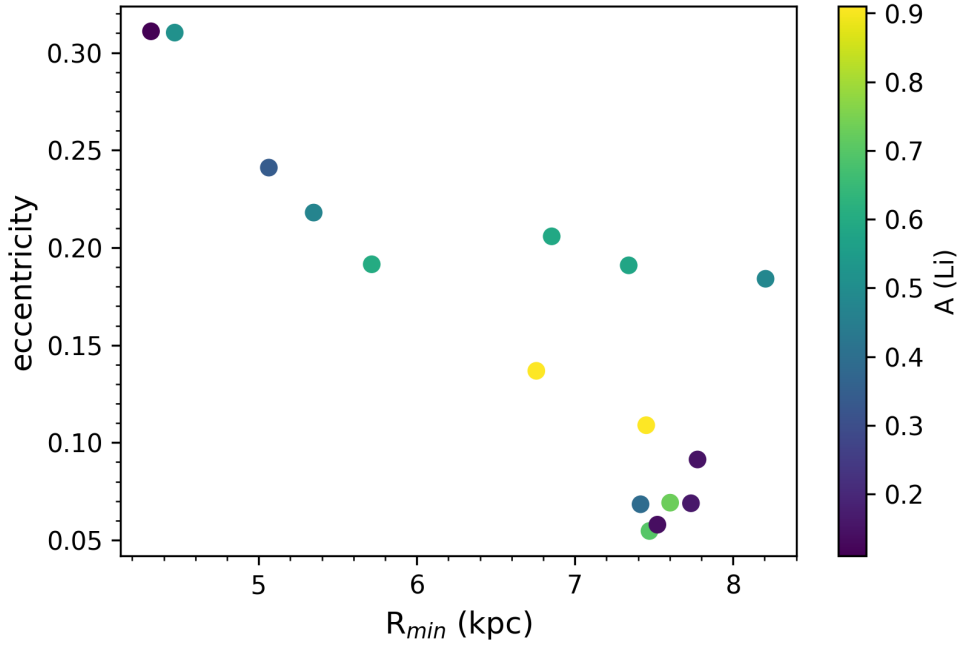


Figure E.1: Eccentricities and minimum distances to the Galactic centre obtained with galpy for the 16 high-metallicity Li-poor objects listed in Table E.1. The symbol colors indicate the lithium abundances for the corresponding sources.

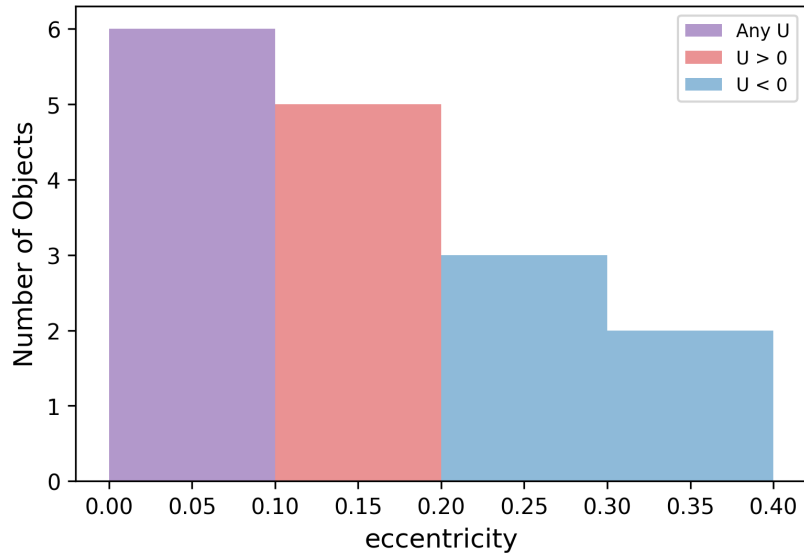


Figure E.2: Histogram showing the orbit eccentricities obtained with galpy for the 16 high-metallicity Li-poor objects listed in Table E.1. The positive values of the radial component of the Galactocentric velocity are clearly correlated with eccentricities below 0.20. The purple bar between $e=0.00$ and $e=0.10$ represents three objects with $U<0$ together with three objects with $U>0 \text{ km s}^{-1}$.